Effects of beam energy deposition and transfer in a plasma-wakefield accelerator on the microsecond timescale

Judita Beinortaitė

University College London

Department of Physics and Astronomy

Supervised by Prof Matthew Wing

Submitted to University College London (UCL) in partial fulfilment of the requirements for the award of the degree of Doctor of Philosophy.

Declaration

I, Judita Beinortaitė, confirm that the work presented in this thesis is my own. Where information has been derived from other sources, I confirm that this has been indicated in the thesis.

Judita Beinortaitė
August 2024

Abstract

Achieving high-repetition-rate operation in plasma-wakefield accelerators (PWFA) is necessary to showcase the applicability of this acceleration scheme in future high-energy physics or photon science facilities, operating at up to the MHz level. Topics ranging from technical design of high-repetition-rate plasma module cooling to repeated or cumulative effects in the plasma itself after electron beam energy deposition must be investigated to progress towards this goal. In this thesis, the effects that repeat after each bunch interaction with plasma are explored. Two processes had been studied at the PWFA facility FLASHForward, long-term ion motion, the initial observation of which indicated nanoseconds-lifetime, and long-term ionisation. This involved observing their lifetime, dependencies, especially comparing two gas species, argon and hydrogen, used in the discharge capillary. To assess the feasibility of MHz-level repetition rates in PWFA, the timescale of interest was of the order of microseconds, where the fastest-rate changes in plasma occur on the nanoseconds timescale. The experimentation involved two separate diagnostics, probe electron bunch pair which interacts with a perturbed plasma as a successive bunch and samples the plasma at a nanosecond resolution, and optical emission spectroscopy set up for discharge capillaries at FLASHForward. The knowledge of the measured lifetimes of long-term ion motion and ionisation and their dependencies will help inform the fundamental high-repetition rate limitations in PWFA as well as plasma parameter ranges for future operation.

Impact statement

High-energy particle accelerators are the essential tools for a broad range of contemporary scientific research topics, such as particle physics (e.g. LHC), and a wealth of fields that benefit from photon science facilities (e.g. European XFEL). These machines are synonymous with large-scale facilities, and new projects may stall either due to high costs or because their ecological and environmental impact may be prohibitive. Moreover, high demand for light sources and lack of accessibility results in many such facilities being oversubscribed.

Plasma-wakefield acceleration (PWFA) proved to be a very promising high-gradient alternative to future electron acceleration methods, which could reduce the footprint of future facilities and thus help make the building of new particle physics or light source facilities more feasible. However, for confirmation of applicability, experimental demonstration of high energy gain without spoiling the bunch quality at high energy efficiency and high repetition rate is needed.

The focus of this work is on the development of high-repetition-rate operation in PWFA, thus plasma effects which occur on the nanosecond-microsecond timescale in plasma and may need to dissipate before repeating the acceleration are investigated. A range of parameters, namely two gas species, different degrees of ionisation, and initial gas density were investigated, and their relations to the timescales of the effects were explored.

The results suggest that fundamentally, with the right choice of plasma parameters, MHz rates could be operated in plasma accelerators, which are compatible with currently running and future accelerators. This makes PWFA a likely application as a single-module plasma energy booster at the end of an FEL linac, such as European XFEL [1], or as staged PWFA in the collider proposal HALHF [2].

Jo's breath gave out here; and, wrapping her head in the paper, she bedewed her little story with a few natural tears; for to be independent, and earn the praise of those she loved, were the dearest wishes of her heart, and this seemed to be the first step toward that happy end.

Louisa May Alcott, *Little Women*

A little nervous breakdown can really work wonders for a girl.

Rory Gilmore in *Gilmore Girls*

Measure nine times, cut the tenth.

Lithuanian proverb

Acknowledgements

The Lithuanian proverb *measure nine times, cut the tenth* has perhaps taken a too-literal meaning in my doctorate project. To this day, I am still not sure whether 200 hours of FLASHForward beam time was too much just for *preliminary* data, which all culminated in a gruelling $\gg 8\,\mathrm{h}$ shift and a final set of results last year in August as well as a decision on the key conclusion of this project, well, very recently. However, I deem myself very lucky to have had the ideal guidance and support during this PhD adventure.

A very big and very first thanks goes to Matthew, whose grounded, patient, and caring approach to everything made this a very smooth and enjoyable project. Thanks to him, I am learning to balance the perfecting process with realistic timelines for undertaken tasks, making this project and its materialization to text a timely reality. With his keen attention to data analysis, I have learnt what makes research truly valuable.

As with all PhD journeys, this one was not spared by a whole range of challenges. However, if there is one person who is always capable of solving the most dead-end, urgent issues, always "putting out the fires at FLASHForward", that is Richard. Cheering me on everything including the smallest wins such as my first science slam, or partaking together in many of the data-taking shifts, even if it meant flying out from Oxford, his support has been indispensable to the achievements of this PhD. For this, I am immensely grateful.

Jon has taken the reigns of FLASHForward very recently and yet has become a very important member of this supervisor team. I cannot thank Jon enough for dedicating so much time this last year to help me with the analysis and the write-up. With him lie the secrets of some pretty broken English and questionable physics insights I had made in this work, some of which should have been hopefully removed by now.

To James, I am indebted greatly. His work has been such a crucial basis for this project. To help progress this topic further, he has been continuously contributing every step of the way, for all four years. Thanks to his generous help and guidance,

learning this topic was a steady and pleasant process.

The secret behind FLASHForward's smooth sailing should be mostly attributed to the tireless work of Stephan. Very responsible, yet a cool and composed attitude to some pretty stressful situations on shifts has kept me and everyone involved in this project sane. With great attention to detail, he has helped me enormously during the analysis of the data and the writing of this work, and I hope the result of this is a fair representation of our lovely FLASHForward in this thesis.

The first two years of my project at FLASHForward would not have been so smooth and straightforward to dive into if it were not for Gregor and Sarah. In my first year, Gregor introduced me to accelerators, plasmas, and PWFA — their combination. I learnt a lot from partaking in, what seemed to me at the time, a whole range of spontaneous data-taking or shift preparation adventures around DESY. I am thankful to have had such an approachable and friendly first postdoc to mentor me at the beginning of this journey.

In my second year, Sarah guided me through the tumultuous time of FLASH-Forward shutdown, where I had a last chance to take some data before the machine was shut. After a long year of slowly realising that the data was not so helpful, she made sure the year was not wasted, helping with the analysis, planning for the next shifts and the direction of the thesis together. Thanks to her, I learnt to stand on my own two feet more confidently.

One day, when I had just started at FLASHForward, always comes back to my memory, and that is when Carl sat me and Felipe down and told us to always think about our "whys". Thanks to this first lesson, and many other ones, Carl has taught me how to refine one's scientific goals so that they are based on genuine motivation and benefit to the world. Additionally, I cannot express enough how crucial it was that Carl's non-judgemental and honest guidance helped me pick up many things while struggling with my silly little fears about asking questions. Thank you one thousand times, Carl!

Now, let's return to the $\gg 8\,\mathrm{h}$ shift right about one year ago. As much as I wanted to be heroically taking the measurements to the very finish line, instead, I had assumed a wrapped-burrito state with a blanket I had the wisdom to bring with me to the control room. In the meantime, the true heroes were Advait and Lewis, taking the remaining sets of data, who were barraged by unclear instructions coming from my direction. Thanks to them, there is something I had to write about in this little piece of work. In general, it is moving to remember just how united, supportive, and dedicated everyone at FLASHForward had been during many of such shifts leading to these results. Jonas, Felipe, Pau, Stephan, and the rest of the team, including FLASHForward technicians, overcame a whole range of curveballs,

bringing the accelerator from being fully shut down to generating scientific results in just a few months. Thanks to them, I was able to gather the data necessary for this work.

On the plasma side of FLASHForward, I owe it to Jimmy, Gregor, and Harry for teaching me the ancient art of optical emission spectroscopy, how to wield the spectrometer and the FLASHForward plasma system without accidentally running the electrical discharge in a gasless capillary, or without breaking the turbopumps. In addition, I had the honour to source my code from the sacred scrolls of Harry's H-Alpha analysis scripts. Thanks to him, I was able to perform complex transmutation spells to convert all those recorded H-Alpha lines into meaningful plasma density values.

Finally, my thanks goes to the leaders of our plasma accelerator community at DESY, to Jens and Andi, for all the care and support, for the leadership that makes me proud to be part of this team.

***

I was warned about it, and I was afraid of it, and to no one's surprise, it came true: a PhD project consumed my life like how I would consume the *lussebulle* baked by Jonas. Many students will relate how challenging this can be emotionally and physically, how your whole being gets tested to the core and everything which fails this test can very much undermine the PhD project. Neither the supportive supervisors nor the most interesting topic can keep one on track when something inside breaks. From the deepest chambers of my heart, I thank all who have been with me along this journey and made sure this does not happen. Firstly, to my university mentor Jeanna, for helping me learn how my mind works, how to keep promises to myself, and that energy conservation laws apply to humans as well. To all who supervised me, especially Matthew and Richard, to whom I felt I could always turn. To dynaMENT, the mentoring program for female researchers, my mentor Elisa, and all the inspirational women scientists I met there, for giving me a whole new perspective, understanding, and confidence about being a woman in STEM. To all supportive colleagues at DESY: to Jonas, for the countless advice and helpful chats in the office; to Rob, with whom inspiring chats could happen anywhere from 28m in DESY to a pub in Ottensen. Finally, to my brothers in the FLASHForward PhD alliance, Felipe and Advait, who supported me in states of confusion of varying orders, and with a form of communication appropriate for all life situations, i.e., memes.

The four years in Hamburg which took me from being a very confused girl to a slightly less confused girl, but now with a 200-page document, were excellent because I was surrounded and supported by a whole bunch of great scientists and

lovely people. However, the many years leading to this cannot be ignored. Firstly, I can hardly imagine myself being anywhere close to achieving this dream were it not for the encouragement and support of my Jesus College tutor Malcolm. From my very first internship to that push in my final year to consider doing research, Malcolm helped me find a direction in my scientific career with which I am very pleased. During my PhD years, I felt the true value and warmth of belonging to the community of Jesus College whenever I met Laura, who was also my tutor, at the conferences I attended. Her encouraging words have sparked the same welcoming feeling and confidence, and a sense of belonging to our plasma accelerator community. Thank you, Malcolm, Laura, John, and all the other great tutors at my first university.

Naturally, no university-level physics would have made much sense to me were it not for the basics, taught by my school teachers, the physics teacher E. Rudminas and the mathematics teacher B. Budvytis at the Vilnius Lyceum. Equally, very little high-school physics could be understood without being taught my first Newton's laws, and I have been very lucky to have learnt that from the great physics teacher R. Beinortienė.

More importantly, Mrs Beinortienė also happens to be the best mother in the universe, joining the excellent parent team together with the best father in the universe. My *Mamytė* and *Tėvelis* have brought me up to be a very happy and fortunate person. All their efforts, sacrifices, and love are the principal foundations on which I could build the life I wish for, one where I can also support and take care of them as much as they have done that for me.

This education I have had the privilege to acquire is true wealth and an everlasting source of dignity. It is a core value my parents practise, a value they carry on for the next generation. Its liberating force was no secret to the most evil of forces in the world. For my great-grandfather, in the 1940s, education was the reason to be imprisoned for twelve years. For my grandfather, in the 1950s, education was not accessible because his father was a political prisoner. Because of this, and because such powers continue to underestimate women, it fell onto the women of my family to carry this torch. Thanks to my grandmother's and mother's strive for educational independence, I am humbled to call myself a third-generation woman in the field of STEM, with my mother being the key example for studying physics. Unlike my ancestors, however, I was privileged to become educated in a free Lithuania, with access to the rest of Europe which one should not take for granted. For half of the time this project took, the fragility of these privileges was continuously showcased. Just two to three thousand kilometres away, lives are sacrificed for the hard-fought Europe's freedom, for the atrocities my ancestors lived through to not repeat. Slava Ukraini, Heroiam slava.

To complete a PhD project, one must ensure to have reliable sources for sanity replenishment. For this, I am grateful to the rest of my family and my friends. My sister Emilija and Daumantas have been a stronghold I could turn to, a source of example and motivation. Norbertas and Eleonora are the sunshine in my life. My aunt Lorita, who has to deal with a whole lot of graduate projects herself, gave me a priceless perspective, which was a really necessary last push in the final stretch of this work.

For the chance to escape to a whole new world, I thank all of my companions in the three Dungeons and Dragons campaigns I took part in. Firstly, thank you to Miranda, Saanjh, Laurence, and Alex, for the support, the giggles, and being an inspiration yourselves: look, I have a whole essay of my own now! Secondly, Sascha, Manuel, Rosa, as well as Elvis and Flora, thank you for the D&D sessions and the chats, for the friendship which has made many lovely memories here in Hamburg. Last but not least, Dainora, Kristina, Mantė, Antanas, Kostas, and Arnas, for giving me the chance to lead you through a new adventure, and have a reason to see you more frequently, something that was so needed given how much I have missed my Lithuanian friends.

Fear not, dear reader, not all I did these four years was playing Dungeons and Dragons. Thank you to Jonas, Amalia, Viggo, and Lovis, for your friendship and the cherished moments in the wild west of Hamburg. Big thanks to Justas for his patience with me not practising the guitar enough so that we could start our musical project. However, I believe he is also in a similar PhD predicament, so I might have some time to catch up. Finally, thank you to my girls, who are so inspirational and above beyond smart and successful: Dainora, Dominyka, Gytė, Kristina, Mantė, and Monika.

Finally, no life achievement would be possible without my two soulmates.

There is no physical constant that is more constant in this universe than the constant of my life, Rūta. No matter how difficult things got, my truest identity was a foundation I could fall back on, and it is inseparable from my friendship with her. No matter how joyful an achievement is, it is meaningful only if I share it with her. When we were eleven, and desperate to prove that magic, mermaids, and space-time wormholes exist, I realised that the most realistic goal in achieving this is to become a scientist. Rūta, I'm on it!

"Perhaps Owen should work for DESY now" said an anonymous member of FLASHForward, jokingly. Perhaps that would not be such a bad idea. If any other researcher could benefit from the support and camaraderie that I received from Owen, without whom this project would not have come close to completion - be my guest. The perks include on-demand motivational speeches, comforting words for a

whole range of research situations, accompanying in daunting international conferences, round-the-clock care during night shifts or months-long thesis writing crisis. Although that does come with the condition of being in a long-term committed loving relationship with him. It sounds like a fair deal to me!

Contents

Table of Acronyms

Notation	Description
PWFA	Plasma-wakefield acceleration.
LWFA	Laser-wakefield acceleration.
FEL	Free electron laser.
RF	Radio-frequency.
CSR	Coherent synchrotron radiation.
PIC	Particle-in-cell.
MHD	Magnetohydrodynamic.
FWHM	Full width at half maximum.
RMS	Root-mean-square.
STD	Standard deviation.
ROI	Region of interest.
OES	Optical emission spectroscopy.
ESPEC	Electron spectrometer.
LEMS	Low-emittance measurement spectrometer.
LTIM	Long-term ion motion.
LTI	Long-term ionisation.

List of Figures

List of Tables

Chapter 1

Introduction

1.1 The instrument for modern discoveries

The understanding of the natural world has been driven by the ability to observe and interact with the different length scales of the universe. The discovery of the electron by J. J. Thomson [3] and the atomic nucleus by H. Geiger, E. Marsden, and E. Rutherford [4] validated the atomic theory of matter, which, in the modern age, was proposed by J. Dalton. The atomic theory was already a basis for the fields of science such as the kinetic theory of gases in physics [5–7], and the periodicity of elements in chemistry in the 19th century [8]. In addition, the discovery of radioactivity by H. Becquerel and further investigations by P. Curie and M. Curie hinted at the subatomic phenomena involving particles and interactions previously unknown. This marked the beginnings of quantum mechanics, particle, atomic, and molecular physics, leading to breakthroughs in physics and chemistry. Such advances would lead to new scientific tools, and vice versa: the frontier of progress in science would be set by the instrumentally achievable scale. For instance, the discovery of alpha rays led to their use as 10 MeV particle probes in the gold foil experiment by H. Geiger, E. Marsden, and E. Rutherford [4]. This revealed that energetic particles would be the key method in the investigation of micro-, atomic, and subatomic length scales. The acquisition of such particles necessitated the emergence of another crucial scientific field: particle accelerators, which have proven to be an essential instrument for modern discoveries.

Since their invention, particle accelerators have investigated a large range of phenomena, from chemical reactions to the fundamental interactions in the Standard Model of particle physics. Early accelerators, such as the first particle accelerator by E. Rutherford, J. D. Cockcroft, and E. T. S. Walton at the Cavendish Laboratory in Cambridge, accelerated protons to energies of 300 keV, which resulted in the first splitting of the lithium nucleus, with J. D. Cockroft and E. T. S. Walton

receiving a Nobel Prize in 1951 [9]. Bigger machines built over the 20th century such as the 20-GeV-electron linear accelerator at the Stanford Linear Accelerator Center (SLAC), where the composite nature of protons was discovered in 1968, and further explored in the circular lepton-proton collider HERA at DESY; 450-GeV-proton-antiproton circular accelerator Super Proton Synchrotron (SPS), where the W and Z bosons where discovered in 1983; a similar circular collider the Tevatron, which discovered the top quark in 1995; 200-GeV-electron-positron circular Large Electron–Positron Collider (LEP), used for precision measurements of the Standard Model in the 1990s. Naturally, this led to the Standard Model being empirically established. Furthermore, the discovery and harnessing of synchrotron radiation allowed the imaging of nm-scale processes [9]. It arises as charged particles, such as electrons, emit electromagnetic radiation when their velocity changes during deflection, an effect also broadly known as bremsstrahlung. Such light has a wide range of applications in biochemistry, material science, archaeology, and more. To be more precise, synchrotron radiation can probe samples and diffraction imaging of molecules, chemical reactions, and structures of proteins can be performed; it can image crystal structures for material science [9].

This reveals a trend, that the smaller the length scale of interest is, the higher the energy of accelerated particles is needed, and so the accelerator must be larger. This scaling can be understood as the manifestation of the momentum-wavelength relation in quantum mechanics, expressed by the de-Broglie wavelength [10]:

$$\lambda = \frac{h}{p} \tag{1.1.1}$$

The particle accelerators which are at the frontier of fundamental science, such as Large Hadron Collider (LHC) at CERN, reach sizes on the order tens of kilometres. Consequently, it is the tool which produced one of the most important discoveries in particle physics to date, i.e., the detection of the Higgs boson in 2012.

The balance between requirements for high-energy particle accelerators and the prohibitive machine sizes has been one of the drivers in the development of new techniques of acceleration. The first particle accelerators were based on the application of DC fields; however, despite complex methods, such as charge-transporting belts in Van-de-Graaff accelerators, the electrical fields were limited to $E \sim \mathcal{O}(1)\,\mathrm{MV\,m^{-1}}$, and so are only limited to MeV-level energies [9]. This issue brought the invention of the radio-frequency (RF) AC-fields acceleration method in a linear machine by R. Wideroe in 1928, which has been the workhorse of particle acceleration since then. From this point, the increase of the final particle energy came essentially from increasing the length of the machines. This is managed by the introduction of circular accelerators with bending magnetic fields, where the path the particles take to get accelerated in an electric field now becomes compacted into a spiral, e.g, the

cyclotron, or compacted and repeated in a circle, i.e., the synchrotron. The circular machines, also known as storage rings, have been the highest energy accelerators in the world, such as the LHC. Furthermore, for other applications, electron storage rings are used with moderate energies to produce synchrotron radiation.

While circular storage rings have a clear dominant role in many fields of research, linear particle accelerators maintain their relevance, specifically in the field of coherent light source production. Free Electron Lasers (FELs) [11] require high-energy, short electron bunches which are transported through undulators (magnets of alternating field), and can produce coherent, short-pulse synchrotron radiation. For this, a linear accelerator is more practical, as short bunches can be accelerated and electrons would not lose energy through incoherent synchrotron radiation in the bending magnets of a storage ring. Some examples of FEL facilities are FLASH [12], LCLS [13], LCLS-II, and EuXFEL [1]. At FLASH, an $E = 1.35\,\mathrm{GeV}$ electron beam produces vacuum-ultraviolet (VUV) light or soft x-rays in the nm-wavelength range. On the other hand, LCLS and EuXFEL, due to having much longer linear accelerators (linacs) of a few kilometres, can accelerate to 10-20 GeV energies and access hard x-ray ranges (keV energy, sub-nm wavelengths). However, FEL users are not always interested in the shortest x-ray wavelengths as much as the structure of the x-ray pulses. With short pulses (usually on a femtosecond scale), the rotation and diffusion time of molecules may be imaged [9].

In conclusion, particle accelerators are essential tools in a broad range of scientific topics, but the requirements of science lead to the need for higher energies, whether it is a GeV-level light source or a particle collider at the energy frontier. In turn, this has necessitated the machine size to be large.

1.1.1 Luminosity and brightness

Besides accelerated particle energy, a key parameter for particle colliders, which determines the output of the machine, is luminosity $\mathcal{L}$. Together with the cross-section of a specific event, it indicates how many such events per second a collider can produce:

$$\frac{dR}{dt} = \mathcal{L}\sigma, \tag{1.1.2}$$

where $\frac{dR}{dt}$ is the event rate and σ is the event cross section. The luminosity is calculated as follows, presented here for colliding trains of bunches [14]:

$$\mathcal{L} = Q_1 Q_2 f N_b K \iiint_{-\infty}^{+\infty} \rho_1(x, y, s, -s_0)\rho_2(x, y, s, s_0)\, dx\, dy\, ds\, ds_0, \tag{1.1.3}$$

where Q_1 is the charge of the colliding bunch from one direction, Q_2 is the charge of the bunch from the other direction, f is the train collision frequency, N_b is the

number of bunches in a train, K is the kinematic factor, with $K = 2$ for head-on collisions at the speed of light, ρ_1 and ρ_2 are the bunch density distributions. The bunches are described in the curvilinear Frenet-Serret coordinate system, where x, y are the transverse coordinates and s is the longitudinal coordinate along the ideal path for a particle in an accelerator [15]. The variable s_0 denotes the point of collision in a collider. For Gaussian bunches with densities uncorrelated in different planes [14]:

$$\rho(x, y, s) = \frac{1}{(2\pi)^{3/2}\sigma_x\sigma_y\sigma_s} e^{-\frac{x^2}{2\sigma_x^2} - \frac{y^2}{2\sigma_y^2} - \frac{(s \pm s_0)^2}{2\sigma_s^2}}. \tag{1.1.4}$$

Substituting eq. (1.1.4) for the density in eq. (1.1.3), the luminosity is:

$$\mathcal{L} = \frac{Q_1 Q_2 f N_b}{4\pi\sigma_x\sigma_y}. \tag{1.1.5}$$

Thus, the luminosity of a collider is directly proportional to the charge of the bunches, the number of bunches in a train, and the average train collision frequency. It is also inversely proportional to the transverse size of the bunch, which at the point of interaction is determined by the focusing optics and the parameter β, and the bunch emittance ϵ, both of which are explained in section 2.1.1.

Similarly, the output and the quality of the generated light in synchrotron-light sources are determined by the repetition rate of the machine and the brilliance of the light, which in turn is determined by the brightness of the electron beam, the formula of average brightness being:

$$B = \frac{Qf}{4\pi^2\epsilon_x\epsilon_y\sigma_E}, \tag{1.1.6}$$

where Q is the charge of radiating bunch, f is the average frequency of the bunches, $\epsilon_{x,y}$ is the the emittance in x, y transverse directions (see section 2.1.1), and σ_E is the energy spread of the bunch. The latter determines the frequency bandwidth of radiated light, and so the energy spread must be small.

Both the luminosity and the brightness set a certain standard on the bunch quality, specifically high charge and small emittance. Furthermore, a small energy spread is necessary for both synchrotron light sources and colliders. It is a direct factor in the formula for brightness B, whereas it is an important parameter when considering the spectral luminosity of a collider. In most cases, a narrow luminosity spectrum is desired for colliders, hence the need for a small energy spread. Furthermore, due to the very high gradient and thus chromatic focusing fields near the collider interaction point, achieving a consistently small size for the whole energy range of the bunch if it has a large energy spread would be impossible.

Finally, the output of an accelerator naturally depends on the frequency of

the acceleration. When considering the average brightness or luminosity, equally, the average frequency should be considered. So while a machine could produce very high-frequency bunches in trains, e.g., $\mathcal{O}(1)$ GHz in CLIC [16], the average frequency might be comparable to other accelerators if, for instance, the trains and the duty cycle are short.

1.1.2 Future accelerators

Future particle physics research, namely Higgs precision measurements, necessitate higher energies in colliders than current ones. To begin with, the next particle physics research phase in the post-LHC era will focus on precision measurements of the electroweak and the Higgs sector, and thus leptonic collisions are needed. The reason for this is the fact that electrons and positrons are fundamental particles, and unlike compound particles such as protons, their detector signal contains fewer background collision products, and the input parameters of the collision are more certain [17]. However, if the FCCee 100-km-circumference tunnel is built, after finishing its measurement campaign, the FCChh collider could be built in the same tunnel for high-energy reach, repeating the lepton $\rightarrow$ hadron and thus precision $\rightarrow$ high-energy particle physics research cycle established by the collider succession of SPS, LEP, and then LHC.

However, there are disadvantages to circular lepton machines. First of all, bending electrons and positrons in a magnetic field results in synchrotron radiation and energy loss in the particle beam. While this is precisely what is employed in light sources, in particle colliders, the emitted radiation would have to be managed. In addition, the loss of energy may have serious implications for the overall energy efficiency of the machine. Precisely because of this, it is favourable to use hadron machines, and other concepts for a future collider, where heavier leptons, less susceptible to synchrotron radiation, are used, such as the International Muon Collider [18]. Nevertheless, for energies which are planned for FCCee, there are strategies for maintaining efficiency and managing photon radiation. Thus the true major issue of such a collider plan is the size it requires to achieve those energies. Bending high-energy particles in a circular collider like at LHC requires very strong magnetic fields $B = 8.3\,\mathrm{T}$ [19]. For even higher energies of FCC, the necessary magnetic fields are currently beyond the technological reach. Consequently, when a short enough bending radius cannot be achieved with magnets, a larger radius machine must be built, such as the 100-km-long FCC. Because of this, linear colliders such as ILC and CLIC become a serious alternative to circular colliders.

Specific parameters of the future collider proposals are presented in table 1.2. The goal of these machines is to reach the Higgs production threshold and beyond, and the peak achievable energy of these leptonic designs varies from 365 GeV for

Facility	Type	Centre-of-mass energy	Luminosity ($10^{34}\,\mathrm{cm}^{-2}\,\mathrm{s}^{-1}$)	Frequency pattern (linear colliders only)	Total facility size	Power consumption
ILC [20]	electron-positron superconducting linear collider (31.5 MV/m)	1 TeV	1.8 (at 500 GeV)	5 Hz trains of 1312 bunches at 554 ns separation	50 km	300 MW
CLIC [16]	electron-positron normal-conducting linear collider (100 MV/m) with two-beam acceleration scheme	3 TeV	2	50 Hz trains of 312 bunches at 0.5 ns separation	48.4 km	582 MW
CCC [21]	electron-positron cryo-copper linear collider (120 MV/m)	550 GeV	2.4	120 Hz trains of 75 bunches at 3.5 ns separation	8 km	175 MW
FCCee [22] (CEPC in brackets [23])	electron-positron superconducting circular collider	365 GeV (360 GeV)	1.6 (0.5-0.8)	-	97.8 km (100 km)	359 MW (similar)
FCChh [24]	proton-proton superconducting circular collider	100 TeV	8	-	97.8 km	580 MW

Table 1.2: Proposed future collider designs. Some of these facilities, such as CLIC or FCCee, have earlier operation phases with lower centre-of-mass energy, but the highest proposed value is presented here.

FCCee to 3 TeV for CLIC. In terms of luminosity, no machine has a clear advantage. On the other hand, in terms of achievable energy, total facility size and power consumption, by a simplistic comparison, the designs for CLIC and CCC seem to be the more effective. The reason for this is the high electric field gradients $E \sim \mathcal{O}(100)\,\mathrm{MV\,m^{-1}}$ achievable with those designs, the two-beam acceleration scheme for CLIC and cryogenic copper cavities for CCC, hence the reduction in the facility size. In addition, there is no energy loss due to synchrotron radiation unlike for circular colliders FCCee and CEPC. For CLIC, the power consumption is rather extreme; however, it is proportional to accelerated energy by a comparable amount as for ILC, so its energy efficiency is not worse. Although CCC (together with CLIC) is one of the most efficient designs in table 1.2 in terms of size, it is not as mature as the proposals for ILC and CLIC.

Higher gradient accelerators would also benefit light-source facilities. While the energies and thus wavelengths demanded by the users do not require such extreme machines as for particle physics research, building few-km-length facilities such as EuXFEL also comes at a financial and environmental cost. Whether it is extending the wavelength range of existing facilities to reach shorter wavelengths without expanding the facility size or building new, but smaller facilities to solve oversubscription of current facilities, high-gradient technology in accelerators would help achieve this.

In summary, when considering the objectives of future facility designs, the proposals deliver on energy and luminosity, but financial and ecological sustainability considerations concerning the facility size favour high-gradient designs such as CLIC or CCC, with the caveat that no design can avoid the extreme power consumption in the hundreds of megawatts range. Clearly, the environmentally safe and affordable particle physics and photon science research future lies in the development of high-gradient technonology.

1.2 High-gradient technology

The main obstacle to operating high-electric fields in conventional RF (normal or superconducting) acceleration cavities is the electrical material breakdown, which limits the field in such cavities to $E \sim \mathcal{O}(100)\,\mathrm{MV\,m^{-1}}$. Because of this, alternative media have to be considered which could sustain even higher fields, such as plasma and dielectric accelerators. The acceleration conditions in both media are generated by driving an electromagnetic field wave, or a wakefield, with an energy source such as a laser pulse or a particle bunch. A driven wakefield resembles a conventional RF field in a cavity in that it also has a range of wave phases where the electric field can accelerate particles. For this technology to be applicable in future facilities, besides

high energy reach and size efficiency, these concepts must also prove they are equally as energy efficient and can adhere to the luminosity and brightness standard set by the proposals in section 1.1.2. It is worth mentioning that the beam-driven dielectric wakefield acceleration of electron bunches [25, 26] or laser-driven acceleration [27] has been a successful field so far; however, it is outside of the scope of this work. Here, acceleration in plasma is considered, and it shows promise as a serious contender for future applications in high-energy physics and photon science facilities.

The concept of acceleration in plasma was first proposed by G. I. Budker and V. I. Veksler [28], and two decades later T. Tajima and J.M. Dawson in ref. [29] proposed the first laser-driven plasma acceleration concept. Within a few years an idea for beam-driven plasma acceleration emerged [30, 31]. Since then, two different methods of driving the wakefield in the plasma, namely by laser in laser-wakefield acceleration (LWFA) and by charged particle bunches in plasma-wakefield acceleration (PWFA), have been developed.

1.2.1 Laser-wakefield acceleration

LWFA were operated initially in so-called beatwave mode, where two different-frequency laser pulses would be combined to form a plasma-frequency resonant train of pulses, capable of driving a wakefield [29]. However, high-intensity single-laser-pulse drivers became a reality with the invention of chirped-pulse amplification [32]. Since then, the field progressed greatly, first by achieving very high wakefields at hundreds of GV/m [33], then reaching high bunch quality (high charge $Q \sim \mathcal{O}(100)\,\mathrm{pC}$, low energy spread $\sigma_E \sim \mathcal{O}(1)\%$) and high energy goals with the "dream beam" milestone [34–36], and accelerating electrons to energies as high as 8 GeV with a petawatt laser [37]. Reaching higher electron energies and smaller energy spreads is possible in a plasma wakefield driven by a laser pulse by overcoming laser diffraction, trailing accelerated electron bunch dephasing, and laser pulse depletion. Each of these obstacles reduces the length of efficient and productive electron acceleration in plasma, the shortest limit being diffraction and the longest being depletion; however, the dephasing and depletion length are similar in the non-linear wakefield regime [38].

First of all, a laser pulse diffracts in a single Rayleigh length, which is shorter than the length of dephasing or depletion [38]. However, this can be circumvented with laser waveguides, such as the ones implemented in gas discharge capillaries [39–41]. The waveguide is created as a plasma refractive index channel, created by hydrodynamic redistribution of plasma, heated either by inverse bremsstrahlung [42], or optical field ionisation [43]. This allows for centimetre-scale LWFA and achievement of very high energies $E \sim \mathcal{O}(1)\,\mathrm{GeV}$ [37, 44]. Secondly, the acceleration length in laser-wakefield accelerators can be limited by dephasing. As the laser group ve-

locity in plasma is subluminal, the driven wakefield also has phase velocity $v_{ph} < c$. As a result, when accelerated electrons reach $v_e \sim c$, they can outrun the wakefield and dephase into the decelerating phase of the wakefield, thus spoiling the acceleration energy gain, efficiency, and energy spread. This can be partially prevented by plasma density tapering [38, 45]. Finally, laser energy depletion ultimately limits the length of the LWFA plasma [46, 47].

In order to be applicable in future facilities, LWFA must operate with higher energy efficiency and higher repetition rate than currently, where the wall-plug-to-beam efficiency is $\eta \sim 0.1\%$ and average repetition rates are $f \sim \mathcal{O}(1)\,\mathrm{Hz}$ for the commonly used Ti:Sa laser [48]. While this is the case for Joule-level laser pulse energies, millijoule-scale pulses can be produced at 1 kHz with the Ti:Sa lasers, and with intense self-focusing acceleration can be achieved [49, 50]. Furthermore, schemes of driving a wakefield with multi-pulse lower energy lasers can be utilised for high-repetition-rate LWFA, similarly to the beatwave LWFA [29]. In general, this is referred to as the multi-pulse LWFA [51, 52]. More specifically, in order to generate pulse trains capable of driving the wakefield in plasma at a resonant frequency, a single pulse is modulated with same-density plasma to achieve resonant modulation, resulting in the plasma-modulation plasma acceleration scheme [53, 54]. Lastly, the same Joule-level pulses can be used at kHz repetition rates at higher efficiencies if the laser technology is improved, i.e., developing diode-pumped and fibre or thin-disk lasers, or improving Ti:Sa operation efficiency and energy dissipation in the first place [48, 55, 56].

By progressing with the solutions for these issues, LWFA can present itself as an attractive small-scale acceleration technology for the future. To name a few, an LWFA module could be used as injectors for conventional accelerators, or replace the RF accelerators in FELs [38, 57, 58]. The latter would open the possibility of building compact, university laboratory-sized photon source facilities, increasing the accessibility to the users.

1.2.2 Plasma-wakefield acceleration

Future linear particle colliders and currently running FELs are designed to run at an average frequency $f \sim \mathcal{O}(10)\,\mathrm{kHz}$. For colliders, this can be seen in the bunch train patterns in table 1.2. Similarly, an FEL such as FLASH operates at 10 Hz pulse rate with 1 MHz bunch trains of $\sim 500\,\mu\mathrm{s}$ length, thus resulting in kHz-scale average frequency. Moreover, most RF-based accelerators perform with energy efficiency $\eta \sim 10\%$. Consequently, unless lasers are developed to match current RF parameters in terms of repetition rate and energy efficiency, they cannot compete with existing accelerator technology. However, in order to address the size issue of the proposed future accelerators, part of the machine could be replaced with

high-gradient technology, such as beam-driven plasma wakefield acceleration.

In plasma wakefield acceleration, the wakefield is driven by a charged particle beam, which is accelerated in a conventional accelerator [30]. If the density of the beam is sufficiently high, i.e., $n_{bunch} \gg n_{plasma}$, where n_{plasma} is the plasma electron density, the wakefield is nonlinear [31, 59, 60]. The advantage of this is that the nonlinear wakefield results in full electron expulsion from the axis during the single plasma period, resulting in an evacuated ion cavity. This provides a linear focusing field for the traversing driving and trailing electron bunches in the plasma [60]. While there are focusing phases in a linear wakefield, the dependency on the longitudinal coordinate of the focusing field and thus its limited spatial extent within one plasma oscillation does not allow for the preservation of the trailing bunch emittance [31, 61]. The detailed theoretical framework for a beam-driven plasma wakefield has been developed in refs. [62–64]. Furthermore, the wakefield was experimentally mapped in refs. [65, 66], where the transverse wakefield was confirmed to be radially linear and longitudinally uniform. As a result, both the driving and the trailing bunches are focused in the ion cavity. For the driver, this means that the bunch does not diverge, and thus a similar issue as the unguided laser diffraction in LWFA is avoided. As for the trailing bunch, the linearity of the radial fields preserves the beam emittance, a crucial feature in achieving high-quality acceleration standards for future applicability.

The trailing bunches in both LWFA and PWFA can be injected externally or internally from the background plasma electrons that get caught in the accelerating and focusing part of the wake. The latter tends to be the main method of trailing bunch injection in LWFA in order to circumvent the need for a separate particle accelerator and develop an all-optical LWFA module. On the other hand, in the context of development to replace future accelerator RF cavities, PWFA is usually operated with external injection. It is important to note that internal-injection PWFA can be a highly advantageous accelerator part in that it can boost the brightness of the beam by replacing the driver beam with a smaller-emittance high-energy injected trailing bunch [67, 68]. The externally-injected trailing bunch, delayed on the scale of hundreds of femtoseconds, can be produced at the accelerator photoinjector by stacking pulses, by manipulating the phase space of a bunch and performing transverse phase space transformation to longitudinal phase space, or by introducing a charge-cutting mask, see ref. [69] and references therein for more detail. Regardless of the method, both the driving and the trailing bunches, accelerated in the RF part of an accelerator, travel at $v \sim c$. As a result, the driven plasma wakefield phase velocity is also $v_{ph} \sim c$, and so the trailing bunch, despite its high energy gain, would not dephase unlike in LWFA and thus does not limit the plasma length. This promotes PWFA as a candidate for future accelerator methods

since the length of a plasma module only depends on the driver energy depletion.

Extracting as much energy from the plasma driver as possible is intuitively understood to be necessary for a high-efficiency PWFA operation. In addition, the trailing bunch should receive a large proportion of that energy, so that the overall PWFA energy efficiency is not vastly different from the conventional accelerator figures of $\eta \sim 10\%$. The ratio of the maximum accelerating field in the trailing bunch to the maximum decelerating field in the driver bunch is known as the transformer ratio [31, 70]. Efficient driver energy deposition, efficient trailing bunch energy extraction, and high transformer ratio can be achieved by optimised bunch profile tailoring, which in turn results in decelerating field flattening for the driving bunch and optimal beam loading for the trailing bunch [70–74]. A higher transformer ratio allows the achievement of higher trailing bunch acceleration for a given driving bunch energy and thus for a given driving bunch conventional accelerator facility size [70]. In addition, with more optimal bunch shaping, the driving bunch can lose more of its energy in longer plasma modules before the limiting effect of reacceleration kicks in. To be more precise, low-energy driver electrons slip back into the accelerating wakefield phase and thus disturb the optimal beam loading of the bunch as well as changing the transverse field profile, destroying focusing field linearity and emittance-preserving conditions in non-linear PWFA [75]. In parallel, optimal beam loading for the trailing bunch occurs when the longitudinal electric field is flattened by the fields of the bunch and thus all particles in the bunch are accelerated in the same field, preserving the energy spread. In addition, the positioning of an optimally beam-loaded trailing bunch also ensures that the bunch is fully within the range of the linear focusing field, which preserves the bunch charge and, as mentioned, the beam emittance. When these bunch qualities are maintained during acceleration in plasma, and if operated at kHz-level average repetition rates, the luminosity and brightness of a bunch are then expected to be as high as for conventional machines. While not simultaneously, many of these features were experimentally demonstrated in PWFA: high driver energy depletion [75, 76], high-efficiency acceleration [73, 74], energy spread and charge preservation [74], and emittance preservation [77]. A more detailed discussion on efficiency and bunch quality in PWFA can be found in chapters 1.5.2 and 1.5.3.

Additionally, it is necessary to suppress instabilities that may occur during the beam-plasma interaction. In theory, the driving beam enters the plasma with zero transverse offset within the beam; however, in practice, the beam is not perfectly straight. As a result, as the front of the bunch establishes the zero-axis of the transverse wakefield, the centroids of the offset parts of the bunch would naturally start to oscillate around this axis, moving the wakefield transversely with it. Consequently, an exponentially growing oscillation along the driving bunch and then the

trailing bunch develops, which is called the hosing instability [78–80]. This can be suppressed with a wide driving beam [81], as was done in ref. [77], with a large energy spread [82], or with another instability, which is ion motion [83, 84], as will be discussed in section 2.3.1. Some other types of instabilities include Weibel instability [62], which is suppressed by beams denser than plasma and narrower than the plasma wavelength [85], or the self-modulation instability for long proton drivers [86]. In summary, a driving bunch smaller in all its dimensions than the plasma wavelength, dense enough to drive a non-linear wakefield, but to not trigger, e.g., hosing instability, should lead to a stable beam-plasma interaction.

Another issue of future collider design with PWFA to consider is the acceleration of positrons in plasma. Given the ion cavity of the non-linear wakefield, the positrons would be defocused and lost if treated the same way as an electron trailing bunch. As a result, alternative PWFA modes have been investigated to accelerate and focus the positron trailing bunch, e.g., hollow plasma channels [87], finite plasma radius [88], quasilinear PWFA [89], warm PWFA [90], or single-bunch non-linear PWFA [91]. However, given how challenging it is to practically implement a positron PWFA, a future collider design, HALHF, is proposed which circumvents the need to accelerate positrons in plasma [2, 92].

Regarding future accelerators based on PWFA, given that they would need to be arranged from separate plasma modules, quality-preserving staging needs to be designed and experimentally tested. The lengths of PWFA modules are limited by the driving beam energy, which would be depleted over long distances. While single km-long plasma modules are envisioned in proton-driven PWFA schemes [86], electron-driven PWFA could only be as long as a few metres if an approximate average deceleration gradient of $\mathcal{O}(1)\,\mathrm{GV\,m^{-1}}$ and driver electron energy of $\mathcal{O}(1)\,\mathrm{GeV}$ is assumed. Therefore, the trailing bunch should be accelerated in separate staged plasma modules where the wakefield is generated by fresh driving bunches. The issues with staging are bunch divergence when emerging from the plasma, matching of the bunch size to the transverse fields of the next plasma module, removal of the depleted driving bunch and adding a new one, etc. Ref. [93] provides a summary of staging challenges and potential solutions.

The final crucial aspect of acceleration in plasma is the repetition rate. Both luminosity and average brightness of the beam are directly proportional to the frequency of the acceleration, and so without demonstration of equivalent rates as in conventional machines, PWFA could not be considered as an addition to future designs. While generally LWFA high-repetition-rate operation development requires additional progress in laser technology, conventional accelerators solve this question by inherently running at needed frequencies. As a result, PWFA can readily investigate obstacles of high-repetition-rate acceleration which stem from processes in

plasma.

1.2.3 High-repetition rate

The energy transfer from the driving bunch to the trailing bunch via the driven plasma wakefield is not a 100% efficient process [71, 73–75, 94]. Naturally, there is a proportion of driver energy that is deposited into the plasma and not extracted by the trailing bunch. This energy could drive further processes in plasma. If it does not dissipate before the next acceleration event, the conditions in plasma may degrade the trailing bunch quality during the acceleration. Alternatively, it could be benign at first but accumulate over many acceleration events in the form of internal plasma energy. High-temperature plasma could affect the wakefield quality, although not severely for a vast temperature range [90, 95]. A much more impactful effect would be plasma ionisation due to increased temperature. Plasma density, which is the density of free electrons in the plasma, directly determines the wakefield strength, and so drifts in the density would lead to a shift of accelerated trailing bunch energy. Even more crucially, large heat deposition and eventual dissipation could heat the environment, e.g., the structure of a discharge capillary and lead to damage. Thus, these processes, their timescales and their effect on the acceleration in plasma need to be investigated to understand the high-repetition-rate limiting factors originating from plasma and plasma source designs. Given that the conventional accelerators operate at kHz-scale average frequencies and MHz-scale burst frequencies, the timescales of interest are nanoseconds to millisecond.

Currently, PWFA is run by various facilities, described in section 1.3, at 1-10 Hz frequencies. As described in the previous subsection, many achievements of high-quality bunch preservation and high energy gain in PWFA did not show signs of accumulating internal heat or processes which ruin bunch quality. Moreover, LWFA at kHz rates in gas jets as plasma sources did not indicate any malign energy-dissipation processes occurring [49, 50]. However, the gas from which the plasma is formed is continuously refreshed in gas jets and there is no structure which could be damaged by heat. In addition, the plasma is generated on each shot, so any plasma evolution effects, such as plasma recombination or flow, are not experienced by each LWFA event at such rates. As a result, it can be concluded that there are no millisecond-long processes in plasma related to deposited energy that cannot be reset by replenishing the source of the plasma (gas or metallic vapour) and ionising it again. Whether this timescale is sufficient for the imparted heat to dissipate in solid structures, e.g. discharge capillaries, is not known.

The next scale of the temporal evolution in plasma is the MHz frequency. As will be discussed in section 3.2.3, plasma in discharge capillaries at FLASHForward decays over microseconds. As a result, the first plasma evolution effect, which

would influence the PWFA outcome, would be the decreasing plasma density and thus decreasing electric field and final accelerated energy. Furthermore, given that significant plasma evolution is witnessed on the timescale of microseconds, this is the frequency at which plasma heating effects could be noticeable. If there is no idle time between the next PWFA event or generation of the plasma, the heat may accumulate and be an unavoidable influence on further PWFA events. While 100s of eV heating is tolerable [90, 95], higher temperature effects are unknown. Because of this, the microsecond-timescale energy dissipation and density decay processes in the plasma must be understood and strategies for their mitigation found.

Finally, the GHz-level processes in plasma relate to ions, which may be regarded as stationary on the timescale of hundreds of femtoseconds while the wakefield is driven and the trailing bunch is accelerated, but must naturally be impacted by these processes later. The plasma frequency for electrons is:

$$\omega_e = \sqrt{\frac{n_p e^2}{m_e \epsilon_0}}, \tag{1.2.1}$$

where n_p is the plasma density, e is the electron charge, m_e is the electron mass, and ϵ_0 is the vacuum permittivity. Therefore, the difference in the timescale for electron and ion movement can be reasonably expected when the plasma frequency is $\omega_e \sim \mathcal{O}(1)\,\mathrm{THz}$ for $n_e = 10^{16}\,\mathrm{cm}^{-3}$ densities, and $\sim 100\,\mathrm{GHz}$ for hydrogen ions, $\sim 20\,\mathrm{GHz}$ for argon ions. Any ion motion would disturb the uniform plasma density conditions, which, for instance, would preclude the linear focusing field in the non-linear wakefield ion cavity and thus emittance preservation, as discussed in ref. [84] and section 2.3.1. Clearly, the understanding of these developments in plasma is crucial for ensuring high beam quality in PWFA and understanding the limitations of high-repetition-rate PWFA operation, both of which inform the achievable luminosity and brightness of a plasma-based accelerator.

1.3 PWFA facilities

There are six PWFA facilities currently operating around the world. The Argonne National Laboratory was the first to perform PWFA experiments [96]. The FACET-II [97] (FACET at the time [98]) facility was the first to demonstrate energy doubling in a meter-length plasma in PWFA [99] and discover the long-term ionisation as a consequence of driver energy dissipation in ref. [100]. The current focus at FACET-II is on a range of topics from energy efficiency to emittance preservation as well as positron generation and acceleration [101]. A university-scale laboratory at Ludwig-Maximilians University in Munich has developed a hybrid wakefield acceleration scheme, where LWFA injected and accelerated bunches enter another plasma module and drive a plasma wakefield. There, the onset of the long-term ion motion was

observed, as described in ref. [102]. The same onset of ion motion was first theorised and recently experimentally observed at the AWAKE PWFA facility at CERN [103–105]. The driving bunch at AWAKE is a proton bunch of $\mathcal{O}(10)$ cm in length from the SPS accelerator [106]. With a highly energetic proton bunch, it is expected that TeV-level energy transfer to a bunch of externally injected electrons can occur in ~ 10 km of plasma [86]. More PWFA research also occurs at the SPARC Lab at INFN. The final facility to name is the PWFA research facility FLASHForward, at DESY, where this project took place. With unique access to a high-repetition-rate electron driver generation at the FLASH linac, it is a suitable research location for high-repetition-rate PWFA studies. The experimental programme and achievements are described in section 1.4, and the technical aspects of the facility are presented in chapter 3.

1.4 Overview of FLASHForward

FLASHForward (Future ORiented Wakefield Accelerator Research and Development at FLASH) is a beam-driven plasma-wakefield acceleration research facility based in DESY, Hamburg, Germany. The design and scientific programme are focused on the goal of progressing towards a plasma-wakefield accelerator suitable for future applications. This involves the research of high-average-power and high-quality beam acceleration in GV/m plasma wakefields in a reproducible and stable manner [107]. The facility is contained in the third beamline of FLASH, a soft-x-ray FEL user facility [12, 108, 109]. The first two beamlines, FLASH1 and FLASH2, generate soft x-rays [12], thus setting standards of FEL quality beams for the linac that all three beamlines share. As such, 0.4–1.25 GeV, $\sim 0.1\%$ energy spread, up to 1 nC, ~ 1 mm mrad normalised emittance, and $\mathcal{O}(100)$ µm, or $\mathcal{O}(333)$ fs, long (FWHM) beams can be delivered to FLASHForward, allowing precision investigations of PWFA.

1.5 Scientific goals

The scientific roadmap of FLASHForward should eventually lead to the development of PWFA as an accelerator module for use in FELs or colliders. This ultimate goal is more feasibly achieved by deconstructing it into a set of independent targets. In the case of FLASHForward, this is realised in three main objectives, which are displaying PWFA in 1) high average power, 2) high efficiency, and 3) high beam quality [107, 110].

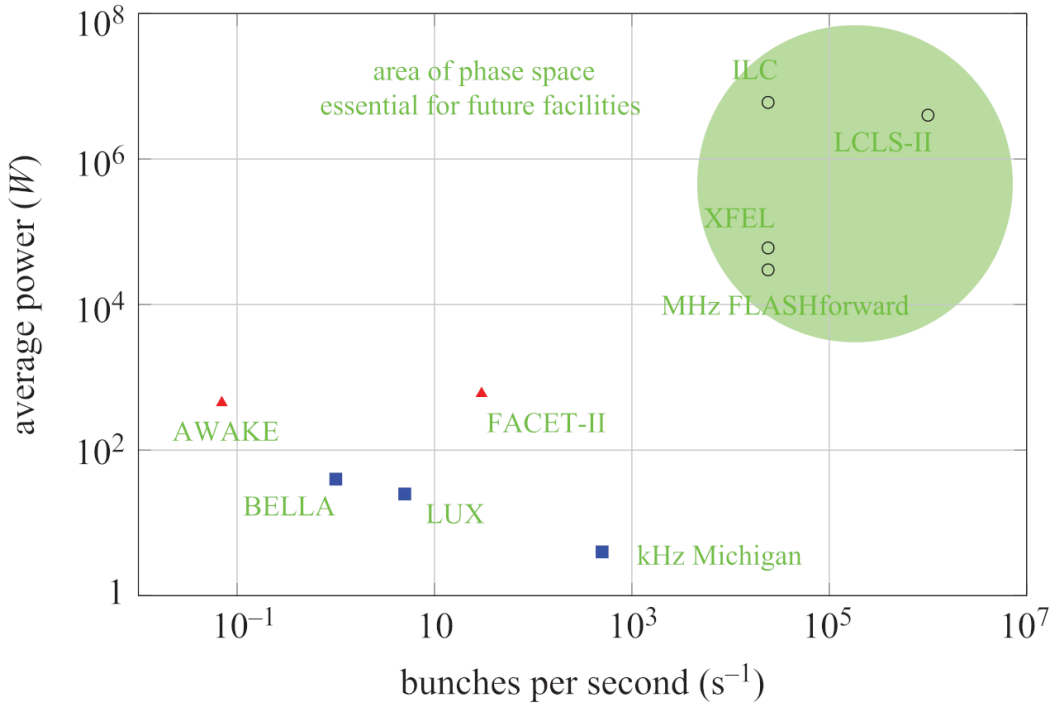

Figure 1.1: Facilities and deliverable power. ILC is a proposed collider, and XFEL and LCLS-II are FEL user facilities. The remaining are R&D facilities. Figure from ref. [107].

1.5.1 High average power

In comparison to other state-of-the-art PWFA research facilities, FLASHForward has unique capabilities to explore high-average-power PWFA, see fig. 1.1. This is owed to the FLASH bunch-train structure, described in section 3.1.1, which currently can deliver up to 30 kW of average power when operated in the highest-frequency burst mode [107]. As a result, FLASHForward is the only PWFA test-bed for high-repetition rate studies in the world. As outlined in ref. [107], these studies can be divided into the following:

1. proof-of-principle demonstration of plasma accelerator recovery,
2. operating PWFA at MHz,
3. diagnostic techniques for the MHz PWFA,
4. capillary cooling and lifetime,
5. separation of the driver from the trailing bunch at high power.

The first point entails the exploration of plasma recovery, i.e., the return of conditions for repeatable acceleration at all relevant timescales. Gas evolution and plasma generation on millisecond timescales, also known as plasma-refill studies, are feasibly done with the two-discharge setup at FLASHForward, see section 3.2.1. The shortest timescales available to explore at FLASHForward are on the nanoseconds

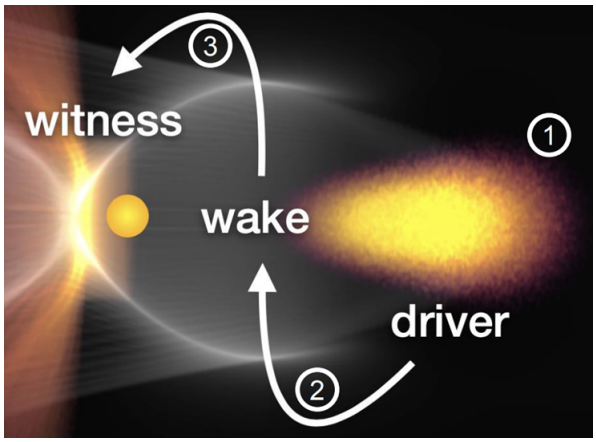

Figure 1.2: Energy transfer in PWFA. Image courtesy: Richard D'Arcy, Alberto Martinez de la Ossa.

timescale, thanks to the two-photoinjector operation mode at FLASH, where the bunch separation minimum is set by the 1.3 GHz RF frequency. At these timescales, ion motion, its recovery, and further plasma density and temperature developments upon the interaction with the bunch can be explored. So far, FLASHForward has been investigating the first point in this set of studies and is also currently focused on the MHz-PWFA efforts. ADVANCE, a laboratory at DESY, studies the plasma generation and evolution in discharge capillaries and their material durability [111]. In other words, ADVANCE lab goals also include points 2) and 4), thus being in close collaboration with FLASHForward.

1.5.2 High efficiency

The efficiency of energy transfer from the wall plug to an accelerated trailing bunch relies on two factors in a plasma-wakefield accelerator. The first is driving-bunch-to-plasma energy transfer or driver energy depletion. The second factor is plasma-to-trailing bunch energy transfer, simply referred to as energy transfer efficiency. They are displayed in fig. 1.2 as "2" and "3", respectively. Wall-plug to driving bunch efficiency is determined by the conventional accelerator part ("1" in fig. 1.2). Such value could be as high as, for example, 55%, based on the proposal for CLIC [16]. For the overall efficiency to be well within the range of current and future facilities ($\sim 10\%$), the two factors related to plasma, "2" and "3", should be somewhere near 20%, each at $\sim 45\%$, and achieved simultaneously.

The main features of the FLASHForward facility that allow investigating this topic are the ability of fs-level beam current profile and ns-level plasma density (corresponding to approximately $10^{14}\,\mathrm{cm}^{-3}$) tuning. Owing to this, beam-loaded wakefield structures can be achieved which increases driving-bunch-energy depletion and trailing bunch energy extraction. Recently, FLASHForward performed separate demonstrations of driving-bunch-to-plasma energy transfer efficiency and of plasma-

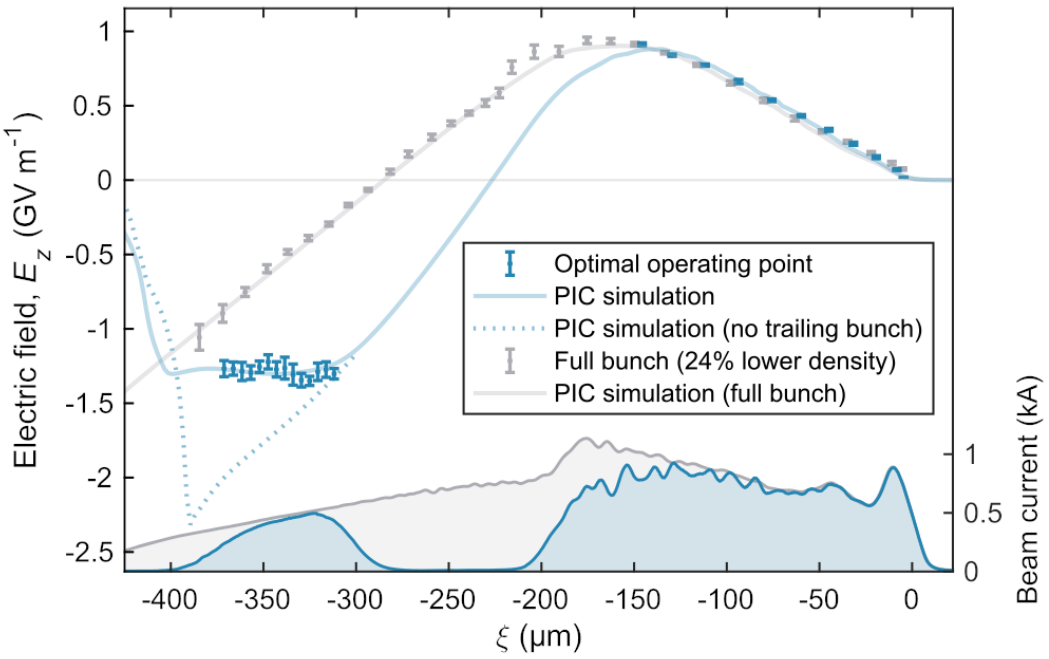

Figure 1.3: Measurement of the wakefield in the unoptimised and the optimal beam-loading and high energy-transfer-efficiency working point. In these settings, the trailing bunch flattens the wakefield thus preserving energy spread. PIC simulations of both working points agree well with the data. Figure from ref. [74].

to-trailing-bunch energy transfer efficiency. The measured values were (59±3%) [75] and (42±4%) [74], respectively. Together, this suggests an overall driver-to-trailing-bunch efficiency of around 25%. Nevertheless, achieving high energy-depletion and energy-transfer efficiencies simultaneously is a further goal of FLASHForward.

The first result, high energy transfer efficiency of (42 ± 4%) [74], was achieved by performing a multi-parameter scan and finding an optimum for preserved energy spread and increased efficiency. The parameters included in the scan were trailing and driving bunch separation and the separator location, and plasma density. A quasitrapezoidal trailing bunch current profile was reached, which flattened the accelerating field, see fig. 1.3. At the optimum, per-mille energy spread was preserved with full charge coupling, where the wakefield at the trailing bunch phase, averaged to 1.3 GV/m, was flattened to a few-percent level. As a result, this high-efficiency working point is reached at the optimum beam-loading point [72], together with the preserved trailing bunch energy spread and charge.

For the efficiency of driving-bunch-to-plasma energy transfer, the experiment focused on finding its maximum for given beam parameters [75]. The alternative could be optimising it by adjusting the driving bunch profile to reach a theoretical maximum, or to achieve high efficiency overall, which will be a future endeavour of FLASHForward. To find this maximum, the driving bunch energy had to reach a point of depletion where no more energy could be extracted without ruining the ac-

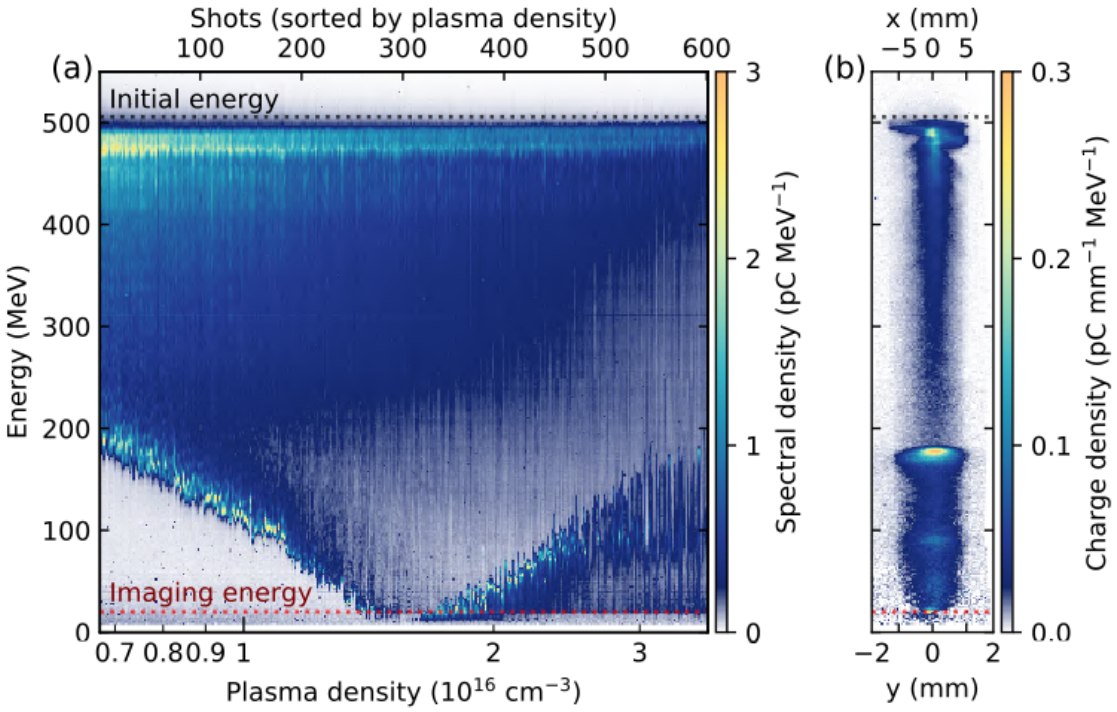

Figure 1.4: Driver bunch energy spectra with the changing plasma density (a) and driver energy spectrum at a high density, when the reacceleration is occurring (b). Figure from ref. [75].

celeration quality. While this can be done by simply extending the length of plasma the driving bunch interacts with, it was more experimentally feasible to change the plasma density instead. With a higher density, the bunch can couple to plasma more and deposit more energy. It was observed that once some of the driving bunch charge reaches non-relativistic energies, a signal of re-accelerated charge appears, limiting the full depletion, see fig. 1.4. This was observed both experimentally and in simulations, where the electrons of the driving bunch, when decelerated to non-relativistic energies, start slipping back in phase while the wakefield travels at c and thus regain energy in the accelerating phase of the wakefield. As a result, with the driving bunch parameters of this experimental campaign, a maximum of $(59 \pm 3)\%$ driver deceleration in a 195-mm-long and $\sim 1.5 \times 10^{16}\,\mathrm{cm}^{-3}$ plasma was reached. If this maximum were to be achieved simultaneously with the optimum found for the trailing bunch in ref. [74], the overall efficiency, combined with a wall-plug-to-driver of 55% (CLIC [16]), would be 14%.

In addition to these results, a method for non-destructively observing the efficiency of plasma acceleration was developed at FLASHForward [112]. It relies on the observed correlation between emitted plasma light intensity and deposited energy in the plasma by the beam. A driving bunch interacted with plasma while its charge was increased. With more charge, more energy was deposited, and the measured plasma light was calibrated with measured bunch energy deposition, see

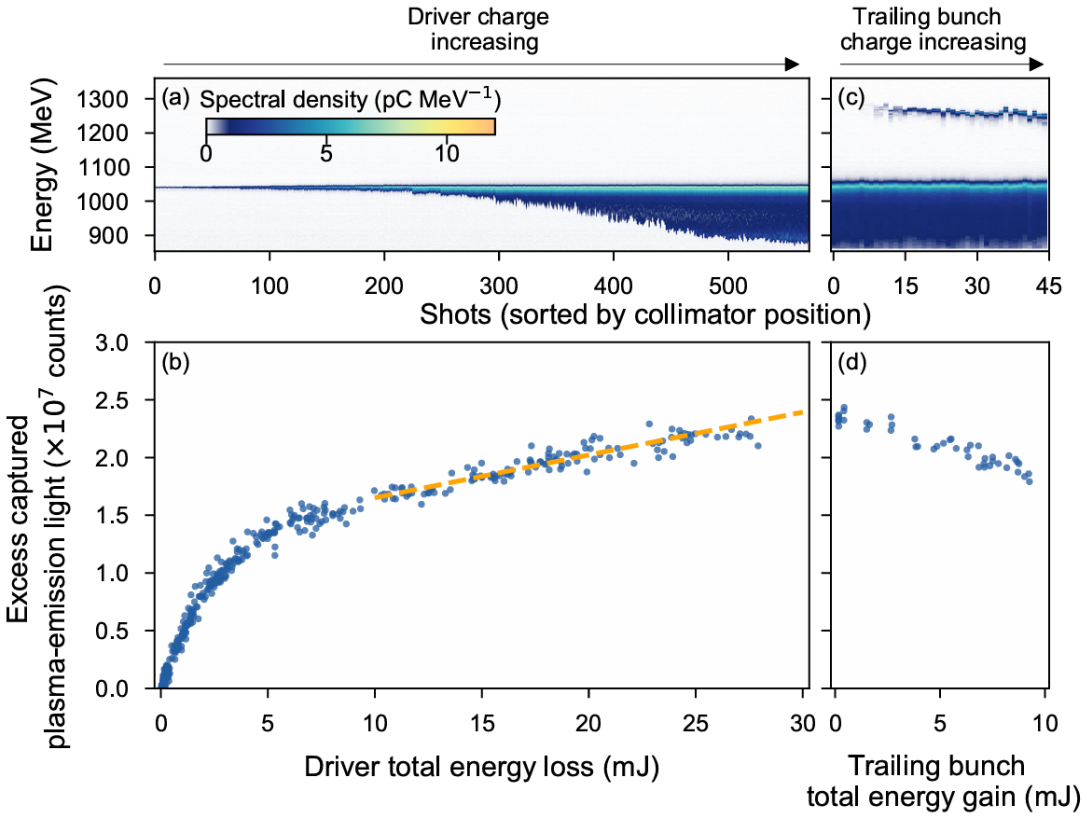

Figure 1.5: Correlating the driver energy deposition and trailing bunch energy extraction to the recorded plasma light. The driver and trailing bunch charge were adjusted with a collimator as described in section 3.1.2. The plasma light was collected with a CMOS camera. Figure from ref. [112].

fig. 1.5. Using this, longitudinally-resolved energy transfer efficiency was measured, with values as high as 58% observed, while also noting the decrease of plasma light when the trailing bunch extracts energy from the plasma wakefield. This proved to be a useful online and non-invasive tool for monitoring the plasma wakefield acceleration efficiency. It was directly used in the driver depletion results [75], where the re-acceleration signal at the electron spectrometer was confirmed by the decrease of plasma light because the electrons started gaining energy from the wakefield. The distance over which the driver was depleted could also be observed, and deduced to be 115 mm (corresponding to 4.3 GV/m) [75].

1.5.3 High beam quality

When considering luminosity for colliders, see equation 1.1.5, and beam brightness for FELs, equation 1.1.6, all factors besides acceleration repetition rate can go under the category of beam quality. Beam emittance, charge, and energy spread are all to be considered when aiming for high-quality acceleration. Luminosity and beam brightness are both directly proportional to beam charge. Beam emittance measures the area the beam spans in the transverse phase space. For a small emittance, the ranges of beam size can be smaller as the beam undergoes betatron phase advances in

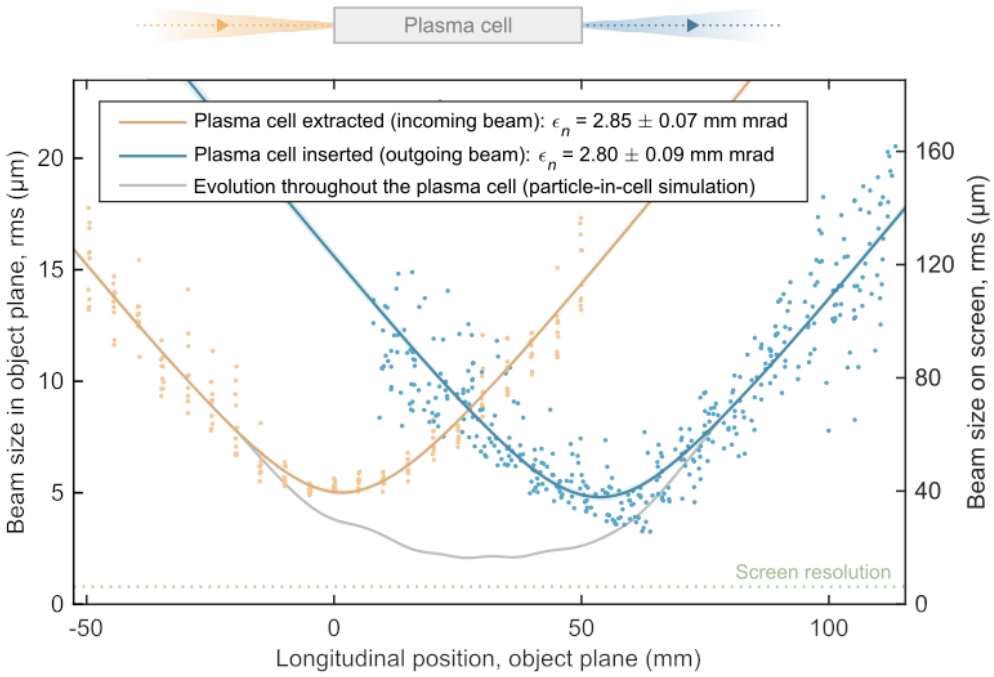

Figure 1.6: Object-plane scans of the trailing bunch as described in section 3.1.4, before and after plasma interaction. The scans are identical within experimental jitter, yielding the same emittance values. Figure from ref. [77].

an accelerator lattice, and for focal planes and interaction points the achieved beam size could be minimal [15]. Finally, beam energy spread is a direct factor in beam brightness. Its minimisation is also crucial for colliders: basic single-plane focusing magnet lattices at interaction points are chromatic, and a small energy spread allows for most of the bunch to be focused to its smallest size at the interaction point [17].

At FLASHForward, a high-efficiency beam-loaded working point helped to achieve the energy spread and charge preservation [74]. Since then, high beam quality preservation experimentation has involved the same optimisation procedure of tailoring the double-bunch profile and selecting an optimal plasma density with nanosecond accuracy.

As for the emittance, an extensive campaign was dedicated to circumventing all typical sources of emittance degradation in PWFA [77, 113]. Firstly, the emittance of a trailing bunch can increase when it undergoes betatron oscillations in the plasma. This is avoided if it is matched to the focusing forces of the wakefield [114–116]. Reaching a size at the plasma entrance that satisfies matching conditions was thus necessary. It was achieved by performing fine final-focusing quadrupole current scans (described in section 3.1.2) to find a working point for optimal focusing and thus preserved emittance. Secondly, if the double-bunch is misaligned, the trailing bunch can sample non-linear wakefields, therefore degrading emittance [65, 117]. As such, another fine quadrupole adjustment was done in the dispersive section of FLASH-

Forward (section 3.1.2). It affected the beam tilts in the downstream parts of the beamline, where the lattice dispersion is zero. Thirdly, plasma-related instabilities, such as hosing [78, 81] and ion motion [84], or beam-material scattering [118, 119] inherent to this interaction, can cause the emittance to not be preserved. In the case of the instabilities, one must avoid a driving bunch with a high density of electrons, and this was built-in for the FLASHForward working point. Due to high chromaticity at the final focusing section, the driver enters the plasma at a positive divergence and thus reduced density, not triggering any instabilities. As for gas scattering, the focusing of the trailing bunch to small beta functions helped reduce the gas scattering cross section to negligible levels [118, 119]. This resulted in 3 µm emittance being preserved in 50 mm of plasma with a peak gradient of 1.4 GV/m, see fig. 1.6. The simulations showed that at this working point, with preserved per-mille energy spread but a slight remaining trailing bunch mismatch, the betatron-oscillation-driven decoherence (and thus emittance degradation) would only be significant for plasmas of tens of metres. This was demonstrated in a simulation, where the beam was accelerated by 700 MeV in 500 mm of plasma with preserved emittance. If one assumed that the result is symmetric in the vertical plane, with preserved energy spread and charge, this outcome would also be consistent with achieving full 6D beam brightness preservation in PWFA. Such an experimental demonstration in a longer plasma is one of the next steps for FLASHForward.

In addition to preserving the beam quality of an externally injected trailing bunch, FLASHForward also investigates the improvements of internally injected trailing bunch beam quality. A PWFA accelerator module used in a multi-stage plasma linac would naturally only be developed for external injection. Nonetheless, to the benefit of future plasma-FEL facilities, an internally injected bunch from a PWFA module could have much higher brightness than the original FEL bunches [120]. This topic was researched at FLASHForward within the framework of the "X-1: high-brightness beam generation" experiment [107].

1.6 Thesis outline and focus

The energy of accelerated electrons, the efficiency of this acceleration, and each factor in the formulas for luminosity and brightness are all equally important in the development of PWFA for future applications. In order to commit to plasma accelerators as a sustainable option for these future facilities, an operation satisfying all aforementioned factors must be demonstrated. As such, the focus of this thesis is on the high-repetition-rate operation of PWFA, and, more specifically, the nanosecond-microsecond timescale processes in plasma after the driver beam energy deposition and incomplete extraction by the trailing bunch. Developments in this area should be a stepping stone towards a high-luminosity and high-brightness PWFA.

This work reviews pivotal experimental observations in ref. [102] in section 2.3.2 and ref. [100] in section 2.3.4, where it was seen how the wakefield dissipation triggered an onset of ion motion [102], which then proceeded to ionise the neutral atoms in the plasma over nanosecond-timescale [100]. The origins of this project lie in the previously carried-out investigation of the plasma density perturbations driven by the long-term motion of ions after wakefield dissipation over tens of nanoseconds in ref. [121]. This culminated in the measurement of the recovery time of the long-term ion motion, published in ref. [122] and described in chapter 4. Finally, the study of ion-motion-driven long-term ionisation, an effect akin to that observed in ref. [100], is presented in chapter 5, where a range of plasma parameters are explored with two distinct diagnostic techniques. It is thus concluded that long-term ion motion and long-term ionisation are the key effects on the nanosecond-microsecond timescale which result in plasma evolution deviation from the usual unperturbed dynamics. The detailed conclusions and further outlook are presented in chapter 6.

Chapter 2

Background and theory

2.1 Particle beam transport and acceleration

2.1.1 Transport in a conventional accelerator

This section deals with the fundamental accelerator physics related to the particle beam transport and evolution of its parameters outside of the accelerating and focusing fields of the plasma. A simplified derivation of the beam envelope evolution in a vacuum drift section is presented together with a definition of the Courant-Snyder, or Twiss parameters, following the formalism in ref. [15].

For electrons travelling in a magnetic field, the centripetal force equals the Lorentz force:

$$\frac{\gamma_e m_e v^2}{\rho}\mathbf{n} + e\mathbf{v}\times\mathbf{B} = 0, \tag{2.1.1}$$

where γ_e is the relativistic factor of the particle, m_e is the mass of the electron, $\mathbf{v} = v\mathbf{n}$ is the velocity of the particle, v being the magnitude and $\mathbf{n}$ being the unit vector parallel to the velocity direction, ρ is the radius of a local curvature, e is electron charge, and $\mathbf{B}$ is the magnetic field. If $\mathbf{B} \perp \mathbf{v}$:

$$\frac{\gamma_e m_e v^2}{\rho} + evB = 0, \tag{2.1.2}$$

and the local curvature:

$$\frac{1}{\rho} = -\frac{evB}{\gamma_e m_e v^2}. \tag{2.1.3}$$

The curvature can be expressed in Cartesian coordinates as:

$$\kappa = \frac{-x''}{(1+x'^2)^{3/2}}, \tag{2.1.4}$$

where x'' and x' are derivatives along a longitudinal coordinate s in the curvilinear

Frenet-Serret coordinate system [15]. Using the paraxial approximation $x' \approx 0$, the curvature for an electron in a bending and focusing field is:

$$\kappa \approx -x'' = -\frac{eB}{p}, \tag{2.1.5}$$

where $p = \gamma_e mv$ is the particle momentum. The magnetic field can be deconstructed into the bending, achieved with dipole magnets, and focusing parts, achieved with quadrupole magnets. Thus, $B = B_0 + gx$, where g is the focusing field gradient. In addition, we assume that the particle beam has a finite energy (or momentum) spread $\delta = \frac{\Delta p}{p_0}$, where p_0 is the central momentum of the beam. Expanding particle energy to the first order and setting $v \sim c$ gives:

$$\frac{1}{cp} \approx \frac{1}{cp_0}\left(1 - \delta\right). \tag{2.1.6}$$

Thus, the equation of motion of particles in a beam in a magnetic field is:

$$\kappa \approx -x'' = \frac{ec}{cp_0}\left(1 - \delta\right)\left(B_0 + gx\right). \tag{2.1.7}$$

Only linear terms of x and δ remain:

$$x'' + kx = -\frac{1}{\rho_0} + \frac{1}{\rho_0}\delta, \tag{2.1.8}$$

where $k = \frac{e}{p_0}gx$ is the quadrupole magnet focusing strength. To simplify eq. (2.1.8), we can ignore the first term on the right-hand side as it does not relate to the particle deviations from the ideal beam path:

$$x'' + kx = \frac{1}{\rho_0}\delta. \tag{2.1.9}$$

If the quadratic terms were also included in the particle equation of motion in x:

$$x'' + \left(k + \kappa_{0x}^2\right)x = \kappa_{0x}\left(\delta - \delta^2\right) + \left(k + \kappa_{0x}^2\right)x\delta - \kappa_{0x}kx^2, \tag{2.1.10}$$

where $\kappa_{0x} = \frac{1}{\rho_0}$. The equation of motion in the y coordinate, where bending would not happen $\kappa_{0y} = 0$, is simpler:

$$y'' + ky = ky\delta. \tag{2.1.11}$$

The steps of solving these equations are as follows. First, the homogeneous equation is solved:

$$x'' + Kx = 0, \tag{2.1.12}$$

where $K = (k + \kappa_{0x}^2)$, and the solution is:

$$\begin{bmatrix} x \\ x' \end{bmatrix} = \begin{bmatrix} C & S \\ C' & S' \end{bmatrix} \begin{bmatrix} x_0 \\ x_0' \end{bmatrix}, \tag{2.1.13}$$

where x_0 is the initial particle coordinate, and C and S are the principal solutions:

$$C(s) = \cos\left(\sqrt{K}s\right), \tag{2.1.14}$$

$$S(s) = \frac{1}{\sqrt{K}} \sin\left(\sqrt{K}s\right) \tag{2.1.15}$$

for $K > 0$. If $K < 0$:

$$C(s) = \cosh\left(\sqrt{|K|}s\right), \tag{2.1.16}$$

$$S(s) = \frac{1}{\sqrt{|K|}} \sinh\left(\sqrt{|K|}s\right). \tag{2.1.17}$$

Secondly, the inhomogeneous differential equation is solved:

$$D(s)'' + KD(s) = d, \tag{2.1.18}$$

where D is the inhomogeneous solution and d is a perturbation term. A solution can be found using Green's function, which can be constructed with the principal solutions of the homogeneous equation:

$$D(s) = \int_0^s d\,(\xi)\, G\,(s, \xi)\, \mathrm{d}\xi, \tag{2.1.19}$$

$$G(s, \xi) = S(s)C(\xi) - C(s)S(\xi). \tag{2.1.20}$$

Finally, this solution can be combined with the principal solutions of the homogeneous equation to get:

$$x(s) = aC(s) + bS(s) + \delta D(s), \tag{2.1.21}$$

where a and b are determined by the initial conditions. The third term in eq. (2.1.21) can be interpreted as the transverse offset of the particle trajectory from the ideal path due to having a different momentum/energy. Using matrix formalism, eq. (2.1.21) can be expressed as follows:

$$\begin{bmatrix} x \\ x' \\ \delta \end{bmatrix} = \begin{bmatrix} C & S & D \\ C' & S' & D' \\ 0 & 0 & 1 \end{bmatrix} \begin{bmatrix} x_0 \\ x_0' \\ \delta \end{bmatrix}, \tag{2.1.22}$$

and so the dispersion function $D(s)$ and the δ parameter represent the chromatic aberration in beam optics, which results in the focus of particles occurring at differ-

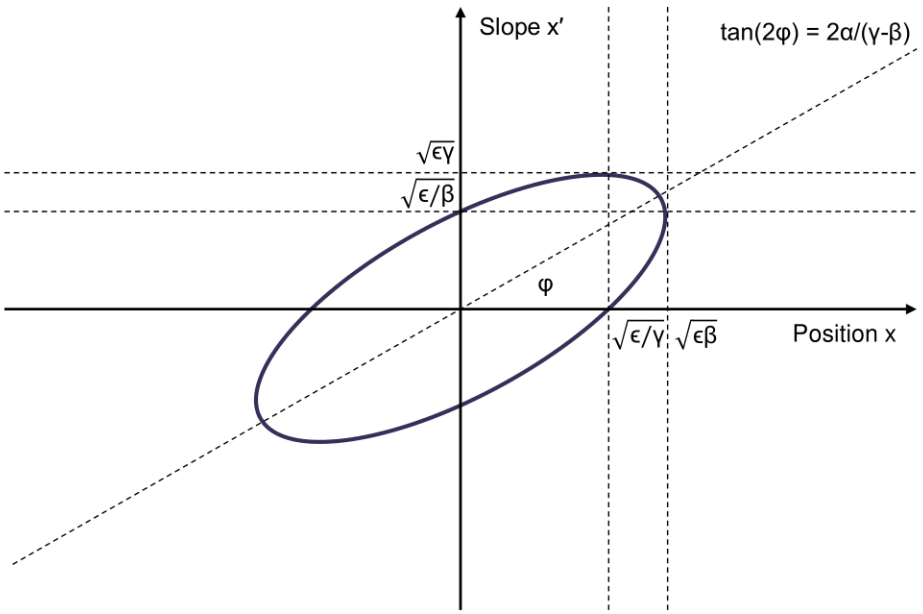

Figure 2.1: Particle beam ellipse in the position-slope phase space. Figure recreated from ref. [15].

ent points due to their energy difference. This matrix is equivalent to a transformation matrix which represents different parts of the accelerator and propagates beam parameters along the accelerator [15]. A drift space of length l would be:

$$\begin{bmatrix} x \\ x' \\ \delta \end{bmatrix} = \begin{bmatrix} 1 & l & 0 \\ 0 & 1 & 0 \\ 0 & 0 & 1 \end{bmatrix} \begin{bmatrix} x_0 \\ x'_0 \\ \delta \end{bmatrix}. \tag{2.1.23}$$

For a focusing quadrupole magnet, $K = k$ and $k > 0$, where an absence of optical aberration is assumed:

$$\begin{bmatrix} x \\ x' \\ \delta \end{bmatrix} = \begin{bmatrix} \cos\left(\sqrt{k}l\right) & \frac{1}{\sqrt{k}}\sin\left(\sqrt{k}l\right) & 0 \\ -\frac{1}{\sqrt{k}}\sin\left(\sqrt{k}l\right) & \cos\left(\sqrt{k}l\right) & 0 \\ 0 & 0 & 1 \end{bmatrix} \begin{bmatrix} x_0 \\ x'_0 \\ \delta \end{bmatrix}. \tag{2.1.24}$$

In the phase space x, x', the particle beam can be described as an ellipse:

$$\gamma x^2 + 2\alpha x x' + \beta x'^2 = \epsilon, \tag{2.1.25}$$

where α, β, γ, and ϵ are the parameters of the ellipse, also indicated in fig. 2.1. Transforming from the x, x' parameters to the ellipse parameters, the beam transfer

matrix (ignoring the optical aberration correction) is:

$$\begin{bmatrix}\beta\\ \alpha\\ \gamma\end{bmatrix} = \begin{bmatrix} C^2 & -2CS & S^2 \\ -CC' & CS'+C'S & -SS' \\ C'^2 & -2C'S' & S'^2 \end{bmatrix} \begin{bmatrix}\beta_0\\ \alpha_0\\ \gamma_0\end{bmatrix}. \tag{2.1.26}$$

For a drift space of length s:

$$\begin{bmatrix}\beta\\ \alpha\\ \gamma\end{bmatrix} = \begin{bmatrix} 1 & -2s & s^2 \\ 0 & 1 & -s \\ 0 & 0 & 1 \end{bmatrix} \begin{bmatrix}\beta_0\\ \alpha_0\\ \gamma_0\end{bmatrix}. \tag{2.1.27}$$

The ellipse parameters have a physical meaning in the phase space of the beam. The area of the ellipse, $\pi\epsilon$, corresponds to the geometric beam emittance ϵ, which, according to Liouville's Theorem, stays constant under the influence of conservative forces. The geometric emittance represents the particle-occupied part of the coordinate (x) and slope (x') phase space. In order to refer to the area in the coordinate (x) and momentum (p') phase space, which is preserved during acceleration, normalised emittance must be used:

$$\epsilon_n = \beta_e\gamma_e\epsilon, \tag{2.1.28}$$

where $\beta_e = v/c$ is the beam velocity and γ_e is the relativistic factor. The parameters β and γ (ellipse parameter, not the relativistic factor) represent the beam spatial and angular envelopes via the relations:

$$\sigma = \sqrt{\epsilon\beta}, \tag{2.1.29}$$

$$\sigma' = \sqrt{\epsilon\gamma}. \tag{2.1.30}$$

Only three parameters are needed to describe an ellipse uniquely, thus the parameters used here correlate via:

$$\beta\gamma - \alpha^2 = 1. \tag{2.1.31}$$

These ellipse parameters are the Courant-Snyder parameters, which can describe the state of the beam at a given point in a beam transport line. A solution of eq. (2.1.12) using the Courant-Snyder parameters is:

$$x(s) = \sqrt{\epsilon\beta(s)}\cos\left(\sqrt{k}\,(s-s_0)\right). \tag{2.1.32}$$

Thus, the envelope for the whole beam, i.e., when $|\cos\left(\sqrt{k}\,(s-s_0)\right)| = 1$, is expressed as:

$$\sigma(s) = \sqrt{\epsilon\beta(s)}, \tag{2.1.33}$$

which is already interpreted from the phase-space ellipse in eq. (2.1.29). Using the Courant-Snyder parameter transport in a drift space in eq. (2.1.27), the minimum beta function can be calculated:

$$\frac{d\beta}{ds} = -2\alpha_0 + 2\gamma_0 s, \tag{2.1.34}$$

$$\frac{d\beta}{ds} = 0, \tag{2.1.35}$$

$$s_w = \frac{\alpha_0}{\gamma_0}, \tag{2.1.36}$$

$$\alpha = \alpha_0 - \gamma s, \tag{2.1.37}$$

$$\alpha(s_w) = 0. \tag{2.1.38}$$

Thus, the minimum beta function occurs at the beam waist s_w, which is when $\alpha = 0$. Using eq. (2.1.31), the betatron function evolution in drift space can be expressed as:

$$\beta(s - s_w) = \beta_w + \frac{(s - s_w)^2}{\beta_w}, \tag{2.1.39}$$

where s_w is the beam waist location and β_w is the betatron function value at the waist. The whole beam size envelope is then:

$$\sigma(s - s_w) = \sqrt{\epsilon \left(\beta_w + \frac{(s - s_w)^2}{\beta_w} \right)}. \tag{2.1.40}$$

Similarly, for the angular envelope, also known as divergence:

$$\sigma'(s - s_w) = \sqrt{\epsilon \frac{1}{\left(\beta_w + \frac{(s - s_w)^2}{\beta_w} \right)}}. \tag{2.1.41}$$

The beam size envelope can be expressed with the divergence at waist σ'_w and the size at waist σ_w:

$$\sigma(s - s_w) = \sqrt{\sigma_w + \sigma'_w (s - s_w)^2}. \tag{2.1.42}$$

From these equations, the beam emittance can be understood as the parameter which determines the smallest possible size the beam can be focused to. Additionally, the betatron function reflects the focusing and beam size evolution in a beam transport line.

In PWFA, the understanding of the incoming beam size is crucial for matching the beam to the transverse focusing fields of the plasma wakefields, as described in section 2.1.2. Furthermore, a beam emerging from plasma then diverges in size and converges in divergence as described in eq. (2.1.40) and eq. (2.1.41). If the beam transport line is not set to image the beam at the exit of the plasma, the beam would reach diagnostics, e.g., an energy spectrometer dipole at the maximum size. Such

size would be convoluted with the energy dispersion generated by the dipole, and so the uncertainty of energy measurement of each beam slice would be high. Equally, this can also happen when setting the focusing elements at the wrong energy. This is a common problem in PWFA since the driving beam emerges from the plasma with a very high correlated energy spread because each slice is decelerated to a different extent. As a result, an imaging system, set to a specific object plane and energy, can correctly represent only a single energy slice on a dipole spectrometer. Similar chromatic aberration can also happen when both driving and trailing bunches are focused to very small sizes before the entrance to the plasma. Consequently, when the trailing bunch is focused, the driving bunch might not be at its waist.

2.1.2 Beam-driven plasma-wakefield acceleration

As an electron bunch of density n_b traverses the plasma, the plasma electrons are repelled by the electric field of the bunch, leaving a surplus of positive electric charge of the background plasma ions behind. Once the bunch passes, the electric field of the positive electric charge acts as a restoring force. The result is a wave in plasma, in the wake of which an electromagnetic field arises. The wakefield may be used to accelerate and focus a trailing electron bunch [30, 31, 61].

The following non-relativistic fluid equations describe the plasma [31]:

$$\frac{\partial n_p}{\partial t} + \nabla \cdot (n_p \mathbf{v_p}) = 0, \tag{2.1.43}$$

as the continuity equation, where n_p is the plasma electron density, or simply plasma density, and v_p is the velocity of flow in plasma, and

$$\left(\frac{\partial}{\partial t} + \mathbf{v_p} \cdot \nabla\right) m_e \mathbf{v_p} = e\left(\mathbf{E} + \mathbf{v_p} \times \mathbf{B}\right), \tag{2.1.44}$$

as the equation of motion for a fluid, where $\mathbf{E}$ is the electric field and $\mathbf{B}$ is the magnetic field. The wakefield-driving electron bunch causes a density perturbation n_1 in plasma electrons, where the overall density of plasma electrons is n_p. The wakefield-driving electron bunch density n_b and the plasma electron density perturbation n_1 yield the following electric field $\mathbf{E}$ according to Gauss's law [31]:

$$\nabla \cdot \mathbf{E} = \frac{e(n_1 + n_b)}{\epsilon_0}. \tag{2.1.45}$$

For a weak driver in the linear PWFA regime, where $n_1 \ll n_p$, the above equations can be linearized [31]. The continuity equation becomes:

$$\frac{\partial n_1}{\partial t} + n_p \nabla \cdot (\mathbf{v_p}) = 0, \tag{2.1.46}$$

and the equation of motion is:

$$m_e \frac{\partial \mathbf{v_p}}{\partial t} = e\mathbf{E}. \tag{2.1.47}$$

Combining the equations 2.1.45, 2.1.46, and 2.1.47, the following is obtained for the density perturbation evolution:

$$\frac{\partial^2 n_1}{\partial t^2} + \omega_p^2 n_1 = -\omega_p^2 n_b, \tag{2.1.48}$$

where the plasma oscillation frequency:

$$\omega_p = \sqrt{\frac{n_p e^2}{m_e \epsilon_0}}. \tag{2.1.49}$$

Transforming the coordinates $(z,t) \to (\xi = z - ct, \tau = t)$, $\partial_t = -\frac{1}{c}\partial_\xi$, $\partial_z = \partial_\xi$, eq. (2.1.48) is then [31]:

$$\frac{\partial^2 n_1}{\partial \xi^2} + k_p^2 n_1 = -k_p^2 n_b. \tag{2.1.50}$$

Solving this with a Green's function gives [31]:

$$n_1(\xi) = -\int_\xi^\infty n_b(\xi') \sin\left(k_p\left(\xi - \xi'\right)\right) k_p \mathrm{d}\xi'. \tag{2.1.51}$$

The density thus has an oscillatory behaviour, which naturally translates to the electric field of the wake.

The three-dimensional axisymmetric case, with ξ as longitudinal and r as transverse coordinates, becomes more complex. The expression for fields from ref. [62, 123] is:

$$E_z(r,\xi) = \frac{ek_p^2}{\epsilon_0} \int_0^{+\infty} r' \mathrm{d}r' K_0(k_p r_>) I_0(k_p r_<) \int_\xi^{+\infty} \mathrm{d}\xi' n_b(r',\xi') \cos\left(k_p(\xi - \xi')\right), \tag{2.1.52}$$

$$E_r(r,\xi) = -\frac{e}{\epsilon_0} \int_0^{+\infty} r' \mathrm{d}r' K_0(k_p r_>) I_0(k_p r_<) \left(\int_\xi^{+\infty} k_p \mathrm{d}\xi' \frac{\partial n_b(r',\xi')}{\partial r'} \sin\left(k_p(\xi - \xi')\right) + \frac{\partial n_b(r',\xi)}{\partial r'} \right), \tag{2.1.53}$$

$$B_\theta(r,\xi) = -\frac{e}{\epsilon_0} \int_0^{+\infty} r' \mathrm{d}r' K_0(k_p r_>) I_0(k_p r_<) \frac{\partial n_b(r',\xi)}{\partial r'}, \tag{2.1.54}$$

$$W = E_r - cB_\theta = -\frac{ek_p}{\epsilon_0} \int_0^{+\infty} r' \mathrm{d}r' K_0(k_p r_>) I_0(k_p r_<) \int_\xi^{+\infty} \mathrm{d}\xi' \frac{\partial n_b(r',\xi')}{\partial r'} \sin\left(k_p(\xi - \xi')\right), \tag{2.1.55}$$

where $I_0(k_p r_<)$ and $K_0(k_p r_>)$ are modified Bessel functions of the first and second kind, $r_<$ is minimum of r and r', $r_>$ is maximum of r and r', r is the transverse coordinate, and r' is the transverse coordinate over which the integration is performed. Here, the ξ longitudinal coordinate is used which corresponds to the driving beam velocity [62]. As a result, the phase velocity of the wakefield is equal to the velocity of the bunch, which in this case is assumed to be $v_b \sim c$.

Both the longitudinal electric field and the transverse wakefield are oscillatory, with radial and axial fields being 90° out of phase. Thus, there is a 90° phase range of acceleration and focusing fields. The extent of these phases scales with the plasma wavelength, which is determined by the plasma density. As a result, linear PWFA requires a specific trailing bunch positioning for a given plasma density to avoid defocusing fields. In addition, the magnitude of the accelerating and focusing fields is proportional to plasma density and the driving bunch density.

With high enough wakefield-driving electron bunch density, such as $n_b \sim \frac{n_p}{2}$, and $n_b \gg n_p$ in general, the wave-breaking fields, $E \to \frac{m_e c \omega_p}{e} \propto \sqrt{n_p}$, can be reached [59]. In this blowout regime, much higher accelerating fields are created, and all electrons are expelled from the wakefield, creating a bare ion column of uniform density with a linear focusing force [60, 124]. For an ultrarelativistic blowout, the Lu equations for the sheath of the expelled electrons at radius r_b are [63, 64]:

$$r_b \frac{d^2 r_b}{d\xi^2} + 2\left(\frac{dr_b}{d\xi}\right)^2 + 1 = \frac{4\lambda(\xi)}{r_b^2}, \tag{2.1.56}$$

$$\lambda(\xi) = \int_0^{+\infty} r n_{b0}(\xi, r)\mathrm{d}r, \tag{2.1.57}$$

where $\xi \equiv ct - z$, time and length being normalised by the plasma oscillation parameters, i.e., ω_p^{-1} and c/ω_p respectively, and the bunch density n_{b0} is normalised by the plasma density.

As for the transverse wakefield in the blowout regime, the force on the bunch is [114, 123]:

$$F_r = e\left(E_r - cB_\theta\right) = \frac{e^2 n_p}{2\epsilon_0} r = \frac{eE_0 k_p}{2} r. \tag{2.1.58}$$

where E_r is the transverse electric field, B_θ is the azimuthal magnetic field, r is the transverse coordinate, E_0 is the wave-breaking field in plasma. As the electron bunch travels in a non-linear plasma wakefield, its particles will oscillate transverselly around the zero-axis, resulting in the oscillation of the beam size envelope. For single particles in this transverse field:

$$\frac{d}{dt}\left(\gamma m_e \frac{dr}{dt}\right) = F_r, \tag{2.1.59}$$

$$\frac{d^2r}{d\xi^2} = k_\beta^2 r, \tag{2.1.60}$$

where

$$k_\beta = \sqrt{\frac{eE_0k_p}{2\gamma m_e c^2}} = \frac{k_p}{\sqrt{2\gamma}}. \tag{2.1.61}$$

The particles oscillate at the betatron frequency $\omega_\beta = \frac{\omega_p}{\sqrt{2\gamma}}$, which is dependent on the plasma frequency and thus its density, and the energy of particle through the relativistic factor γ. Given the linear focusing force, the emittance would be preserved for a single energy slice of the beam. In general, the beam size envelope evolution in a linear focusing field is [124]:

$$\frac{d^2\sigma_r}{dz^2} = -k_\beta^2\sigma_r + \frac{\epsilon^2}{\sigma_r^3}, \tag{2.1.62}$$

thus the oscillatory part of the solution would also have the betatron frequency ω_β.

Similarly to conventional accelerators, the transverse forces in the plasma wakefield have certain conditions of matching the beam size to the transverse focusing fields [114, 116]. When a beam of finite energy spread undergoes oscillations in such a field, each energy slice will oscillate at a different betatron frequency due to the energy dependence. As a result, the phase space distribution of each slice will rotate by a different angle at the end of a section of such a field, thus increasing the overall projected area of the phase space distribution of the whole beam, i.e., the emittance. As a result, there is interest in avoiding these betatron oscillations to preserve the emittance, therefore, from eq. (2.1.62):

$$\frac{d\sigma_r}{dz} = 0 \Rightarrow \frac{d^2\sigma_r}{dz^2} = 0, \tag{2.1.63}$$

$$k_\beta^2\sigma_r^4 = \epsilon^2, \beta_{matched} = \frac{\sigma_r^2}{\epsilon} = \frac{1}{k_\beta}. \tag{2.1.64}$$

In summary, the basics of plasma-wakefield acceleration theory presented here highlight the dependence of this process on the plasma electron density n_p and the wakefield-driving electron bunch density n_b. To begin with, both of these quantities determine whether the driven field is linear or non-linear. Secondly, for both of these regimes, plasma density directly affects the plasma frequency, which is a factor in the phase of the longitudinal and the transverse wakefields. Thus, the acceleration and focusing of the trailing bunch of the same spatial parameters will be different when the plasma density is varied. Thirdly, the absolute magnitude of the accelerating and focusing forces can also be higher for higher plasma densities and higher driving bunch charge densities. Finally, plasma density determines the betatron oscillation frequency, which results in different sizes and divergences at the plasma exit for an unmatched beam energy slice.

2.2 Micro- and macroscopic physics of plasmas

2.2.1 Particle encounters in plasma

In plasma accelerators, the driven wakefield mediates the energy deposition from the driver to the plasma and the trailing bunch. This energy, which remains in plasma, must dissipate via a range of channels: particle collisions, consequent heat conduction, neutral atom or molecule excitation, ionisation, etc. Spitzer presented the methods of calculating the timescales of these interactions in ref. [125]. A summary is given here.

If a group of test particles enters a plasma, they will collide and diffuse amongst other, so-called field particles. As a result, this group will have their velocity reduced in the original direction $w_{\parallel}$ and the distribution of $w_{\perp}$ velocities will widen. To calculate the rate of such velocity diffusion in the velocity space, mean values of single-encounter velocity changes need to be calculated:

$$\langle (\Delta w_{\perp})^2 \rangle = 8\pi n_f w^3 p_0^2 \ln\left(p_m/p_0\right), \tag{2.2.1}$$

where n_f is the field particle density, $p_0 = \frac{Z Z_f e^2}{4\pi\epsilon_0 m w^2}$ is the deflection impact parameter at 90° deflection, and p_m is the arbitrary cut-off for the integration performed to acquire this average. In p_0, Z is the charge of the test particles, Z_f is the charge of the field particles, e is the electron charge, ϵ_0 is the vacuum permittivity, and m is the test particle mass. This expression may have a factor of correcting functions $\Phi(l_f w) - G(l_f w)$; however, they approach unity when $l_f w$ is large either due to the high velocity w of high field particle mass, where $l = \sqrt{\frac{m}{2k_B T}}$, k_B is the Boltzmann constant, and T is the particle temperature.

The factor $\ln(p_m/p_0)$ may be defined as the Spitzer, or Coulomb, $\ln\Lambda$ factor [125, 126]. The cut-off parameter p_m is defined as the distance where the transverse velocity dispersion of test particles $\langle (\Delta w_{\perp})^2 \rangle$ is not influenced by larger distances. To be more precise, charge density changes are no longer random over distances larger than set by this factor and are rather affected by the macroscopic electrical force scale [125], i.e., Debye shielding allows the Coulomb forces to be disregarded at larger distances [126]. In addition, the factor has to be adjusted for quantum effects when the electron temperature is high, i.e., when an electron gets deflected, its diffraction angle will be large and thus impact distances need to be modified [125]. As a result, the Spitzer $\ln\Lambda$ factor is given by:

$$\ln\Lambda = \ln\left(\frac{12\pi}{Z Z_f e^3}\left(\frac{\epsilon_0^3 k_B^3 T^3}{n_e}\right)^{1/2}\right) = \ln\left(\frac{12\pi n_e}{Z Z_f}\lambda_D^3\right), \tag{2.2.2}$$

where λ_D is the Debye length. For the case of plasmas in this work, $n_e \sim 1 \times$

$10^{16}\,\mathrm{cm}^{-3}$, $T_e \sim 10\,\mathrm{eV} \sim 1.2 \times 10^5\,\mathrm{K}$, implying $\ln\Lambda$ is around 8.5.

The average parallel velocity change is calculated as follows:

$$\langle \Delta w_\parallel \rangle = -A_D l_f^2 \left(1 + \frac{m}{m_f}\right) G(l_f w), \tag{2.2.3}$$

and average square parallel velocity change:

$$\langle (\Delta w_\parallel)^2 \rangle = \frac{A_D}{w} G(l_f w), \tag{2.2.4}$$

where A_D is the velocity diffusion constant:

$$A_D = \frac{e^4 n_f Z^2 Z_f^2 \ln\Lambda}{2\pi\epsilon_0^2 m^2}. \tag{2.2.5}$$

The particle transverse velocity diffusion timescale is defined as:

$$\langle (\Delta w_\perp)^2 \rangle t_D = w^2, \tag{2.2.6}$$

$$t_D = \frac{2\pi\epsilon_0^2 m^2 w^3}{n_f Z^2 Z_f^2 e^4 \ln\Lambda}. \tag{2.2.7}$$

As the velocity diffuses transversely in the velocity space, the velocity of this particle group becomes isotropic. In addition to the development of the isotropy, each collision also results in particle energy exchange ΔE. The average $\langle \Delta E \rangle$ over the speed distribution of the test particles, where ΔE is the energy exchange of a single encounter is:

$$\Delta E = \frac{m}{2}\left(2w\delta w_\parallel + \left(\delta w_\parallel\right)^2 + (\delta w_\perp)^2\right), \langle (\Delta E)^2 \rangle = m^2 w^2 \langle \left(\Delta w_\parallel\right)^2 \rangle. \tag{2.2.8}$$

The timescale for this is:

$$\langle (\Delta E)^2 \rangle t_E = E^2, \tag{2.2.9}$$

$$t_E = \frac{\pi\epsilon_0^2 w^3 m^2}{2 n_f Z^2 Z_f^2 e^4 \ln\Lambda G(l_f w)}, \tag{2.2.10}$$

where $E = \frac{mw^2}{2}$ is original kinetic energy of the particles. With both of these estimations in equations 2.2.7 and 2.2.10, the timescale for achieving both isotropy and a Maxwellian distribution of speeds at temperature T by self-collisions of the same particle species can be calculated. Assume $w = \sqrt{\langle (w)^2 \rangle} = \sqrt{\frac{3k_B T}{m}}$, then $lw = 1.5^{1/2}$ and $t_D \sim t_E$, hence, with the correcting functions factor for $lw = 1.5^{1/2}$ equal to 0.714, the self-collision time is:

$$t_c = \frac{2\pi\epsilon_0^2 m^{1/2} (3k_B T)^{3/2}}{0.714 n e^4 Z^4 ln\Lambda}. \tag{2.2.11}$$

The timescale of equipartition of energy, t_{eq}, among different particle species 1 and

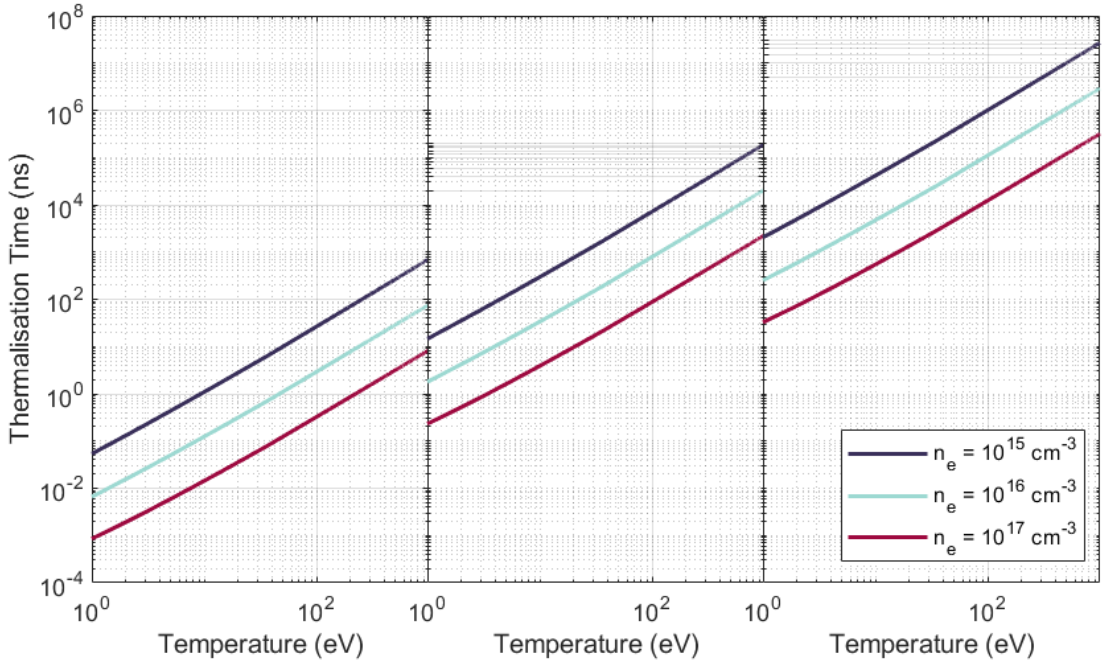

Figure 2.2: Spitzer electron-electron (left), ion-ion (middle) self-collision and electron-ion (right) equipartition times over a range of temperatures and plasma densities in argon plasma. The ion temperature was assumed to be $T_i \approx 0.002 T_e$.

2 (e.g. electrons and ions):

$$t_{eq} = \frac{6\pi^{3/2}\epsilon_0^2 m_1 m_2 k_B^{3/2}}{(2)^{1/2} n_2 Z_1^2 Z_2^2 e^4 ln\Lambda} \left(\frac{T_1}{m_1} + \frac{T_2}{m_2}\right)^{3/2} \tag{2.2.12}$$

where m_i is the mass of the i particle, k_B is the Boltzmann constant, n_i is the density of the i particle, Z_i is the charge of the i particle, e is the electron charge, T_i is the temperature of the i particles.

Using these formulae, the thermalisation timescales among the different species in plasma, namely neutral atoms or molecules, ions, and electrons, can be found. In this work, the nuclear charge is primarily $Z = 1$ because the plasma should not have ions ionised to levels higher than the first at the time of PWFA bunch arrival. Therefore, the term *plasma density*, while normally meant as the plasma electron density as defined in section 2.1.2, is also equivalent to the plasma ion density in the scope of this work.

For typical densities in PWFA, or specifically FLASHForward [127], $n_e \sim \mathcal{O}(10^{16})\,\mathrm{cm}^{-3}$, and temperatures of $T_e \sim \mathcal{O}(10)\,\mathrm{eV}$, the electron self-collision time is $\tau_{ce} \sim \mathcal{O}(100)\,\mathrm{ps}$. However, hot electrons would take much longer to approach a Maxwellian distribution for $T_e \sim \mathcal{O}(1)\,\mathrm{keV}$, since the electron self-collision time would be $\tau_{ce} \sim \mathcal{O}(80)\,\mathrm{ns}$. Due to the $\sqrt{m}$ dependence in the self-collision time, ions would take a much longer time to thermalise, namely $\tau_{c,H^+} \sim \mathcal{O}(5)\,\mathrm{ns}$ for $T_i \sim \mathcal{O}(10)\,\mathrm{eV}$, $\tau_{c,H^+} \sim \mathcal{O}(3)\,\mu\mathrm{s}$ for $T_i \sim \mathcal{O}(1)\,\mathrm{keV}$, and even longer for argon ions, $\tau_{c,Ar^+} \sim \mathcal{O}(30)\,\mathrm{ns}$ for $T_i \sim \mathcal{O}(10)\,\mathrm{eV}$,

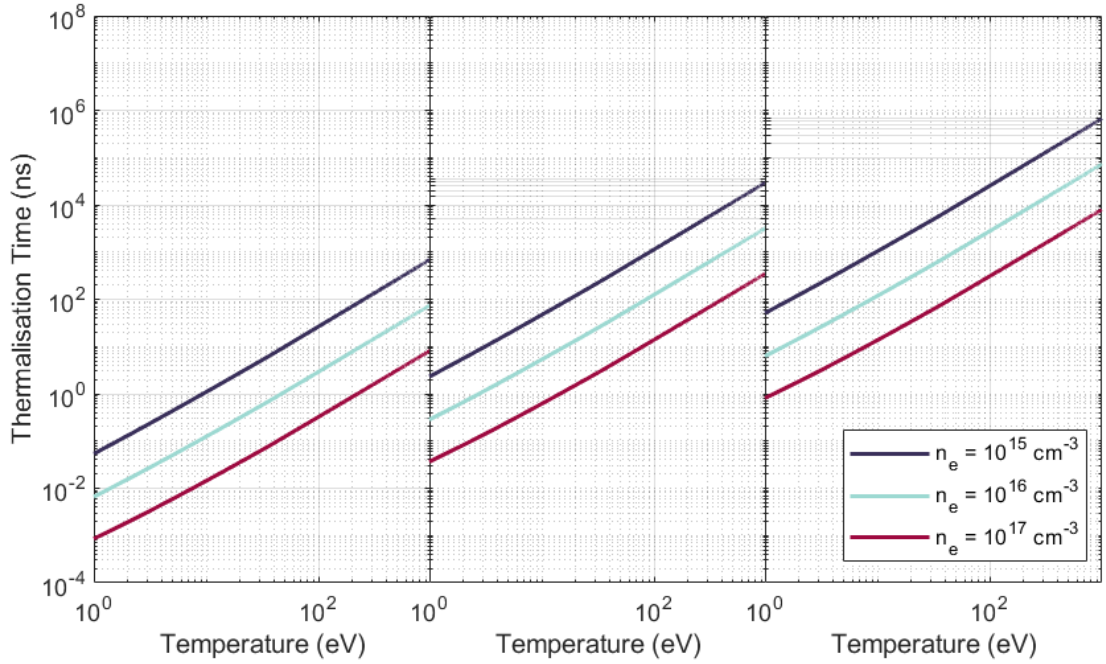

Figure 2.3: Spitzer electron-electron (left), ion-ion (middle) self-collision and electron-ion (right) equipartition times over a range of temperatures and plasma densities in atomic hydrogen plasma. The ion temperature was assumed to be $T_i \approx 0.002 T_e$.

$\tau_{c,Ar^+} \sim \mathcal{O}(20)\,\mu s$ for $T_i \sim \mathcal{O}(1)\,\mathrm{keV}$. The dependence of the self-collision time on particle temperature, density, and particle mass is reflected in fig. 2.2 for argon and fig. 2.3 for hydrogen.

During electron-ion or electron-atom collisions, the energy exchange is not very effective due to the high discrepancy between the electron and ion or neutral atom mass. Thus, the equipartition timescale for electrons and ions is much longer than the ion self-collision time, see figs. 2.3 and 2.2. There, the ion temperature was assumed to be $T_i \approx 0.002 T_e$ based on the example of $T_i = 0.025\,\mathrm{eV}$ in a $\langle T_e \rangle \sim 13\,\mathrm{eV}$ from modelled laser-ionised plasma in ref. [128]. If there is a source of heating for electrons, which maintains electrons at the same temperature, the ions should eventually equilibrate to the same temperature as electrons; otherwise, electrons will cool faster than the interaction with ions. This is similar to HOFI channel formations [129], i.e. ions would take much longer to heat from electrons alone.

For electron-atom collisions, a modification of electron and ion collision frequency is performed to account for electron collisions with neutrals in atomic hydrogen [130, 131]:

$$\nu_{ei,n} \propto \ln \Lambda + \frac{1-\alpha}{4\alpha\left(1+\left(\frac{4m_e e^4}{3\hbar^2 T_e}\right)^2\right)}, \tag{2.2.13}$$

The electron-neutral atom collision frequency is added, where its cross section was assumed to be on the order of the Bohr radius $a_0 = \hbar^2/m_e c^2$ [131]. However, for the

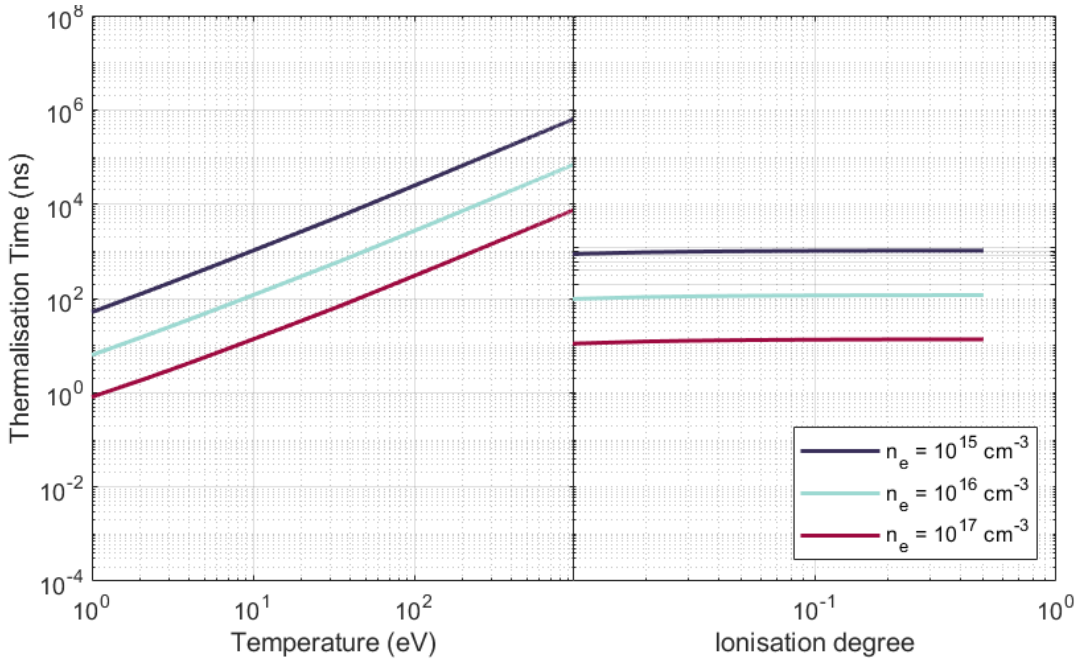

Figure 2.4: Spitzer electron collision timescale with ions and neutrals in atomic hydrogen plasma, for a range of temperatures at ionisation degree $\alpha = 0.5$ (left) and for a range of ionisation degrees at a temperature $T = 10\,\mathrm{eV}$ (right). The ion temperature was assumed to be $T_i \approx 0.002 T_e$.

range of ionisation degree α values typical at FLASHForward, i.e., from 0.01 to 0.5, this factor is not significant, see fig. 2.4. There, the timescale of electron collisions with neutrals and ions is almost identical to collisions with ions alone (fig. 2.3), and the change in ionisation degree does not affect the timescale in this range of α. As a result, the thermalisation of electrons and neutrals is expected to last even longer than that of electrons and ions.

In the case of ion-atom collisions, it should not have a strong dependence on the impact energy if it is higher than a few eV [132]. Given the experimentally measured value of $\sigma_{ia} \approx 2.5 \times 1 \times 10^{-15}\,\mathrm{cm}^2$ for argon from ref. [132], the timescale for ion-atom collisions:

$$\tau_{ia} = \frac{1}{\sqrt{2\langle v_i^2 \rangle} n_i \sigma_{ia}} = \frac{\sqrt{m_i}}{\sqrt{6 k_B T_i} n_i \sigma_{ia}}, \tag{2.2.14}$$

where m_i is the ion mass, T_i is the ion temperature (and thus also neutrals temperature), and n_i is the ion density. This timescale ranges from nanoseconds to tens of microseconds for the temperature and density range of ions used in fig. 2.2 assuming the collisional cross section stays constant.

In summary, the Spitzer formalism can be used to estimate the collisional timescale among the charged particles in the plasma, and some simple estimates can also be done for encounters with neutral particles. Electron energy exchange

with heavier particles is ineffective, especially if the electron temperature is very high. For moderately high electron temperatures (around 100 eV), thermalisation of the species in the plasma should occur over hundreds of nanoseconds, up to tens of microseconds in hydrogen, and even longer for argon.

2.2.2 Plasma generation and decay

In the context of high-repetition-rate operation in PWFA, the knowledge of the background evolution of the plasma is crucial when identifying key processes that occur after a driven wakefield. The understanding of these conditions is possible with the knowledge of the dynamics that lead to plasma generation and decay, which may also resemble the effects the electron beam may have on the plasma after the interaction. Here, an overview is presented of the methods of plasma generation and the mechanisms of its decay.

For beam-driven wakefield acceleration, a variety of plasma generation methods may be used. First, the medium from which the plasma will be created should be considered. The first-level ionisation energy of an atom, or the overall necessary ionisation energy to dissociate a molecule and ionise the atom, determines the order of the magnitude of energy necessary to deliver to the medium by the ionising mechanism. For example, the ionisation of Rubidium vapour, given the 4.2 eV ionisation energy of the first Rubidium level, would require much less energy than the full ionisation of a hydrogen molecule, 15.4 eV. However, low-ionisation degree elements, such as alkali metals in the I group of the periodic table, form metallic bonds, and therefore have to be vapourised in ovens from their liquid or solid states at room temperature [133, 134]. Such ovens necessitate intricate design to contain the vapour in the oven pipes [134]. While diatomic or inert gases such as hydrogen and argon may have high ionisation energies, they can be removed from a vacuum environment with vacuum pumps. The gas can be contained in structures such as gas jets, cells, and capillaries. The gas jets have the disadvantage of high gas load in their environment, but this is less of an issue when using a gas cell or a capillary [134]. Finally, as discussed below, the ionisation source can be more flexibly chosen with a capillary gas target, since it is the only one which, in addition to ionising laser or particle beam, can be operated with a high-voltage electrical discharge [134].

Secondly, various methods may be used to dissociate the particles into ions and electrons. All major PWFA facilities globally, such as FACET [97], AWAKE [135], or FLASHForward, have used lasers to generate plasma. Two ionisation mechanisms may be used to ionise the neutral particles: multi-photon ionisation or field ionisation. The former is possible for typical lasers used in LWFA and PWFA, i.e., in the infrared and optical spectrum by achieving high intensities of the laser pulse [134]. Field ionisation can be achieved with strong fields of the laser pulse. More precisely,

the process by which a neutral atom may be ionised is barrier-suppression ionisation (BSI). For this mode of ionisation, pulses of intensity of at least $\mathcal{O}(10^{14})\,\mathrm{W\,cm^{-2}}$ are needed to ionise hydrogen, or $\mathcal{O}(10^{16})\,\mathrm{W\,cm^{-2}}$ for helium [134]. However, the necessity to synchronise the laser to the arrival of the electron (or proton) bunches may add complexity to the operation of the PWFA. Even more crucially, the method of generating plasma with lasers is disadvantaged in terms of energy efficiency and repetition rate in light of the alternatives: driving-beam ionisation or high-voltage electrical discharge.

Similar to an intense laser pulse, a high-density electron beam can carry a high electric field sufficient to cause barrier-suppression ionisation [134]. Considering a one-dimensional simplified case for an electron in an atom of nuclear charge Z, to which an external electric field E has been applied, the potential field would be:

$$V(x) = -\frac{Ze^2}{4\pi\epsilon_0 x} - eEx. \tag{2.2.15}$$

The barrier of this field is represented by the maximum of this potential:

$$\frac{dV}{dx} = \frac{Ze^2}{4\pi\epsilon_0 x^2} - eE, x_{max} = \sqrt{\frac{Ze}{4\pi\epsilon_0 E}}. \tag{2.2.16}$$

Thus, in the classical consideration, the ionisation can occur when the barrier is suppressed by E, i.e., the potential equals the ionisation potential:

$$V(x_{max}) = U_I, \tag{2.2.17}$$

thus above the external threshold fields of:

$$E_t = \frac{\pi\epsilon_0 U_I^2}{Ze^3}. \tag{2.2.18}$$

However, in quantum formalism, a potential barrier results in an evanescent wavefunction solution to Schrodinger's equation. As a result, there is a probability of electron tunnelling when the barrier is not fully removed, and the probability grows with the applied electric field. This tunnelling ionisation can be described by a simplification to Schrodinger's equation solution, known as the Ammosov-Delone-Krainov model, for example, as done in ref. [136]. Nevertheless, the calculated electrical threshold field for barrier-suppression ionisation can inform of the range of beam fields and thus bunch charge densities which could cause significant ionisation when traversing a gas or additional ionisation for pre-ionised plasma. Such threshold field for atomic hydrogen is $32\,\mathrm{GV\,m^{-1}}$, for the first level of argon it is $43\,\mathrm{GV\,m^{-1}}$, for the second level of argon it is $133\,\mathrm{GV\,m^{-1}}$, and for the first level of lithium atom it is $5\,\mathrm{GV\,m^{-1}}$. If a simplified beam model of cylindrical shape is considered (Gaussian bunch RMS parameters are approximated as the dimensions

of a cylinder), the maximum electric field of this beam would occur at its density boundary, and be equal to [134]:

$$E_{max} = -\frac{en_b r_b}{2\epsilon_0}, \tag{2.2.19}$$

where n_b is the bunch density and r_b is the bunch radius. In the case of hydrogen, the ionising field could be reached with a driver of approximately 400 pC, 40 µm long and 10 µm in diameter. For a driver of normalised emittance 10 mm mrad, this would necessitate a betatron function of 20 mm. At FLASHForward, such sizes are on the lower end of the operated range, so some additional tunnelling ionisation by the driver could be expected as the beam field is close to the threshold. Lithium, on the other hand, could be ionised with such an electron beam via barrier suppression, which is a plasma generation method utilised at FACET [76, 97, 100]. However, the drawback of beam ionisation is head erosion, where lack of plasma, and thus lack of driven wakefield, results in divergence and emittance growth of the driver head [100, 137, 138]. Nevertheless, its inherent advantages such as synchronisation, efficiency and repetition rate make it an attractive form of plasma generation in PWFA.

Finally, high-voltage electrical discharge [130, 139, 140] is another possible gas ionisation method for PWFA, and it is the primary ionisation method utilised at FLASHFoward. While it offers many advantages to the operation of PWFA, the choice of ionisable media may be limited and the container for discharge capillaries would have specific requirements. To begin with, the container should be conducive to the generation of the discharge current, i.e., a small cross-sectional area and with a structure housing electrodes. For this, a capillary drilled in a solid such as sapphire is used at FLASHForward. As for the ionisable material, the source can be the solid of the capillary itself, such as in the wall-ablated discharge capillaries [141], or the gas supplied through capillary inlets. The latter method can be used in laser waveguiding [39–41] and proves to be useful in PWFA [127]. The advantages lie in the efficiency and the repetition rate by which plasma can be generated in the capillaries. Possible disadvantages could be the lifetime of such a device.

The mechanism by which a discharge ionises the neutral atoms or molecules is electron-impact ionisation [134]. As voltage is applied to the gas in the capillary, any pre-existing ionised particles (e.g., from cosmic radiation) will start gaining energy in the electric field. Electrons being lighter, they can be accelerated and reach high enough energy so that a collision with a neutral particle or an ion can result in ionisation. The applied voltage determines the energy electrons can achieve in the discharged material and thus the density of ionised particles in the gas and the density growth rate, as is reflected in the current-voltage characteristic in fig. 2.5. In addition, the mean free path of electrons in the gas determines how much energy the electron can gain in the field before colliding with another particle. Together

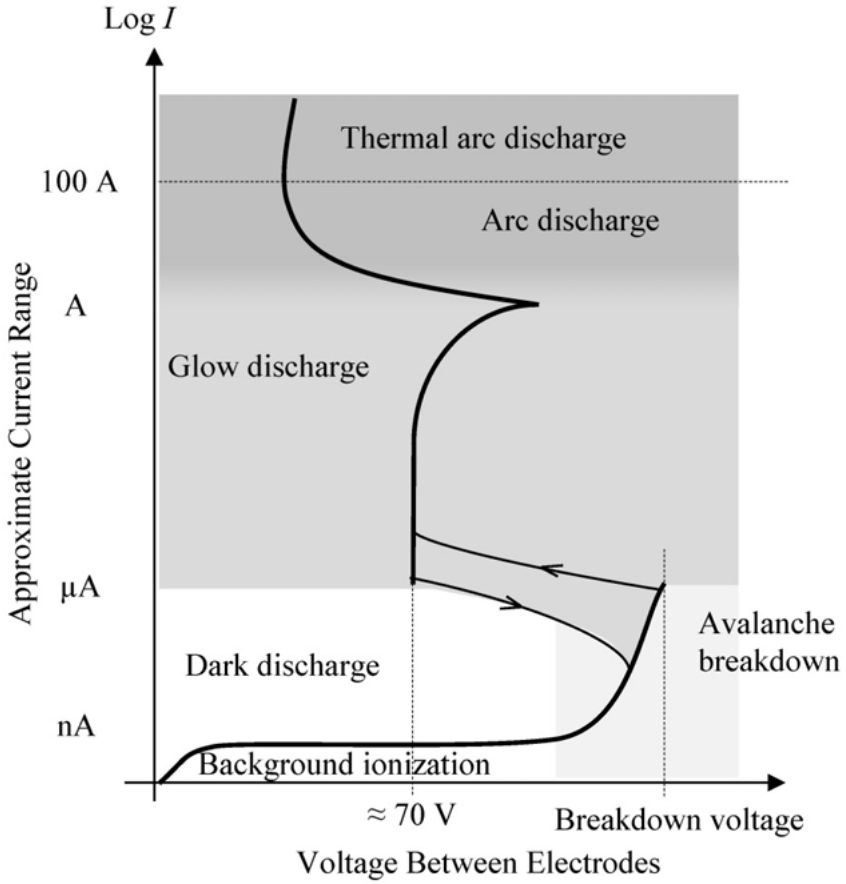

Figure 2.5: Generalised current-voltage characteristic for gases. Figure from ref. [134].

with the distance between electrodes, these quantities set the probability of electron collision. Consequently, when the distance between electrodes is larger, the applied voltage should be higher since the increased collision probability necessitates the colliding electron to have gained enough energy. Equally, if the gas density in the capillary is higher, and thus the mean free path is shorter:

$$\lambda = \frac{1}{\sigma n}, \tag{2.2.20}$$

where σ is the collisional cross section and n is the gas density in the capillary, then a higher voltage is also needed so that electrons gain enough energy before a collision. Furthermore, for very low gas densities and short distances between electrodes, a high voltage is necessary for the breakdown. The reason for this is that the mean free path is long, and the overall extent of the gas is also short, therefore the collision probability decreases, and so the electron energy should be very high in case of a collision. This balance of voltage, neutral gas density, or simply the pressure of the gas, and the distance between electrodes that is necessary for gas breakdown can be described by the Paschen curves, see fig. 2.6. Once the breakdown occurs, further ionised gas evolution is also determined by the voltage, as shown in the current-

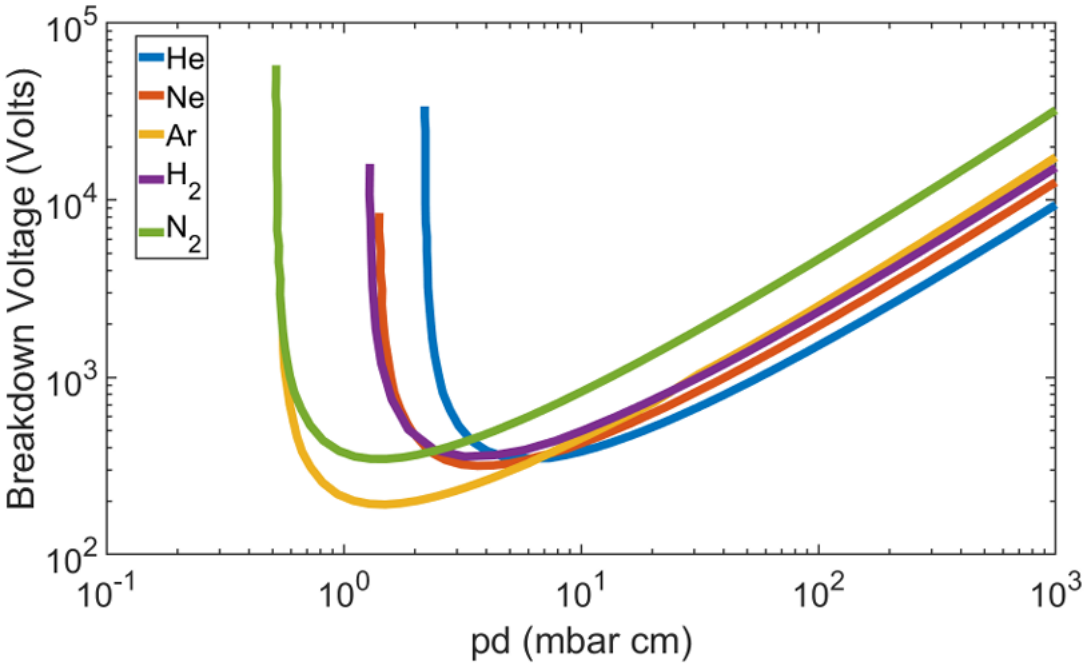

Figure 2.6: Paschen curves for a range of gases. Figure from ref. [134].

voltage characteristic in fig. 2.5. If, after breakdown, the voltage is sustained at values as high as $\mathcal{O}(1)\,\mathrm{kV}$, i.e., the breakdown voltage of gas, and the capillary conditions (pressure and length) are in the high range of the Paschen curves, the plasma is generated and maintained during the discharge via the process of avalanche ionisation [134]. Also referred to as the Townsend avalanche, this regime results in the current (or plasma density) growth rate which is proportional to the current (or plasma density) in the capillary at that time [142, 143]:

$$\frac{dn_p}{dt} = \alpha_T n_p, \tag{2.2.21}$$

where n_p is plasma density, and α_T is the first Townsend ionisation coefficient, and so:

$$n_p = n_{p0} e^{\alpha_T t}, \tag{2.2.22}$$

the plasma density growth is exponential. The plasma generation can thus be modelled as an exponential growth in its density as the electrons accelerated in the applied voltage impact-ionise the neutral particles.

In general, additional ionisation of plasma can also occur without the applied voltage. Electron-impact ionisation, which specifically takes form in avalanche ionization such as in high-voltage discharge capillaries, is utilised, for example, in the waveguide heating [42, 132, 144–146]. There, collisional ionisation is triggered by electron heating with a laser pulse. Avalanche ionisation becomes a dominant process of plasma density generation for higher pressures [42, 144]. The collisional ionisation lasts on a timescale of a few nanoseconds; however, ions in that time

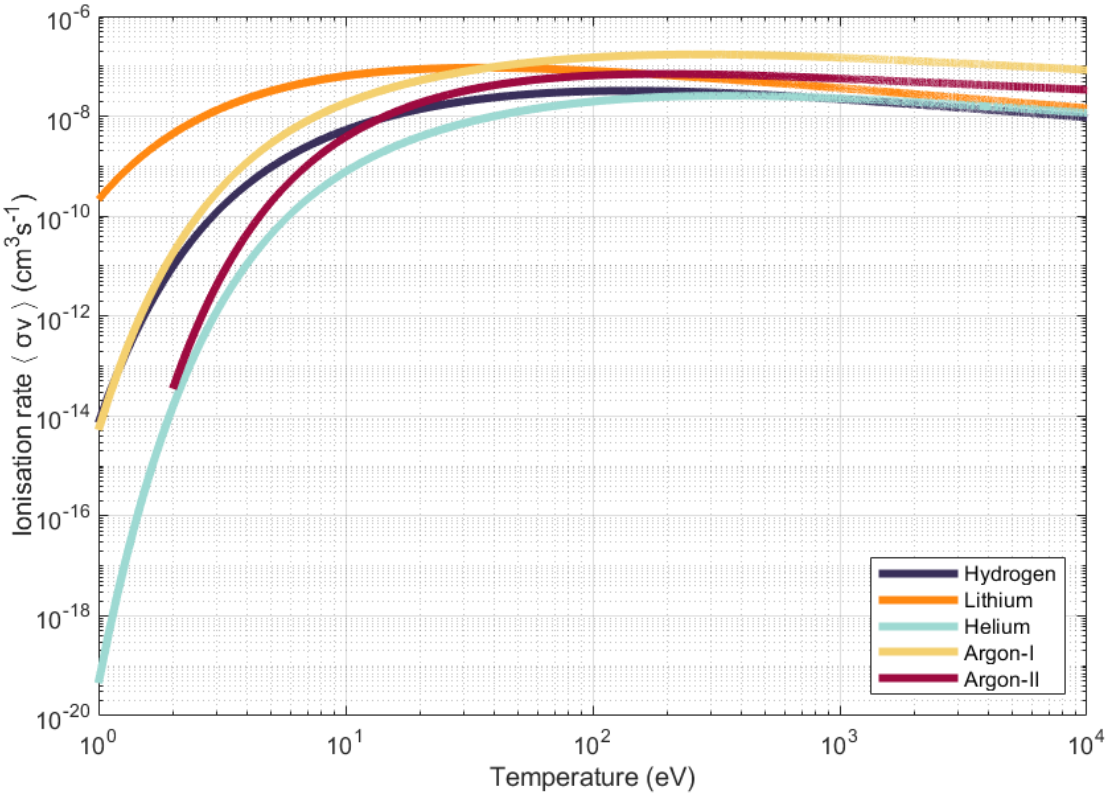

Figure 2.7: Ionisation rate $\langle \sigma v \rangle$ for a range of electron temperatures and gases. Argon-II refers to argon ionisation to the second level.

remain cold due to inefficient energy exchange [42, 132].

Under normal circumstances (no additional source of heating in plasma), the source of ionisation would be the fast electrons in the high-velocity tail of the thermal velocity distribution of electrons. Naturally, an increased plasma temperature would result in a bigger proportion of electrons with high enough energy to ionise a particle upon impact. However, the fraction of such electrons is still smaller than in the case of applied voltage, therefore the cross-section of ionisation upon electron impact is an important parameter in addition to the plasma temperature and the density of both the ionising particles and neutrals and ions. The electron-impact ionisation cross-section for most gases can be modelled as [147]:

$$\sigma(E) \propto \frac{\ln\left(E/U_I\right)}{EU_I}, \tag{2.2.23}$$

where E is the energy of the electron and U_I is the ionisation energy of the neutral or ion. The proportionality constants for this relationship were determined empirically for a range of atom species and summarised in ref. [147]. The cross-section is finite for ionising electrons with energy $E > U_I$, it reaches a maximum at $E = U_I * \exp(1)$ and decreases with electron energy from there onwards. This reflects the fact that the more energetic the electron is, the higher the probability of ionisation; however,

at a certain point, the electron speed is too high that the general collision probability is reduced, and so the ionisation probability decreases.

The total rate of electron-impact ionisation per unit volume in plasma is:

$$R_I(E) = n_e(n_0 - n_e)\sigma(E)v_e(E), \tag{2.2.24}$$

where n_e is the plasma density, n_0 is the initial gas density, σ is the electron-impact ionisation cross section for a specific energy of all electrons E and their velocity v_e. Naturally, the plasma contains a range of electron energies and velocities represented by the Maxwell-Boltzmann distribution:

$$f(v) = \left(\frac{m}{2\pi k_B T}\right)^{3/2} 4\pi v^2 e^{-\frac{mv^2}{2k_B T}}. \tag{2.2.25}$$

Given such strong dependence of the electron-impact ionisation cross section on the energy of the electron, it is important to take into account the whole range of velocities that exist in a plasma for a given temperature T_e. As such, the last two parameters in eq. (2.2.24) should be averaged over these velocities:

$$\langle \sigma v \rangle = \int_0^\infty v(E)\sigma(E)f(v)\mathrm{d}v, \tag{2.2.26}$$

and so the total rate per unit volume is given by:

$$R_I = n_e(n_0 - n_e)\langle \sigma v \rangle. \tag{2.2.27}$$

A similar formalism is applied in refs. [128, 132]. The electron-impact ionisation rate $\langle \sigma v \rangle$ can be calculated with an empirically-fitted formula from ref. [148]:

$$\langle \sigma v \rangle = A\frac{1 + PU^{1/2}}{X + U}U^K e^{-U}, \tag{2.2.28}$$

where $U = E/U_I$ is the relative electron temperature, A, K, and X are the empirical parameters from refs. [148–150]. P, equal to 0 or 1, is meant to improve the fit for specific cases when the electron energy is near the ionisation energy. This assumes that the dominant mode of ionisation is from the ground state to full first-level ionisation. However, multi-step ionisation can occur, where an electron may only excite a neutral, and ionisation is completed by another electron impact out of this excited state [132]. Such detailed modelling should be implemented for accurate simulations; however, the current model is sufficient to make comparisons between different working points and gases. The electron-impact ionisation rate is shown in fig. 2.7 for a range of temperatures and a few different gas species as well as the second argon level. For typical FLASHForward plasma temperatures $T_e \sim \mathcal{O}(10)\,\mathrm{eV}$, the ionisation rate varies greatly for different atomic species; however, the two gases

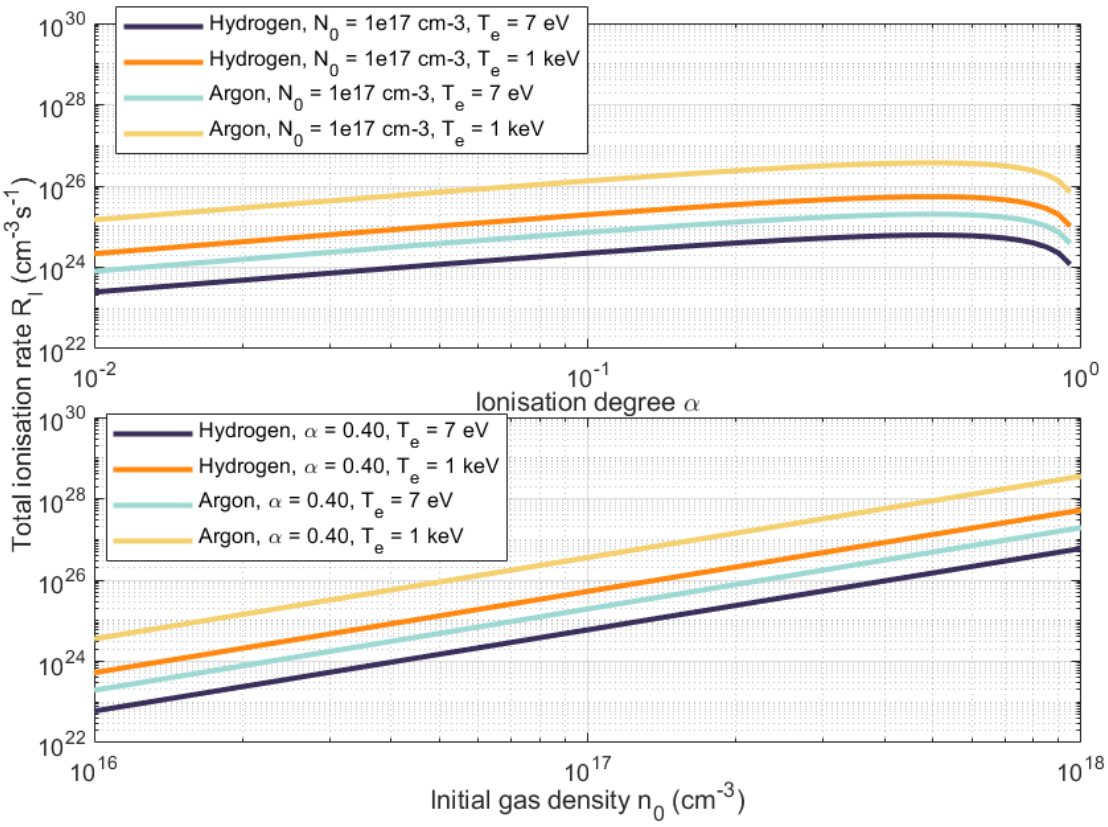

Figure 2.8: Total ionisation rate per unit volume of hydrogen and argon at low and high plasma temperatures for a range of ionisation degrees and initial atomic gas densities.

usually used, hydrogen and argon first level, are similar. For high temperatures $T_e \sim \mathcal{O}(1)\,\mathrm{keV}$, all atomic species converge to similar ionisation rates, though argon first level and hydrogen diverge more than before. The second argon level seems to have a higher ionisation rate than hydrogen for high temperatures, which implies that ions can also be ionised further by electron impact in argon.

The total rate can also be expressed in terms of the ionisation degree $\alpha = n_e/n_0$ and the initial gas density n_0:

$$R_I = n_0^2 \alpha(1-\alpha)\langle\sigma v\rangle. \tag{2.2.29}$$

Consequently, the rate of electron-impact ionisation in the plasma without the applied voltage has a quadratic dependence on the ionisation degree and the gas density from which the plasma is generated, and is directly proportional to the average product of the electron-impact ionisation cross section and the thermal velocity distribution of the electrons. In turn, the latter is dependent on the temperature of the plasma, the ionisation energy of the neutral particle or the ion, and other empirically determined parameters, unique to the species of gas. The dependence of R_I on the ionisation degree α and the initial gas density n_0 for typical operating ranges at FLASHForward are shown in fig. 2.8. While the initial gas density depen-

dence is straightforward, for ionisation degree, the total rate of ionisation is directly proportional to α until $\alpha = 0.5$, after which the lowering density of neutrals results in decreasing total rate of ionisation. Argon has slightly higher rates due to the higher ionisation cross section for it, and higher plasma temperature leads to more ionisation, by about one order of magnitude in R_I.

It is important to note that in this work, hydrogen plasma generation and other dynamics are considered for atomic hydrogen, specifically for atomic hydrogen atoms, even though the hydrogen gas comprises molecules. A similar simplification was used in the model in ref. [140]. The plasma there comprised four species: hydrogen molecules, hydrogen atoms, hydrogen atomic ions and electrons. Other configurations, such as excited molecular states of hydrogen or molecular ions, are expected to be short-lived and thus make up small fractions of the density when interacting with high electron temperature [140].

Unisolated and without a continuous source of ionisation, the plasma will interact with its environment, cool, and recombine. Firstly, collisions in plasma between ions and electrons at low velocities can lead to recombination. As detailed in ref. [126], the rate of plasma loss to recombination would be:

$$\frac{\partial n_p}{\partial t} = -\alpha n_p^2, \tag{2.2.30}$$

where n_p is plasma density, and α is the recombination coefficient, dependent on the plasma electron temperature $\alpha \propto T^{-1/2}$, the ion charge $\alpha \propto Z^2$, and other factors related to the electron capture probability by the ion to a specific energy state [125]. By inspection, a solution is proposed, where [126]:

$$n_p(t) \propto \frac{1}{\alpha t}. \tag{2.2.31}$$

Consequently, one should expect to have faster plasma decay for high initial gas densities.

Secondly, plasma interaction with the wall of a capillary results in thermal conduction and heating of the capillary structure. Heating of the discharge capillary wall was observed in refs. [130, 140]. In addition, the charged particles thus slow down at the wall and have a higher probability of recombination. This process can be described as ambipolar diffusion [126, 151], following:

$$\frac{\partial n_p}{\partial t} = D_a \nabla^2 n_p. \tag{2.2.32}$$

By separation of variables, the solution for temporal evolution turns out to be:

$$n_p(t) \propto e^{-t/\tau}, \tag{2.2.33}$$

where τ is a constant set by the boundary conditions and inversely related to the diffusion coefficient $\tau \propto 1/D_a$. An in-depth discussion of plasma diffusion is ref. [151].

Finally, the plasma and gas can leave the capillary through the open ends of the capillary. Following the simple model presented in ref. [130], the loss of density due to the outflow should also be exponential:

$$n = n_0 e^{-t/\tau}, \tag{2.2.34}$$

where n_0 is the initial density, $\tau \sim \frac{l}{c_i}$ is the timescale of the outflow, l is the length-scale of the capillary, $c_i = \sqrt{\frac{T_e}{m_i}}$ is the ion acoustic velocity. For short discharge capillaries (3-5 mm long), the timescale was 150-250 ns [130, 139]. At FLASH-Forward, the outflow and thus replenishing of the capillary with new gas from the continuous flow through the inlets should thus occur on the microsecond timescale, contributing to the overall plasma decay, see section 3.2.3 and ref. [127]. In addition, the scaling of this outflow timescale with the ion mass via the ion acoustic velocity suggests that hydrogen would outflow faster.

To summarise, a plasma can be generated from a contained gas or metallic vapour by an electron or laser beam, or a high-voltage discharge. The process which is the basis of the latter method is electron-impact ionisation, which can also occur if electrons are heated. An evolving plasma interacts with its environment, which in the case of discharge capillaries is the capillary wall and the surrounding vacuum. The result is a decaying plasma, cooling at the wall, recombining, and being expelled through the capillary ends.

2.2.3 Optical emission spectroscopy

Discrete wavelength light is emitted from plasma as atoms undergo radiative recombination or deexcitation. With the knowledge of the origin of these lines and the dependencies of their features on the conditions in the plasma, optical emission spectroscopy (OES) of the plasma light can inform about these conditions, namely plasma density, temperature, or composition. Plasma atomic composition determination is the most straightforward task since it mainly requires the identification of the lines in the measured spectrum. As for the plasma density and temperature, the methods are slightly more complex.

To begin with, the physical model of the line emission needs to be understood before information can be extracted from the spectrum. Similarly to eq. (2.2.27), the intensity of the line is proportional to the number of the emitters, i.e., ions and neutral atoms, and electrons which, upon collision, undergo recombination, or cause the initial excitation of the neutral. As such, the intensity is proportional to

the plasma density. Moreover, the rate of the light emission events is proportional to their average electron-impact cross-section over the whole electron Maxwellian distribution of speeds. This results in the dependence of the electron temperature as well as the probability of certain atomic energy level sequences for a given impacting electron speed and species of ion or atom. Thus, in order to extract information on plasma conditions from the lines, population models must be developed. This is done for the line-ratio technique, where two lines in the emission spectrum are chosen and their population models are built [152, 153]. By comparing the expected emission event rate ratio, which depends on the plasma density and temperature, to the measured emitted intensity ratio, these plasma conditions can be determined [152].

Furthermore, the width of the line carries information about the conditions in the plasma, e.g., the line can shift, split, or broaden from the temperature effects of the emitter through Doppler broadening, or from the electric field of the plasma electrons during collisions through Stark broadening [154]. In addition, the measurement apparatus broadening has to be considered [154]. Equivalently to the line-ratio method, an emission model also has to be developed to find the relation between a measured linewidth and the density and plasma temperature it corresponds to.

Such a model was produced by Gigosos-Cardeñoso in refs. [155, 156], where collision broadening (Stark effect) is considered. Only hydrogen is investigated since it is especially convenient given that the Stark effect of hydrogen atoms is linear [155]. In addition to the Stark effect on the emitters by the electrons, the field of ions is another source of perturbation which is necessary to include [155, 156]. The perturbation stems from the kinetic interactions of the emitting and the perturbing particles, thus the model requires the knowledge of the ion mass investigated, especially when the H-Alpha line is observed in hydrogen-doped gases of a different kind. Moreover, the temperature of emitters and perturbing ions was included in this Stark model. In general, the Gigosos-Cardeñoso model only includes Stark broadening, thus, in experiments, additional considerations for Doppler and instrument broadening are needed [156].

This model is used at FLASHFoward, and a detailed discussion of how this method is implemented at FLASHForward is presented in subsection 3.2.2. There, two different plasma density diagnostic techniques, temperature-independent laser interferometry and temperature-dependent H-Alpha linewidth measurement with OES, were used to find the typical temperature range of plasmas produced at FLASHForward [127]. In addition to the Stark model, instrument broadening was considered. Other broadening mechanisms, such as Doppler, fine-structure, van der Waals, or self-absorption, were omitted, as their Gaussian components were simply not observed in the measured linewidths. As a result, the temperature of $T_e \sim 0.5$–5

eV was deduced, and the following relation between the linewidth $\Delta\lambda$ and plasma density n_p is used from the Gigosos-Cardeñoso model:

$$n_e = \left(\frac{\Delta\lambda}{a}\right)^b * 10^{17}\,\mathrm{cm}^{-3}, \tag{2.2.35}$$

where a and b are parameters from the Gigosos-Cardeñoso model, which are $a = 1.098\,\mathrm{nm}$ and $b = 1.4713$ in the case of FLASHForward. Naturally, any global temperature changes beyond this range would result in inaccuracies in the deduced density. In addition, the relation here is developed with an assumption of local thermal equilibrium of electrons and ions, which may not be present while the discharge is running [127]. For a plasma of $n_e = n_i \sim 10^{16}\,\mathrm{cm}^{-3}$, $T_e = 5\,\mathrm{eV}$, and $T_i = 0.5\,\mathrm{eV}$, using Spizter self-collision time eq. (2.2.11) for electrons:

$$\tau_{ee} = 50\,\mathrm{ps}, \tag{2.2.36}$$

for hydrogen ions:

$$\tau_{ii} = 126\,\mathrm{ps}, \tag{2.2.37}$$

for argon ions:

$$\tau_{ii} = 794\,\mathrm{ps}. \tag{2.2.38}$$

Thus there is very minimal delay in the plasma constituents reaching thermal equilibrium after the discharge on the microsecond-level of the plasma evolution.

In conclusion, optical emission spectroscopy is a method to extract information on plasma composition, density, and temperature. It requires modelling the emission of specific lines, but once that is established, straightforward relations of plasma density and temperature and features of the line can be utilised.

2.3 Ion motion and plasma recovery processes

2.3.1 Limits of stationary ions assumption

The understanding of beam-driven plasma wakefield acceleration has been primarily built on the models with an assumption of stationary ions. The first analytical descriptions of the linear wakefields [30, 31, 61] and one-dimensional non-linear regime [31, 59], as introduced in section 2.1.2, represented ions with a static density term, providing an electrostatic background to the wakefield process. However, it was anticipated that this may not be a valid assumption for reasonable scenarios of non-linear wakefields. To drive such fields in plasma, a high-density electron (or equivalent) driver would be needed. This was first investigated in ref. [157], where a multiple-fluid model revealed a significant motion of ions when plasma electrons

Driver Parameters	Afterburner	FLASHForward
N_b	1.5×10^{10}	2.5×10^9
σ_z rms	35 µm	42 µm
γ	$\leq 1 \times 10^6$	2055
$\epsilon_{n,x}$	0.62 µm	4 µm

Table 2.1: Driver parameters used in the afterburner design [84] (and ref. [159] therein) and in emittance preservation campaign at FLASHForward [77]. The latter are close to typical FLASHForward operation values, whereas the former are meant to represent a realistic scenario of a single PWFA stage in a linear collider. The emittance for the FLASHForward driver is estimated to be just slightly higher than the trailing bunch; however, due to difficulties in removing beam dispersion, the overall projected emittance of the driver can be even higher (see section 3.1.2).

reach relativistic momenta i.e., the non-linear regime of wakefields. Later, a realistic scenario was considered in ref. [84]. With a driving beam $n_b \gg n_p$, a non-linear wakefield is created [59, 60]; however, such large beam density can perturb the ions in the blown-out cavity. This work highlighted a serious challenge for the PWFA afterburner concept, where a single stage at the end of a conventional linear accelerator would boost the electron energy before the interaction point [158, 159]. Because the beta functions and thus the beam size must be small at that point, this leads to the bunch having a very high density. Equally, the same is anticipated for plasma lenses in final focusing [160]. A simplified formalism from ref. [84] is presented here to assess how much of such ion motion should be anticipated.

A matched beam β function in the ion focusing field can be expressed differently from eq. (2.1.64) as [116, 124]:

$$\beta_m = \sqrt{\gamma / 2\pi r_e n_p}, \tag{2.3.1}$$

and thus the size is:

$$\sigma_m = \sqrt{\beta_m \epsilon_n / \gamma}, \tag{2.3.2}$$

where r_e is the classical radius of an electron, n_p is the background plasma density, ϵ_n is the the normalised beam emittance, assuming the transverse force on the beam only stems from the electrostatic field of ions, i.e., non-linear blowout. Choosing a bi-Gaussian transverse distribution of the driver with equivalent parameters in both planes x and y, the average driver bunch density:

$$n_b = \frac{N_b}{(2\pi)^{3/2}\sigma_x^2\sigma_z} = \frac{N_b}{2\pi\epsilon_n\sigma_z}\sqrt{r_e n_p \gamma}, \tag{2.3.3}$$

where N_b is the number of electrons in the driver and σ_z is its length. For a driver with a density $n_b \gg n_p$, its electric field is predominantly radial [84], so it is as-

Trailing Bunch Parameters	Afterburner	FLASHForward
N_b	0.5×10^{10}	2.5×10^8
σ_z rms	-	11 µm
γ	$\leq 2 \times 10^6$	2133
$\epsilon_{n,x}$	4 µm	2.85 µm

Table 2.2: Trailing bunch parameters used in the afterburner design [84] (and ref. [159] therein) and in emittance preservation campaign at FLASHForward [77].

sumed that ions move predominantly under the influence of this radial force. For a cylindrical surface inside the beam, using Gauss' law:

$$E_r(r) = -2\pi e n_b r = -\frac{eN_b}{\epsilon_n \sigma_z}\sqrt{r_e n_p \gamma}\, r. \tag{2.3.4}$$

An approximate, nonrelativistic equation of motion for the ions:

$$\frac{d^2 r}{dt^2} \simeq \frac{ZeE_r}{Am_a} = -\frac{Ze^2 N_b}{Am_a \epsilon_n \sigma_z}\sqrt{r_e n_p \gamma}\, r, \tag{2.3.5}$$

where Z is the ion charge and A is the atomic mass. In the driver/wakefield rest frame $\xi \equiv z - ct$, $r \equiv r$:

$$\frac{d^2 r}{d\xi^2} = -\frac{Z r_a N_b}{A\epsilon_n \sigma_z}\sqrt{r_e n_p \gamma}\, r \tag{2.3.6}$$

$$= -k_i^2 r, \tag{2.3.7}$$

where r_a is the classical radius of a singly charged ion of A atomic mass. The eq. (2.3.7) is a simple harmonic oscillator with spatial wave number k_i. For a beam of effective length $\Delta\xi = \sqrt{2\pi}\sigma_z$, the phase advance of ion motion is thus:

$$\Delta\phi = k_i \Delta\xi = \sqrt{\frac{2\pi Z r_a \sigma_z N_b}{A\epsilon_n}}\,(r_e n_p \gamma)^{1/4}\,. \tag{2.3.8}$$

Tables 2.1, 2.2, and 2.3 contain the parameters used in the estimation of the phase advance of the ion motion in the afterburner scenario [84] and at FLASHForward. The original value stated in the work is $\Delta\phi \simeq 6.45$, which, unlike the matched β function, was calculated with r_e in SI units. As shown in fig. 2.9, the collapse of ions occurs very quickly during the beam passage, and two extrema of the ion oscillation occur within the beam. This ion collapse during beam passage was confirmed in PIC simulations [84]. In the case of the high-quality preservation working point of FLASHForward, the driver-caused ion motion phase advance is $\Delta\phi_d \simeq 0.006$, and even smaller for the trailing bunch $\Delta\phi_t \simeq 0.001$. In this simple harmonic oscillator model for the ion motion, the total collapse of ions occurs at $\Delta\phi = \pi/2$.

Plasma Parameters	Afterburner	FLASHForward Ar
Initial density n_p	$0.9 \times 10^{16}\,\mathrm{cm}^{-3}$	$1.2 \times 10^{16}\,\mathrm{cm}^{-3}$
Ion charge Z	1	1
Ion mass A	1	40
Matched β-function β_m	112 mm (31 mm)	3 mm (0.9 mm)
Matched driver density n_b/n_p	1.5×10^5	50

Table 2.3: Plasma parameters used in the afterburner design [84] (and ref. [159] therein) and in emittance preservation campaign at FLASHForward [77]. The values in the brackets correspond to calculated β_m with eq. (2.3.1) using the CGS units for r_e, resulting in 31 mm matched beta function for the afterburner case as quoted in ref. [84]. However, eq. (2.3.1) is used with a factor of 2π in the denominator, which stems from an expression for r_e in SI units, $r_e = e^2/4\pi\epsilon_0 m_e c^2$. Therefore a value using r_e in SI units is presented first.

For the case of the FLASHForward driver, the ion phase is only 0.4% advanced towards the collapse. The insignificance of this can be noted in fig. 2.9, where the collapse of ions may occur hundreds of plasma wavelengths away. In the case of the first afterburner proposal [84, 158], the $\Delta\phi_{afterburner} = 0.1$ or FACET experiments [161] the $\Delta\phi_{FACET} = 0.3$, so 6% and 20% towards the collapse respectively, and both were considered significant. Furthermore, as described in section 3.1.4 and ref. [77], the FLASHForward double bunch enters the plasma with high chromaticity. Because of this, when the trailing bunch is focused to the matching β function at the plasma entrance, the driver enters the plasma at positive divergence, thus larger beam size and smaller beam density. If the driver's waist is 21.3 mm upstream from the plasma entrance [77], given its waist β function was actually around 17.5 mm and normalised emittance approximately 4 µm, it should be around 1.6 times larger than the matched size, following eq. (2.1.40). This would reduce the phase advance by a factor of 1.6, leading to $\Delta\phi_d \simeq 0.004$, 0.3% of the collapse. Interestingly, this same FLASHForward driving bunch in atomic hydrogen plasma of the same density would result in ion motion 10% towards the collapse, which is much more significant, see fig. 2.9.

These values indicate that while ion motion may not be extreme, it is an important feature of PWFA to recognise. Since the ions move further after the passage of the beam, this undoubtedly has a stronger perturbative effect on the trailing beam. The collapse of the ions naturally destroys the linear focusing field medium of the ion cavity inside the wake, thus spoiling the emittance of the accelerated bunch. In ref. [84] alone, some in-bubble ion motion mitigating strategies were proposed e.g., the use of smaller N_b, or the use of hollow plasma channels [162, 163]. Following this, some more advanced schemes were conceptualised. Firstly, a method of adiabatic matching was proposed in ref. [164]. There, a plasma module would be used where

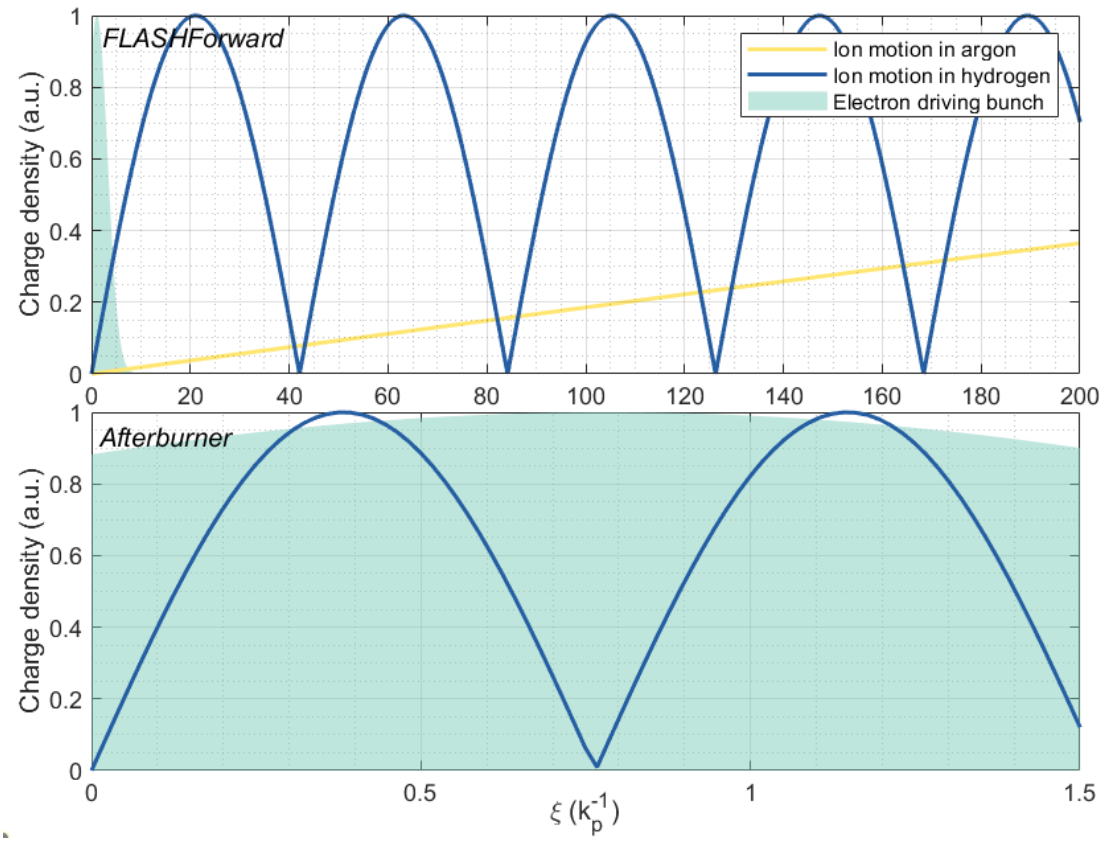

Figure 2.9: The $|sin(k_i\xi)|$ ion motion during the passage of the electron driving bunch for three different cases: FLASHForward bunch in argon and hydrogen and afterburner in hydrogen [84].

the species of ions change longitudinally i.e., ion mass is reduced adiabatically. For a lower-mass ion, the ion motion is greater, see equation eq. (2.3.8) and the inverse dependency on A, the atomic mass. As the beam traverses the plasma module, it can become sufficiently focused to each region of the plasma to be matched to the non-linear focusing fields. To achieve this, an optimum ion mass profile was determined to minimise emittance growth, involving gases from Xenon to Lithium, spanning 40 cm. Secondly, a solution offered by authors in ref. [165] involved tapering the beam transverse profile longitudinally rather than making modifications to plasma. Here, each beam slice would be matched to the ion-perturbed focusing field at the wakefield phase of the slice. Rather than overcoming the challenges posed by ion motion, other work noted its potential benefits. One of them, ref. [166], explored how collapsed ions introduce head-to-tail decoherence for beam hosing. It is an instability caused by positive feedback from beam centroid transverse displacement which is coupled to the transverse wakefields, which can majorly spoil the acceleration quality [78]. Finally, another supposed benefit could be the amplified wakefield amplitude [167]. It was observed in simulations that material redistribution of ions towards the axis also leads to wave energy redistribution in the beam path, thus increasing the longitudinal electric field just before the wave breaks. To conclude, there are concepts and a choice of parameters for PWFA that could minimise the

effects of ion acceleration. That being said, such effects turn out to be minimal in moderate PWFA facilities such as FLASHForward when operating with argon plasma and did not result in emittance spoilage [77].

Other work in the field of laser-plasma interaction has shown how a pulse laser in plasma transfers its momentum to ions, thus triggering a longitudinal plasma drift [168]. Therein, an overview of ion motion's influence on travelling plasma waves and oscillations was given. This analysis was extended to other wakefield-driving mechanisms in ref. [169].

2.3.2 Long-term ion motion

Ion dynamics that last beyond or are triggered after the femtosecond-duration processes in the wakefield bubble may not be of any more relevance to the quality preservation of the PWFA accelerated beam. However, they are pertinent to the long-term evolution of plasma and its recovery before receiving the next driver-trailing-bunch-pair for acceleration. High-repetition operation in PWFA may be fundamentally limited by these processes, and the understanding of their nature is crucial.

While the regular-density electron or short-pulse laser beam may not impart enough momentum to move ions during its passage, the plasma electron response in a form of a linear or non-linear wave lasts for more than one plasma period, eventually perturbing the ions. This effect was first described by L. M. Gorbunov for laser-driven schemes [170, 171]. To be more precise, the ponderomotive force of the oscillating plasma wakefield was identified as the cause of initial ion redistribution. It was derived that both the onset of ion motion and the formed plasma radial profile depend directly on the form of the laser pulse and the intensity [170], where the onset:

$$\eta = \frac{C_{laser}}{a_0^2 \sqrt[3]{\delta}},$$

where η is the distance from the driving pulse, C is laser pulse shape factor, a_0 the normalised vector potential, $\delta = \frac{Zm_e}{m_i}$. The resulting plasma channel would lead to plasma wave breaking, limiting the number of usable wakefield cycles [170, 172, 173]. It is an important consideration in schemes that accelerate electrons at some later cycle of the wakefield, for example, multi-pulse laser-wakefield acceleration (MP-LWFA) [51], where the wake is built up with several lower-intensity pulses at plasma-period separation rather than one high-intensity pulse. Similarly, AWAKE [174], driving the wakefield in a single stage with the long proton bunch formed in SPS, achieve acceleration by allowing the bunch to self-modulate into bunchlets mirroring the temporal structure of the wakefield. These bunchlets then drive the wakefield in each of their corresponding plasma phase buckets, building up fields.

As a result, the acceleration of electrons occurs at a much later plasma evolution stage than in the first-cycle schemes. In argon ($m_{ion} = 40$ a.m.u.) plasma of $n_{ion} = 1 \times 10^{14}\,\mathrm{cm}^{-3}$ density, the ion period would be $T_{ion} = 2\pi\sqrt{\frac{m_{ion}\epsilon_0}{n_{ion}e^2}} \approx 3\,\mathrm{ns}$, so no motion of ions would be anticipated. However, for hydrogen ($m_{ion} = 1$ a.m.u.), $T_{ion} \approx 480\,\mathrm{ps}$, which is already on the proton-length timescale. For FLASHForward argon plasma of $n_{ion} = 1 \times 10^{16}\,\mathrm{cm}^{-3}$, $T_{ion} \approx 0.3\,\mathrm{ns}$, magnitudes later than the femtosecond-long bunches. The long-term ion motion onset is a more pertinent topic for experiments which want to prevent onset in a single acceleration event, but the interest for a high repetition rate is the recovery to a point where a continuation of MHz operation can happen.

Plasma ion evolution from the wakefield breaking to a few thousand plasma periods was investigated in ref. [175]. The simulations were performed in the context of the FACET PWFA setup, thus similar to ref. [100]. Four stages of ion motion, which precede the observed processes in ref. [100], were identified.

The first stage is essentially the creation of an on-axis ion density spike as a consequence of beam radial fields and the ponderomotive force of the wake, as discussed below and in ref. [102–104, 170, 171, 176]. Here it was noted how without the contribution of the wake to the ion motion, the near-axis ions would reach the on-axis density peak about ten times slower. Then, the second stage involves ion-acoustic soliton formation and travelling both outward and inward to the radius. They originate from the on-axis density peak and the ion movement to the axis, propagate at the ion-acoustic velocity, and last while any ions still travel to the axis. The velocity of the soliton and its peak density imply that the electron temperature is $T_e \sim \mathcal{O}(1)\,\mathrm{keV}$.

The last two stages are the processes described in ref. [177], which are relevant to plasmas of finite radius. The former stage involves electron expulsion and pulling of the ions radially outward. The arising azimuthal magnetic field begins to focus the ions back toward the axis, leading to a high-amplitude compression wave, which is the final stage of the ion motion investigated in ref. [177]. This culminates in another on-axis density peak, but now formed from the sharp fronts evolving from these waves, and it also results in ion-acoustic solitons and inhomogeneity due to the on-axis plasma pinch. Later, the simulations in this study indicate a density channel with steep walls at $\omega_p t \sim 1500$ and increased-density filament at $\omega_p t \sim 3000$. In summary, ref. [175] revealed the dynamics of initial ion density redistribution in the plasma after wakefield dissipation.

The onset of this wakefield-driven long-term ion motion was first observed by authors in ref. [102], see fig. 2.10. Their experimental setup consisted of a 100 TW-class Ti:sapphire laser and two hydrogen gas jets. The first of the two jets

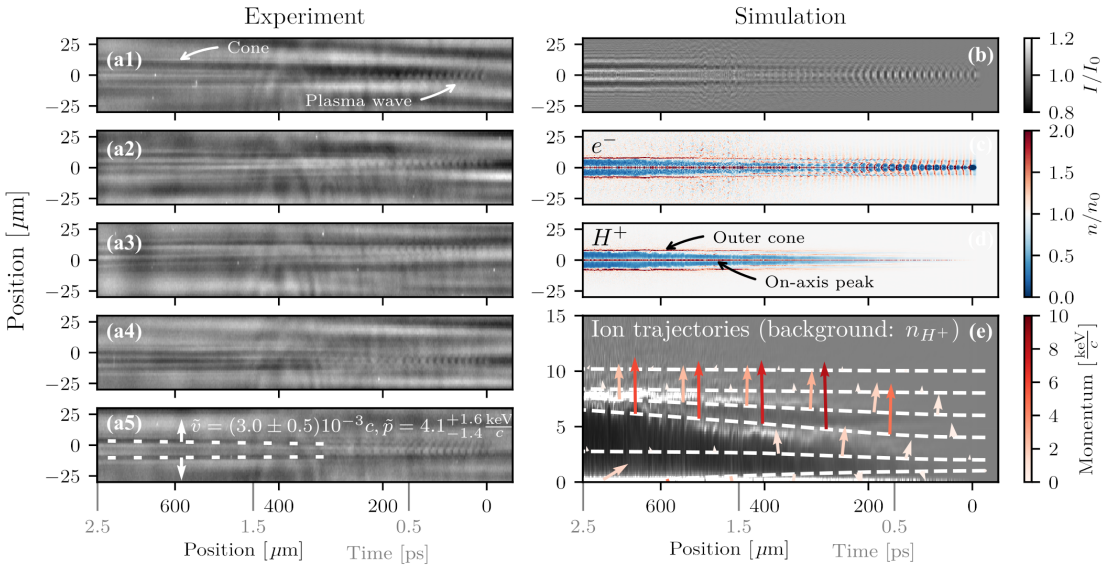

Figure 2.10: The experimentally observed (left) and simulated (right) ion motion. The left column consists of five consecutive shots of observed ion motion, where plasma wakefield can also be seen in early timescales. The bottom left shot is also marked to indicate where ion density peaks form, and their measured momenta. The top three plots on the right show the density distributions obtained in simulations: (b) as seen with the shadowgraphy method, (c) electron-only, (d) atomic-hydrogen-ion-only. The bottom right plot presents the momentum distribution of the outwardly streaming ions. Figure from ref. [102].

was operated as a laser-wakefield accelerator with shock-front internal injection, the shock front being generated by a silicon wafer inserted in the flow of the gas. As a result, 150 MeV and 900 pC electron beams with a large energy spread would emerge from this jet, suitable to drive a wakefield in the second jet, preionised with a counterpropagating laser pulse. A small part of the same laser is used as a few-cycle probe pulse to form femtosecond-resolution shadowgraphy images of the plasma density modulations in the second jet, as seen in fig. 2.10. Firstly, a wakefield is observed, which spanned 400 µm behind the driver. As it undergoes phase-mixing, the charge separation in the plasma vanishes, leading to quasineutrality. Shadowgraphy only images electrons in the plasma. Thus, because of quasineutrality, any redistribution of background ions after wakefield dissipation can also be observed. To be sure, the electron thermalisation timescale can be estimated using the Spitzer electron self-collision time in eq. (2.2.11), and estimations in sections 2.2.1 and 2.2.3, which yield electron thermalisation over 0.2 ps. This is evaluated using a cold plasma temperature and the operating density in ref. [102]; undoubtedly the density in the redistribution features of ions is different and the temperature may be higher. What's more, the use of Maxwellian velocities may not be valid as there could be a small proportion of very high-energy electrons that formed the non-linear wakefield. Nevertheless, the estimation is an order-of-magnitude guide, thus on the timescale of a nanosecond, the on-axis peak electrons should have thermalised.

A transverse movement of an increased-density ring was observed at the end of the plasma oscillations 400 µm after the driver lasting up to 700 µm, see fig. 2.10. This has led to the plasma density redistribution resembling the shape of a cone as it evolves in time. An on-axis density peak was also observed. The certainty that this phenomenon is indeed ion motion comes from the fact that the measured transverse group velocity of this ring (0.0017c) is far too low to overcome charge separation forces if it were only electrons moving in a static ion background. Equally, the existence of the on-axis density peak implies that this is not a formation of ion channel due to Coulomb explosion ([178, 179] as cited in ref. [102]), nor is it a shock-formed plasma channel like ones used in high-intensity guiding [42, 43, 180]. The latter, however, may be used to understand the further evolution of these peaks.

As similarly predicted in refs. [103, 104, 170, 171], the motion of ions on this timescale is caused by the ponderomotive force of the plasma wave. In the experiment and simulations carried out by authors in ref. [102], the ions resulted in a momentum of $\sim 4\,\mathrm{keV}\,c^{-1}$.

Based on the proton-driven scheme of AWAKE, ion motion formalism was developed for narrow-beam conditions, $\sigma_r \ll \sigma_z$, in the linear PWFA regime [103, 104]. To arrive at the equation for ion motion based on fluid theory in cold plasma driven by the transverse fields of the wake [103]:

$$m_i c^2 \frac{\partial^2 n_{i1}}{\partial \xi^2} = -\frac{n_p Z e^2}{4 m_e \omega_p^2} \nabla_r^2 \hat{E}_r^2, \tag{2.3.9}$$

the following assumptions and relations were used [103]:

- Time-differentiated linearized ion continuity equation $\partial n_{i1}/\partial t + n_p \nabla \cdot \boldsymbol{v}_{i1} = 0$, where $n_i = n_p + n_{i1}$ is the ion density, equivalent to background plasma density n_p but for a first-order perturbation $n_{i1} \ll n_p$.
- Euler's equation $d\boldsymbol{v}_{i1}/dt = Ze\boldsymbol{E}/m_i$ with an assumption of cold ions $T_i = 0$, where Z is the ion charge.
- $\boldsymbol{E}$, the electric field acting on ions expressed by $e\boldsymbol{E} = kT_e \nabla (n_i/n_p) + \boldsymbol{F}_p$, if plasma quasineutrality, $n_i = n_e$, is assumed during ion motion.
- The ponderomotive force of the wake $\boldsymbol{F}_p = e^2/\left(4 m_e \omega_p^2\right) \nabla \hat{\boldsymbol{E}}^2$, from ref. [181] as referenced in ref. [103], where $\hat{\boldsymbol{E}}$ is the electric wakefield envelope.
- In narrow-beam limit, $\sigma_z \gg \sigma_r \Leftrightarrow \partial_z \simeq \frac{1}{\sigma_z} \ll \partial_r \simeq \frac{1}{\sigma_r}$ and so $|\boldsymbol{F}_{p\perp}| \gg |\boldsymbol{F}_{p\parallel}|$; in addition, $\sigma_r \ll c/\omega_p \Rightarrow E_z \ll E_r$. This leads to the radial electric field as the dominating contribution in the ponderomotive force.

The expression for E_r of the wakefield is acquired by using Dawson's sheet model

[172] under the assumption of low-amplitude wakes. For a small displacement of electrons to its initial radial position $\Delta r = r_e - r_{e0}$, neglecting $\mathcal{O}\left(\Delta r_e\right)^2$:

$$\frac{d^2\Delta r}{d\xi^2} = -\left[\omega_p^2 + \frac{d}{dr_0}\left(\frac{eE_r^b}{m}\right)\right]\Delta r - \frac{eE_r^b}{m}, \tag{2.3.10}$$

during the passage of the beam. Each term in the equation corresponds to the fields inside a ring of plasma electrons in this superposition: $E_r = E_r^i + E_r^e + E_r^b$. In other words, this is a wakefield transverse field as a superposition of the ion channel focusing field, the electrostatic repulsion of plasma electrons in the ring, and the field of the beam. The solution to eq. (2.3.10) is an anharmonic oscillation of Δr around an equilibrium position, and the phase of this oscillation depends on r_{e0}. This leads to the fine-scale mixing of electron sheets when they are $\sim \pi/2$ out of phase. After this, the Dawson sheet model is no longer valid. In the case of eq. (2.3.10), the sheet crossing happens because of the transverse field gradient of the driving bunch. Once the driver passes, the free oscillations in the plasma may be modelled as sheets under no-crossing conditions:

$$\frac{d^2\Delta r}{d\xi^2} = -\omega_p^2\Delta r + \frac{\omega_p^2\Delta r^2}{2r_{e0}}, \tag{2.3.11}$$

The second term, while neglected during the passage of the driver, informs of the anharmonic aspects of the plasma electron motion in wakefield. As noted in ref. [104], this term is a consequence of 2D cylindrical geometry of this problem; it is not present in 2D flat geometry (or in 1D) [104, 172]. The phase of this oscillation also results in dependency on r_{e0} as well as the amplitude of the oscillation, all of which result in fine-scale mixing. Interestingly, onset estimations in ref. [104] suggest that plasma wave breaking due to fine-scale mixing of electrons trajectories occurs later than ion motion driven by the ponderomotive force of wakefield oscillation.

The solutions to eq. (2.3.10) and eq. (2.3.11) are inverted in ref. [104] to acquire an expression for the transverse electric field in the wake, both during and after the passage of the beam. For the ponderomotive force, E_r is averaged over one oscillation of the wakefield. In ref. [104], this results in

$$\langle E\rangle = -\frac{1}{2}\nabla_r\left(E_r^b\right)^2, \tag{2.3.12}$$

during the passage of the beam, and

$$\langle E\rangle = -\frac{1}{4}\nabla_r\frac{e\hat{E}^2}{m_e\omega_p^2}, \tag{2.3.13}$$

ignoring higher order terms and thus being left with the term of plasma ponderomotive force from linear theory. The initial fields in the free-oscillation expression

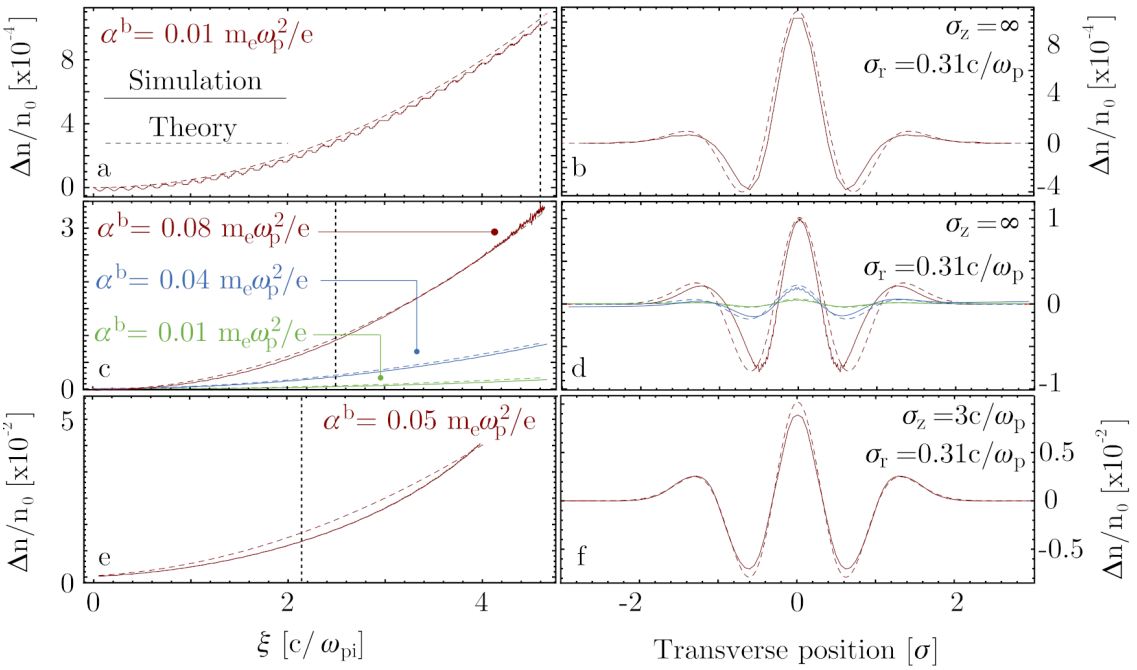

Figure 2.11: Relative change of ion density due to the wakefield ponderomotive force, with the temporal/longitudinal coordinate (left) and radially (right). Different α^b values here represent different strength drivers. Figure from ref. [103].

develop during the passage of the beam [176]. With this, the solution to ion equation of motion eq. (2.3.9) after the passage of AWAKE-like beam turns out to be:

$$n_i = n_p \left(1 - \frac{m_e Z \omega_p^2 \xi^2}{m_i c^2} \left(1 - \left(1 - \frac{e^2 \left(\nabla_r \hat{E}_r\right)^2}{m_e^2 \omega_p^4}\right)^{-1/2}\right)\right) \tag{2.3.14}$$

A more general ion density perturbation is derived in ref. [104]; however, as shown in ref. [103], this is sufficient for order-of-magnitude estimations. Equation eq. (2.3.14) illustrates the tendency of ion density to develop a peak on the axis and voids near the edge of the wakefield, see fig. 2.11. A similar plasma channel was obtained in ref. [171]. Whether it is by a depression in a channel [170, 171], or an on-axis ion density peak [103], this inhomogeneity leads to electron trajectory crossing. The flow of electrons changes from coherent to turbulent, reaching quasineutrality. As a result, a formed profile of ions is reflected in the overall plasma density profile, hence the ability to observe this with shadowgraphy methods like in ref. [102].

It is important to note that this formalism is grounded on the assumptions of a narrow long bunch and linear plasma waves. As investigated by [176], this model still reproduced their experimental observations. Indeed, the annular profile with a density peak on-axis could be deduced even from a simplified version of this model, as stated in ref. [176]. For a case of a tophat driver in cylindrical symmetry of length $\sigma_z = \lambda_p/2$, large width, and transverse electric field $E_r^d(r_0)$, the field variation is then

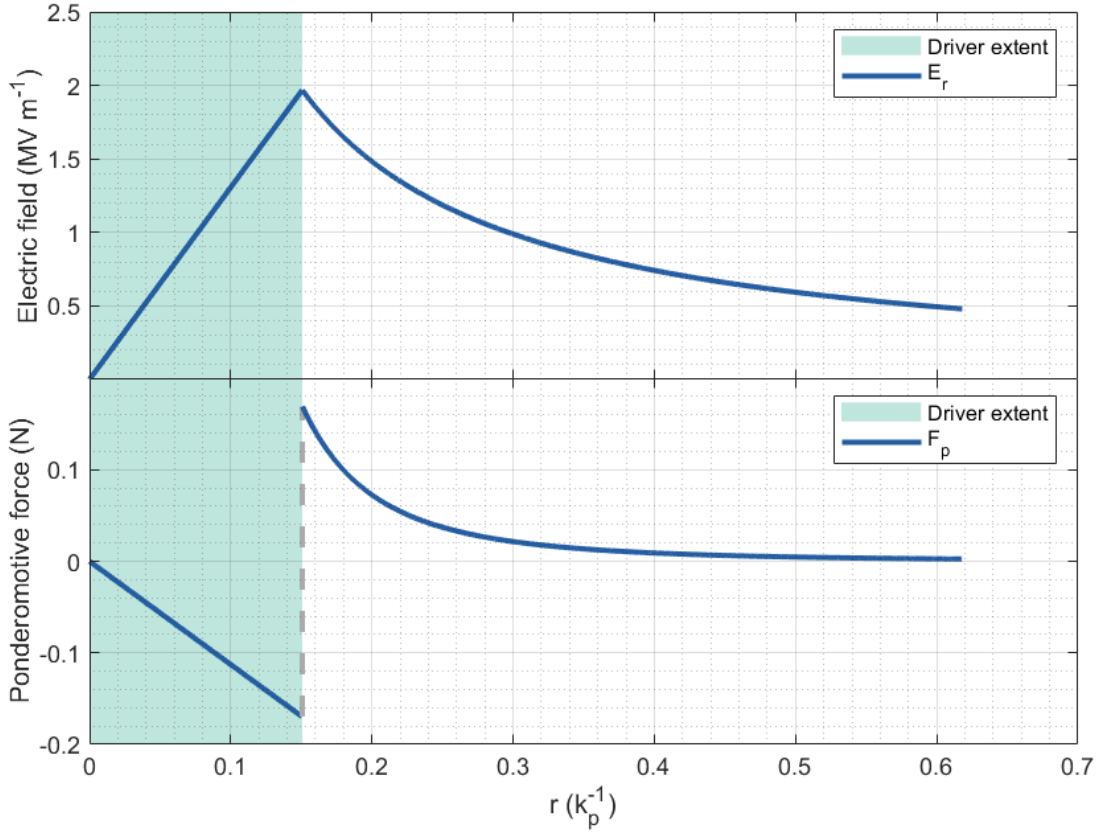

Figure 2.12: The radial electric field of a simplified cylindrical beam (top), as also used in ref. [176] and the resulting ponderomotive force (bottom).

supposedly small over the range of plasma electron displacement, i.e., $\frac{e}{m_e\omega_p^2\nabla_r E_r^d} \ll 1$. Because of this, all orders of $\nabla_r E_r^d$ may be ignored, reducing the displacement of the plasma electrons during the passage of the driver beam to:

$$\Delta r_{beam} = \frac{eE_r^d}{m_e\omega_p^2}[1 - \cos(\omega_p\xi/c)],$$

and after the beam:

$$\Delta r_{free} = -2\frac{e}{m_e\omega_p^2}E_r^d(r_0).$$

Given the length of the beam, the free oscillations region starts with the electron ring at a phase of oscillation extrema, yielding an amplitude $A = 2eE_r^d/m_e\omega_p^2$. From [104] and [176], the expression for the electric field of the wake during the free oscillations is $\hat{E} = m_e\omega_p^2 A/e$, which leads to $\hat{E}_w = 2E_r^d$ in the simplified scenario. The ponderomotive force of the wakefield on the ions, which is acquired by averaging $\hat{E}$ over one oscillation, is thus $F_p(r) = -q_i\nabla_r[E_r^d(r)]^2$, where q_i is the ion charge [176]. For a simplified cylindrical beam, its radial electric field is shown in fig. 2.12. As a result, the ponderomotive force of the wakefield would be negative in the beam region, which causes ions to move toward the axis and build the on-axis peak, see fig. 2.12. Outside of the beam region, the ponderomotive force is positive, resulting in ions forming the cone-like structure observed in ref. [102].

One can thus recognise the indirect impact of the driver transverse electric field radial gradient on the ion (and thus plasma density) radial profile. As for the kinetic energy, or momentum distribution of the ions, it was also investigated in ref. [102]. Naturally, the initial wakefield ponderomotive potential over the timescale of its existence imparts kinetic energy on ions depending on their radial position. Because of this, ions closer to the centre of the wakefield would reach higher velocities. After wakefield depletion, the plasma is quasineutral, and the radial momentum distribution of ions transforms into a radial spatial distribution, where innermost ions overtake slower outer-layer ions from $r_0 \gg 3k_p^{-1}$. With shadowgraphy, the observed off-axis peaks are therefore defined by the contrast of the high and low density, bounded by these slower ions, see fig. 2.10.

The ion motion observed here formed and lasted at least up to 50 ps, and the nominal density used was $\mathcal{O}(10^{19})\,\mathrm{cm}^{-3}$. However, it is suggested that this may be much longer for densities typically used in PWFA, such as $10^{16}\,\mathrm{cm}^{-3}$ for FLASHForward. For even smaller densities ($10^{15}\,\mathrm{cm}^{-3}$), authors in ref. [102] suggest this ion motion structure may form on the timescale of nanoseconds. In a similar vein to formalism in ref. [84] and section 2.3.1, a simple estimation of the onset timescale was performed in ref. [122] for FLASHForward parameters. The plasma ions experience a radial impulse:

$$\Delta p_r(r) = \int F_r(t,r)\mathrm{d}t = \int \frac{eZ_i I(t) r}{4\pi c \sigma_r^2 \epsilon_0}\mathrm{d}t = \frac{eZ_i Q r}{4\pi c \sigma_r^2 \epsilon_0}, \tag{2.3.15}$$

which would result in radial velocity of ions $\Delta v_r = \Delta p_r(r)/m_i$, where Z is the ion charge, $Q = \int I(t)\mathrm{d}t$ is the bunch charge, σ_r is bunch transverse size. As a result, the ions may all be focused on the axis in time:

$$\Delta t_{ion} = \frac{r}{v_r} = \frac{4\pi c \epsilon_0 m_i \sigma_r^2}{eZ_i Q}, \tag{2.3.16}$$

which for $Z = 1$, argon $m_i = 40$ a.m.u., $Q = 590\,\mathrm{pC}$, and $\sigma_r = 5\,\mu\mathrm{m}$, $\Delta t_{ion} = 0.5\,\mathrm{ns}$. Both of these estimations point to the nanoseconds as the key timescale of long-term ion motion dynamics.

The plasma density redistribution as a consequence of the ion motion driven by the wakefield ponderomotive force on the timescale of a hundred picoseconds was recently observed at the AWAKE PWFA facility experimentally and in simulations [105]. The arising plasma density on-axis peak would lead to loss of coherence in the wakefield oscillations, disturbing the development of the wakefield along the self-modulated proton bunch, and leading to reduced transverse forces of the wakefield and less diverging longitudinal slices of the proton beam. These would manifest as a strong bunch density signal at the diagnostics, thus signifying the onset of ion motion. Two experimental settings were adjusted: the ion mass by changing the

discharged gas (helium, argon, xenon) and the wakefield amplitude by changing the plasma density by integer factors. As expected from theoretical investigations [103, 104], the increased ion mass would delay the ion motion onset while the increased wakefield amplitude, or, more precisely, the square of the transverse wakefield envelope, would forward the onset as the force on ions of any mass would be greater. A similar plasma density distribution structure was observed in simulations as in ref. [102], with a high on-axis density peak, reduced density around it, and then another density peak off-axis, in cylindrical symmetry. This again confirms the theory of long-term ion-motion-driven plasma density redistribution on hundreds-of-picoseconds timescale [103, 104].

Clearly, while the in-bubble ion motion is avoidable, the long-term ion motion is not, it is inherent to the process of wakefield dissipation. Because of this ion motion onset, the self-modulation in the proton bunch at AWAKE would be suppressed, which would dampen plasma wakefields and prevent significant electron acceleration in the linear regime. Equally, laser schemes such as the multi-pulse LWFA would also only be functional up to the point of ion redistribution [51, 52]. Specifically for the AWAKE scheme, this investigation offers a strategy to use a lower ion charge to mass ratio, e.g., singly ionised argon plasmas [104].

Furthermore, the energy transport channels from beam energy deposition and wakefield dissipation were explored in ref. [100]. A similar optical-probing technique was used here to measure the density evolution in perturbed plasma, and matching simulations were performed. The latter helped inform on the actual distribution of the energy density remaining in plasma across different dissipation channels. Clearly, on the nanosecond timescale, the dynamics of ions dominate the plasma evolution. Section 2.3.4 will be investigating this work further.

2.3.3 Ion motion and hydrodynamic plasma evolution

For a typical FLASHForward bunch in argon plasma, the onset of ion motion is expected to occur on a nanosecond timescale. At that point, an annular plasma channel with an on-axis density peak is formed if it were to follow the same process as observed in ref. [102]. The thermal distribution of this channel is not specified in ref. [102] or ref. [104]; however, it is known that the density peaks contain ions with momenta of $\sim 4\,\mathrm{keV}\,c^{-1}$. As these high-momentum ions gather around the axis, they collide with ions approaching from other directions and ions that were already there. Given that the collisional timescale $\tau_{ii} \propto T_i^{3/2} \propto \langle v \rangle^3$, it will take a much longer time for ions to thermalise at such momenta. We can then naively assume that the bulk of these ions on-axis has a momentum distribution with a mean of somewhere under $4\,\mathrm{keV}\,c^{-1}$, but much higher than $1\,\mathrm{eV}\,c^{-1}$. Naturally, such speeds are much higher than the ambient plasma acoustic velocity, and thus a shock could

be created. Either way, the on-axis density peak must have a high ion temperature compared to the surroundings, and thus a high-pressure gradient may build there. We assume that such pressure build-up is enough to drive a shock wave travelling outwards in the ion density at the local ion sound speed or higher, as described in ref. [42]. Indeed, this has been the key mechanism in creating plasma waveguides for high-intensity laser pulse, where plasma electrons are heated on the axis, thus creating a pressure gradient capable of driving a shock and forming a channel [42, 43, 132, 180]. As the shock wave expands, ion-ion and ion-atom collisions form the boundary of hot and cold plasma [132].

Some of these schemes use the Sedov-Taylor shock expansion model to describe a plasma channel development from an on-axis density peak e.g., HOFI [43]. While plasma may exhibit additional effects due to charge separation or collective motion, the general hydrodynamic methods may be valid in this case. Unlike in Coulomb-explosion based schemes [178, 179], the quasineutrality is maintained in the plasma once the wakefield phase mixing occurs, with Debye length $\lambda_D = \sqrt{\frac{\epsilon_0 k_B T}{n_e e^2}} \approx 0.2\,\mu\text{m}$. Because of this, plasma can be modelled as a neutral medium, where the same particle and energy transport processes such as thermal conductivity and diffusion can be anticipated. Under quasineutrality, plasma particles respond to density gradients with ambipolar diffusion, where, as a response to charge separation forces, the movement of electrons and ions is governed by the heavier and slower species i.e., ions [126].

The Sedov-Taylor analysis is based on the similarity principle i.e., the derived relations of shock dynamics would be equivalent on all scales [182–184]. There, Rankine-Hugoniot conditions for the physical properties of gas before propagated shock and after were used, through which the adiabatic index factor appears in the analysis. A solution of shock position in time for cylindrical geometry would be [184, 185]:

$$r_s^4(t) = \frac{(\gamma+1)^2}{\pi}\frac{E_l t^2}{\rho_m}, \tag{2.3.17}$$

where γ is the adiabatic factor of the medium, E_l is the energy per unit length which creates the shock, ρ_m is the mass density of the unshocked region. As the plasma expands cylindrically, it cools and slows [145]. Conserving mass within the boundary of the shock, the average density there in cylindrical geometry [185]:

$$\overline{n_a} = n_{source}\frac{R_s^2}{r_s^2}, \tag{2.3.18}$$

where n_{source} is the density of initial density peak and its radius R_s. This suggests that the average density in the channel would scale as:

$$\overline{n_a} \propto \frac{1}{t}. \tag{2.3.19}$$

Furthermore, the formation of such channels also involves a certain amount of thermal conduction ahead of the shock wave, the so-called thermal precursor wave, which contains heated electrons that may ionise the recombined neutral gas collisionally [132]. This depletes energy from the wakefield region; the high-energy electron expulsion from the axis in reviewed in section 2.3.4.

A resulting plasma density channel, which evolves over a few nanoseconds in argon, and even quicker in lighter gases, is the final post-wakefield structure caused by the motion of ions. In hundreds of nanoseconds, the whole wakefield region plasma should have thermalised, as discussed in section 2.2.1. As a result, this plasma density profile may decay under ambipolar diffusion, which, since it is governed by the ions, should occur on the ion-neutral collisions timescale, i.e. hundreds of nanoseconds. With a dissipated plasma channel and under no additional ionisation, the plasma should be equivalent to its initial conditions in density, while potentially having a higher temperature.

2.3.4 Deposited-energy dissipation channels in plasma-wakefield accelerators

When traversing a plasma, the driving bunch charge density is a source for the plasma electron density perturbation, blowout cavity formation, the wakefield generation, and under certain circumstances, short-term ion motion. In general, as it couples to the plasma constituents via the Coulomb interaction to cause these effects, it deposits energy to the plasma, some of which can be transferred to the trailing bunch. The energy efficiency of PWFA, as discussed in chapters 1.2.2 and 1.5.2 and measured refs. [73–76], does not reach 100%, and so there is a proportion of the driving bunch deposited energy, which remains in plasma and dissipates.

Previous work on wakefield energy dissipation included simulations of plasma wave breaking, which leads to the energy gain of plasma electrons and their movement radially away from the axis [177]. This was explored in both finite-radius plasmas and infinite-radius ones, where the former is pertinent in plasmas generated by a laser or electron beam, thus having a sharp boundary. The outward movement of the hot electrons would create charge separation and thus an electric field. In addition, in the laboratory frame, this movement of electrons has a longitudinal component. For a plasma with a finite radius, as the electrons move longitudinally, they take away a negative current in the plasma, which results in a positive current and an azimuthal magnetic field around the plasma. This field structure and the hot electrons contain the majority (up to 80%) of the initial wakefield energy. However, that does not last indefinitely, as this structure can be broken by ion motion or ionisation of surrounding neutrals. In ref. [177] it was estimated that the onset of such ion motion would be at 1.2 nanoseconds for the AWAKE

PWFA settings ($n_p = 7 \times 10^{14}\,\mathrm{cm}^{-3}$). As for ionisation, using the mean free path $\lambda = \frac{1}{n_0 \sigma_c}$ for collisional ionisation of cross-section σ_c in a gas density of n_0 and the lower estimate of hot electron energy of 1 keV, the collisional timescale would be $\sim 5\,\mathrm{ns}$. As a result, the ion motion would dominate the following evolution on the nanosecond timescale once it breaks the field structure. In infinite plasmas the cold electrons in the bulk plasma would replace the escaping charge; this may be considered for radially-broader plasma sources such as discharge capillaries. As such, a different source of energy for the motion of ions would have to be considered, i.e., the wakefield ponderomotive force as discussed in section 2.3.2.

The channels of this energy dissipation were first modelled and experimentally observed in ref. [100]. This study revealed the processes, which happen in a perturbed plasma of specific conditions on the timescales of a nanosecond, thus being crucial to the understanding of plasma recovery for high-repetition-rate operation. A summary of it is given here.

This study was carried out at FACET [98], using a metre-long lithium-vapour plasma source at initial atomic density $n_0 = 8 \times 10^{16}\,\mathrm{cm}^{-3}$ and a driving electron bunch with 20 GeV and 2 nC charge, thus carrying 40 J of energy. The plasma is generated with the electron beam-field ionisation, in which the bunch drives a wakefield and deposits around 2.6 J of energy, leading to $2.2\ \mathrm{J\,m}^{-1}$ energy density deposition for a 1.2 metre-long plasma. Similarly to the work in ref. [102], the plasma evolution over the energy dissipation in this study was observed using optical shadowgraphy. The observations were then compared to the simulations with a specially built plasma model.

Initially, the laser probe observed a plasma expansion at a nearly constant velocity of $v_p \approx 0.7 \times 10^6\,\mathrm{m\,s}^{-1}$. Because of the lack of significant change in the velocity, two scenarios were ruled out: plasma expands due to hot electrons from the dissipated wakefield, or a radial ion acoustic shock wave forms from the dissipating wakefield. The former would manifest itself in a reduction of the expansion velocity since the electrons would cool as they propagate radially and collide with other plasma particles. Similarly, the ion acoustic wave, with a velocity of [126]:

$$v_{ion} = \sqrt{\frac{k_B T_e}{m_i}}, \tag{2.3.20}$$

where k_B is the Boltzmann constant, T_e is the electron temperature, and m_i is the ion mass, would slow down since the electrons are cooler in the plasma periphery. Therefore, the constant nature of the observed velocity is associated with a moving front of ions, accompanied by electrons, ionising the neutral vapour away from the axis.

Then, to verify this observation, a model was built for long-term (over one picosecond) simulations. It was verified that no energy went to the trapping of plasma electrons in the wakefield, and, after wakefield phase mixing, it was distributed among hot electrons, streaming ions as well as collective ion motion, radiation, and electrostatic fields. The model consisted of elastic collisions among electrons, ions, and neutral atoms, including relativistic particles. In addition, electron- and ion-impact ionisation were part of the model as well as the two-step ionisation of lithium atoms via its excitation. Consequently, the model which matched the experimental observations was one where ions moved radially together with electrons generating plasma off-axis via impact ionisation. The ions do not lose much energy on each impact given low lithium ionisation energy, they also have long mean-free-paths and small angle elastic scattering, hence the constant velocity of this ionisation front. At around 1 ns after wakefield dissipation, the dominant process of ionisation was the two-step ion-accompanying electron-impact ionisation via lithium excitation. While energetic electrons which exit the plasma at early timescales could (and did) result in some ionisation of the surrounding lithium gas, it was not consequential due to the low electron density and low impact-ionisation cross-section due to their high speeds. As a result, the long-term plasma perturbation is fully attributed to the moving front of energetic ions. The escorting electrons may not have a lot of energy, which may promote the electron-impact ionisation due to the cross-section temperature dependence.

Finally, the experimental and numerical observations can be combined to reveal the following order of events. The wakefield wave breaking occurs, resulting in fast electrons travelling outwards. The fast electrons escape the axis, and so create a charge separation which accelerates ions. In addition, radial wakefields move ions outward at $E \sim \mathcal{O}(10)\,\mathrm{keV}$. This can be attributed to the ponderomotive force of the wakefield, which attracts ions that are within the beam radius towards the axis, and the ions which are beyond the radius of the beam are pushed outward, as discussed in section 2.3.2. This outward movement dominates the first 100 ps. As the plasma retains quasineutrality, the moving ions are escorted by electrons. The radially streaming ions and electrons carry most of the wake's energy, with the fastest ions accelerating to 400-keV energies, where 20 keV is enough for significant ionisation. This front of high-energy ions and electrons excites and ionises the surrounding neutral lithium vapour. The growth of density was observed to be nearly exponential and thus can be likened to a Townsend avalanche process, described by eq. (2.2.22) [142, 143]. However, here, instead of the electrons and ions acquiring a drift velocity in an applied voltage, the one-directional drift of both particle species is set by the accelerated ions. In this study it was observed that the process forms over the first nanosecond, thus illuminating the key process which occurs in the GHz-scale PWFA recovery, see fig. 2.13.

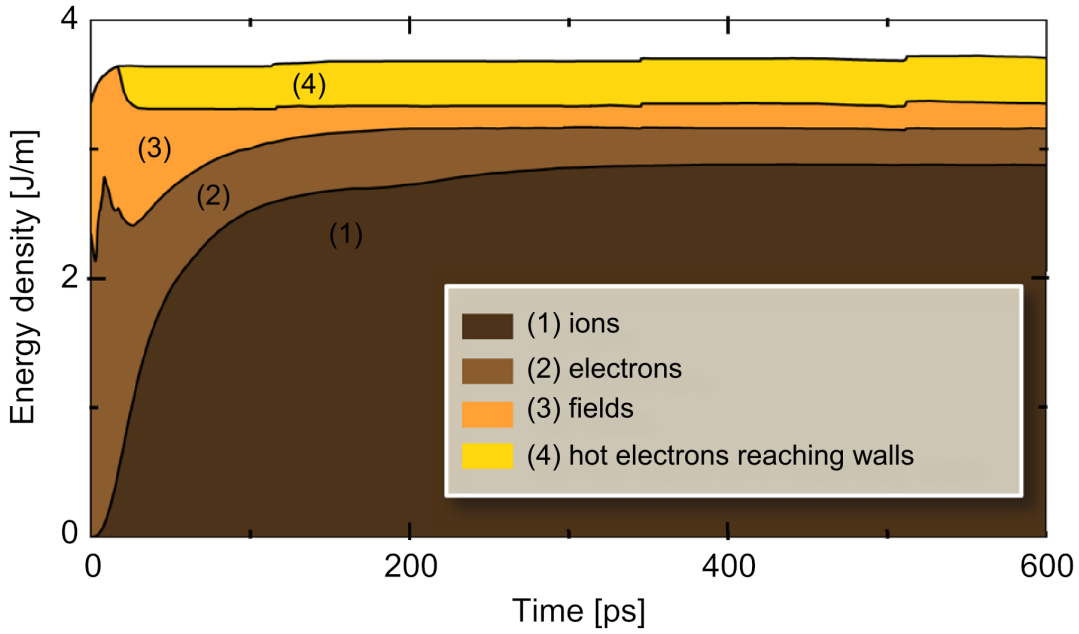

Figure 2.13: Energy density distribution over different energy transport channels in the recovering plasma over 600 picoseconds. Figure from ref. [100].

To conclude, this is the first experiment where the PWFA beam-deposited energy dissipation was investigated, and the nanosecond-scale ionisation of the surrounding plasma as a consequence of ion motion was observed. This process in plasma will be referred to as long-term ionisation (LTI). This naming should highlight the timescale similarity to long-term ion motion described in section 2.3.2. In addition, the two processes are not strictly separate, since the long-term ion motion, which leads to plasma redistribution as detailed in section 2.3.2, is the same wakefield-ponderomotive-force-driven ion movement which results in the long-term ionisation observed by ref. [100]. However, it is meaningful to treat them as separate topics. This is because long-term ion motion always occurs as a result of a dissipating wakefield and thus precludes equivalent acceleration before it recovers, while long-term ionisation is not a necessary consequence of the dissipated wakefield and the long-term ion motion.

2.3.5 Plasma-wakefield acceleration in a plasma channel

The initial considerations here propose that the longest-lasting structure in the plasma would be an evolving and then dissipating plasma channel, all of which would take place on nanoseconds timescale. A dissipated channel and thus a recovered plasma density in the vicinity of the driven wakefield should allow the next acceleration even to occur in the same conditions. As a result, these processes set the minimal accelerator bunch-train temporal density, i.e., the shortest separation between two pairs of driving and trailing bunches which is not impacted by this plasma density redistribution driven by long-term ion motion. Nevertheless, it is

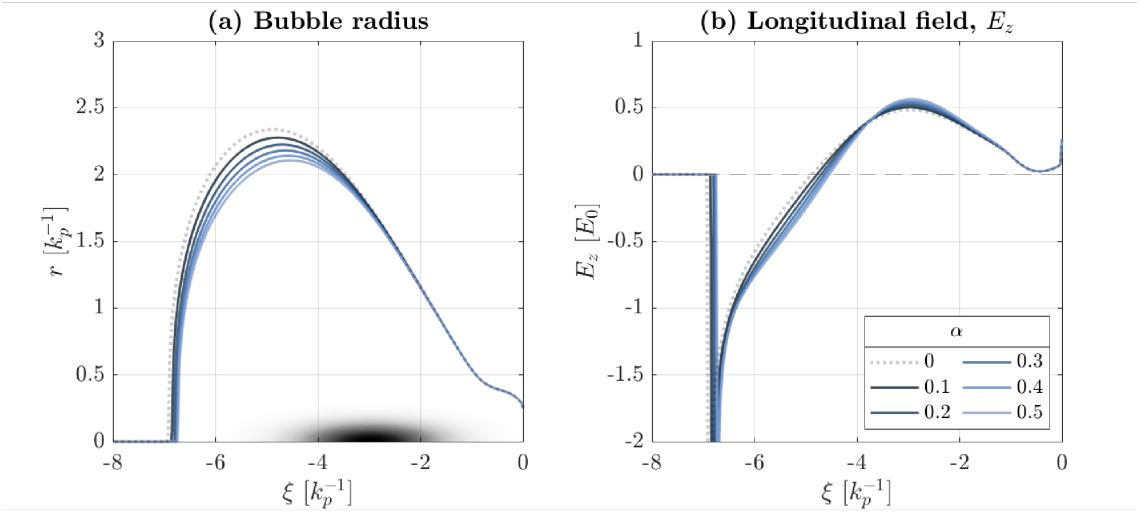

Figure 2.14: (a) The radial extent of the non-linear wakefield cavity for different plasma channel curvature values θ (denoted in figure as α, discussed in section 4.3.1) and (b) the longitudinal field for different θ. Figure from ref. [121].

important to understand what may happen to a following bunch and a driven wakefield in a non-recovered plasma. Using the non-linear PWFA formalism developed in ref. [63, 64], one can investigate how a non-uniform plasma channel would modify the wakefield. Following the derivation performed in ref. [121] and using Lu equations presented in section 2.1.2:

$$r_b \frac{d^2 r_b}{d\xi^2} + 2[\frac{dr_b}{d\xi}]^2 + 1 = \frac{4\lambda(\xi)}{r_b^2}, \tag{2.3.21}$$

for a uniform plasma density, where r_b is non-linear wakefield cavity (bubble) boundary, $\lambda(\xi) = \int_0^{r \gg \sigma_r} r' n_b(r', \xi) \mathrm{d}r'$ is the normalised driver charge per unit length, $n_b(r', \xi)$ is the driver density and σ_r is the transverse size of the bunch. To describe the non-uniform plasma channel, the lowest order, the parabolic shape was used [121, 122]. A parabolic ion distribution $n_i(r) = n_i 0\,(1 + \theta r^2)$ would modify the pseudopotential of the wakefield:

$$\psi(0, \xi) = \int_0^{r_b} \frac{dr}{r} \int_0^r \left(1 + \theta r'^2\right) r' \mathrm{d}r' = \frac{r_b^2}{4}\left(1 + \frac{\theta r_b^2}{4}\right). \tag{2.3.22}$$

Using this new pseudopotential form, the equation of motion of plasma electron forming the wakefield cavity may be acquired, using non-linear wakefield cavity formalism [63, 64]. The expressions can be simplified with the assumption that for an ultra-relativistic blowout, $n_b \gg n_p$, n_p being the plasma density. Because of this, the width of the cavity can be assumed to be much larger than the surrounding sheath of the wakefield, leading to:

$$r_b \frac{d^2 r_b}{d\xi^2} + 2[\frac{dr_b}{d\xi}]^2 + \frac{r_b^3}{4}\theta \frac{dr_b}{d\xi} + 1 = \frac{4\lambda(\xi)}{r_b^2}. \tag{2.3.23}$$

The equation of motion for the plasma electron at the cavity boundary therefore acquires an additional factor due to the parabolic ion density profile in a cavitated wakefield. The two equations were numerically solved for different θ values in ref. [121], revealing that the radial and longitudinal extent of the wakefield bubble become shorter with higher channel curvature, see fig. 2.14. The same was observed in ref. [121] when using the Dawson plasma sheet model instead of the nonlinear wakefield bubble radius formalism. By comparing the plasma response to a driver when the plasma density was uniform, and when it had a parabolic channel, the same narrowing and shortening of the wakefield cavity was noted. Numerical solutions for r_b can be then inserted into the expression for the electric field[121]:

$$E_z = \frac{1}{2} r_b \frac{dr_b}{d\xi} \left(1 + \frac{\theta r_b^2}{4}\right) \tag{2.3.24}$$

to obtain the longitudinal field of such wakefield, also shown in fig. 2.14. A higher curvature of the channel shifts the zero-crossing of the field downstream, shortening the range of phases of the decelerating field, and also increasing the amplitude of the decelerating field. In the accelerating phase, there is now a curvature in the field where normally the field gradient was uniform and there is a slight increase in the amplitude as well. Furthermore, the radial nonuniformity of ions in the cavity also results in a transverse focusing force that is not linear with radial position r. Such changes to the wakefield result in difficulty in optimally loading the non-linear longitudinal accelerating field and spoilage of emittance due to the non-linear transverse focusing field. A curved ion channel can thus result in an accelerated trailing bunch with slightly higher energy as well as a higher energy spread and increased emittance. A similar outcome in simulations was observed by [170, 171], where constant phase surfaces of the wakefield curved, changing the structure of the axial and radial fields. While this was an effect experienced by the same wakefield that drives the ponderomotive force moving the ions, it shows the sensitivity of wakefields to a non-uniform distribution of ions. Moreover, while this analysis explored the effects of channel curvature on the wakefield, it is also important to consider the consequence of a plasma density depression in the channel with respect to nominal density. In other words, a developing plasma channel will not only reach a certain curvature, but it will also have the absolute plasma density value decrease on the axis. Given the strong dependency of the wakefield and the plasma density, see section 2.1.2, an acceleration of a trailing bunch in a plasma channel would result in a much-reduced energy gain, deviation from optimum beam loading (thus broader energy spread), and loss of transverse matching resulting in emittance growth, all with respect to the acceleration in original plasma density.

All these effects are clearly malign, therefore the following acceleration event can only occur if a plasma channel dissipates. Equally, the evolving channel imprints

certain signatures on the driver-trailing-bunch pair, therefore it can be used as a diagnostic of the recovery processes in plasma. Pump-probe laser techniques are often used in diagnostics of PWFA e.g.: two-colour interferometry for plasma density measurements with a resolution of $\approx 1 \times 10^{15}\,\mathrm{cm}^{-3}$ (for a $\approx 30\,\mathrm{mm}$ long plasma) [127], and shadowgraphy measurements of plasma density modulations with a resolution of $n_p = 10^{18}\mathrm{cm}^{-3}$ (at the central laser wavelength of 800 nm) [102]. The latter can resolve the wakefield formation at $n_p = 1 \times 10^{18}\,\mathrm{cm}^{-3}$ densities and the following motion of ions as was done in ref. [102]. The electron beam has been used as a tool to infer plasma density and its changes at FLASHForward, and it has shown to have a resolution of $1 \times 10^{13}\,\mathrm{cm}^{-3}$ [121]. Because of this, it could resolve plasma channel changes via the response of the wakefield to the on-axis plasma density and the curvature of the channel. While not a direct diagnostic, PIC simulations can be performed with an equivalent bunch-pair for a range of plasma profiles, and the ones matching the experimental results can help map the plasma channel evolution, radially and longitudinally/temporally [121]. In addition, a direct plasma density diagnostic such as optical emission spectroscopy (OES) can inform of average plasma density changes. Given that at FLASHForward, it collects plasma emission light at a single longitudinal slice at the side of the capillary, it would not be able to resolve the channel radially. Yet, it can measure an increase in average plasma density transversely and, in this case, confirm whether the assumption of no additional ionisation is correct. If, during the plasma channel evolution, the average independently measured density is unchanged, this implies that the long-term ion motion resulted only in plasma density redistribution and no additional plasma was created. However, at FLASHForward, the OES only allows the density resolution of $5 \times 10^{15}\,\mathrm{cm}^{-3}$ [127] and temporal resolution of $\approx 100\,\mathrm{ns}$. As a result, the plasma evolution imprinted on the beam would have to be the dominant diagnostic for the long-term ion motion.

Chapter 3

Experimental facility FLASHForward

3.1 Accelerator operation

3.1.1 FLASH

FLASH, the Free-electron LASer in Hamburg, is an extreme-UV and soft-x-ray laser pulse facility [108, 109, 186], where the short coherent light pulses are produced by undulating accelerated electron bunches in a periodic magnetic structure [11]. The production is based on the self-amplified spontaneous emission process [187], which necessitates the use of ultra-short sub-picosecond electron bunches of high quality, i.e., low energy spread $\mathcal{O}(0.1\%)$ and low emittance $\mathcal{O}(1)$ mm mrad. The soft x-ray light pulses are used to image the evolution of atoms and molecules in chemical reactions, phase transitions, and expanding plasmas, encompassing a wide range of scientific topics in chemistry, biology, medical research, etc. To achieve these wavelengths, electrons are accelerated to 0.5—1 GeV. In addition, to supply the pulse frequency for high statistics, FLASH can be operated in a MHz-burst mode, achievable with its superconducting linear electron accelerator. Due to high user demands, FLASH has been operating with two beamlines, FLASH1 and FLASH2 since 2016 [12].

For the preservation of FEL beam quality and overall acceleration efficiency in plasma at FLASHForward, FLASH offers suitable parameters given by the design of delivering FEL-quality beams. The specific parameters are outlined in table 3.1.

The driver-trailing bunch generation method at FLASHForward involves dividing the beam current into a driver and trailing bunch using energy collimators in a dispersive beamline [69], further explained in section 3.1.2. This allows for fs-level control of the beam profile as well as bunch length modifications in addition to the

Electron Energy (highest)	1.35 GeV
Uncorrelated Energy Spread	0.1%
Bunch Charge	0.1—1 nC
Length	$\mathcal{O}(100)$ fs
Current	up to 2.5 kA
Normalised Sliced Emittance	2 mm mrad

Table 3.1: Beam parameters at FLASH [12, 107, 109, 188].

bunch compression at FLASH. The exact shaping is necessary to produce bunches that undergo necessary beam loading in the plasma wakefield, achieving high plasma-to-trailing bunch efficiency and energy spread preservation [72, 74, 189]. Such longitudinal beam current shaping is achievable thanks to the monotonic longitudinal phase space of the FLASH beam, i.e., chirp. Moreover, this chirp has three controls of its shape by the presence of the third-harmonic RF cavity at FLASH: controlling the chirp itself, and its curvature via its first and second derivative. This allows the production of shapes of the driver or trailing bunches that are non-Gaussian, e.g. trapezoidal. In the case of the trailing bunch, this shape achieved the ideal beam loading for energy spread preservation and high efficiency in plasma [74, 107, 189].

The bunch train pattern at FLASH, see fig. 3.1, and the availability of two simultaneous laser systems at the photocathode allow the exploration of several orders of bunch temporal separations and total delivered power ranges in PWFA. At maximum capacity, the bunch train can deliver 8000 bunches per second to FLASHForward with the 800 µs long RF pulse repeating at 10 Hz and the bunch frequency of 1 MHz [12]; however, in practice, the pulse is usually operated for $\sim 650\,\mu s$ [190]. This is limited only by the radiation safety requirements at FLASHForward and the lack of a dedicated beam dump, and so only about 20 Watts of electron beam power may be delivered [190]. As for the two photoinjector lasers, their only limit is the RF field itself and available accelerating-phase buckets. For high-repetition-rate experiments at FLASHForward, any two-bunch separation within the bunch train can be chosen to investigate the repetition limits in a plasma capillary. Using the two photoinjector lasers and injecting a second bunch in the next 1.3 GHz RF field accelerating-phase bucket, one can achieve temporal resolutions of 0.77 ns. The two-injector setup allows the exploration of the most fundamental limits of plasma recovery on nanosecond to microsecond timescales. Secondly, using the bunch train itself at MHz rates, this frequency regime can be researched and necessary developments for the plasma source made. Overall, this high-repetition-rate functionality at FLASH allows FLASHForward to explore high-average-power regimes in microsecond and nanosecond timescales in plasma accelerators, unlike any other PWFA facility in the world [107].

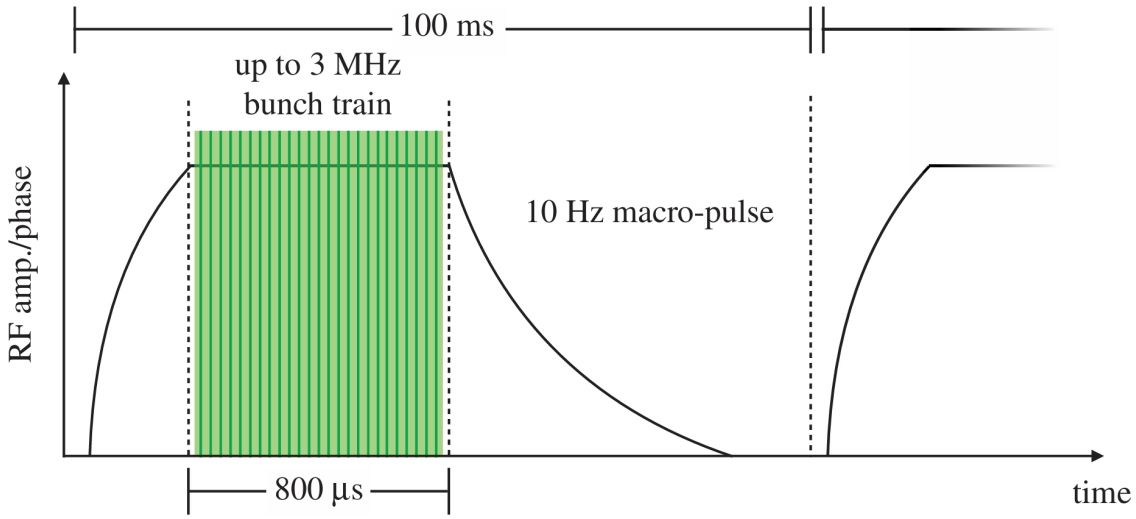

Figure 3.1: FLASH bunch train pattern. Figure from ref. [107].

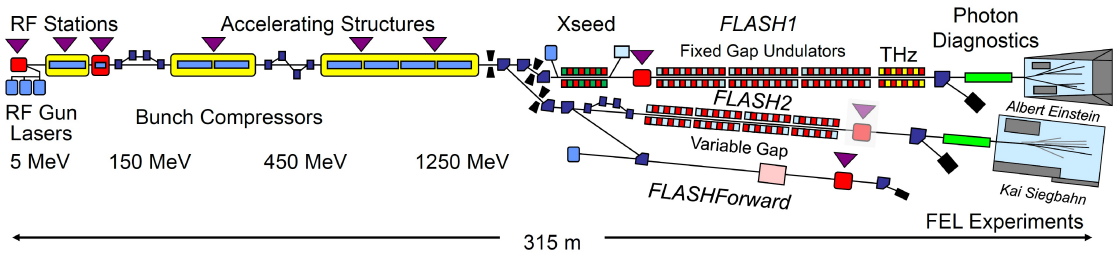

Figure 3.2: FLASH layout from ref. [191].

High-quality and finely controlled beams at a wide range of temporal separations are not the only functionalities setting FLASHForward up for precision-phase plasma wakefield research. The high stability and reproducibility of FLASH electron bunches allow for high-statistics experiments and demonstrations. While the low shot-to-shot jitter at FLASH is due to stable machine technology [109], the overall stability, especially against drifts, is maintained by an active feedback system, which sustains the same energy, bunch length, orbit, and charge over many experimental hours [74].

The facility can be divided into four parts, see fig. 3.2:

- injector;
- linac, comprising of accelerator modules and bunch compressors;
- undulators for FEL radiation production;
- experimental stations to use said radiation in research, for each of the two beamlines FLASH1 and FLASH2 [12, 109].

Since FLASHForward, instead of the undulators and end-stations, consists of a beamline with a plasma accelerator and diagnostics, only the first three parts of

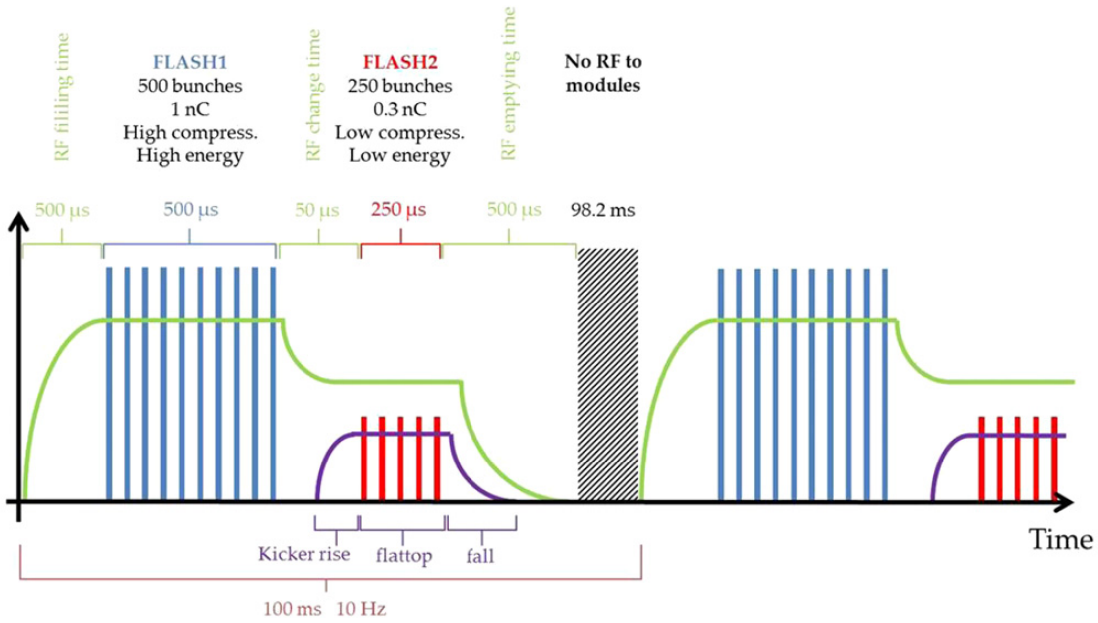

Figure 3.3: An example of FLASH1 and FLASH2 bunch patterns, RF filling and kicker rise times during the two-beamline operation mode, figure from ref. [12].

FLASH are of interest in this work.

The injector comprises a UV laser system and a photocathode, where the electrons are directly injected into an RF accelerating field, also known as the RF-gun [109, 192]. The immediate acceleration reduces the effect of the space-charge-related emittance growth [109]. A separate so-called "dark current" bunch also emerges from the gun; however, it is of a low current (10 µA), and in normal operation mode it is removed by a kicker—collimator system in the gun. The gun has two almost-identical injector lasers (pulse length 4 and 6 ps rms [122]), designed to run FLASH1 and FLASH2 in parallel [12, 109]. Both lasers are run by an oscillator synchronised to the 1.3 GHz frequency of the RF accelerator, and each are able to deliver 800 pulses (1 MHz) in one RF flat-top (see FLASH1 only operation in fig. 3.3) at 10 Hz or 2400 pulses (3 MHz) at 5 Hz [109]. The 1 and 3 MHz frequencies are defined by the fastest rate of Pockels-cell pulse selection [122]. In addition, both lasers can be operated simultaneously in a single-bunch-in-train mode, producing two bunches separated only by the frequency of the RF, i.e., 0.77 ns. When operating both lasers, the dark current kicker magnet has to be off to avoid affecting a delayed injected bunch from one of the lasers. Thus, the extra dark current charge is present during this two-laser operation.

After the RF gun, seven accelerator modules and two bunch-compression chicanes follow. The modules contain eight TESLA-type superconducting niobium cavities, with gradients of 25 MV/m, and some cavities go beyond 30 MV/m [107, 109]. With them, the FLASH beam can be accelerated up to 1.25 GeV, even if the bunch arrives at an off-crest RF phase. In addition, the RF amplitude and phase are

stable thanks to a low-level RF system. The RF filling time lasts for 500 µs and the 800 µs available acceleration duration follows that, see fig. 3.3. To distribute these bunches into the two FLASH beamlines, a kicker-septum system splits the electron bunch trains at a desired temporal point. As a result, the 800 µs burst is separated into two parts, and $20-50$ µs of the RF pulse is lost because of the kicker switching, as demonstrated in fig. 3.3.

The two bunch compression chicanes are positioned in the beamline to receive a bunch at energies of 150 and 450 MeV respectively [109]. To compress these bunches, they are accelerated at an off-crest RF phase, introducing an energy chirp this way. Furthermore, FLASH has the capability to change the shape of this chirp. It is usually utilised to maintain a linear chirp (where it is necessary in most cases). This is done with a third-harmonic (3.9 GHz) module, containing four cavities, that follows the first accelerator module [109, 193]. To avoid strong space charge effects in the RF gun, a long bunch is injected. Because of the cosine form of the accelerating RF field, the imprinted non-linear shape on the longitudinal phase space of the bunch can be corrected by a third-harmonic decelerating field [194]. As such, the linearised and chirped bunch can undergo a compression in the first chicane to 1 ps (300 µm). The control of the amplitudes and phases of these initial modules allows the adjustment of the bunch length, current, and shape of the longitudinal phase space [109]. Using the second compressor, since the bunch is at higher energies and space-charge forces scale with $\frac{1}{\sigma_z \gamma^2}$, it can be compressed to a final typical value of 167 fs (50 µm) length and kA-level currents avoiding space charge effects [109]. After this compressor, the bunch is brought to its final energy of 1.25 GeV by the remaining four accelerating modules [193]. Recently, FLASH has undergone an upgrade, where two of the accelerator modules were replaced to increase the final electron energy from 1.25 to 1.35 GeV [195].

The linac stability over longer time durations, i.e., prevention of drifts is ensured by an active online feedback system. It uses a diagnostic as a monitor, e.g., bunch length, and a setting as an actuator, e.g., RF settings for compression, which is adjusted once a measurement of a monitor leaves predetermined bounds. This way FLASH can ensure a stable charge from the photoinjector, stable bunch compression by adjusting the RF settings, and a stable orbit with changes in magnet correctors. However, while operating in the two-bunch mode in short temporal separations (0.77—O(100)) ns, the diagnostics in the linac measure over longer timescales than the bunch separation, thus one of the bunches influencing the monitors of the other. In this case, the online feedback system cannot be used.

Once accelerated and compressed, the FLASH beams are distributed into the two beamlines, FLASH1 and FLASH2. As mentioned above, a kicker system (three fast kickers and a DC Lambertson-septum [196]) is used to divert bunches at necessary

points in time to the FLASH2 extraction arc. At the end of this arc, the beam is steered by a DC bending magnet into FLASH3, the FLASHForward beamline [190, 196].

3.1.2 Optimal PWFA setup at FLASHForward

To operate a plasma wakefield accelerator, a drive beam of specific parameters has to be prepared. In addition, some constraints are set on the trailing bunch, since it can influence the PWFA process via beam loading, matching to plasma focusing forces, and longitudinal positioning. To drive a strong GV/m wakefield, and to accelerate a trailing bunch efficiently while preserving quality, the following parameters must be considered:

- Wakefield strength (GV/m) and accelerating field:
  1. Driver bunch density:
     - bunch current: $\mathcal{O}(1\text{ kA})$,
     - bunch transverse size at plasma interaction: $\sigma = \mathcal{O}(10\,\mu\text{m})$, $\beta = \mathcal{O}(10\text{ mm})$, $\epsilon = \mathcal{O}(10\,\mu\text{m})$.
  2. Double-bunch profile:
     - trailing bunch position: fs-scale.
- Wakefield shape (GV/m^2) and acceleration efficiency:
  1. Driver bunch profile:
     - bunch length: fs-scale.
  2. Trailing bunch profile:
     - current and temporal shape: fs-scale.
- Bunch quality preservation:
  1. Trailing bunch profile, to preserve energy spread:
     - current and temporal shape.
  2. Trailing bunch matching, to preserve emittance:
     - size at interaction: $\sigma = \mathcal{O}(1\,\mu\text{m})$, $\beta = \mathcal{O}(10\text{ mm})$, $\epsilon = \mathcal{O}(1\,\mu\text{m})$.
  3. Double-bunch alignment, to preserve emittance:
     - first and second order dispersion: $\text{D} = 0$, $\text{D}' = 0$.

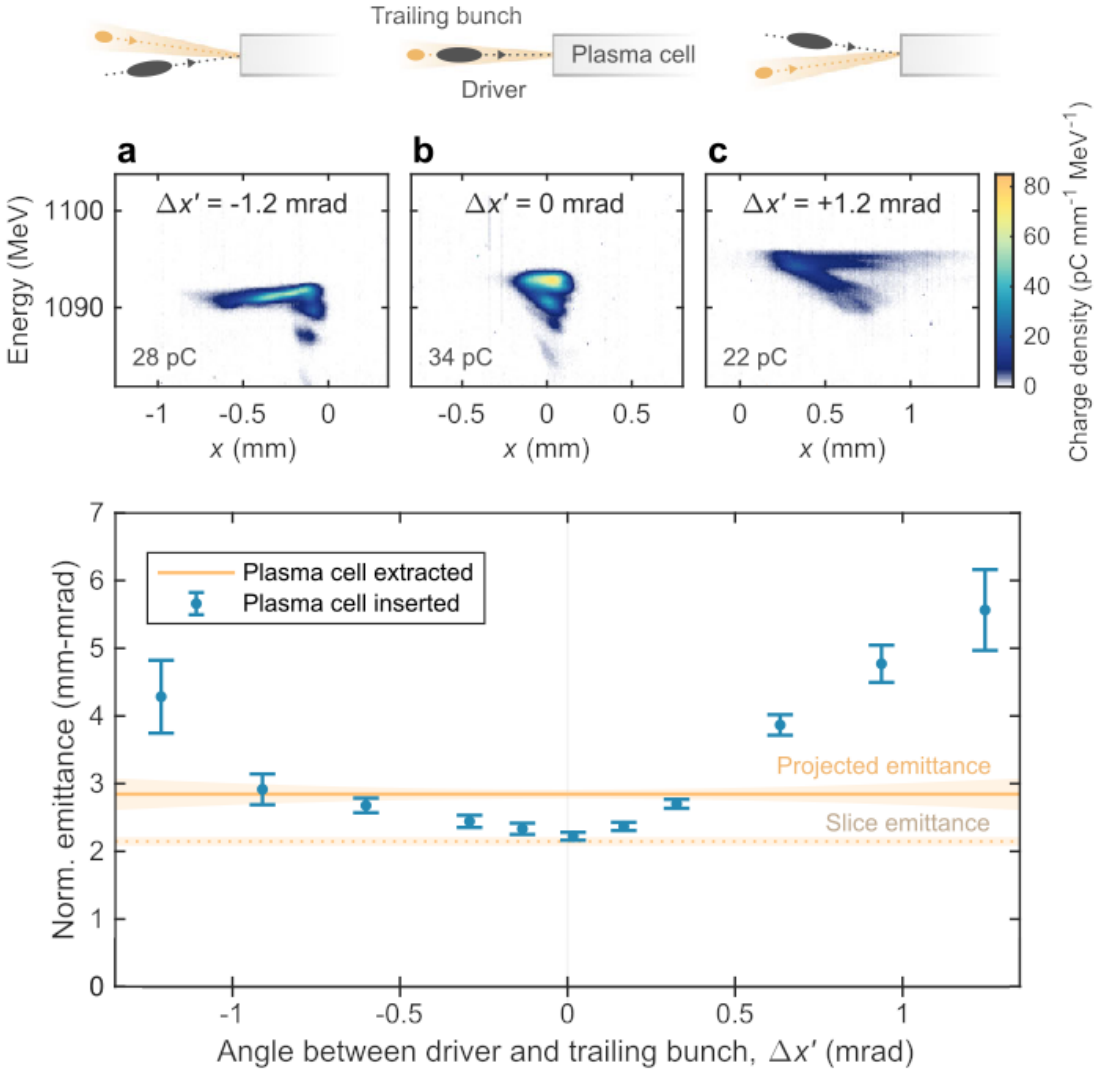

Figure 3.4: (a-c) Accelerated bunch imaged at the spectrometer at different beam-alignment settings. At severe misalignment, the beam is distorted and emittance grows (d). Figure from ref. [77].

FLASH bunch longitudinal phase-space properties align with the needs of PWFA: bunches can be compressed to lengths of 150 fs and currents of $1 - 2.5$ kA. This allows the formation of strong wakefields in the timescale/lengthscale of typical PWFA densities, i.e., $\mathcal{O}(10^{16})\,\mathrm{cm}^{-3}$. In addition, the monotonic (usually linear) shape of the longitudinal phase space allows cuts to be made on the longitudinal profile of the beam by simply dispersing it, and forming double-bunches of the desired profile by scraping [107, 197], as described in section 3.1.3.

FLASH emittance is favourable for achieving high driver bunch charge densities and trailing bunch matching into the transverse plasma wakefield. By scraping the full FLASH bunch and measuring each slice emittance, it was observed in ref. [66] that the tail, from which the trailing bunch is formed, had an advantageous emittance for hard focusing (beta functions $\beta \sim \mathcal{O}(10)\,\mathrm{mm}$), 1 mm mrad. The front

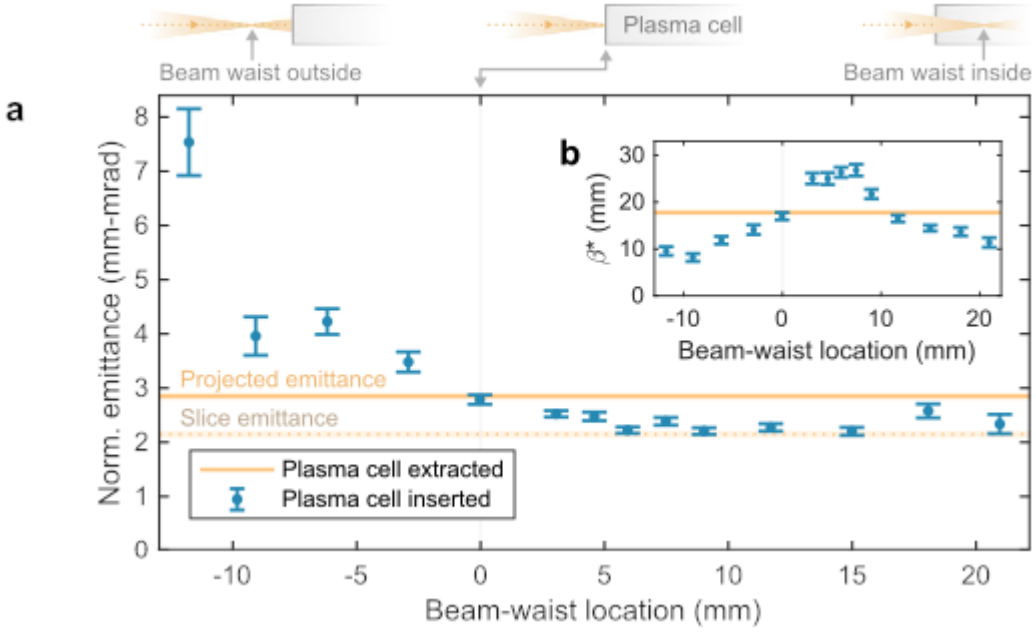

Figure 3.5: (a) Emittance growth suppression when the matching condition is satisfied by moving the trailing beam waist location, with virtual waist-beta-function variation shown in (b). Figure from ref. [77].

of the bunch, or the driver front, on the other hand, was 10 mm mrad, potentially due to coherent-synchrotron-radiation (CSR) kicks [74, 198]. Similar results were also seen in ref. [74], where the divergence of the beam, tail to head, ranged from 0.23 mrad to 1 mrad; the minimum bunch transverse size, tail to head, ranged from 2 to 10 µm, and the normalized slice emittances ranged from 1 to 20 mm mrad. Vertical emittance had not been measured in FLASHForward until very recently, thus the emittance measured at the gun, i.e., 0.5—1 mm mrad, is assumed to persist. Ultimately, effort must be invested in maintaining low projected emittance while delivering the beam to the FLASHForward plasma. This can be achieved by avoiding strong bunch compressions, fully removing first and second-order dispersion in the dispersive section, and precisely aligning the bunch with fine dispersion control. Fine dispersion control not only benefits the bunch slice alignment and thus emittance, it also is crucial for the overall driving and trailing bunch alignment, shown in fig. 3.4. The double bunch must have minimal to no transverse tilts; otherwise, the trailing bunch would sample non-linear off-axis fields, spoiling the high beam quality. Finally, with low bunch emittance, sizes of microns can be achieved, so that the trailing bunch is injected close to matching conditions [116, 199], see fig. 3.5.

However, emittance alone does not determine the beam size: small beta functions of 10 mm in both planes are reached at FLASHForward with strong quadrupole magnet fields. This comes at the expense of inducing a high chromaticity in the beam, thus causing the driving bunch to enter the plasma at a divergence. While efforts are put to focus this driver to small sizes to drive strong wakefields, the

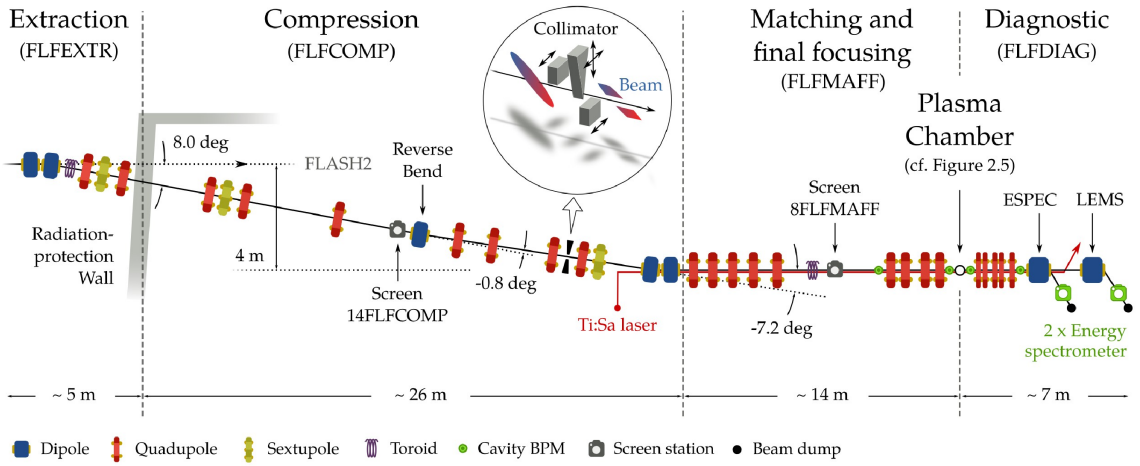

Figure 3.6: The FLASHForward beamline showing the extraction, compression, matching, final focusing, interaction, and diagnostics sections. Figure from ref. [189].

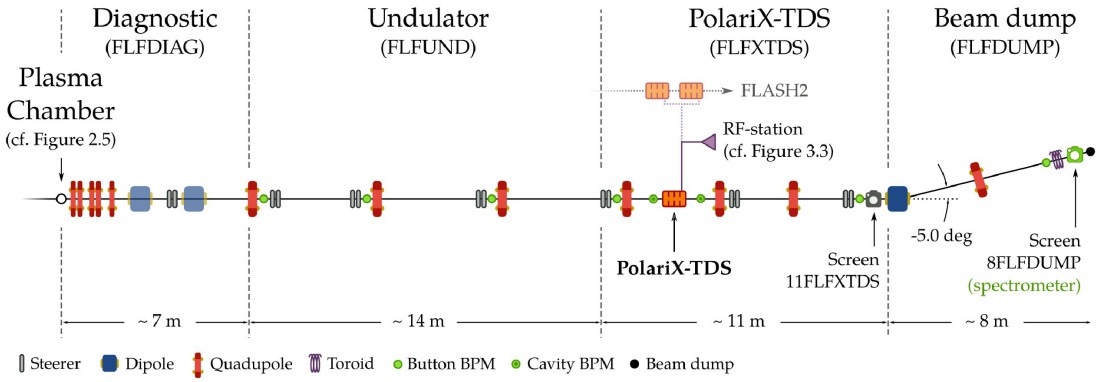

Figure 3.7: The FLASHForward beamline showing the diagnostics and TDS sections. The undulator section was designed to contain undulators; however, it is serving as a transport beamline from the interaction point to the TDS. Figure from ref. [189].

chromaticity and thus divergence results in a reduced charge density. Nevertheless, as reported in section 1.5.3 and ref. [77], this has not been an issue for driving wakefields, rather the opposite; the lower charge density of the driver prevents the development of hosing instability and in-bubble ion motion.

3.1.3 Sections of FLASHForward

FLASHForward is divided into seven sections, where the first three are concerned with beam preparation for plasma interaction: extraction, compression, and matching with final focusing, see fig. 3.6. The plasma is generated in the central interaction area. The post-plasma beam is investigated in the initial diagnostics, then transported to an X-band TDS section via the undulators section, which is reserved to have undulators in the future but is presently a beam transport line. Finally, the beam is discarded in the dump, see fig. 3.7.

The extraction and compression sections follow the FLASH2 extraction arc,

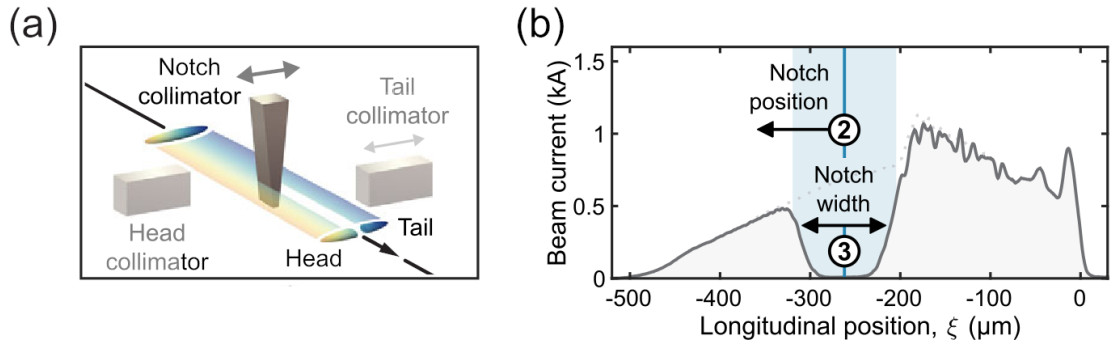

Figure 3.8: (a) FLASHForward collimator system in the dispersive section, and (b) a scraped beam current profile, with the wedge/notch movement directions indicated for the optimum beam-loading experiment, "2" being the horizontal movement, "3" being the vertical movement. Figure from ref. [74].

where the two beamlines are separated by dipole magnets. It ends with another set of dipole magnets, resulting in a 4 m transverse separation from the FLASH2 beamline. The section itself is designed to have the first and second-order dispersion removed. As for the longitudinal beam properties, this section has a variable $R_{5,6}$, which is the coupling parameter of the beam momentum and longitudinal coordinate. R is the beam transport matrix as in eq. (2.1.22) but extended to include both transverse coordinates x and y as well as the longitudinal coordinate along the beam. This section allows for further beam compression. In addition, the double-bunch generation system, i.e., the energy collimator, or scraper, is installed in this section, since here the beam is dispersed and thus its longitudinal profile can be tailored [107, 200].

The energy collimator consists of three parts: two beam masks at each end, one of which can cut the low energy side of the dispersed beam, and thus the front of the beam longitudinally given the negative chirp of the beam. The other mask cuts high energy, or the back part of the beam. The third part of the collimator system is a wedge, which, when moved vertically, changes its horizontal extent in the beam path, and thus the horizontal length of the charge cut in the dispersed beam. When moved horizontally, the location of the cut is changed, thus allowing a flexible double-bunch generation, see fig. 3.8. With the collimators, one can select either just the driving bunch or trailing bunch alone by blocking the other. The system can also select a small energy/longitudinal slice, all of which is needed for precise PWFA double-bunch characterisation. In general, this precise tailoring aids in PWFA optimisation. For instance, the head of the driving bunch can be cut, which often suffers from collective effects upon compression and thus has smaller charge density and strong centroid offsets [190]. Such action increases the stability of PWFA [66]. In addition, the collimators tailor the trailing bunch profile, which is crucial for optimum beam-loading [74]. Overall, femtosecond-level bunch profile

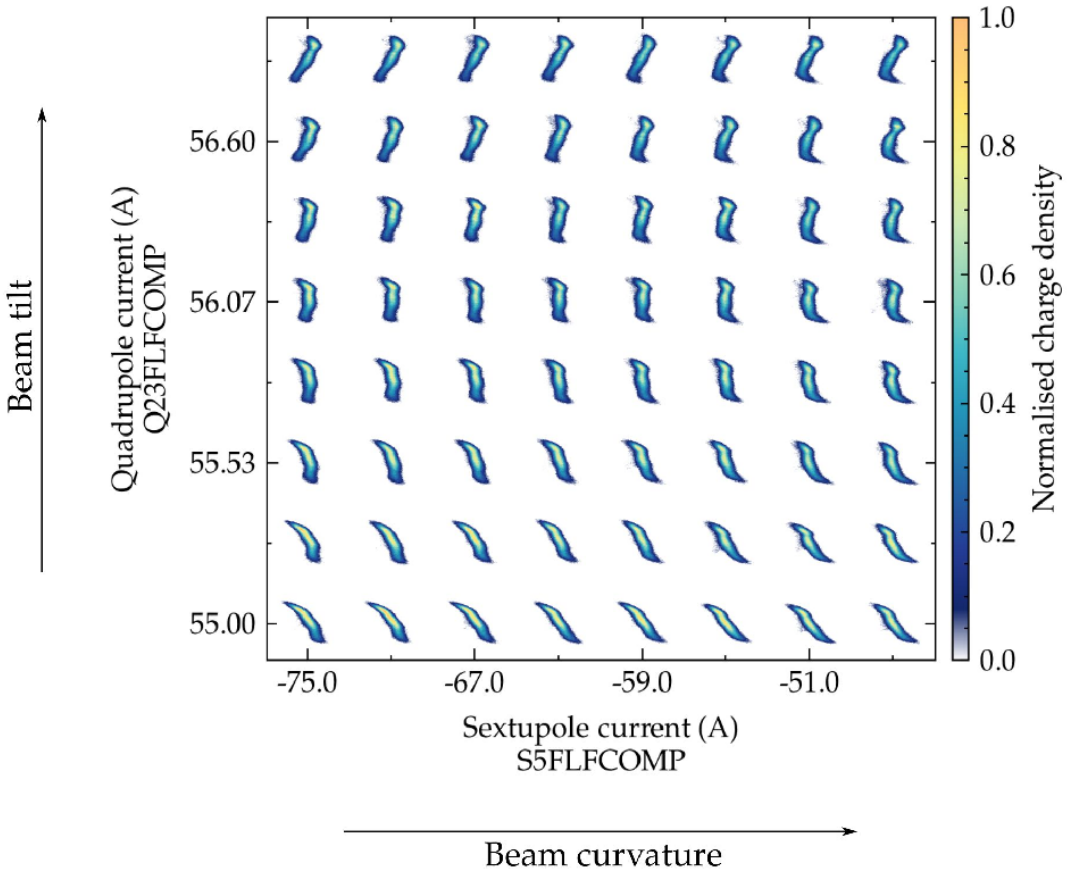

Figure 3.9: Transversely deflected trailing bunch with PolariX-TDS (section 3.1.4), where the horizontal axis of each image corresponds to the transverse coordinate, and the vertical axis corresponds to the longitudinal coordinate, and the large axes correspond to quadrupole and sextupole adjustments in the dispersive beamline section. Figure from ref. [189].

control is possible with the scraper, exactly the detail of movement needed in PWFA [69].

When starting the machine, loaded accelerator lattice values based on the theoretical design of the beamline can often deviate due to the magnet hysteresis effects, thus the setup of FLASHForward begins with achieving zero dispersion at the end of the extraction and compression section. By varying the RF amplitude of one of the FLASH modules and thus the beam energy, and recording beam position changes horizontally and vertically, a dispersion value can be deduced, and by making fine adjustments to the optics, the dispersion can be minimised. Equally, even though the beamline is designed and set in an achromatic way, the bunch itself can still arrive at plasma interaction with dispersion, i.e., tilts and even curvatures due to kicks from wakefields or collective effects in the linac. By observing the longitudinal distribution of the beam in one axis and one of the transverse displacements on the other, the quadrupole and sextupole magnets in the dispersive section are adjusted to straighten the beam and thus align the driving and trailing bunch transversely

[74, 77, 189, 201], see fig. 3.9. Alternatively, energy spectrum may be observed instead if the bunch longitudinal phase-space is confirmed to be linear.

The third pre-plasma section, a 13 m long matching and focusing beamline, prepares the double-bunch for plasma interaction. Firstly, after all the optical adjustments for removing the dispersion, beam tilts, and curvatures, the beam Twiss parameters are measured and matched by the optics of this section. The optics are set to produce a beam waist at the plasma entrance and beta function of around 10 mm in both planes at that point [74], while minimising first-order chromaticity [77]. The beta function is calculated at each optical element in the beamline, an example of which is shown in fig. 3.10. This helps deduce which of the nine quadrupoles have decoupled control over key beam parameters, such as the beta function at the waist in both x and y planes, and the location of the waist itself in each plane [77]. With those controls one can do fine adjustments and reach beta functions of the trailing bunch that match at the plasma entrance, usually, 10 mm in both planes for a hard-focus mode [74], translating to a $\mathcal{O}(10\,\mu\text{m})$ size [200]. The adjustments can also help increase the charge density of the front of the driving bunch for intense wakefield formation and energy deposition or even triggering of instabilities such as hosing or ion motion [77].

3.1.4 FLASHForward beam diagnostics

The FLASHForward beam, whether interacted with plasma or being prepared for it, can be characterised by a vast array of available diagnostics. They can be categorised into the following three groups: beam position monitors (BPMs), screen stations with preceding sets of quadrupoles, with and without a dipole for beam spectrometry, and a transverse deflecting cavity. To use these diagnostics for singular parts of the beam, the scraper system is important.

Beam position monitors (BPMs) measure the vertical and horizontal beam position. Cavity BPMs [202] are also used to measure charge. However, charge-measuring toroids (toroidal current transformers) also exist in several parts of the beamline [67]. Beam position measurements are most straightforwardly used for beam orbit corrections and observation of orbit fluctuations. The latter is especially critical in front of the scraper because position jitter translates directly to beam profile changes. Charge measurements inform how much of the beam has been cut by the scraper, how much is lost along the beamline because of, for example, strong quadrupole focusing, and how much charge is lost after interaction with plasma.

The BPMs can be used to reconstruct the transverse beam qualities by the method of two-BPM tomography [203]. This is a technique developed at FLASHForward for monitoring the beta function at the waist and the waist location while

adjusting final focusing quadrupoles. It is non-invasive and fast, providing approximate information on beam parameters on a few-tens-of-seconds timescale. It was found that when the beam is focused to beta functions on the order of 10 mm, so-called hard-focus mode, the beam-centroid jitter phase space corresponds very closely to the actual phase space of the beam, thus being an online proxy for determining Twiss parameters of the beam. The beam-centroid position is directly read from the records of the BPMs, while the angle, necessary for full transverse phase space representation, can be deduced from the measurements of two consecutive BPMs. At FLASHForward, these measurements are done where the hard focus is set up and where the knowledge of beam transverse properties is most crucial, that is in the plasma interaction section. It is surrounded by two cavity BPMs, upstream and downstream, which are then used to deduce the centroid jitter phase space and thus beam transverse properties. The parameters of most interest here are the beta function at the waist and the waist location. Once the matching and final focus lattice is set up, by using this method and making fine adjustments in the final focusing section, one can reach the approximate desired beta function at the plasma entry with millimetre precision [74, 203]. After this setup, the beam parameters can be determined more precisely with the diagnostics section after the plasma module.

The investigations done at FLASHForward to develop this technique, which is reported in ref. [203], demonstrate the common features of the beam that is set up in FLASHForward, see fig. 3.10. Firstly, in the hard-focus mode (beta around 10 mm), the beam has a highly pronounced chromaticity, see fig. 3.11. As such, 2-BPM tomography should only be performed for small energy slices in the beam (thin slices with 0.1% root-mean-square (rms) energy spread). For a general plasma-wakefield acceleration experiment, the trailing bunch has strict requirements on the beta function at the plasma entrance to match it to the plasma focusing fields. When matched (or being close to matching), the emittance growth can be avoided (or minimised). Because of this, and since it corresponds to a small enough slice in the beam, 2-BPM tomography is used for final matching and focusing adjustments on the trailing bunch alone.

The bunch is focused to a small beta function at the entrance of the plasma, a large energy spread is generated in plasma for driving bunches, and the longitudinally varied focusing conditions in plasma due to the energy spread result in variable betatron phase advance along the beam [66]. The consequence of this is the emergence of beams from the plasma with high divergence and chromaticity. To capture and transport the beams in these conditions to a screen station, the screen stations with capturing and imaging quadrupoles and spectrometry dipoles are installed as close as possible to the exit of the plasma. The TDS diagnostic station, on the other hand, had to be installed further away along the beamline due to stringent

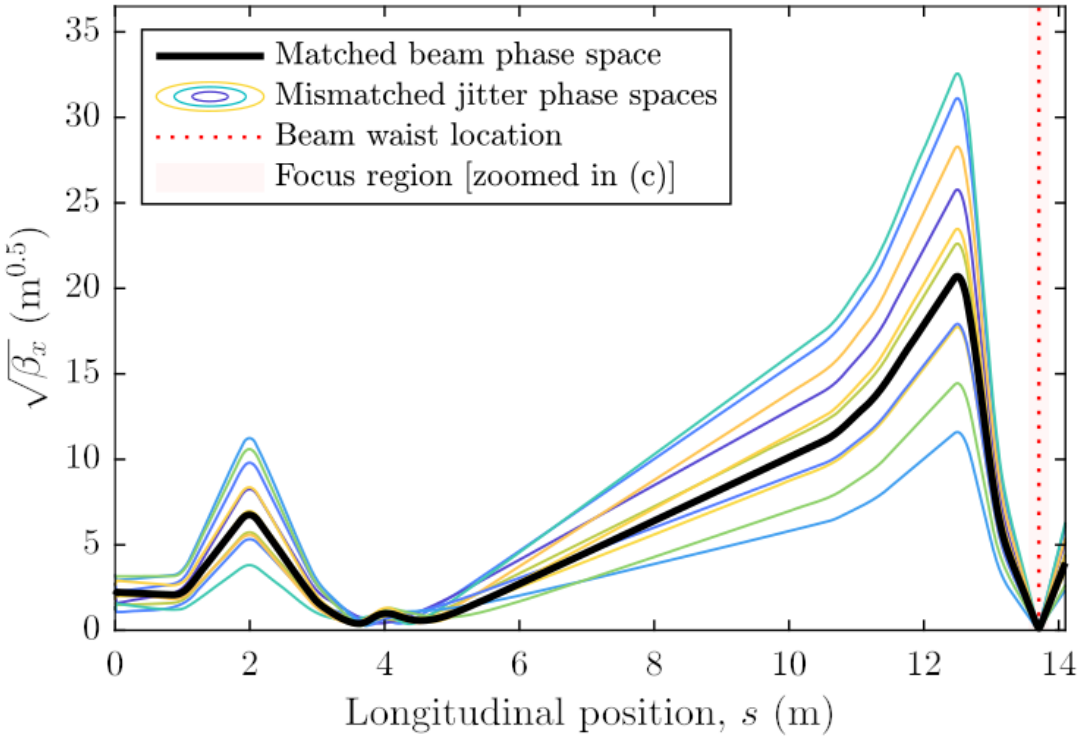

Figure 3.10: Typical FLASHForward optics in the matching and final focusing section. Figure from ref. [203].

vacuum conditions for such a device [66]. As a result, the plasma-interacted double-bunch undergoes diagnosis usually only in the screen stations following straight after plasma, whereas the TDS is used for FLASHForward beam setup and pre-plasma beam characterisation. The exception is the extensive study with the TDS on the PWFA beam loading effects on the trailing bunch reported in ref. [189].

The diagnostics section after the plasma consists of three different screen stations: ESPEC, electron spectrometer consisting of a dipole and a series of screens covering an energy range from few MeV to 2.4 GeV [67]; LEMS, low emittance monitoring screen consisting of a dipole and a high-resolution screen; and DIAG, a recently-installed screen with no dipole, where vertical emittance was recently begun to be regularly measured. The former two use a 1.07 m long vertically dispersive dipole magnet [77]. As such, the horizontal properties of each energy slice can be investigated at these stations. All diagnostics are preceded by five capturing XQA quadrupoles [67, 204], which are set as a triplet to point-to-point image the beam from the interaction point and its surroundings to the screen with desired magnification and energies up to 2.5 GeV [74, 77, 107].

Located 4 m downstream of the interaction point [77], the ESPEC screen station is used the most often due to its broad band of imageable energies. However, when operating with plasma, while it can display the double-bunch on the screen, it is severely limited by the large energy spread and chromaticity of the emerging

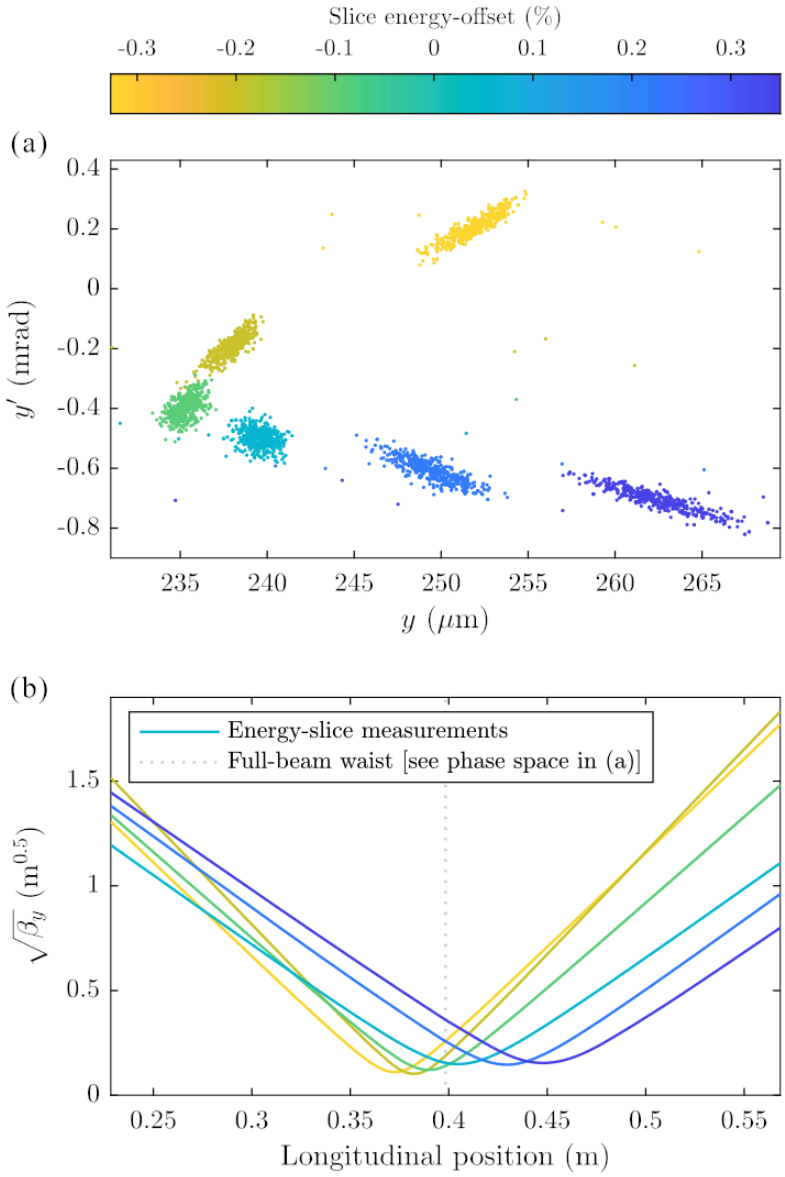

Figure 3.11: Phase space and chromatic focus of each energy slice at FLASHForward. Figure from ref. [203].

plasma-interacted beam. Because of this, only a selected energy slice is imaged, while the spectrum away from imaging energy is not accurately represented due to beam divergence and slice angular differences. As a result, for accurate beam energy spectrum and spectral density reconstruction, an imaging energy scan must be performed, where the five quadrupoles are adjusted as a triplet to transfer different energies at the same object plane for each scan point. The bunches are imaged onto a scintillator screen (GadOx, LANEX (fine)) outside of the vacuum, crossing the vacuum stainless steel wall of 1 mm thickness [66, 122]. The screens are recorded with CMOS cameras of 3.45 µm pixel size, while the whole imaging system results in 50 µm resolution, corresponding to 2 pixels [122], and energy resolution of 0.05% when imaged at the correct energy [66, 75, 122].

LEMS is a European XFEL-type screen station, which was designed to specifi-

cally measure very low emittances in high-resolution accurately, i.e., $\mathcal{O}(1\,\mu m)$ which the ESPEC station cannot resolve. The high resolution is achieved by the screen station being furthest away among all three stations and thus allowing high beam magnification. To be more precise, the LEMS is located 7.3 m downstream of the plasma interaction point, allowing for a maximum of -12 horizontal magnification, while ESPEC can only magnify to -6 [110]. The screen itself is GAGG:Ce, and as opposed to LANEX, and it can resolve 6.2 µm while GadOx is limited to 50 µm rms resolution [77]. As a result, the emittance resolution can be as low as 0.1 mm mrad [110]. In this case, the beam does not have to traverse a vacuum separation because the screen is installed in vacuum.

Both screens were calibrated in terms of position, energy, and charge [205]. While the position is measured upon the installation of the screens and their imaging cameras, both energy and charge calibrations were performed using the electron beam. For energy, a simple dipole current scan is performed with a small scraped energy slice of the beam. Using this scan, the position of the beam can be related to its energy for a given dipole current. As for the charge, a scraper scan is done, where the scraping and thus the decreasing charge is observed both on the screen and a preceding toroid. At the end, the signal seen on the screen is related to the charge measured by the toroid, with a few other corrections for geometry, lensing effects, and temporal evolution of scintillation light [110]. To account for scintillating screen saturation at high charge density, Birks' law was taken into account [77]. For the ESPEC screen, the saturation limit is set at $5\,\mathrm{nC\,mm^{-2}}$, thus necessitating a defocusing of one of the planes with intense bunches that have not interacted with plasma [110].

Using the quadrupoles to image selected energy and observing the double-bunch spectrum on the ESPEC screen, one can record changes in the spectrum at different plasma interaction conditions. For instance, energy deposition by the driving bunch into plasma can be calculated by recording the spectrum at each imaged energy that the driving bunch spans over [75]. In addition, the quadrupoles and the dipole can be used to calculate energy-resolved horizontal bunch parameters with the LEMS screen. With no focusing forces, the beam phase space evolves ballistically, corresponding to a beam size evolution of

$$\sigma_x = \sqrt{\epsilon_{gx}(\beta_x + \frac{(s-s_0)^2}{\beta_x}) + R^2} \tag{3.1.1}$$

the ballistic beam waist envelope model, analogous to eq. (2.1.40), where R is the resolution limit of the screen. By imaging the beam at different object planes s, the beam size σ_x is measured at the imaging plane, see fig. 1.6. One can then fit the data to obtain the parameters in the equation: the normalised emittance $\epsilon_{nx} = \epsilon_{gx}\gamma$

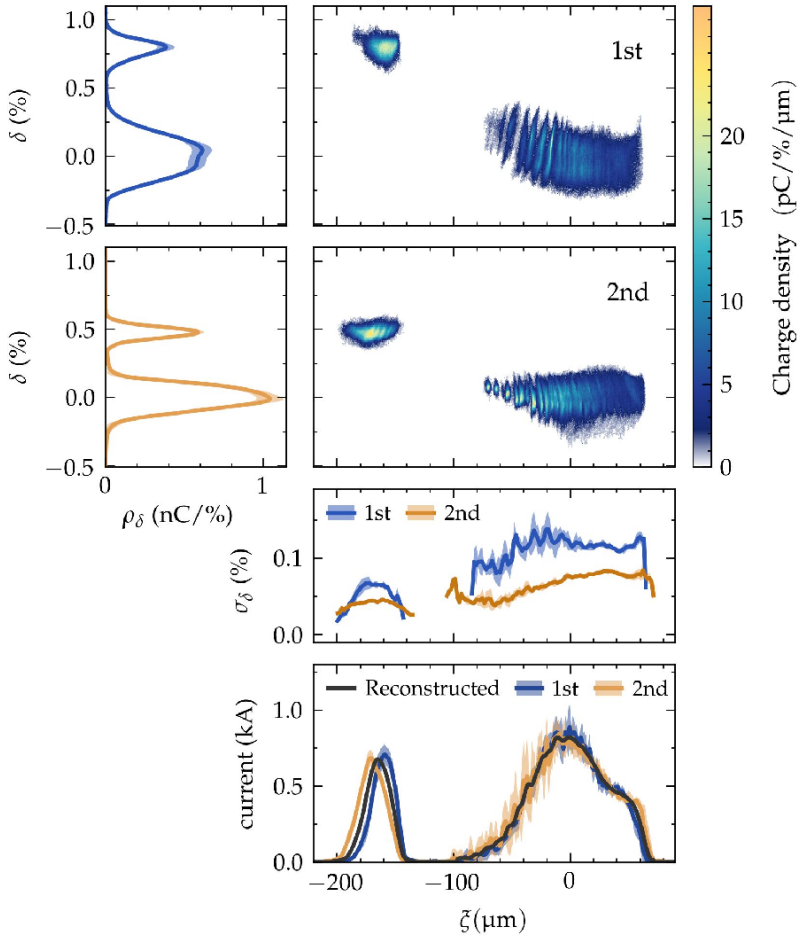

Figure 3.12: Longitudinal phase space images of the double bunch at the 1st (top right) and 2nd zero-crossing of the TDS field, with spectral distributions δ on the left, slice energy spreads σ_δ, and double-bunch current at the bottom. Figure from ref. [189].

and the beta function at focus β_x, also the divergence at the plasma exit $\sqrt{\frac{\epsilon_{gx}}{\beta_x}}$ and the focal plane s_0. Each object plane (and magnification) can be calculated using the measured energy of the slice or the bunch and the recorded quadrupole currents. Such bunch tomography for transverse parameter deduction is most often done at the LEMS screen since it can resolve the measured emittance, while the ESPEC screen can only provide information on the dispersion (see eq. (2.1.41)) [77].

The longitudinal bunch characterisation can be done at the TDS diagnostic station, located 33 m away from the interaction chamber for the aforementioned reasons relating to gas load as well as to allow the space necessary to set the optics for the TDS measurements [190]. As a result, a whole section, referred to as the undulator section, consists of quadrupoles that can further transport the bunch from the interaction chamber to the TDS area. This can be achieved with a soft-optics mode, where beta functions are $\mathcal{O}(1)$ m, and thus yield a low divergence beam [74]. Because of this, the transport of a plasma-interacted bunch is complicated and is usually not done, except for transporting the trailing bunch alone as was done in ref. [189].

Once transported, the beam is transversely deflected in an X-band (11.998 GHz) TDS and onto a screen, resulting in an image with femtosecond-level longitudinal resolution with correctly set soft-optics [206], where the resolution is governed partly by the RF frequency [207], hence the use of an X-band cavity. The X-band TDS at FLASHForward, also known as PolariX, is one of three systems of this kind in the world, developed by DESY, PSI, and CERN [207, 208], with other systems installed in DESY (FLASH2, SINBAD) and PSI (ATHOS at SwissFEL) [207]. It is unique in its capability to deflect the beam at any angle in the plane normal to the beamline, which is achieved by a variable phase shifter controlling the phase difference of two counterpropagating waves creating the RF field in the TDS cavity [207, 208]. As a result, by employing both the PolariX TDS and quadrupoles, the FLASHForward TDS can be used to perform 5D (horizontal and vertical positions and divergences, and the temporal distribution) beam phase space tomography [209]. In addition, the bunch charge density distribution can be fully reconstructed [207]. Transverse bunch properties in each plane and for each longitudinal slice, e.g., slice emittance for both planes may also be measured [188, 207]. The TDS system is followed by a final beam dipole spectrometer, where in combination with vertical transverse bunch deflection, the longitudinal phase space of the bunch can be observed on the in-vacuum GAGG:Ce screen. For increased resolution, there are another three quadrupoles in between the TDS and the dipole for imaging [77]. In the energy dispersive plane, the optics are set for point-to-point focusing of the bunch onto the screen, while the transversely streaking plane is set to parallel-to-point imaging [77]. Two different zero-crossings may be observed at the TDS screen. Taking measurements at each zero-crossing allows the removal of longitudinal centroid offsets in the reconstructed longitudinal phase space [77, 190]. As the FLASH beam, in the normal FLASHForward operation mode, has a linear chirp, a simple mapping of longitudinal slice position to energy could extend the phase space characterisation to 6D [188, 207]. With the display of the longitudinal bunch profile, changes in the dispersive section for bunch alignment can be monitored, as shown in fig. 3.9. Then, proceeding to also disperse the bunch with the dipole and observe the longitudinal phase space, one may characterise how the bunch is scraped at the tail and the head, and record the double-bunch current profile and energy distribution, see fig. 3.12. It can also be investigated how different compression settings at FLASH, i.e., the RF settings in 1.3 GHz and 3.9 GHz modules, manifest in the linearity or curvature of the longitudinal phase space, in the peak bunch current and its overall length. Finally, as was done in ref. [189], plasma-interacted trailing bunch longitudinal phase space can be investigated as it goes through different levels of beamloading of the wakefield. Besides the multi-polarity feature, this X-TDS cavity is run by a µs-level modulator pulse. When its arrival time is modified, it can thus act on any single bunch in a MHz train, thus allowing high-repetition rate single-bunch diagnostics

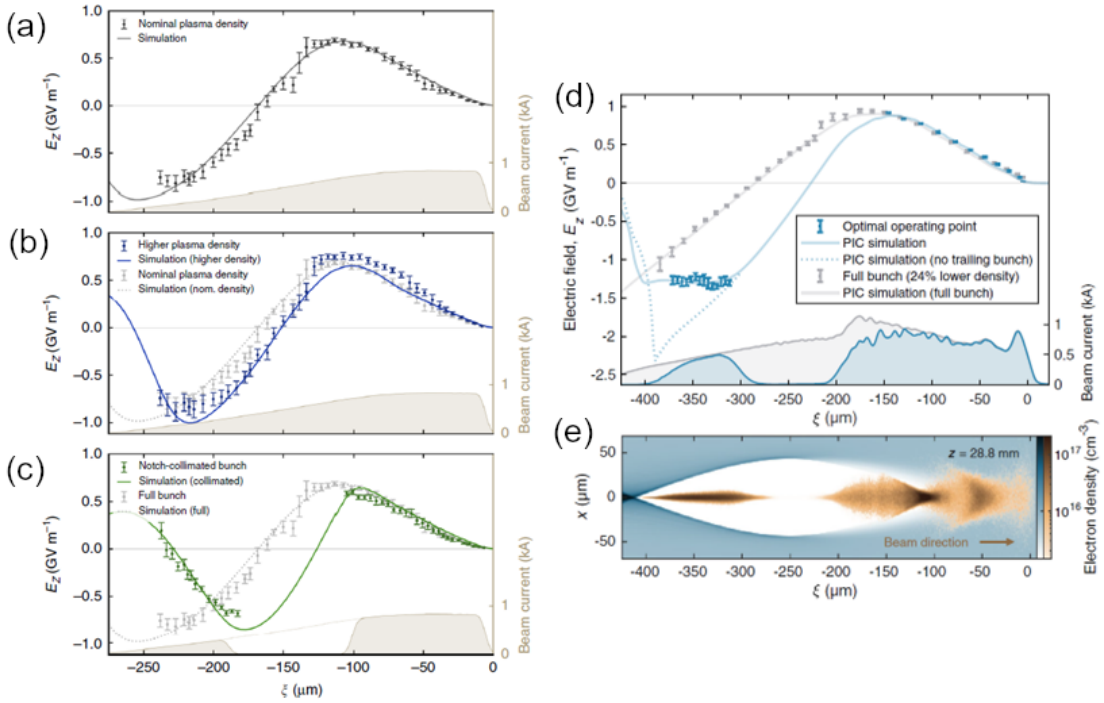

Figure 3.13: Typical FLASHForward plasma wakefield. (a) Wakefield with full uncollimated bunch; (b) same as (a) but with 80% higher plasma density; (c) same density as (a) but with collimated double bunch; (d) wakefield with a full bunch and an arbitrary plasma density (grey), and with the collimated bunch at an optimum beam-loading point; (e) the collimated bunch from (d) in a simulation. Solid lines correspond to PIC simulation, while the data was measured with the wakefield sampling technique [66]. (a-c) figures are from ref. [66], (d-e) ref. [74].

at FLASHFoward. After the longitudinal phase space diagnostics section, the beam is dumped [107].

A typical FLASHForward current profile measured with the X-TDS is reported in ref. [77], where the driving bunch had an average peak current of 1.0 kA and bunch length of 140 fs rms; the trailing bunch had an average peak current of 0.44 kA and a bunch length of 37 fs rms. The two bunches were separated by 650 fs when measuring from their centroids.

3.2 Plasma operation

3.2.1 FLASHForward plasma generation

A typical FLASHForward beam is prepared specifically to drive a plasma wakefield in a quasi-linear and at times non-linear regime and to ensure high-quality acceleration of the trailing bunch. However, an optimised plasma accelerator also requires careful consideration for the design and tunability of the plasma itself. For typical FLASHForward double bunches, the decelerating phases of the wakefield should span around 420–750 fs (125–225 µm) from the driver's head, while the peak accel-

erating field should occur at around 175–350 µm from the driver's head for a range of plasma densities, see fig. 3.13. These wakefield lengthscales correspond to plasma densities of $2 \times 10^{16}\,\mathrm{cm}^{-3}$ down to $7 \times 10^{15}\,\mathrm{cm}^{-3}$, typical working points of FLASHForward. FLASH drive bunches of $\sim$ 100–200 µm and such plasma half-wavelengths [31] correspond to a plasma frequency of 8 THz down to 5 THz and plasma density of $2 \times 10^{16}\,\mathrm{cm}^{-3}$ down to $7 \times 10^{15}\,\mathrm{cm}^{-3}$ (respectively). Given the bunch collimator resolution and thus the variation of the bunch length by $\sim 0.1\%$, which corresponds to $\mathcal{O}(1)$ fs variation in $\sim 300\,\mu\mathrm{m}$ ($\sim 1000\,\mathrm{fs}$) bunch length, the tunability of the plasma should allow density steps of $\sim 2.5 \times 10^{13}\,\mathrm{cm}^{-3}$.

The wakefield mapping technique was developed and performed at FLASHForward. This method involved comparing the spectrum of a single bunch, which was interacted with plasma, to one of a non-interacted bunch. This was done for each longitudinal slice of the bunch, by scraping from tail to head and subtracting the consecutive longitudinal slice of the bunch from a previous one to obtain the spectrum of a slice alone. This method is supported by the fact that the wakefield properties at a specific point are the same regardless of bunch-plasma interaction temporally after that point due to causality since the bunch travels very close to the speed of light [66]. Using this, a peak -1.8 GV/m gradient was observed for a plasma density of $2.6 \times 10^{16}\,\mathrm{cm}^{-3}$, which is consistent with quasi-linear regime condition, see fig. 3.13 [66].

Unlike at FACET, where the electron beam can both ionise the lithium vapour and drive a wakefield [210], beams at FLASHForward require a pre-ionised gas, either by laser [67] or high-voltage discharge. This is because the beam charge densities of $\sim 10^{19}\,\mathrm{cm}^{-3}$ are not sufficient to field-ionise gas to a plasma, whereas collisional ionisation from a luminal electron bunch would be negligible. In addition, intending to explore the high repetition regime, using high-voltage discharges as the primary ionisation method is more favourable as opposed to laser ionisation. Lastly, FLASHForward aim to develop a high-energy-gain stage, which necessitates bunches interacting with a long plasma. A long and high-voltage discharge pre-ionised plasma is most conveniently generated in a discharge capillary as opposed to a vapour oven or a gas jet [39]. This is the plasma source type used at FLASHForward.

The capillaries are formed with two blocks of sapphire. In each of the blocks, half of the channel and gas inlet profile is milled, thus forming a circular capillary with two gas inlets when the blocks are attached, see fig. 3.14. While the facility can swap between two capillaries of 50 mm and 195 mm in length, the diameter for both is 1.5 mm [127]. The experiments presented here have been carried out with the 50 mm capillary. To ensure high beam quality when transporting it to plasma, the are no end-caps or windows in the path of the beam; the capillary is open on both ends [122]. The choice of material has been motivated by its hardiness in an

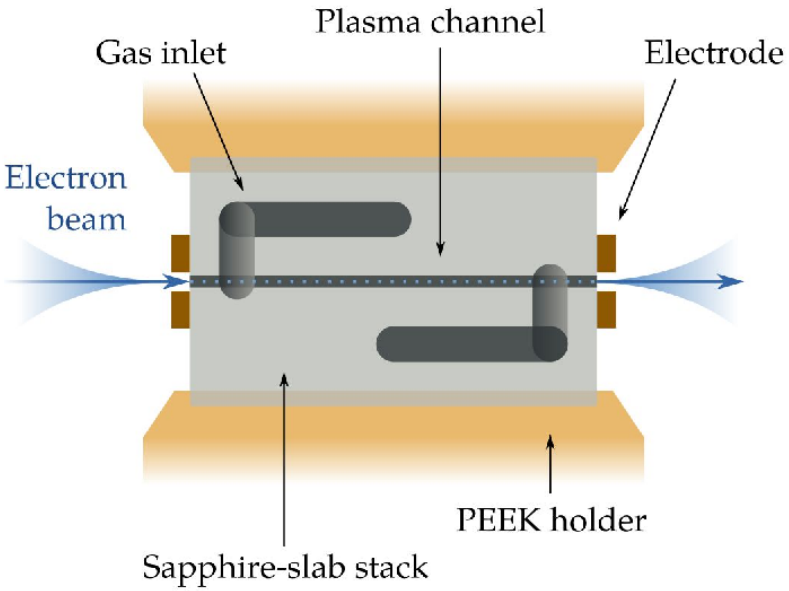

Figure 3.14: FLASHForward sapphire high-voltage discharge capillary fillable with gas. Figure from ref. [189].

environment for generation and confinement of the plasma. Furthermore, sapphire transmits plasma emission light [211], which is crucial for diagnostics, described in section 3.2.2. The sapphire arrangement of the two slabs, i.e., the cell is mounted on a PEEK (polyether ether ketone) plastic holder, allowing multiple cells to be stacked and selected and put into the beam path during experiments.

The gas inlets in the sapphire cell are placed at 2.5 mm from each end [74], and are connected to a gas supply system, which consists of winding PEEK tubes near the high-voltage electrodes. With equal gas pressure applied in both inlets, a constant neutral gas density, i.e., continuous gas flow can be achieved in the capillary [127, 212]. The winding tubes are then followed by gas pipes leading to a buffer volume, which, upon the opening of valves, is filled to pressures ranging from 10—50 mbar by a line sustained at ~ 1 bars. This line is connected to a pressure regulator, which is preceded by another series of a pipe and a regulator, which are fed directly from a gas bottle. There are three such lines, one for argon, which is doped with 3% hydrogen (by volume) for diagnostic purposes, one for pure nitrogen, and one for hydrogen, which is operated together with a nitrogen purge system for safety. The pressure of the gas system is measured in the buffer volume, with a capacitive gauge [127], which is usually used as a measure for the amount of gas in the capillary. The gas flow is measured in the pipes to the buffer volume and can also be used as a gauge for the amount of gas in the capillary when in a steady state.

Despite these measurements, the amount of gas in the capillary is unknown. However, it can be deduced by simulating the buffer-to-capillary gas system section, which relies on a precise geometric description of the system and can be partially

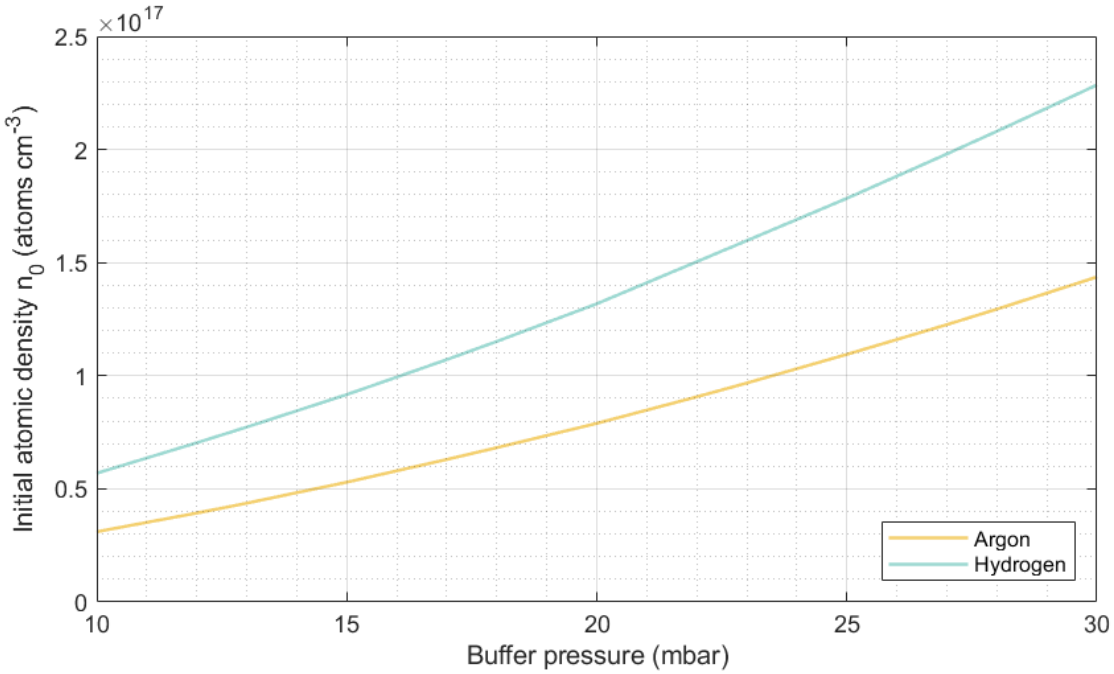

Figure 3.15: Estimations for the neutral atomic gas density of hydrogen and argon in the 50 mm FLASHForward capillary based on the buffer pressure measurements and gas-system simulations.

benchmarked with the aforementioned gas flow and pressure measurements. During the timespan of this work, FLASHForward has undergone three variations of the gas system, and an ANSYS Fluent model for simulations has been built for each. However, the latter ones provide only preliminary values and are in development. Nevertheless, a calculator for estimating the neutral atomic gas density in the capillary for a given buffer pressure or gas flow for all three gases and vice versa was developed. It uses a look-up table based on simulations for mapping simulated neutral atomic gas density values to measured buffer pressure values or measured gas flow values. For exact values, a linear interpolation is used, see fig. 3.15. For a selected gas flow value and thus buffer pressure, an expected approximate neutral atomic gas density is then reached in the capillary, where one can proceed with the generation of plasma.

The open-ended gas-filled capillary is located at the designed interaction point along the beamline. Given the ultra-high vacuum standards at the superconducting FLASH linac, the plasma source system is encased in a vacuum chamber which is directly connected to a turbo pump system [200]. At certain points away from the vacuum chamber along the beamlines, there are six turbo pump stations, which all together form a differential pumping system, reaching ultra-high vacuum conditions of 10^{-9} mbar at the entrance of FLASHForward beamline and before the FLASHForward TDS diagnostic section [67, 107, 122, 200]. In the meantime, while the gas escapes from the capillary through the open ends, the chamber is pumped to an ambient pressure of 4.3×10^{-3} mbar (up to 0.1 mbar). During the timespan of this

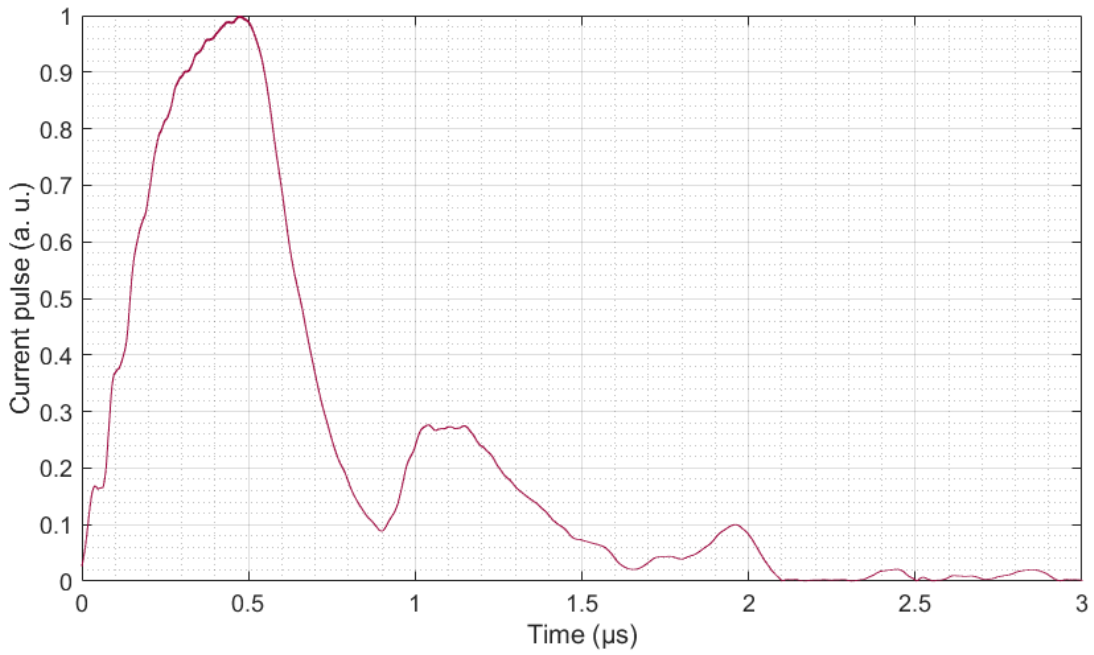

Figure 3.16: An example of FLASHForward high-voltage discharge current pulse shape. Due to unmatched impedance, there are another few small pulses after the main pulse, at $\sim 1.20\,\mu s$, at $\sim 1.95\,\mu s$, and a few smaller pulses before the signal turns to noise.

work, the facility has had two types of chambers. The first one, operated until 2021, was a 500-mm-diameter cylindrical chamber (curvature radius parallel to the floor); the second one, operating since 2022, is a 975 x 690 mm (length x width) rectangular chamber. Both chambers consisted of a patented double-chamber design, one on top of the other [200]. This setup avoids having too many moving parts in a vacuum: all the capillary cell PEEK holders are mounted on a base plate in the top chamber and they are controlled in position and angle by a hexapod in the bottom chamber via a mechanical feedthrough where the vacuum conditions can be more relaxed.

The plasma is generated with a high-voltage discharge system. Each end of the capillary has a copper electrode attached, cathode upstream and anode downstream, each with a hole for free passage of the beam [107, 122, 127]. The electrodes are part of a pulse forming network (PFN) of 4.1 nF capacitance, where a range of voltages can be generated, up to 27 kV, with the lowest voltage of choice usually being loosely informed by the estimated pressure in the capillary and Paschen curves. The current pulse is generated by a thyratron switch, and it lasts for around 400 ns (FWHM), peaking at 500 Amps. The circuit is matched with an impedance of 50 Ω; however, the pulse still results in a few more high-current pulse reflections of around 50–120 A, usually two, see fig. 3.16. The discharge is triggered by the FLASH timing system, thus being synchronised with the arrival of the beam; however, there is jitter from the discharge system, specifically due to the thyratron switch. Moreover, the process itself of discharging a neutral gas with avalanche ionisation is stochastic due to the

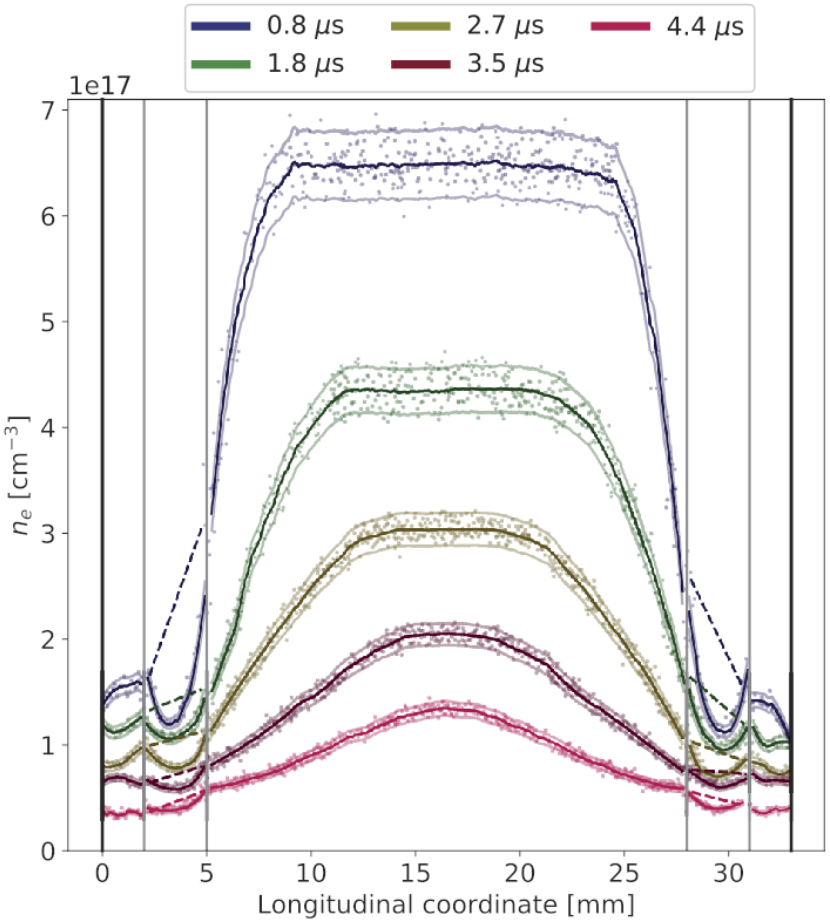

Figure 3.17: Longitudinal argon plasma density profiles in a 33-mm capillary at different times after the high-voltage discharge current pulse. Figure from ref. [127].

necessary initial condition of some background ionisation. As a result, the timing of the current onset varies. This can be alleviated by the use of a gas that is easier to ionise, such as argon rather than helium. Because of this, argon is used most often at FLASHForward for its discharge stability, and as of 2021, it had been operated for more than 10^5 shots without capillary degradation [110].

Besides the high-voltage discharge system, the is also a possibility to deliver a laser to the FLASHForward capillary longitudinally for ionisation (with peak intensity of around $3 \times 10^{14}\,\mathrm{W\,cm^{-2}}$ [68]), and transversely for density downramp injection. Both arms are generated by splitting a pulse generated by a 25 TW, 25 fs, 10 Hz titanium-sapphire CPA laser system [67, 107].

Once the plasma is generated, it decays on the microsecond timescale, with a decrease of $\sim 2.75 \times 10^{13}\,\mathrm{cm^{-3}/ns}$ in 6 mbar argon (estimated $\sim$ 6 mbar in the capillary, 24 mbar in the buffer volume). The timing of the discharge trigger can be changed with respect to the beam arrival time in steps of 9.23 ns and also fine steps of 0.923 ns. By changing the timing, the plasma density with which the beam interacts can thus be changed. A full FLASHForward capillary argon plasma density

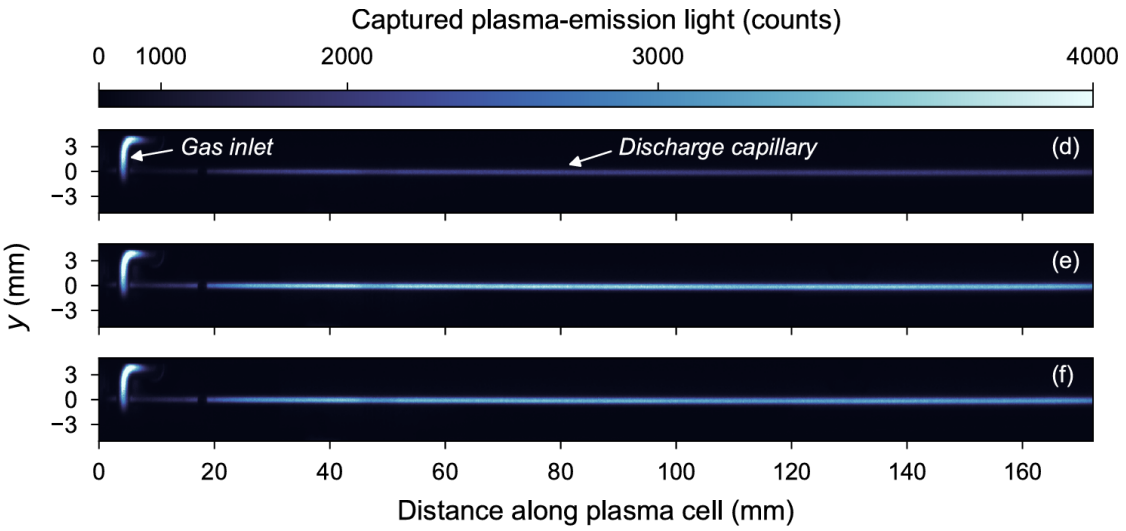

Figure 3.18: Plasma-emission light from the capillary, with: (d) no beam interaction, (e) driver energy deposition, and (f) trailing bunch energy extraction. Figure from ref. [112].

evolution characterisation has been reported in ref. [127]. It can be observed that by changing the discharge timing, not only is the peak plasma density along the capillary changed, but also its longitudinal profile. With later timing, i.e., after a few microseconds, it is departing from a flat-top profile towards a Gaussian one, see fig. 3.17. As a result, the beam interacts with density ramps of different lengths and gradients. This can be useful upstream since it relaxes matching conditions [116, 199], while the upramp increases the focusing force, reducing beam size even further [213]. The downstream downramp is also beneficial since it captures and transports the beam avoiding high divergence, and serving as an underdense plasma lens [214].

Different plasma density conditions at a given double-bunch current profile and charge density lead to a differently evolving wakefield and different beam loading of the trailing bunch. With a setup FLASHForward beam, final adjustments have to be made to the double-bunch scraping and plasma density to achieve satisfactory beam loading [74]. Additionally, adjustments to the plasma density, beam alignment, and final focusing must be made for satisfactory driving bunch and plasma interaction and trailing bunch quality preservation [77].

3.2.2 FLASHForward plasma diagnostics

One of the most straightforward ways of accessing information about the plasma is via its radiation of the visible part of the spectrum. Both plasma light directly and its spectroscopy carry information about its density and temperature, as discussed in section 2.2.3, and more specifically, energy deposited and extracted by the beam.

At FLASHForward, the plasma light transmitted through the sapphire of the cell and vacuum chamber flange windows is recorded with a sideview CMOS camera.

It has recently undergone an upgrade, where an 11.3 x 11.3 mm and 5.5 µm pixel size camera chip was exchanged with a larger aspect-ratio 14.1 x 7.5 mm chip with a smaller pixel size of 3.45 µm. This allows $\sim$ 100 mm field of view and 33 µm/pixel pixel-limited resolution at the object plane with a f=50 mm objective. While it can collect light from the entire plasma glow (see section 2.2.3) window by having an integration time of 38 µs, it can also operate in a fast-shutter mode of 2 µs thus temporally resolving parts of plasma density evolution. Despite the improvements of the new imaging system, the old one has been of great benefit to two important results at FLASHForward [75, 112] (see fig. 3.18). These results mapped the plasma light intensity, recorded by this side view camera, to the energy deposited into the plasma. In addition, it has the general function of monitoring cell movements, alignment, and plasma discharge in the vacuum chamber.

Much more information can be retrieved from the spectral analysis of plasma light. At FLASHForward, light can be collected either by a light collimator placed outside the chamber, directed at any longitudinal position of the cell or by a fibre directly connected to the side of the sapphire cell. A further optical fibre transports this light to a spectrometer HORIBA iHR550 behind the radiation-protective wall, where a high-sensitivity Andor iStar DH334T camera then records selected wavelengths. This camera contains an intensified photo-multiplier CCD (iCCD) with a fast integration time down to 2 ns, and a chip of 1024 x 1024 13 µm size pixels [127].

To deduce plasma density, optical-emission spectroscopy (OES), or more specifically, H-Alpha linewidth measurements are used, based on the work of Gigosos and Cardeñoso [155, 156], and the biggest campaign of these measurements at FLASHForward is reported in ref. [127]. To be able to use this technique in other gases than hydrogen, for example, the argon gas supply used in FLASHForward is 3% doped with hydrogen. However, while calculating the plasma density from measured H-Alpha linewidths, a temperature range for the plasma has to be assumed. Thanks to the investigations done in ref. [127], these assumptions are based on empirical observations. For this, two independent plasma diagnostics were used: plasma OES and two-colour interferometry with a laser [215]. By measuring the argon plasma density along the longitudinal axis in the centre of the capillary with the latter method, an average density was deduced. Then, an optical emission spectroscopy measurement was performed by collecting plasma light in the transverse direction to the capillary, in the middle of it longitudinally. For a given H-Alpha linewidth, different plasma densities could be inferred for different temperature models; however, with the two-colour interferometry value, a temperature of 0.5 eV–5.0 eV was selected to match both density measurements. This temperature evaluation was then done for the whole microsecond-level plasma density evolution, but not earlier than 0.5 µs after discharge initiation because the local thermodynamic equilibrium was not

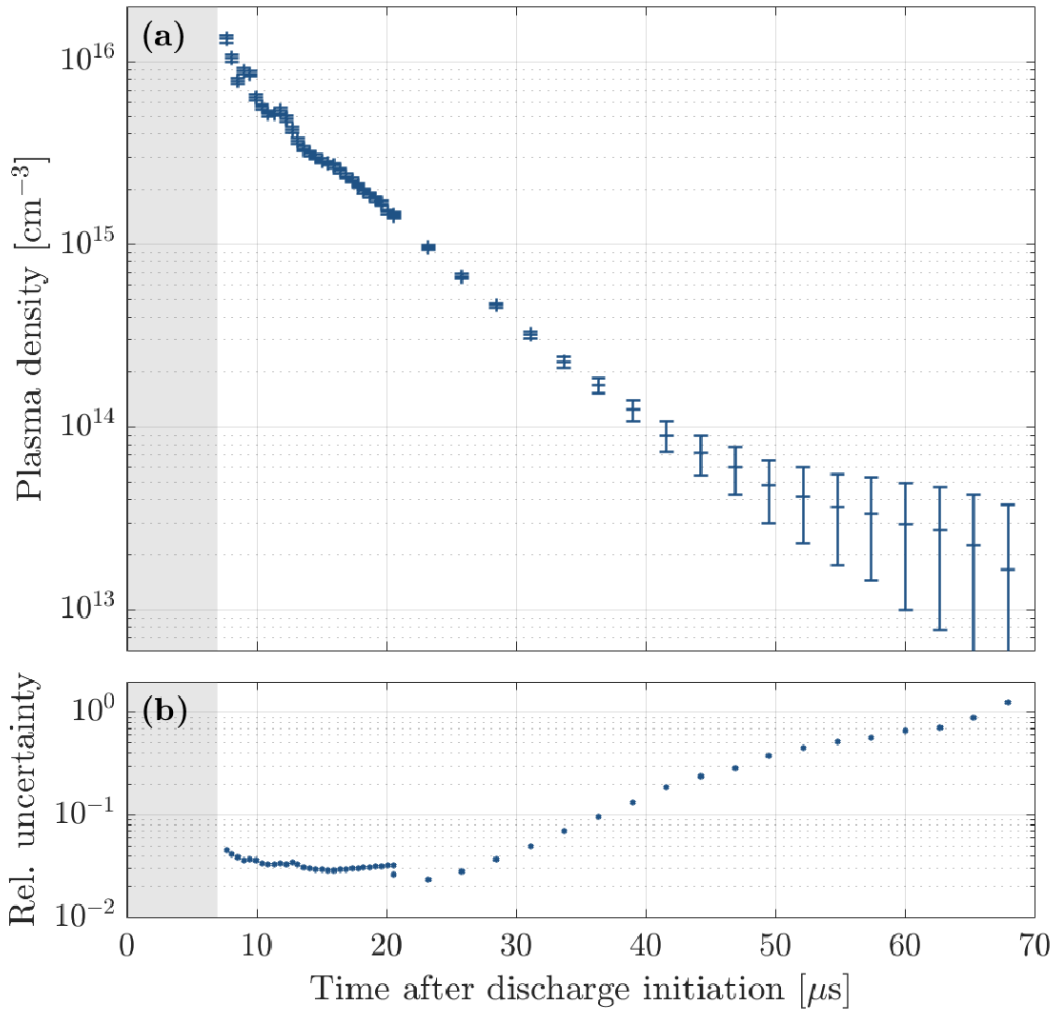

Figure 3.19: Longitudinally-averaged krypton plasma density (buffer pressure 15.1 mbar) measured with electron beam deceleration and calculated with PIC simulations (a), and its relative uncertainty (b). Figure from ref. [121].

reached yet. The temperature ranged 1 eV—7 eV. OES measurements, whose resolution is $5 \times 10^{15}\text{cm}^{-3}$, confirmed that the density ranged from $0.5 - 2.5 \times 10^{17}\text{cm}^{-3}$. When OES measurements were longitudinally resolved, a profile evolution was also recorded, see fig. 3.17. While this rigorous characterisation can still be done with the FLASHForward cells and the light collimator, it is more favourable to use the fibre connected directly to the cell even if its position is static longitudinally. This is because it collects more light, and the integration time of the iCCD camera can be selected to be shorter, e.g., 50—100 ns instead of 100—200 ns. Thus, the H-Alpha images have a higher signal-to-noise ratio, and the plasma density evolution is better resolved temporally. For argon, this is especially crucial, as the light component from hydrogen recombination, due to its small amount, is weak.

Besides plasma light, features of plasma, specifically density, can be investigated by interacting a laser pulse or particles with a plasma. The aforementioned method

of two-colour interferometry, or specifically the common-path two-colour spectral interferometry [215, 216] used for the experiment in ref. [127], interacts two laser pulses of different wavelength but same path with the plasma. For this method, a single laser pulse is divided into two pulses, one of which is frequency doubled. As both pulses go through the plasma longitudinally, each pulse acquires a different group velocity delay and a different phase shift, both of which are dependent on the wavelength of the pulses and the plasma density [215]. The value for the line-of-sight averaged plasma density can then be calculated from the observed delay and phase difference of the pulses by performing spectral interferometry [215], where one of the pulse wavelengths is halved by second harmonic generation to match the other after the plasma.

Equally, one can interact an electron bunch with the plasma, and retrieve information on density based on the resulting bunch energy spectrum, as described in ref. [121]. Both of these methods, when used in a discharge capillary, interact with plasma along the longitudinal axis, with a possibility of transversely resolving the density profile, but integrating the plasma density effect longitudinally. However, at FLASHForward, the electron beam-based methods are more favoured. Firstly, it is more readily available than a laser system setup for such interferometry at FLASHForward. Secondly, an electron beam interacts with a plasma of density as low as $10^{13}\mathrm{cm}^{-3}$, thus having a much higher resolving power. It is important to note, however, that this method is limited for densities that are high enough to result in the bunch length being too long for the first wakefield cavity. As a result, such a long bunch would be defocused and the charge would be lost, and the estimation of density made impossible.

To deduce a plasma density from an interacted bunch spectrum, plasma wakefield simulations have to be carried out to map features of plasma interaction in the bunch to the plasma density. It takes into account that for certain plasma densities, the plasma length is also different, as revealed in ref. [127]. Thus the average bunch energy loss can be compared to a simulation where a uniform plasma density profile was used, and thus an effective plasma density experienced by the bunch is inferred, see fig. 3.19. This becomes less certain for low densities, where due to weak beam and plasma coupling, the bunch energy loss per unit length is not constant in the initial millimetres of plasma interaction. Because of this complexity, analytically derived bunch final energy and plasma density relationships would not be as accurate as simulations used in this case. This highlights a drawback of this method, where simulations become a necessary part of plasma density deduction, thus not being as straightforward, as, for instance, optical emission spectroscopy.

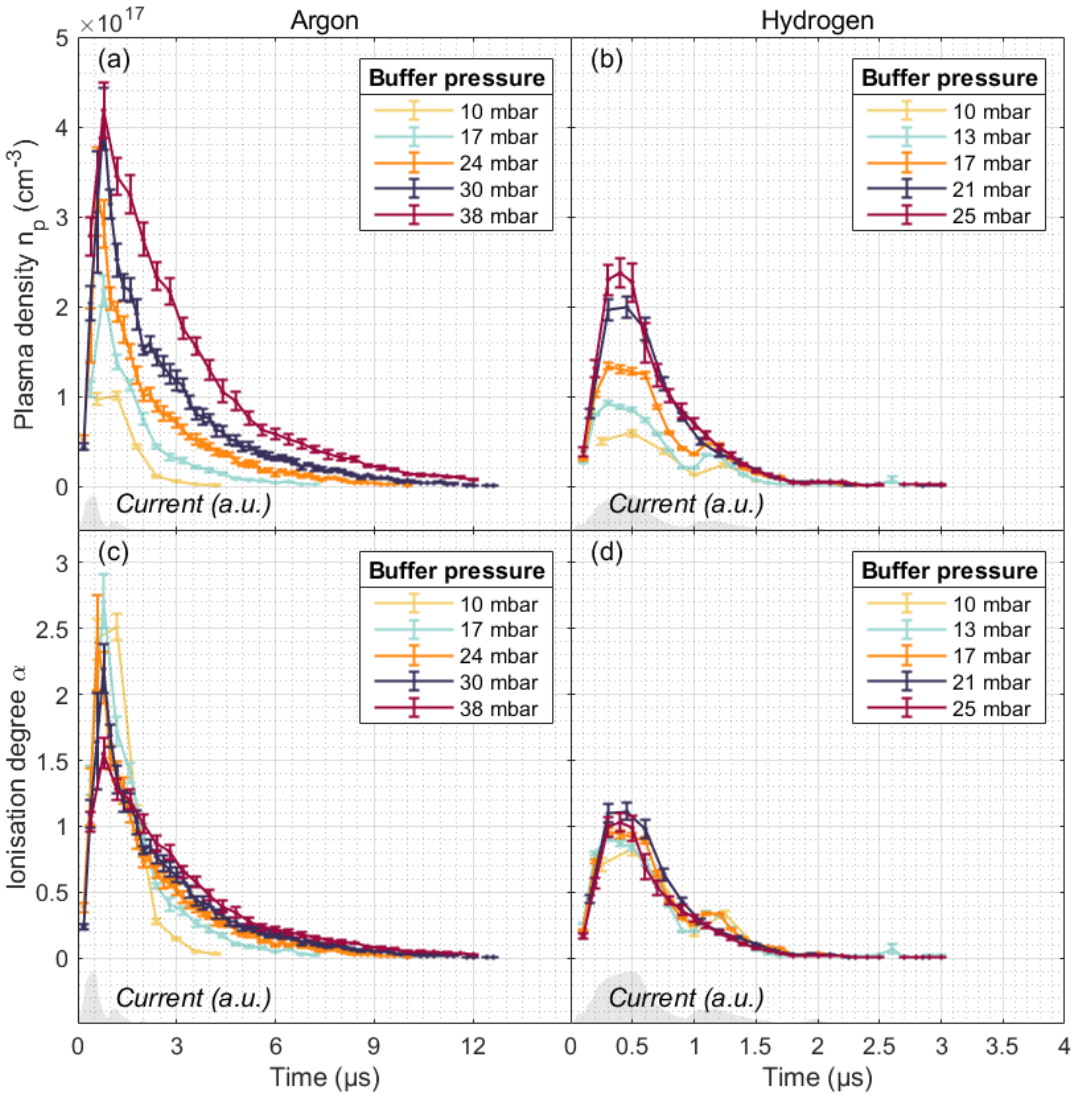

Figure 3.20: Argon (a) and hydrogen (b) plasma density measurements with OES and ionisation degree estimations (c, d) in the FLASHForward 50 mm capillary for a range of buffer pressures corresponding to different capillary gas densities. The electrical discharge was operated at 27 kV. The electrical discharge current trace is shown in grey. Unlike other working points, the plasma is reionised by the discharge at 1–1.5 μs for hydrogen at buffer pressures of 17, 13, and 10 mbar, see panels (b) and (d).

3.2.3 Unperturbed plasma evolution in a FLASHForward capillary

The FLASHFoward plasma high-voltage discharge capillary can be operated with argon or hydrogen and at a range of gas densities, determined by the gas system settings such as the buffer pressure, as explained in section 3.2.1. In order to understand how the plasma density evolves in these different settings, an OES (see section 2.2.3) measurement campaign was carried out.

The 50 mm-long, 1.5-mm-diameter capillary is continuously filled with gas flow-

ing from a buffer container. The measurements of the gas flow and buffer pressure can be compared to full gas system simulations, and so the pressure in the capillary and the initial gas density are estimated, as described in section 3.2.1 and fig. 3.15. The validity of these estimations can be checked by discharging the gas and recording what peak plasma density value is achieved. Operating under the assumption that the 27 kV and 500 A electric discharge system at FLASHForward reaches an ionisation degree of $\alpha = 1$ at the peak of the current pulse in hydrogen, it can be seen in fig. 3.20 (d) that the estimated initial gas density indeed matches closely the peak plasma density value achieved in the capillary. In other words, the hydrogen ionisation degree peaks at approximately $\alpha = 1$ in hydrogen.

While this gives some faith in the estimations, some caveats preclude this from replacing further, more accurate simulations and measurements of the gas system to know the amount of gas in the capillary in the future. Firstly, the original simulations which are used for this estimation do not include the high-voltage discharge acting on the gas. During experimentation at FLASHForward, when the discharge is initiated, plumes of luminous material are seen to exit the capillary. This is attributed to the rapid heating of the material during the discharge, building a pressure gradient which leads to material expulsion out of the capillary, both into the inlets of the gas and out to the vacuum chamber through the open ends of the capillary. The plasma in the material further cools and recombines on the timescale of microseconds, see the timescale of the evolution in fig. 3.20. Naturally, this plasma creation and decay process disturbs the steady state conditions achieved by the gas system, and the estimated initial gas density may be higher than the amount that is present in the capillary during the plasma evolution given that a proportion of the material is expelled and it has not been replaced by new gas from the inlets. Because of this, the real ionisation degree at the arrival time of the beam is not known exactly, and instead, an ionisation degree with respect to the initial state is quoted in this work.

Such an approximate ionisation degree can be used for comparisons at a single capillary pressure working point. The reason for this is that for a given discharge system voltage and current, the proportion of expelled material should depend on the initial capillary pressure. To be more precise, the applied ionising power by the electrical system should result in more heating for a smaller amount of material in the capillary. As a result, a bigger proportion of material would be expelled due to the higher pressure gradient. Hence, the factor by which the neutral gas density at beam arrival is decreased would be larger at smaller buffer pressures [121]. The ionisation degrees at smaller buffer pressures could therefore be underestimated in comparison to higher buffer pressure working points. Future MHD simulations of the high-voltage discharge in the FLASHForward capillary could help illuminate the ionisation degree evolution; however, in the meantime, caution is taken when

comparing the estimated ionisation degrees at different initial capillary pressures.

Another important takeaway from unperturbed plasma evolution in the capillary is the differences in plasma creation and decay for different initial capillary pressures and gases, namely argon and hydrogen. In argon, the plasma density at the highest operated pressures, e.g., 38 mbar in the buffer, can be detected with OES for $\sim 10\,\mu s$, therefore the current pulse and its following reflections, see fig. 3.16, which all last $\sim 2\,\mu s$, are not present for most of argon plasma evolution. Conversely, OES-detectable hydrogen plasma lives for $\sim 2\,\mu s$, thus some magnitude of the discharge current is running during hydrogen operation. The second pulse seems to reionise the plasma at low pressures, see fig. 3.20 (b) and (d) at 1–1.5 µs for hydrogen at buffer pressures of 17, 13, and 10 mbar. In high-pressure working points, the plasma has not decayed low enough for this current pulse to make an impact. As a result, there are more fine features in the evolution profile of the lower buffer pressure plasma density, necessitating higher temporal resolution of the scan. Without it, the uncertainty of the measured plasma density in between the pulses, where density is often suitable for FLASHForward beam acceleration, and where the current effects can be avoided, is higher. However, for low pressures, the higher resolution is often unattainable, because low-pressure working points result in lower discharged plasma densities and thus a lower H-Alpha signal, the consequence of which is the long gating time of the spectrometer camera. Because of this, the measurement of low-pressure plasma density evolution in hydrogen is low in temporal resolution.

The other notable difference between the two gases is the decay rate dependence on the initial capillary pressure. In argon, different initial pressure working points reach a value below the OES-apparatus resolution at different timings: the higher the pressure, the later the timing, see fig. 3.20 (a). The timescale at which similar density could be reached for all pressure working points is unknown, and therefore without thorough data analysis and simulations comparison, the difference in rates for different pressures is not obvious. This could be the same situation for hydrogen; however, the second current pulse raises the density of the plasma of the lower-pressure working points to match one of the higher-pressure working points, see fig. 3.20 (b) and (d) and buffer pressures of 17, 13, and 10 mbar, thus creating conditions where the decay rate and the overall plasma density value are similar for all pressure working points. As a result, while in argon selecting typical plasma density operation points results in intuitive scaling of the plasma density with the initial pressure in the capillary, the hydrogen plasma tends to lose this scaling after the second current pulse due to its rapid decay.

Chapter 4

Long-term ion motion in argon

4.1 Long-term ion motion at FLASHForward

The first FLASHForward campaign investigating the evolution of long-term ion motion and plasma channel dissipation has been the focal topic of ref. [121], with key results published in ref. [122]. The experimental setup, main and additional results, and dependencies of long-term ion motion will be presented here.

The main focus of this campaign has been the key features of ion motion and its timescale in argon, as observed with the probe bunch. The data was taken over two different shifts, both of which differed slightly in the bunch setup, or more specifically, the scraping settings for the probe bunch [122]. The first shift block focused on the features of the channel, such as the curvature and the on-axis density evolution, therefore a low-energy spread (close to optimally beam loaded) and slightly mismatched to plasma density trailing beam was crucial. For this, a 320 pC (driver) and 90 pC (trailing) bunch pair was cut from a 900 pC beam, and the bunch and plasma were set up in the typical FLASHForward way as described in section 3.1.2. The second shift block aimed to measure the lifetime of the long-term ion motion, which is marked by the complete dissipation of on-axis density depression and channel curvature. While similar settings were achieved, it was less important to have the exact same conditions, and for this FLASHForward setup the probe bunch was cut into a 242 pC driver and 48 pC trailing bunch.

4.1.1 Role of the author

The investigation presented here is originally described in ref. [121]. The author contributed to the data taking and the running of the simulations. In addition, the author carried out the analysis of the probe trailing bunch transverse phase space measurements, shown in fig. 4.6, and worked on subtraction technique improvements.

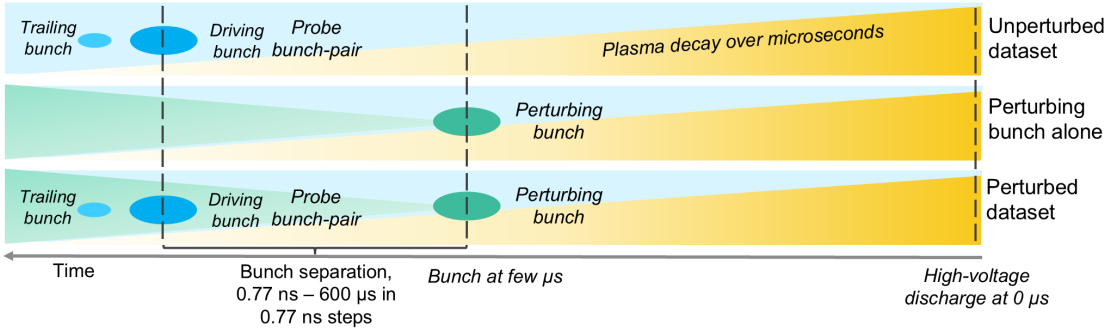

Figure 4.1: Perturber and probe scheme at FLASHForward.

4.2 Experimental method: perturber and probe bunches

The electron bunches at FLASHForward can be used as a probe for long-term ion motion evolution in plasma as described in section 2.3.5. This method has been the key diagnostic in the study presented here and in the refs. [121, 122]. Thanks to the possibility of accelerating two bunches at FLASH using two separate photoinjector lasers with temporal separation of $\tau_{bunchsep} \geq 0.77\,\text{ns}$ (see section 3.1.1), one can utilise a pump-probe type diagnostic with electron beams, see fig. 4.1. The bunch arriving first, referred to as the perturber bunch, usually unscraped and thus not divided into a driver-trailing-bunch pair, would drive a wakefield in the plasma, setting off the long-term ion motion. The resulting plasma channel can then be probed by the second, the probe bunch, usually divided into a driver and a trailing bunch, and signatures of density depression and channel curvature can be observed in the driver and trailing bunch energy spectra and transverse-plane bunch properties (size, divergence, emittance). It is important to note that such temporal resolution of 0.77 ns would not be able to resolve the same features that [102] have been able to resolve with shadowgraphy. This method should be utilised for the long-term ion motion evolution in the form of a plasma channel, which should last for nanoseconds.

Two changes were made to make sure that the perturber is only scraped on either front or back. Firstly, the perturber bunch is accelerated to a higher energy, 1061 MeV as opposed to the nominal 1054 MeV of the probe bunch by being injected at a slightly different RF phase. Secondly, the position of the photoinjector pulse on the cathode is modified slightly. The result of both of these adjustments is that in the dispersive section of FLASHForward, where the position on the horizontal axis is a result of a combination of both the actual horizontal position of the bunch in the linac and its energy, the bunch can travel past the scraping system without being cut in the middle. Because of the differing perturber bunch energy and initial position, the setup orbit in the linac, which favours the full transport of the probe bunch, results in a complicated orbit for the perturber bunch. As it travels off-axis through

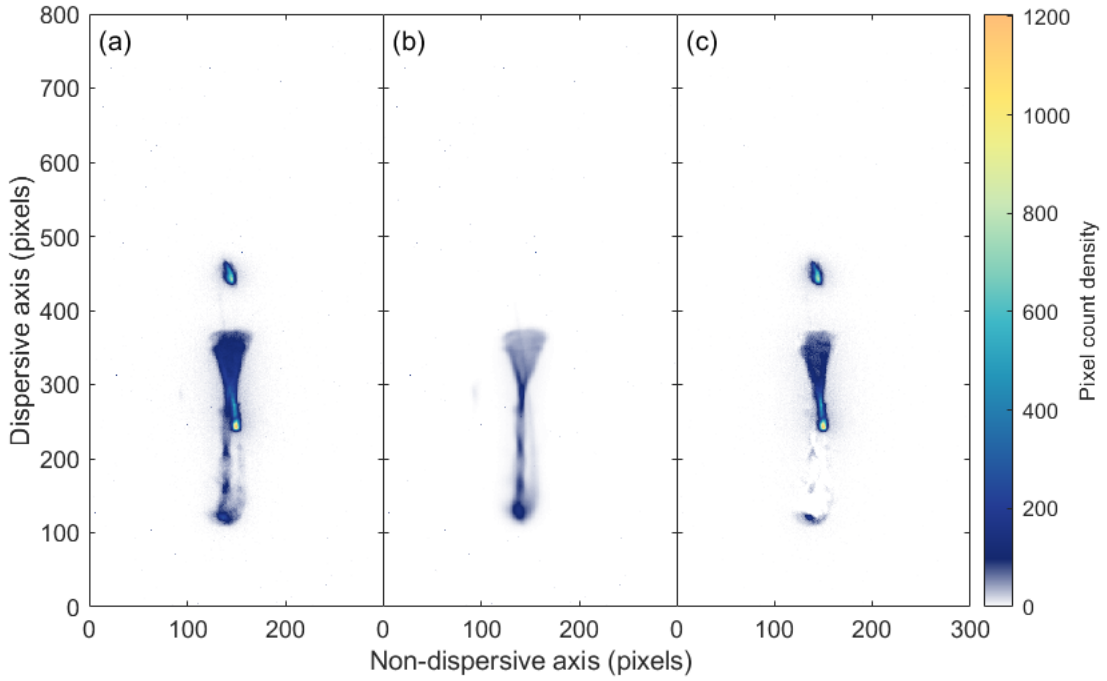

Figure 4.2: Probe bunch-pair images from the ESPEC. (a) Image of superposed pertuber and probe bunch-pair; (b) average perturber image; (c) probe bunch-pair image after subtraction.

the quads in the accelerator, the overall state of the bunch optics is unknown. In addition, since matching conditions are much more crucial to the probe bunch, there is no work done in the linac to optimise the perturber beam. Ultimately, the quality of this bunch is not a high priority, only a strongly driven wakefield is necessary. Therefore, the perturber is only modified using settings at the injector, such as the time of arrival of the photoinjector laser pulse. This setting determines the phase at which the perturber bunch gains a chirp in the ACC139 module in FLASH and therefore fixes the longitudinal compression acquired in the first bunch compressor (see section 3.1.1). The result of this is a perturber bunch with a high current of 1.5 kA and length 650 fs (195 um) rms, while the probe bunch (unscrapped) is 1 kA and 1400 fs (420 µm) rms.

At the FLASHForward capillary, the perturber interacted with a high-voltage discharged argon plasma of $(1.75 \pm 0.27) \times 10^{16}\,\mathrm{cm}^{-3}$ density, which resulted in a 1.6 GV/m wakefield [122]. Plasma-interacted bunches are then focused by a triplet of quadrupole magnets onto a scintillator screen for a given object and imaging energy and dispersed by a dipole magnet (described in section 3.1.4).

4.2.1 Subtraction of the perturber signal

The screen, which is installed after the ESPEC dipole in the high-energy range $\mathcal{O}(1)$ GeV, is a LANEX screen; while it has a relatively small resolution of 50 µm necessary for accurate energy spectra measurements, its scintillation lifetime is long,

i.e., $\approx 380\,\mu s$ [122]. Naturally, when the perturbing bunch and the probe bunch-pair are separated on the nanoseconds timescale, the signal of the perturbing bunch will still be present on the screen when the probe bunch-pair arrives, see fig. 4.2 (a). To remove this signal and account for its introduced error, a subtraction technique was developed [121].

The separation of the probe bunch signal from the first, while not a simple task, may only be achieved with the most straightforward method, i.e., simple subtraction of the perturber image. One cannot use image separation methods such as Independent Component Analysis [217]. These techniques, which are based on the knowledge that for a given number of components in mixed signals there is also the same number of signal mixtures, would not apply here. This is because both bunches have a shot-to-shot jitter, which is a consequence of the bunches interacting with a plasma density which jitters itself due to variation of the discharge onset timing. Thus, there are no two images with identical perturber bunch (and the same applies to the probe).

In addition, both bunches have very similar features in the energy spectrum, such as the area in the image or the average intensity of the signal. Given these circumstances, the most accommodating methods would be to gather a statistical dataset of perturber images alone, number of shots being $\mathcal{O}(100)$, use them to obtain an average image of the perturber, such as in fig. 4.2 (b), and subtract this signal from the superimposed data, as was done in ref. [121] and fig. 4.2 (c). Given the shot-to-shot jitter in the perturber beam, the subtraction is never clean, and some minimal signal remains. As a result, a thresholding value is applied which can eliminate the majority of post-subtraction surplus signal in the superimposed images.

4.2.2 Probe bunch pair image processing

Once the subtraction and the thresholding value are applied, the bunches are further selected as two largest-area connected components. Following this, the image dispersive axis is scaled to transform from millimetre units to MeV, and the whole image is rescaled to transform pixel counts to Coloumbs.

The energy-calibrated axis is calculated with $E = \frac{aI}{x-b}$, where I is the spectrometer dipole current and x is the bunch position on the scintillating screen. The parameters a and b in this formula are acquired from fitting $x = a(\frac{I}{E}) + b$, a measured dependency of position and spectrometer dipole for a single energy slice of a constant E, measured in the linac.

While the single slice should represent a delta function at energy E, in reality, the slice has a finite energy spread, and thus a finite dispersion in the dipole field.

For typical spectrometer dipole currents used at FLASHForward experiments, the dispersion corresponds to $\approx 180\,\mu\text{m}$, approximately 1.5 MeV.

As for the charge calibration, first, a scraper scan was performed for the bunch used in this data, where the charge measured in the toroid was related to the sum signal on the scintillating screen. The scale of Q_{toroid}/C_{screen} is then used to calibrate each pixel in the image. Using this linear relationship between the scintillator signal and charge is valid until the screen starts to saturate, which was not the case for these measurements [75].

However, this saturation limit should be incorporated into the systematic uncertainty of this measurement as the resolution of the screen. A focused small bunch will appear as a fully saturated area on the screen at $\sim 50\,\mu\text{m}$ size. For the given energy calibration, this corresponds to around 0.4–0.5 MeV.

At this point, the rescaled image represents a charge density distribution in the MeV × mm 2D space, $\frac{d^2Q}{dxdE}$. It is projected onto the dispersive axis, thus acquiring the spectral density distribution for the driver and the trailing bunch, $\frac{dQ}{dE}$. A charge-weighted mean is calculated for both bunches:

$$E_{c.w.mean} = \frac{\int_{E_{low}}^{E_{high}} E\frac{dQ}{dE}dE}{\int_{E_{low}}^{E_{high}} \frac{dQ}{dE}dE}, \tag{4.2.1}$$

where E is the energy axis acquired in the calibration and its increments dE, $\{E_{low}, E_{high}\}$ is the range recorded in the spectrometer screen. This procedure is performed on each shot, where there are $N \sim \mathcal{O}(15)$ shots taken for each temporal separation. The mean of the energy values $E_{c.w.mean}$ of such a set of shots is chosen to represent the trailing/driving bunch energy of that perturbation timing, and, for the uncertainty of this energy, the standard error $\hat{\sigma_E} = \frac{std(E_{c.w.mean})}{\sqrt{N-1}}$ is combined with the two systematic uncertainties: screen resolution and beam dispersion. For the driver, the subtraction error is also included. Having acquired energy values for each timing and both perturbed and unperturbed working points, the residuals are calculated with eq. (4.3.6).

Similarly, the trailing bunch transverse size is extracted by projecting it onto the axis transverse to the direction of the dispersion, $\frac{dQ}{dx}$, and by calculating the RMS value from the charge-weighted distribution:

$$\sigma_x = \sqrt{\frac{\int_{x_{low}}^{x_{high}} (x - x_{c.w.mean})^2 \frac{dQ}{dx}dx}{\int_{x_{low}}^{x_{high}} \frac{dQ}{dx}dx}}. \tag{4.2.2}$$

4.3 Key ion-motion perturbation observables

The long-term ion motion experiments resulted in the identification of three key signatures in the probe bunch pair which inform about the state of the plasma channel.

4.3.1 Driving probe bunch betatron bands

Firstly, when the probe bunch driver was interacting with a plasma which was perturbed by the perturber bunch, a shift of betatron bands was observed for a range of temporal bunch separations. A betatron band is a part of the driving bunch spectrum which has a high spectral density, mostly manifested as a peak in the spectrum, see dashed red line in the driver energy spectrum in fig. 4.3. When the driving bunch is mismatched to the plasma transverse fields, each longitudinal slice will undergo betatron oscillations, the frequency of which depends on the transverse fields in the longitudinal phase of the wakefield and the energy of slice (described in section 2.1.2). As the driver is decelerated in the plasma, it acquires a large projected, or correlated, energy spread, therefore each longitudinal slice corresponds to a much larger array of energies than before the interaction of plasma. When the driver emerges from the plasma, each of these slices has undergone a different number of betatron oscillations since they have different energies and therefore possess different transverse sizes and divergence. As a result, when the driver is imaged onto the scintillator screen, the different slice sizes correspond to a different spectral density for that energy of the slice.

However, to accentuate the betatron-oscillation phase difference of each slice, instead of imaging the driver energy, the trailing bunch energy is imaged. The result of this is that now the transverse size on the scintillator screen and thus the spectral density of each slice correspond to the divergence at the plasma exit: a small divergence slice leads to a spectral density peak on the screen. These peaks, or betatron bands in energy, are therefore always observed for a mismatched driver and best seen when the imaging system is set away from the driver energy as the low-divergence bands are better contrasted with respect to the high-divergence bands, thus providing a higher resolution to the band energy measurement.

The bands are constant for a range of plasma densities for the same driver bunch [122]. The fact that these bands are not dependent on the on-axis density could suggest that the transverse wakefields are linear in that region, especially since the loss of energy of these slices is rather low [121, 122]. This is not unexpected given that when the final focusing at FLASHForward is set to minimise the trailing bunch beta-function, the driver's head has low charge density and the driven wakefield is weak, as well as the head of the bunch usually having low density due to CSR effects

[122] (see section 3.1.2). This turns out to benefit this technique, because, in order to sample the non-linear focusing fields stemming from the non-linear ion density profile, the driver transverse size should be large [122].

Further into the decelerated driver spectrum, the betatron band of lowest energy tends to be the broadest, which is due to the longitudinal increase of the transverse focusing fields in the wakefield, where the driven wakefield is stronger [122]. Given that for the same bunch, the second-highest-energy betatron lines are independent of plasma density, their observed shift in the perturbed probe bunch spectrum implies that there was some other process happening in the plasma that could have altered the transverse focusing force. With the anticipation of a curved plasma channel being present on these timescales, the shift in the betatron bands was attributed to the changing curvature of the channel θ, where the channel profile [121]:

$$n_{axis}(r) = n_{axis,0}(1 + \theta r^2). \tag{4.3.1}$$

As outlined in ref. [122], the focusing force is:

$$\frac{F_r}{r} \propto \Delta^{3/2}, \tag{4.3.2}$$

where Δ is the magnitude of deceleration of a slice experiencing this field. Given that for a non-uniform ion profile [121]:

$$F_r \propto -\frac{1}{2} r(1 + \frac{\theta}{2} r^2), \tag{4.3.3}$$

the channel curvature θ and a single probe driver bunch slice can be related by [122]:

$$\Delta_\theta = \Delta_0(1 + \theta r^2)^{2/3}. \tag{4.3.4}$$

This relation can be applied to any slice, thus for most signal readability the second-highest-energy betatron band is chosen. Then, the

$$\Delta_{\theta,0} = E_{deceleration(\theta,0)} - E_{initial}, \tag{4.3.5}$$

where $E_{deceleration(\theta,0)}$ is the deceleration of this betatron band in curved (θ) or uniform (0) ion profile, $E_{initial}$ is the initial energy of the band before interaction with the plasma. Since the energy spectrum of the driving bunch before plasma interaction is very narrow, the initial betatron band energy corresponds to the mean initial energy of the driving bunch. By measuring these energy values and thus Δ, and by taking r to correspond to the transverse extent of the driving bunch, the θ values can be calculated.

4.3.2 Trailing probe bunch size oscillations

Similarly to the betatron band origin, the trailing bunch also undergoes betatron oscillations in the plasma if not matched to the fields. Since the trailing bunch may be approximated to be a single energy slice, it can be expected that it would emerge with a specific size and divergence which corresponds to a number of betatron oscillations it has undergone in the plasma. In the same vein as the betatron bands, when the imaging is set away from the trailing bunch energy, a clear signal of either a high or a low divergence can be produced on the scintillating screen. Given the almost-uniform energy of the trailing bunch when a working point close to optimum beam loading is achieved, the different size of the bunch on the screen then corresponds to a different plasma density, as described in section 2.1.2.

When the probe trailing bunch interacts with a perturbed plasma, different temporal separations from the perturber would result in a different sampled on-axis density, which would lead to a different size on the screen. Especially since the trailing bunch transverse size is much smaller than that of the driver, it does not witness the fields due to the non-linear ion density channel. This allows for an on-axis density measurement independent of the curvature.

The size evolution of the probe trailing bunch with the bunch separation can be recreated in PIC simulations if the initial density is known, or deduced by comparing the simulated and measured probe bunch pair energy spectra, as was done in refs. [121, 122]. Since the emerging divergence changes periodically with the plasma density, a small range of densities around the initial density value was simulated. In this range, one-to-one correspondence of divergence and density could be found, so maximum and minimum divergence values were assigned to different densities. Following this, the size of the trailing bunch was measured on the screen for the initial plasma density and assigned to the value of the divergence in simulations. This way, the size evolution could be mapped to an on-axis density evolution with temporal bunch separation [121].

4.3.3 Mean energy of the probe bunches

The measured charge-weighted energy means of the probe driving and trailing bunches can be calculated from the data. The mean energies of both bunches should be calculated from spectrometer images where the imaging system was set to the respective energy of the bunch, while this is the opposite case for the transverse trailing bunch size and driver second betatron band energy. These values result from a combination of plasma channel effects, i.e., both the on-axis density and the curvature of the channel change the final driver deceleration and trailing bunch acceleration, as described in section 2.3.5. Thus, their best use is to inform when

conditions in the plasma have returned back to the initial state. Energy residuals are calculated as follows:

$$R = \frac{E_{perturbed} - E_{unperturbed}}{E_{unperturbed} - E_{initial}}, \tag{4.3.6}$$

where E is the charge-weighed mean of a bunch, *perturbed/unperturbed* are the working points in the plasma, and *initial* corresponds to no plasma interaction. With these residuals, one can quantify the timing of this recovery, by defining the recovery time to the the point where residuals are zero within the measurement uncertainty and remain this way from that time onwards.

4.4 Plasma channel evolution

The features of the channel were investigated in the first shift block. The perturber-probe-bunch temporal scan resulted in the following evolution of the probe bunch pair energy spectra and size, see figs. 4.3, 4.4, and 4.5. For the unperturbed probe-bunch dataset, it can be seen that the energy and the transverse distributions are approximately constant, other than the slow change in the accelerated trailing bunch energy and driver deceleration because the background plasma is decaying on the microsecond timescale [122, 127]. Equally, the plasma length is expected to stay at an almost constant value, 32 mm flat top at $1.75 \times 10^{16}\,\mathrm{cm}^{-3}$ density, thus granting more certainty to the analysis techniques described earlier based on betatron oscillations and acquired phase through the plasma length [121].

The subtraction technique (section 4.2.1) applied to this dataset resulted in less surplus signal thanks to the relatively low jitter in the bunch profiles, thus a relatively low thresholding value of $c = 15$ pixel counts sufficed. It was applied to the driver to remove the subtraction leftovers.

The second betatron band energy data was extracted from measurements done with imaging energy set to the trailing bunch, highlighted by the dashed red line in fig. 4.3. The betatron band mean energy measurement was used to calculate the channel curvature value. Another set of data was taken with imaging set to the driving bunch energy of 1030 MeV, which provided accurate information of the driving bunch mean energy and the trailing bunch size oscillations, presented in figs. 4.4 and 4.5. The probe trailing bunch size was extracted following the procedure described in section 4.2.2. In order to extract the plasma density information from this size data, as described in section 4.3.2, a set of PIC simulations were performed for a range of plasma densities with the bunch of same parameters as the experiment. A summary of this study from ref. [121] is presented here.

The range of on-axis plasma density values was chosen to recreate the energy gain

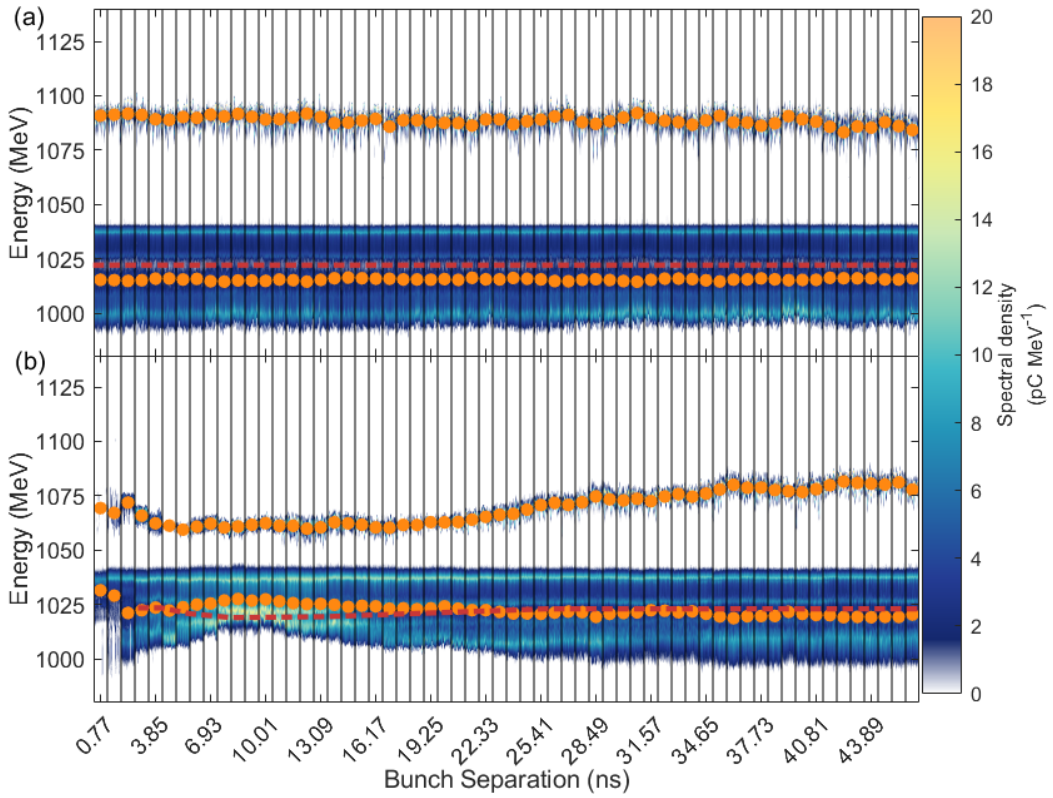

Figure 4.3: Energy spectrum evolution of the probe bunch-pair in (a) unperturbed and (b) perturbed plasma. Imaging is set to the trailing bunch energy. The orange points denote the mean energy of the trailing and driving bunches in the probe for each perturber-probe bunch separation. The slow energy gain (loss) reduction of the trailing (driving) bunch in (a) unperturbed plasma over this range of timings is consistent with the slow microsecond-timescale decay of plasma. In contrast, the changes in energy gain (loss) of the trailing (driving) bunch in (b) perturbed plasma indicate nanosecond-timescale effects in plasma caused by the perturber. The dashed red line denotes the second highest-energy betatron band in the driving bunch spectrum, a spectral density peak which is a result of an energy slice of the driving bunch exiting plasma at a low divergence. The highlighted betatron band in (a) unperturbed plasma is unchanging, whereas in (b) perturbed plasma, there is a significant effect on the highlighted betatron band.

of the trailing bunch seen in the experiment; in addition, they matched the plasma density measurement performed with OES. By matching the out-coming divergences of the simulated trailing bunch for a given on-axis plasma density to the transverse size on the scintillator screen in the measurements of the unfocused trailing bunch, the density evolution was recreated. To be more specific, the peak perturbation at 9 ns corresponded to an on-axis plasma density of $n_p \sim 3.5 \times 10^{15}\,\mathrm{cm}^{-3}$. In addition, other size oscillation extrema corresponded to on-axis densities of $n_p \sim 5.5$, 8.5, $12.5 \times 10^{15}\,\mathrm{cm}^{-3}$ at 13, 18, 29 ns timings respectively as cited in ref. [121], which can also be seen in fig. 4.6 (a). Thus the on-axis density seems to decrease by a factor of five at the deepest point of the plasma channel.

To confirm that the size oscillation does indeed correspond to the divergence

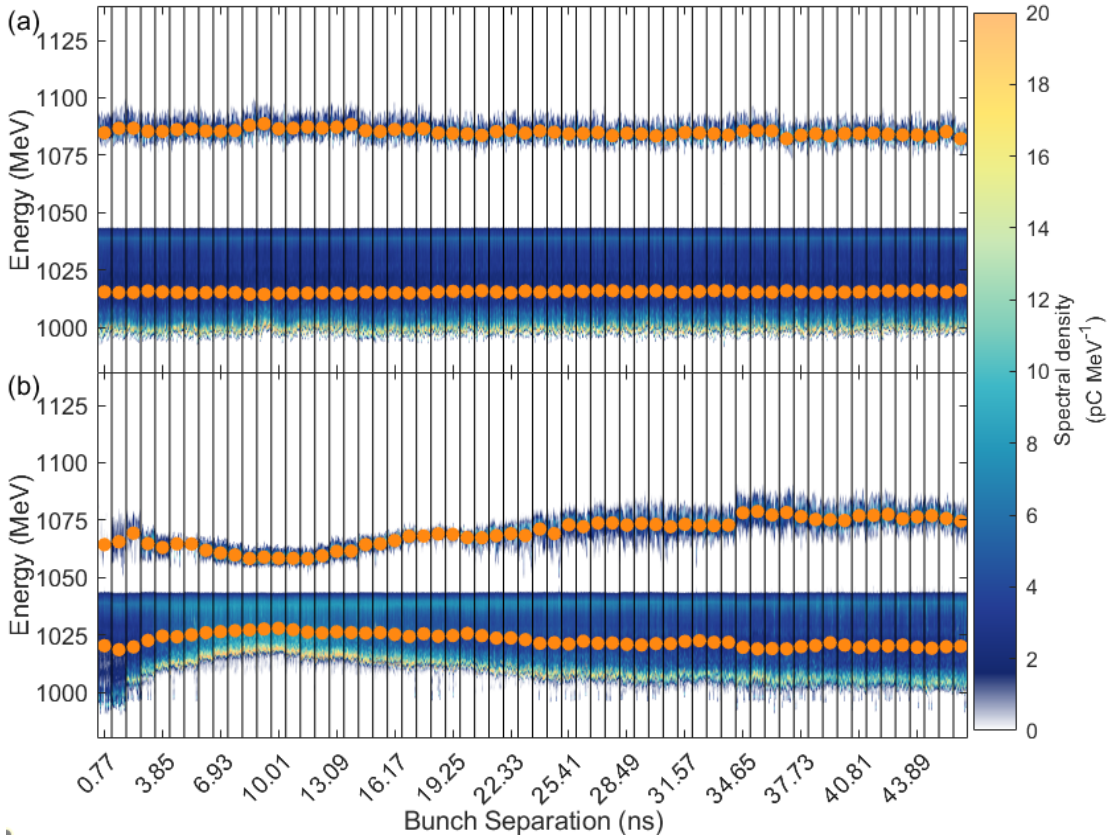

Figure 4.4: Energy spectrum evolution of the probe bunch-pair in (a) unperturbed and (b) perturbed plasma. Imaging set to the mean driving bunch energy. The orange points denote the mean energy of the trailing and driving bunches in the probe for each perturber-probe bunch separation. The slow energy gain (loss) reduction of the trailing (driving) bunch in (a) unperturbed plasma over this range of timings is consistent with the slow microsecond-timescale decay of plasma. In contrast, the changes in energy gain (loss) of the trailing (driving) bunch in (b) perturbed plasma indicate nanosecond-timescale effects in plasma caused by the perturber.

at the plasma exit, transverse phase space in the x-plane (transverse to the dispersion axis) measurements were additionally performed. For this, the FLASHForward LEMS spectrometer (see section 3.1.4) was used, which has a high enough resolution to also provide reliable measurements for the emittance of the trailing bunch. The transverse phase space was measured by performing an object plane scan. There, the trailing bunch size changes as the imaging quadrupoles are set to such strengths which correspond to an imaging lattice starting at the adjustable object plane. This, as described in section 3.1.4, is then fitted to the beam envelope function, equation 2.1.40, to acquire the bunch Twiss parameters, and for divergence at the waist, or plasma exit, equation 2.1.42 is used. The results are shown in fig. 4.6. As expected, the size oscillations measured with unfocused imaging quadrupoles at the ESPEC spectrometer follow the LEMS-measured divergence evolution closely while the beam size at the plasma exit follows a different trend. This validates the use of this experimental observable in estimating the on-axis plasma density evolution. Furthermore, the trailing bunch emittance and charge information is acquired from this scan. Sig-

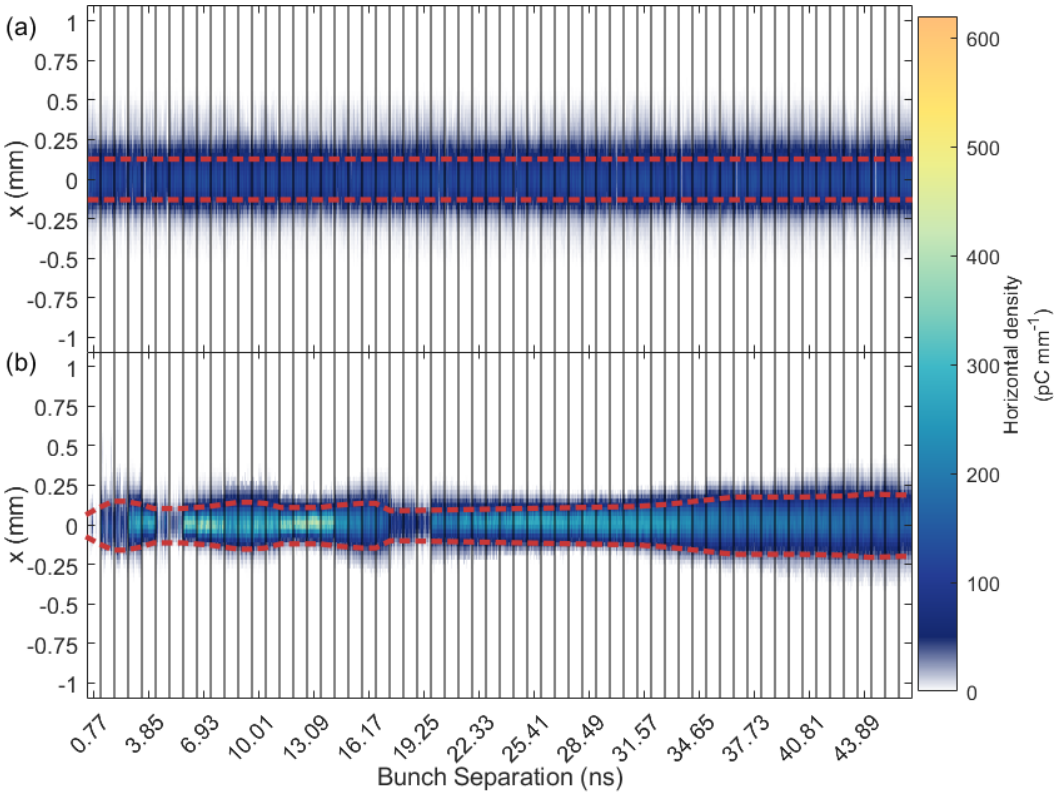

Figure 4.5: Evolution of the transverse projection of the probe trailing bunch in (a) unperturbed and (b) perturbed plasma. Imaging is set to the mean driving bunch energy. The dashed red lines trace the transverse extent of the trailing bunch, highlighting the almost-unchanging trailing bunch size in (a) unperturbed plasma and oscillations in the size in (b) perturbed plasma.

nificant charge loss is detected twice, almost identically for both screens: in short timescales and at around 15-20 ns. In the case of the former, the charge is lost due to the high on-axis density from the decaying peak, while the latter charge loss occurs due to the high divergence of the beam and clipping at the quadrupoles [121]. Interestingly, there is a point in the plasma channel evolution where more trailing bunch charge is preserved than in the unperturbed plasma, implying that a lengthened wakefield cavity due to on-axis plasma density depression provides better transverse focusing conditions to preserve more charge. Equally, an improvement in emittance is also seen, which may be attributed to better matching conditions reached during the evolution of the channel and to the loss of charge. This reveals the strong effects the channel evolution has on the transverse properties of the bunch. Ultimately, despite some benign effects of the perturbation on the transverse phase space properties of the bunch, the perturbation impedes the energy gain in the plasma accelerator. Thus, when considering the effects of the perturbation, both the transverse phase space and the energy spectrum of the bunch need to be investigated.

From the beginning of the measurement up to the peak perturbation timing of 10 nanoseconds, the channel evolves from an on-axis density peak to an on-axis

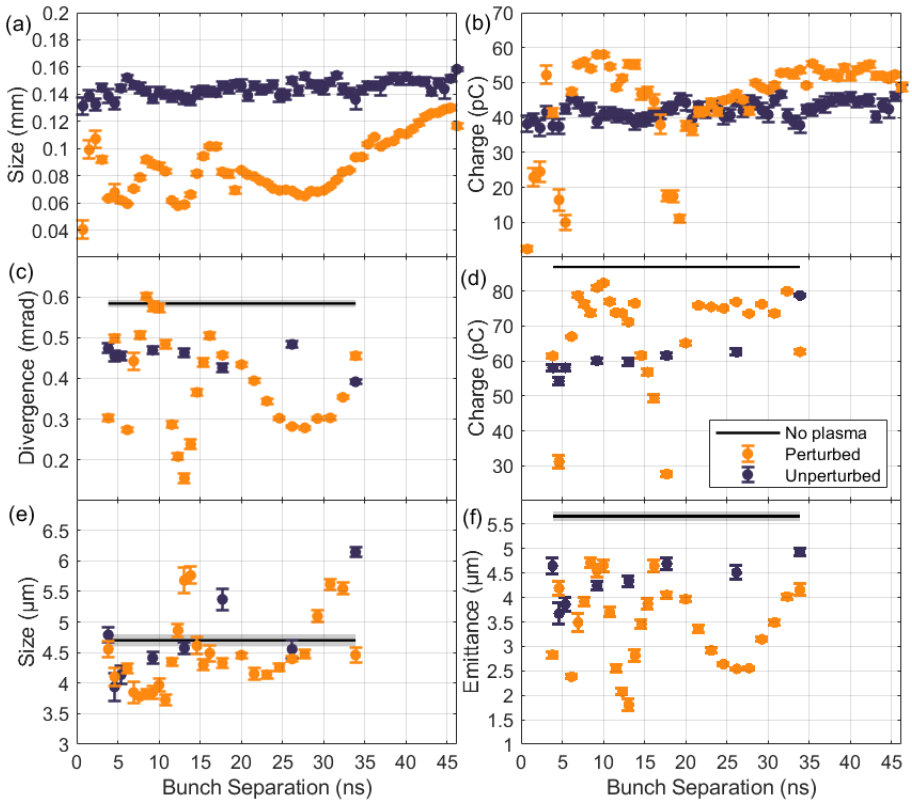

Figure 4.6: Unperturbed and perturbed unfocused probe trailing bunch (a) size and (b) charge evolution at different plasma channel evolution timings as measured directly from energy spectrometer ESPEC images. Unperturbed and perturbed probe trailing bunch (e) size and (c) divergence at waist/plasma exit, (d) charge and (f) emittance as measured at the high-resolution screen LEMS. The parameters of the trailing bunch not interacting with plasma are provided as the black line with a grey area corresponding to measurement uncertainty.

density depression, increasing in curvature. This first part of the evolution could then correspond to the Sedov-Taylor shock dynamics proposed earlier. If it were a simple diffusive and conductive evolution of the channel after deposition of a certain amount of energy on-axis, the timescales would be slower, as shown in a numerically calculated example in ref. [121]. Once the channel formation stops at peak perturbation, diffusive and conductive dissipation processes take place, lasting for tens of nanoseconds or longer, which could be measured.

4.5 Recovery time of long-term ion motion

Measuring the lifetime of this dissipation, and confirming that it is the final effect caused by long-term ion motion, would lead to defining the plasma recovery time when the next acceleration event could occur under same conditions. This was done in the second shift block, where the same perturber and probe-bunch temporal scan was performed over longer timescales, see fig. 4.8. The analysis was performed as outlined in section 4.2.2. The energy residuals R were calculated using the equation

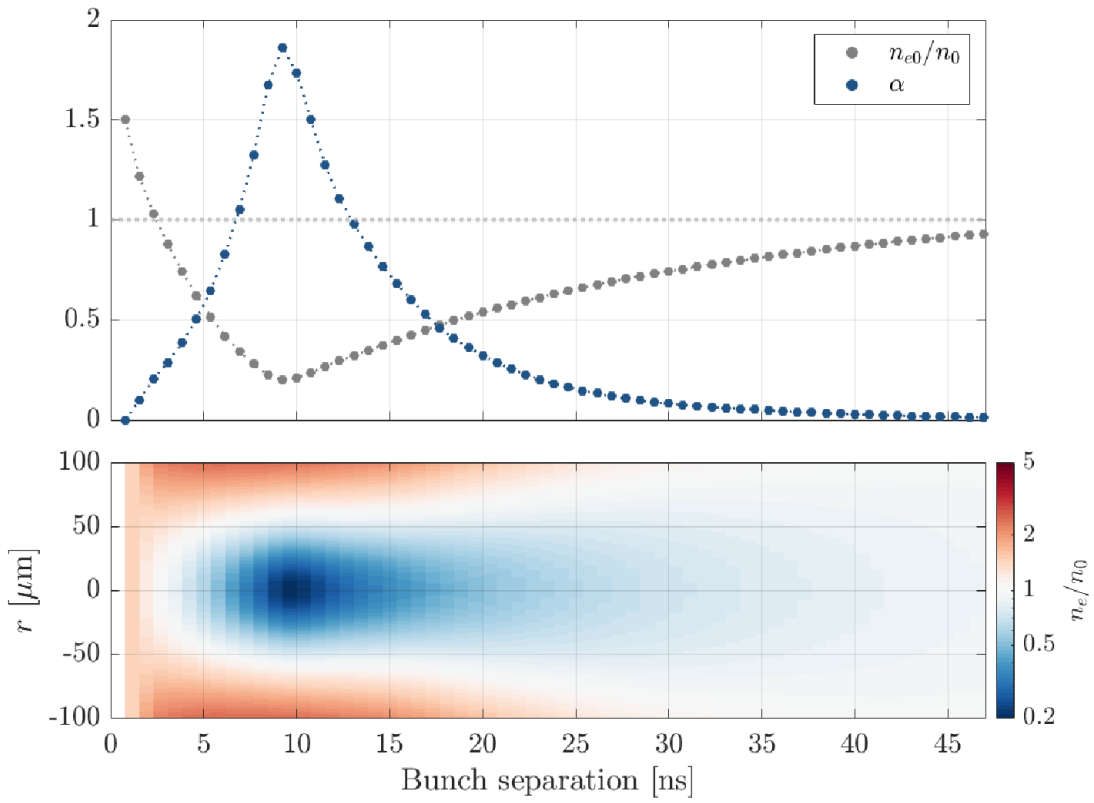

Figure 4.7: Experimentally measured on-axis density n_{e0} and curvature θ (denoted in the figure as α) values (top) and recreated radial profile evolution (bottom). Figure from ref. [121].

4.3.6 and the plot are shown in fig. 4.9.

To illustrate the plasma channel evolution reflected in these measurements more quantitatively, an empirical function is fitted [121]:

$$f(t) = At^{1/2}e^{-Bt}. \tag{4.5.1}$$

The two parameters help describe two features of the overall plasma channel evolution: magnitude of the on-axis density depression A, and rate of the formation and dissipation of the channel B [121]. The extremum of this function occurs at $t = \frac{1}{2B}$, which corresponds to the timing of peak perturbation, also helping to inform of the overall timescale of this evolution. For the fit of the data, following the same analysis procedure as in ref. [121], energy residuals whose difference from fit is larger than the combined uncertainty of the measurement and one of the fit by a factor of three (3 sigma) are marked as outliers. This combined uncertainty is marked as the orange band in fig. 4.9. The B parameter helps to pin-point the exact timing of peak perturbation, which also confirms the expectation that the plasma channel will evolve and dissipate over nanoseconds.

If the recovery time of the perturbed plasma is defined as the timing when the

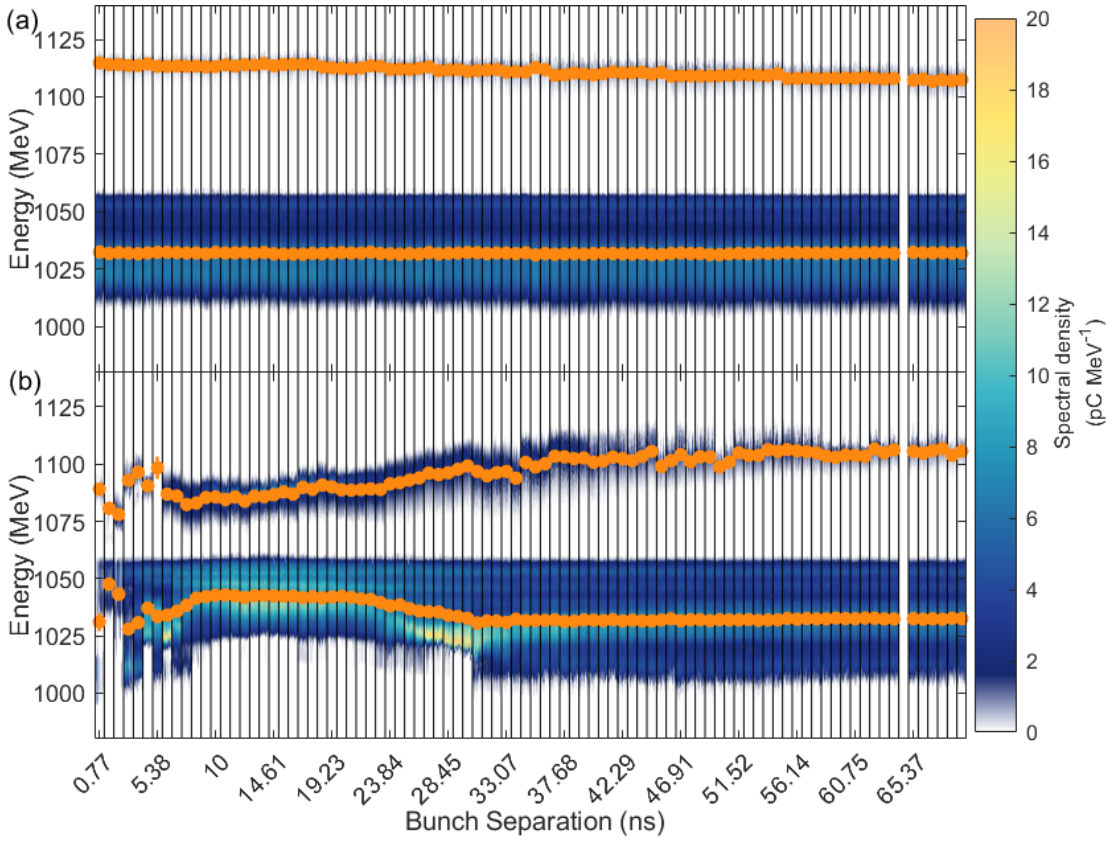

Figure 4.8: Energy spectrum evolution of the probe bunch-pair in (a) unperturbed plasma and (b) perturbed plasma up to 70 ns. Imaging set to the trailing bunch energy. The orange points denote the mean energy of the trailing and driving bunches in the probe for each perturber-probe bunch separation. The slow energy gain (loss) reduction of the trailing (driving) bunch in (a) unperturbed plasma over this range of timings is consistent with the slow microsecond-timescale decay of plasma. In contrast, the changes in energy gain (loss) of the trailing (driving) bunch in (b) perturbed plasma indicate nanosecond-timescale effects in plasma caused by the perturbed. Beyond 63 ns, the energy gain (loss) of the trailing (driving) bunch is the same for (a) unperturbed and (b) perturbed plasma because the plasma recovers from the long-term ion motion.

probe trailing bunch energy residuals are zero within measurement uncertainties and stays zero from that timing onwards, then the recovery time is $\tau_{rec} = 63$ ns [122]. One could also be stricter and use the fitted function to derive the recovery time. However, the function has an exponential factor, which means that the function approaches, but never reaches zero for late timings. As such, a resolution has to be defined, and so the combined measurement and fit uncertainty is used, marked as the orange band in fig. 4.9. The timing at which the fit crossed into the range of this resolution can be defined as recovery time, marked by the dashed line in fig. 4.9. In this case, $\tau_{rec} = 72$ ns. A longer separation scan up to 160 ns was performed to demonstrate that the recovery lasts in ref. [122]. The trailing bunch size oscillations and driver second betatron band energy measurements from this data were not used to reconstruct the density profile evolution of the plasma channel, since the lifetime measurement of the evolution was more crucial.

The measurement of the recovery time, resulting in 63 ns, is a major result when considering high-repetition-rate operation in PWFA. The measured recovery time defines the fundamental limit to repeatable acceleration, suggesting a possibility of $\mathcal{O}(10)$ MHz repetition rate. Naturally, if, by using a different working point of plasma and perturber bunch, one could measure an even shorter recovery time, that could help inform the flexibility of this limit. Nevertheless, further studies with a number of bunches beyond two would have to be carried out to check if there are no other, cumulative effects which could limit the number of bunches in a train of, say, 10 MHz repetition rate. One of such effects could be slow (microsecond timescale) plasma heating as the plasma density channel recovers after each perturbation. As discussed in ref. [122], previous simulation work implies that thermal heating on the order of $\mathcal{O}(100)$ eV should not affect the PWFA process greatly [90, 95].

4.6 Long-term ion motion dependencies and discussion

The evolution of this long-term-ion-motion triggered plasma channel and its recovery has been measured with a specific set of settings: argon plasma of $1.75 \times 10^{16}\,\mathrm{cm}^{-3}$ density and a perturber beam of 1.5 kA. Naturally, one can expect there to be a dependency on these settings. Three such dependencies were identified that could directly change the nature of this evolution: perturber charge density, initial plasma density, and ion mass. All three were explored in ref. [121]. The parameter for observing perturbation in plasma was different from the one used in this work, which is defined in eq. (4.3.6). Instead, the following relative perturbation parameter is used:

$$\Delta\tilde{\mu} = \frac{E_{unperturbed} - E_{perturbed}}{E_{unperturbed} L_p}, \tag{4.6.1}$$

where $E_{unperturbed}$ and $E_{perturbed}$ are the energy defined the same way as in eq. (4.3.6), and L_p is the estimated length of plasma in the capillary.

The perturber charge density can be controlled in FLASH via the bunch current and thus length, as described in section 4.2. By changing the injector pulse arrival time, the bunch accelerates at a different RF off-crest phase and results in a higher energy chirp. With this, the bunch is compressed more in the bunch compressors and thus results in a larger current (more details in section 3.1.1 and section 4.2). Such a bunch, when interacting with a plasma, would drive a different strength wakefield, and decelerate by a different amount, and this therefore determines how much energy it can deposit in the plasma. However, it has an upper limit for the charge density to avoid significantly ionising the plasma with the bunch (see section 2.2.2). While the driver-deposited energy is manifested in various forms in the plasma, dominantly as ion motion [100], different amounts of it can change the

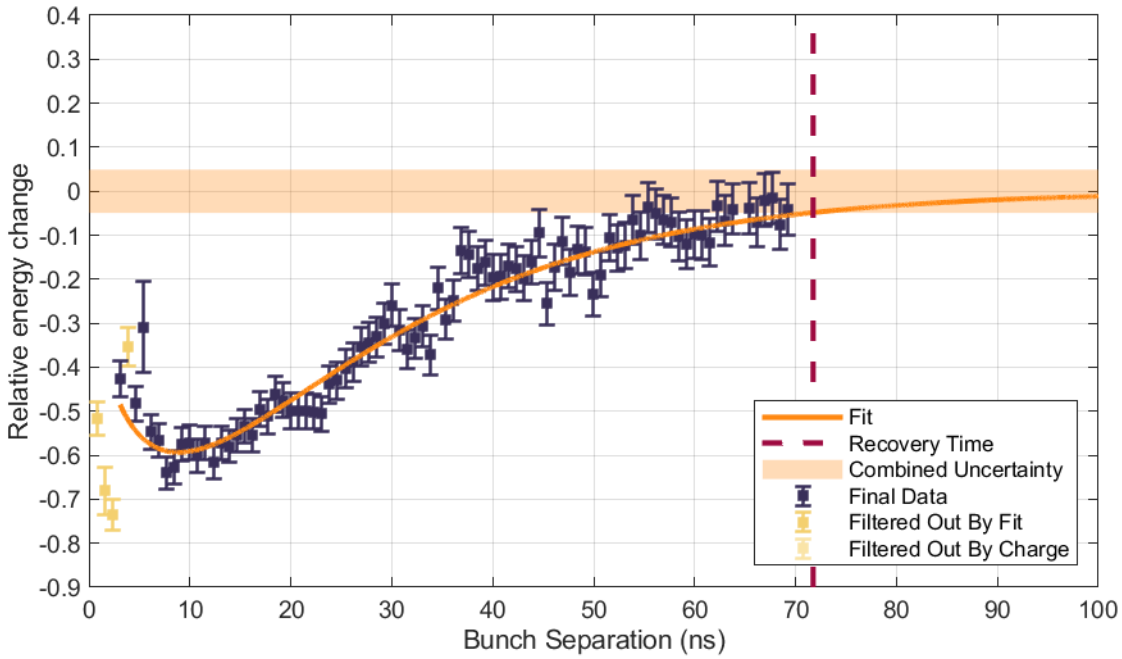

Figure 4.9: Probe trailing bunch relative energy change. The data is fitted (orange line) with function $R(t) = A\sqrt{t}e^{-Bt}$ like in ref. [121]. Yellow points are the outliers selected using the first fit attempt, i.e., energy residuals whose difference from the first fit is larger than the combined uncertainty of the measurement and one of the fit by a factor of three (3 sigma) are marked as outliers. The goodness-of-fit was $\chi^2 = 69$ for 87 degrees of freedom. The orange band around zero corresponds to the combined mean uncertainty of the measurement and the uncertainty of the fit. This band is then used to estimate the earliest recovery time, indicated by the dashed line.

features of the long-term ion motion plasma channel. Considering the Sedov-Taylor shock wave model alone, there is a direct factor for deposited energy density in the shock radius evolution, see eq. (2.3.17). As a result, there is an expectation that the first part of the plasma channel evolution, i.e., the development of the channel, may very sensitively respond to different perturber currents.

Three different perturber strength outcomes were measured with the probe bunch, which corresponded to decelerating gradients of 1.11, 1.32, and 1.74 $\mathrm{GV\,m^{-1}}$ [121]. The probe trailing bunch relative perturbation parameter $\Delta\tilde{\mu}$ was fitted with the perturbation evolution function in eq. (4.5.1), see fig. 4.10. Higher perturber current resulted in higher perturbation magnitude (A parameter in eq. (4.5.1), $A = 0.149 \pm 0.008$ in (a), $A = 0.268 \pm 0.015$ in (b), and $A = 0.356 \pm 0.021$ in (c) of fig. 4.10), or in other words, a larger on-axis density depression is reached for more energy deposition, manifesting in higher peak trailing bunch relative perturbation parameter $\Delta\tilde{\mu}$. However, the timescale of the whole evolution, i.e., B^{-1} parameter in eq. (4.5.1) ($B = 0.056 \pm 0.001$ in (a), $B = 0.069 \pm 0.002$ in (b), and $B = 0.069 \pm 0.002$ in (c) of fig. 4.10)), seemed less reactive to the perturber strength over the measured range of perturbed currents, as stated in ref. [121]. While the former finding was

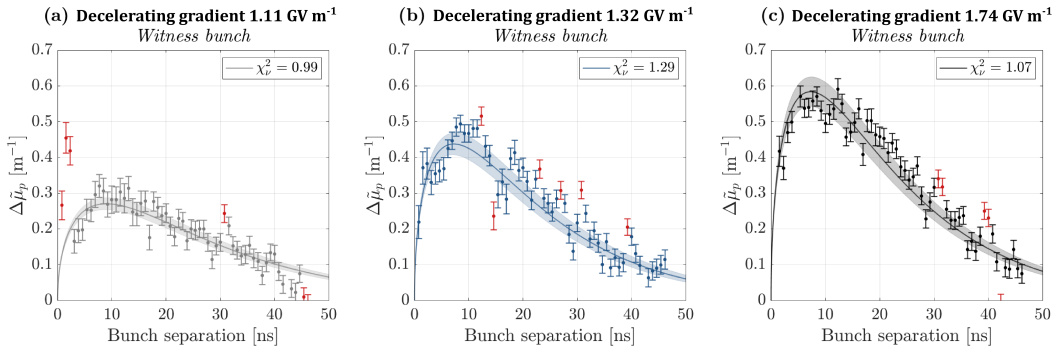

Figure 4.10: Three different perturber strengths, set by the time of arrival setting in the linac, corresponding to different decelerating gradients in plasma, and their resulting probe trailing bunch energy relative perturbation parameter $\Delta\tilde{\mu}$ (defined in eq. (4.6.1)). The data is fit with eq. (4.5.1). The peak of relative perturbation parameter $\Delta\tilde{\mu}$ increases for increasing perturber strength and decelerating gradient (A parameter in eq. (4.5.1)). However, the timescale is similar for the three working points (B^{-1} parameter in eq. (4.5.1), see text for more details). Figure from ref. [121].

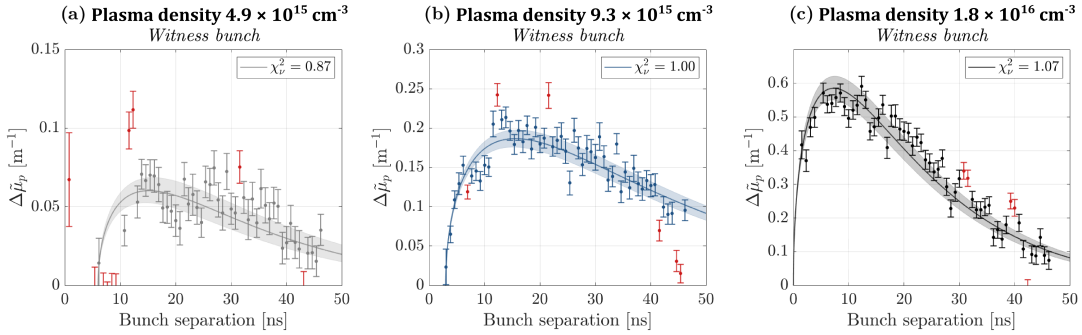

Figure 4.11: Three different initial plasma densities, set by the high-voltage discharge trigger timing, and their resulting probe trailing bunch energy relative perturbation parameter $\Delta\tilde{\mu}$ (defined in eq. (4.6.1)). The data is fit with eq. (4.5.1). The peak of relative perturbation parameter $\Delta\tilde{\mu}$ increases for increasing plasma density (A parameter in eq. (4.5.1)). In addition, the timescale decreases for higher plasma densities (B^{-1} parameter in eq. (4.5.1)). Figure from ref. [121].

expected, the latter is harder to explain. If more energy is deposited, faster perturbation evolution is anticipated, since it would cause steeper pressure gradients, driving faster shocks and faster diffusive and conductive processes. For this, future studies with a more extensive range of perturber strengths could more validly confirm or deny this hypothesis [121].

Equally, the amount of energy deposition in the plasma can be controlled via the plasma density. In addition, plasma density is a direct factor in the Sedov-Taylor shock wave model eq. (2.3.17) as a mass density term, as well as a factor in the diffusion of the plasma, $D \propto 1/n_p$ [126], or the general collisional timescales $\tau \propto 1/n_p$ from equations 2.2.11 and 2.2.12 in section 2.2.1. All of these determine the magnitude and lifetime of both parts of the channel evolution. Experimen-

tally, long-term ion motion was investigated at three different plasma densities: $(4.93 \pm 0.69) \times 10^{15}\,\mathrm{cm}^{-3}$, $(9.34 \pm 1.30) \times 10^{15}\,\mathrm{cm}^{-3}$, and $(1.77 \pm 0.25) \times 10^{16}\,\mathrm{cm}^{-3}$, corresponding to decelerating gradients of 1.16, 1.39, and $1.74\,\mathrm{GV\,m}^{-1}$ [121]. The wakefield strengths here are of a similar range to the perturber strength scan, therefore allowing one to understand the impact of both experimental parameters — plasma density and perturber strength — better. The fitted data revealed that the perturbative timescale (B^{-1} parameter in eq. (4.5.1)) was lower for higher plasma densities, while the magnitude of the perturbation (A parameter in eq. (4.5.1)) was much higher at higher plasma densities, see fig. 4.11. Thus, plasma density changes can recreate a similar effect as the perturber strength, since both of these parameters determine the amount of energy that is deposited in plasma. Moreover, plasma density indeed dictates the timescale of the plasma channel evolution as expected. This initial investigation seems to also suggest that plasma density adjustments result in larger changes in long-term ion motion overall when compared to the adjustments in the perturber strength. However, larger parameter scans would be needed to confirm this. Nevertheless, these observations help conclude that a higher plasma density could help achieve shorter recovery times [121].

Finally, ion mass appears to be the most obvious factor which could impact the lifetime of the plasma evolution, simply by virtue of inertia. However, this could also be interpreted with more nuance. The shock wave evolution, when modelled with the Sedov-Taylor solution 2.3.17, has a square-root-of-ion-mass term through the mass density factor. However, if we define the timescale of this evolution similarly to how the shock-driven plasma-channel waveguides were described [42, 132], i.e., via the ion acoustic velocity $c_s = \sqrt{\frac{k_b T_e}{m_i}}$, the same square-root-of-ion-mass term is present. In addition, the rate of ambipolar diffusion, $D \approx 2D_i \propto 1/\sqrt{m_i}$ via the mean ion speed $\langle\, v_{ion} \,\rangle \propto \sqrt{\frac{k_b T_i}{m_i}}$ [126]. Finally, the square-root-of-ion-mass term is also in equations 2.2.11 and 2.2.12 for collisional timescales. This suggests that while lighter ions would respond with a higher perturbation magnitude [121] and sooner [103–105], they could also evolve and recover quicker. Initial studies with driver bunches only done in ref. [121] explored the following ion species: helium, neon, and argon. This study revealed that, as expected, the timescale of the long-term ion motion was shortened by reducing ion mass.

Other experimental parameters that could influence the timescale and nature of the long-term ion motion and the channel evolution could be:

- temperature, which is also present in the expressions for ion acoustic velocity and collisional timescales (section 2.2.1);
- ion-charge, since all interactions based on electric fields would scale.

However, these are complicated to set directly in experiments, therefore their de-

pendency cannot be investigated at this point.

The findings of the dependency studies in ref. [121] indicate that there is flexibility in the timing of plasma recovery, which can be accessed by easily adjustable experimental settings: plasma density and gas species. Given the expected square-root-of-ion-mass scaling, plasma perturbation in hydrogen could last as short as $\approx 10\,\mathrm{ns}$, theoretically allowing an ultra-high repetition rate of 100 MHz.

This investigation of plasma channel evolution driven by the long-term ion motion assumed that no significant ionisation occurs during the perturbation by the beam or the wakefield, contrary to the observations in ref. [100] and section 2.3.4. No growing plasma density signal was observed in the probe bunch experimental signatures, which otherwise would show an increase in energy and thus density in the perturbed plasma working point. Contrary to this, the plasma density redistribution led to the on-axis density reduction by a factor of 5. To confirm the hypothesis of no ionisation, another experimental diagnostic, OES, can be used to see if the radially-averaged plasma density at a longitudinal point (usually close to the centre) of the capillary displays any growth in plasma density. Furthermore, the conditions in the plasma may be adjusted to allow long-term ionisation to occur, such as increasing the density and the number of neutrals in the plasma, as seen in equation 2.2.27 and section 2.2.2. The additional ionisation may also be verified by an additional diagnostic, that is OES. This may reveal, that despite the possibilities of reducing the recovery time, another long-term effect may prevent the repetition of PWFA on the MHz-timescale.

Chapter 5

Long-term ionisation in argon and hydrogen

5.1 Probe bunch measurements of long-term ionisation in argon

The study presented in chapter 4 was based on the assumption of no additional ionisation occurring in the plasma after interaction with an electron beam. This may hold in certain conditions, such as low beam fields (eq. (2.2.19)), the high ionising potential of the gas (eq. (2.2.28)), relatively low plasma density, and low neutral atomic gas density in the vicinity of the perturbation (eq. (2.2.27)).

At FLASHForward, the beam charge density and the plasma density are set to optimise the plasma wakefield acceleration. As a result, reducing these parameters for the sake of minimal plasma perturbation would come at a cost of the quality of the acceleration in plasma. Nevertheless, both the beam fields and the plasma density at FLASHForward are not in a range that necessarily would result in ionisation (see section 2.2.2), and so it is both much more crucial and practical to adjust the atomic gas density in the capillary to avoid the ionisation. Using the same probe-bunch diagnostic as for the investigation of the on-axis plasma channel evolution, additional ionisation or lack thereof may be observed.

Indeed, such a study is described in ref. [121]. The perturbative signals were only observed in the driving probe bunch as no trailing bunch was set up in the campaign. In order to examine the effect on this ionisation by changes in the plasma and neutral atomic gas density, the pressure of the buffer and the high-voltage discharge trigger timing were adjusted. The buffer pressure sets the initial atomic gas density in the capillary while the timing of the discharge determines at which moment of the plasma evolution in the capillary the beam will arrive. The later the beam arrival

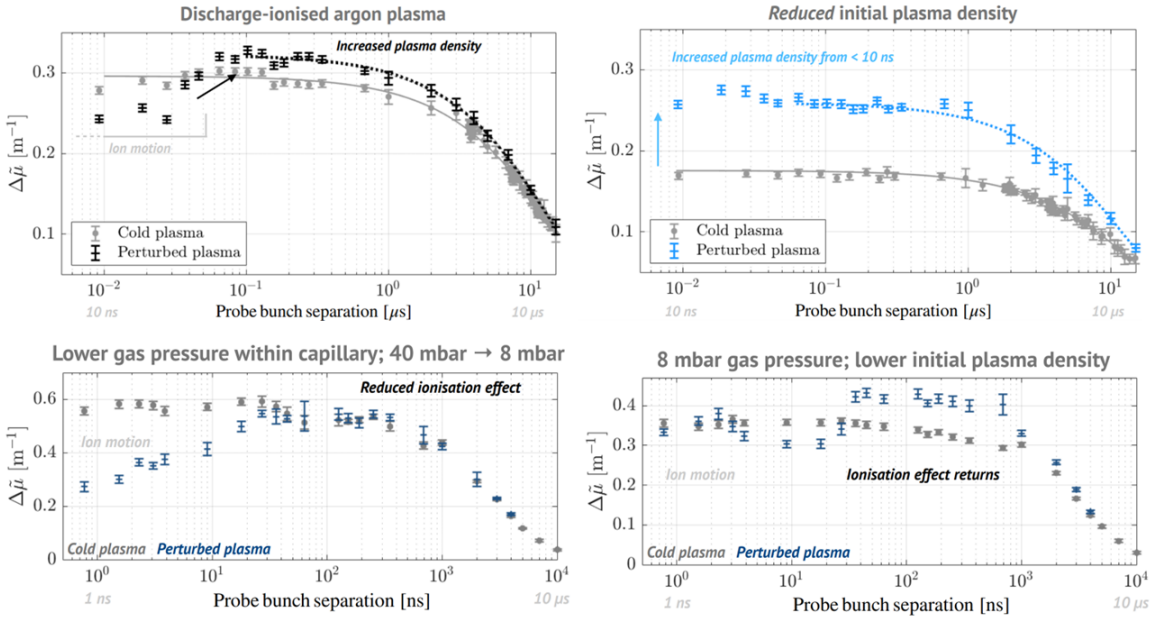

Figure 5.1: Probe trailing bunch energy relative perturbation parameter $\Delta\tilde{\mu}$ (defined in eq. (4.6.1)) evolution in perturbed and unperturbed (cold) plasma. Four working points were investigated: (top, left) high buffer pressure (40 mbar), high initial plasma density; (top, right) high buffer pressure (40 mbar), lower initial plasma density; (bottom, left) low buffer pressure (8 mbar), high initial plasma density; (bottom, right) low buffer pressure (8 mbar), lower initial plasma density. If perturbed plasma $\Delta\tilde{\mu}$ is higher than in the unperturbed plasma (cold) case, this is consistent with higher on-axis plasma density, e.g., see the arrows in the top two panels. If it is lower, there is plasma density reduction on the axis due to density redistribution driven by the long-term ion motion, e.g., denoted as "ion motion" in the two panels on the left. For buffer pressure (40 mbar), which results in high initial gas density in the capillary, there is an on-axis plasma density increase on the nanosecond-microsecond timescale (top, left). It is suppressible by reducing the gas density (bottom, left). This ionisation effect is increased by reducing initial plasma density in both buffer pressure working points (top, right and bottom, right). Figure by J. Chappell from the study in ref. [121].

time is with respect to the plasma initiation, the more plasma in the capillary has recombined, resulting in a larger proportion of neutral atoms (in the case of argon), which may be re-ionised, and in less charged particles than for earlier beam arrival timings.

A signature consistent with higher on-axis density was observed at all examined plasma density working points at 40 mbar buffer pressure, see fig. 5.1. In addition, the onset and the magnitude of observed additional ionisation changed with the discharge initiation timing (or the plasma density at beam arrival), i.e., the lower the plasma density, the more long-term ionisation is observed, and its onset is earlier. However, lowering the buffer pressure to 8 mbar showed the potential to suppress this additional ionisation as observed by the probe bunch. At this pressure working point, two different plasma densities were examined, and while the lower one showed

a small signature of additional ionisation, the higher plasma density working point showed no ionisation signal. This latter working point was then used in ion-motion-driven plasma channel evolution measurements to avoid the complexity of additional ionisation in the perturbation.

The key dependency of additional ionisation observed here was the neutral atomic gas density. The effect started earlier and increased in magnitude when the initial gas density, i.e., the capillary pressure was higher, and at later beam arrival timings, when more plasma had recombined and so more neutrals were present for ionisation. The rate of ionisation seems to be much more dependent on the second factor in eq. (2.2.27). However, given that the probe bunch is only sensitive to changes in the vicinity of the central axis, additional ionisation happening elsewhere in the plasma and at a different timescale before plasma decays cannot be ruled out, both for when the probe bunch displays signatures of ionisation and when it does not. For this, a separate plasma density diagnostic may be used.

5.2 Optical emission spectroscopy for long-term ionisation

An increase in plasma density due to beam-deposited energy dissipation can be confirmed with another diagnostic, independent of the probe-bunch method: Optical Emission Spectroscopy.

As detailed in chapters 2.2.3 and 3.2.2, the spectroscopy is performed on light collected from a finite longitudinal slice in the capillary, radially integrated, over a set temporal window. Whether the gas in the capillary is pure hydrogen or argon doped with 3% hydrogen, the H-Alpha line may be investigated; more specifically, its broadening due to the Stark-effect line splitting can be measured. Following the simulations by Gigosos and Cardeñoso [155, 156], a model can be applied for a specific range of temperatures, and the density deduced from the H-Alpha linewidth [127].

The same model was used for pure hydrogen or argon doped with 3% hydrogen, even though the particles perturbing the light-emitting hydrogen atoms are different: hydrogen atoms and ions in the former case, and argon atoms and ions in the latter. In the simulations by Gigosos and Cardeñoso [155, 156], a reduced-mass relative velocity was used to represent the kinetics of the perturbing particles, and it is given by [156]:

$$v_{0i} = \sqrt{\frac{2k_B T_i}{\mu}}, \tag{5.2.1}$$

where k_B is the Boltzmann constant, T_i is the ion temperature, and μ is the reduced

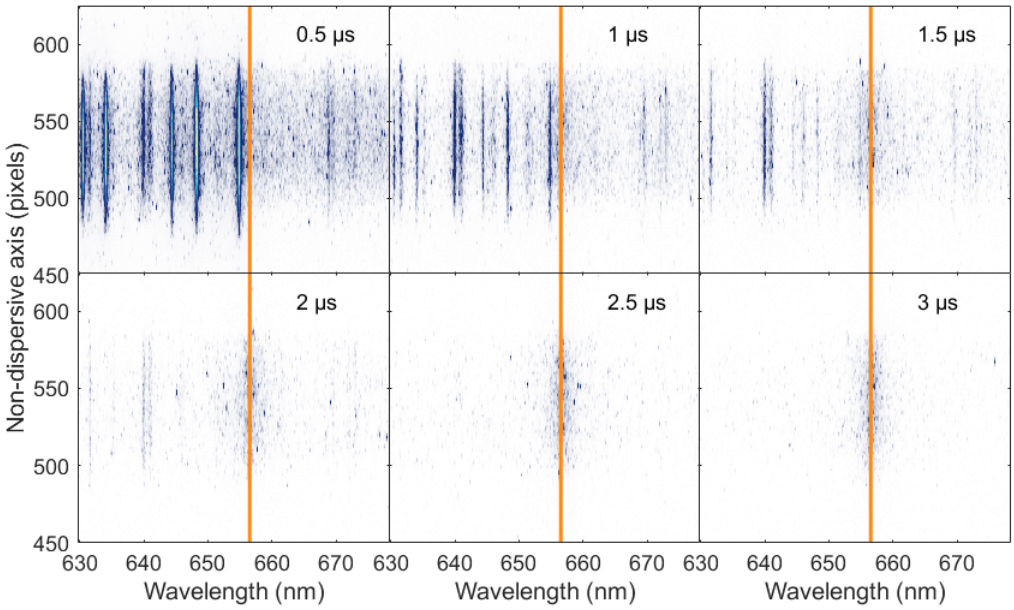

Figure 5.2: Optical Emission Spectroscopy (OES) images of argon doped with 3% hydrogen. As the camera trigger is moved further in time from the high-voltage discharge initiation (0.5 µs to 3 µs), the high-signal argon lines vanish, the hydrogen alpha line at 656.5 nm becomes more apparent without the high-signal lines. The wavelength 656.5 nm is denoted by the vertical orange bar.

mass, which is expressed by [127]:

$$\mu = \frac{m_{emit} m_{pert}}{m_{emit} + m_{pert}}, \tag{5.2.2}$$

where m_{emit} is the emitting particle mass and m_{pert} is the perturbing particle mass. For pure hydrogen plasma, $\mu = 0.5$, and for argon doped with hydrogen, $\mu = 0.98$. The ratio of the reduced-mass relative velocities for both working points would be:

$$\frac{v_{0i,H}}{v_{0i,Ar}} = \sqrt{\frac{\mu_{Ar}}{\mu_H}} = 1.40. \tag{5.2.3}$$

For temperatures of 1 eV, or 12 000 K, such a difference in the factor is minuscule. This can also be seen by comparing the H-alpha line data for specific plasma conditions for $\mu = 0.5$ and $\mu = 1$ in ref. [155]. Thus, this validates the use of the same model for pure hydrogen and argon doped with hydrogen.

A typical image of an argon spectrum is shown in fig. 5.2, where the spectral lines are vertical, with the horizontal axis being dispersive. As discussed in section 3.2.2, the plasma light is collected near the longitudinal axis centre by an optical fibre and transported to a HORIBA iHR550 spectrometer via the fibre and optics in the spectrometer, reaching a diffraction grating after passing a 50 µm vertical slit. Together with the width of the slit, a grating of 900 lines/mm is selected to achieve a balance between a high spectral resolution with a 13 µm pixel-size Andor iStar DH334T intensified photomultiplier CCD camera [127] and wide spectral field-of-

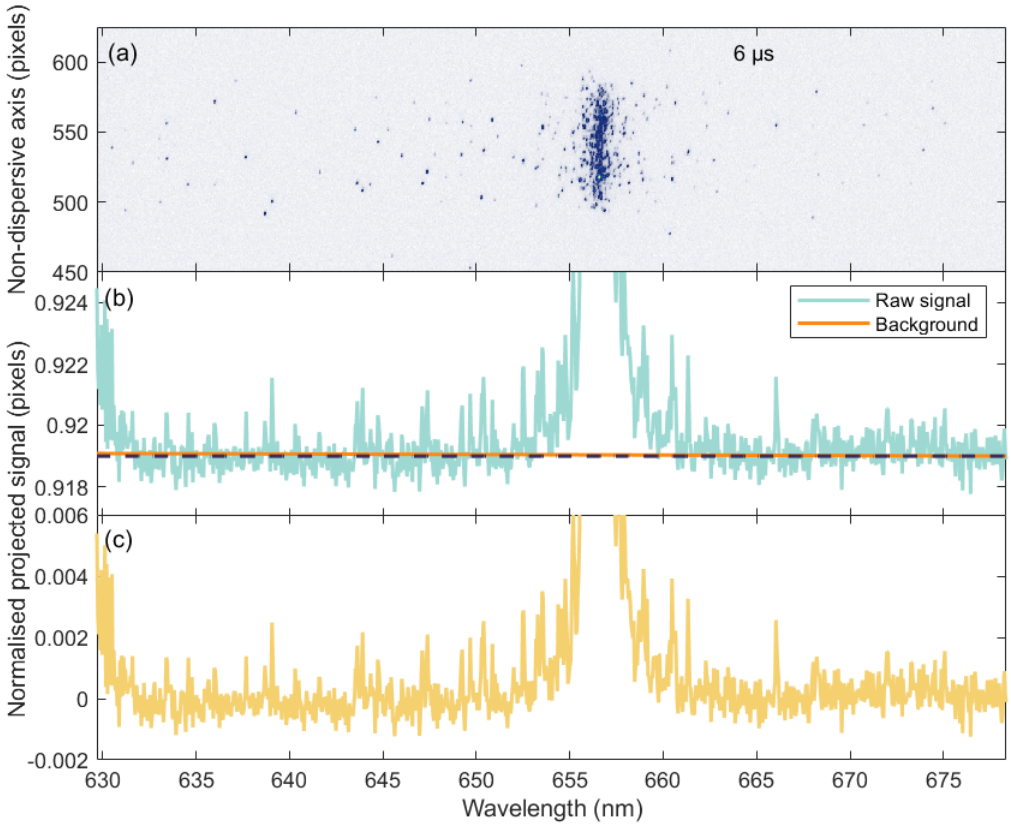

Figure 5.3: Optical emission spectroscopy (OES) of argon doped with 3% hydrogen: H-Alpha line (a) raw image at 6 µs timing from the electrical discharge and (b) normalised signal of projected raw image to the dispersive axis (light blue). The orange line in (b) denotes the background, which is a linear function of wavelength as can be seen by comparing it to the straight dashed dark blue line. Once the background is subtracted, the signal in (c) is obtained, and this is further processed in the analysis.

view with a 13.3x13.3 mm (1024x1024 pixels) camera chip as well as high signal of the spectral lines. Naturally, this optical system has a transfer function, which is assumed to be a Gaussian shape with a 3-pixel width. This has not been measured precisely for the system in the FLASHForward tunnel; however, it has produced satisfactory results for an equivalent setup used in ref. [127].

The OES spectrum image, centred at the H-Alpha line wavelength of 656.5 nm, is projected onto the dispersive axis to acquire the line signal for H-Alpha, as seen in fig. 5.3 (a) and (b), which may then be fitted for parameter extraction. Firstly, the to-be-subtracted background of the signal is identified as a linear function of wavelength, with an intercept equal to the mean background noise on the left-hand side of the image and the slope calculated by comparing the noise on either side of the signal, see fig. 5.3 (b). The background gradient is a consequence of the continuum of the plasma emission light. As for spectral lines, the user-selected ROI (region of interest) avoids ones not needed in the analysis, isolating the H-Alpha line. After background subtraction, see fig. 5.3 (c), and ROI application, the H-

Alpha is fitted with a Voigt function, where the Gaussian factor in the convolution corresponds to the instrument function, the width of which is set to 140 pm, or 3 pixels. The Lorentzian is the spectral line with three free parameters: amplitude, central wavelength, and linewidth. The latter can then be converted to a plasma density using the Gigosos-Cardeñoso model eq. (2.2.35) [155, 156].

5.2.1 Optical emission spectroscopy measurement uncertainty and resolution

The uncertainty for this measurement stems from several sources, i.e., the fitting of the line, the resolution of the apparatus, the collection of the plasma light, the model, the conditions of the plasma, and general shot-to-shot jitter.

The error of the fit for the linewidth γ may be estimated as $\Delta\gamma = \sqrt{K_{\gamma\gamma}}$, where $K_{\gamma\gamma}$ is the element of the covariance matrix corresponding to the linewidth. The covariance matrix can be estimated as $K_{i,j} = (\frac{\sum_k R(\lambda_k)^2}{n_k - n_\theta}) * (\sum_k \frac{\partial V(\lambda_k)}{\partial \theta_i} * \frac{\partial V(\lambda_k)}{\partial \theta_j})^{-1}$, where k is a point in the signal, corresponding to a specific wavelength λ_k, signal value $S(\lambda_k)$, fit function value $V(\lambda_k)$, and residuals of the fit $R(\lambda_k)$, $n_k - n_\theta$ is the degree of freedom of the fit, n_k number of data points, 1024 in total, but usually around 300 in the user-selected ROI, and n_θ is the number of fitted parameters, which is 3. $\frac{\partial V(\lambda_k)}{\partial \theta_i}$ is the Jacobian of the fit function at λ_k and for a fitting parameter θ_i, one of which is linewidth γ. The fit error turns out to be around 3% for the H-Alpha line in doped argon, which is quite small compared to the general jitter, indicating that the fit for the linewidth is usually reliable and consistent. The general OES-measured density jitter in argon is usually around 40%. Thus, such a small error of the fit does not account for how much the data tends to jitter, as well as simply being below the resolution limit of the measurement system.

Indeed, while precise resolution measurements of the whole optical system (fibre-spectrometer-camera) have not been carried out, it is safe to assume that the highest resolution of the apparatus could be 1 pixel, corresponding to a density of $0.99 \times 10^{15}\,\mathrm{cm}^{-3}$. As such, no plasma density or uncertainty values measured below $0.99 \times 10^{15}\,\mathrm{cm}^{-3}$ are trusted. In addition, if a plasma density value is measured below the optical broadening of 3 pixels ($4.97 \times 10^{15}\,\mathrm{cm}^{-3}$), this implies that the Lorentzian component in the Voigt function was similar to or even narrower than the Gaussian, which also thus rules such measurements as unreliable. Nevertheless, this resolution limit is predominantly smaller than the typical OES density measurement jitter.

The general shot-to-shot jitter of the density measurement does not directly imply that the density jitters in such a way. This can be verified by observing the trailing bunch energy gain over many shots, which is sensitive to the density of the plasma. At FLASHForward, the trailing bunch energy gain tends to jitter on a few-

percent level. As such, the jitter of the density experienced by the trailing bunch cannot alone account for the OES density measurement jitter ($\sim 40\%$).

While trailing bunch can sample changes in the capillary gas density and high-voltage discharge timing via the plasma density, it is ignorant of the temperature changes in the plasma. The Gigosos-Cardeñoso model used in this analysis is based on two assumptions: the temperature being in the range of 0.5–5 eV, and not varying greatly in a measurement [127]. The effect of the latter being untrue could cause Doppler broadening in the H-Alpha line, which the model could mistakenly measure as a change in the plasma density. In addition, the first assumption means that the model is simply wrong at certain plasma temperatures. While there is no electron beam interaction with plasma, it is known that this model is correctly applied [127]. However, when the electron beam deposits energy in the plasma, the temperature may be higher beyond this range once the plasma thermalises over nanoseconds, as estimated in section 2.2.1. Since the temperature has not been measured at the moment, it is assumed that after thermalisation, the model is either correct or correct enough for relative comparisons in the experiment. Additionally, the first nanoseconds after the beam interaction (the thermalisation process) should also be ignored in the OES measurement since the model is based on local-thermal-equilibrium conditions [127].

Since there is no straightforward way to estimate the OES measurement uncertainty using the system resolution, fitting errors, potential model errors, and the jitter of capillary conditions, the uncertainty of the plasma density is taken simply as the standard error of the mean. To take into account the considerations made about the OES resolution, the analysis ignores plasma density measurements below $0.99 \times 10^{15}\,\mathrm{cm}^{-3}$, highlights data points with errors below $0.99 \times 10^{15}\,\mathrm{cm}^{-3}$, and highlights data points with mean values below $4.97 \times 10^{15}\,\mathrm{cm}^{-3}$.

5.2.2 Optical emission spectroscopy measurement analysis

A final adjustment to the data to overcome the issue of high overall jitter is rebinning, which reduces the temporal resolution (200 ns instead of 100 ns). While the plasma density may have a significant change over these 200 ns, the binning in some cases is necessary because the chosen temporal resolution of the measurement resulted in the gating widths of the camera being too short to collect high enough signal which can reduce the extracted plasma density jitter. Thus, such binning helps artificially increase the statistics of the measurement by assigning more data to a wider timestep window.

The general OES measurement procedure follows these steps: a camera integration time is chosen, which should balance the temporal resolution with enough

signal recorded; a camera trigger timing is chosen to correspond to a specific time in plasma density evolution from the discharge ignition, and $\mathcal{O}(10)$ images are collected for each of these time windows. The analysis and the model are applied to each image, and the mean of densities and standard error of the mean are calculated for each time window. To compare the plasma density evolution after an interaction with the electron beam to the evolution where no beam traversed the plasma, two quantities are calculated, i.e., relative plasma density change parameter R and scaled absolute plasma density change parameter A of the plasma density:

$$R(t) = \frac{n_{p,BeamOn}(t) - n_{p,BeamOff}(t)}{n_{p,BeamOff}(t)}, \tag{5.2.4}$$

$$A(t) = \frac{n_{p,BeamOn}(t) - n_{p,BeamOff}(t)}{n_{p,BeamArrival}}. \tag{5.2.5}$$

The relative plasma density change parameter R is much more sensitive to the long-term ionisation signal than the absolute plasma density change parameter A, mostly because it occurs in late timescales when $n_{p,BeamOff}$ values are smaller compared to $n_{p,BeamArrival}$. However, the uncertainty of R, which relates to the relative error of the plasma density, tends to also be higher than the one of A for later timescales and lower $n_{p,BeamOff}$ values, where the certainty of the measurement does not scale down with the value. Uncertainties in A, on the other hand, tend to be higher for earlier timescales when plasma density is higher because they are not proportionally scaled by a higher $n_{p,BeamOff}$; instead, a constant $n_{p,BeamArrival}$ is used. This reflects its relation to the absolute error of the plasma density, which tends to correlate with the plasma density. The cause of this is that for higher densities, the density temporal gradient is also higher, which, for example, can be seen in fig. 3.20 (a), meaning that higher densities will result in a larger spread of measured densities for a given time window. Nevertheless, the higher plasma density values are not so relevant for long-term ionisation signal search since it occurs in later timescales, and the relation of A uncertainty to the absolute error is helpful in the later timescales where the uncertainty of the plasma measurement cannot scale down. Both quantities provide useful insight into the changes in plasma density due to electron beam and plasma interaction: R gives a more prominent signal, while A — a more certain one.

5.3 Long-term ionisation in argon measured with OES

In argon, two working points were explored, which correspond to the studies done in ref. [121], presented in table 5.2. Since the H-Alpha emission observed with this

Buffer Pressure (mbar)	Plasma Density at Beam Arrival n_p (cm^{-3})	Atomic Gas Density in the Capillary n_0 (cm^{-3})	Ionisation Degree α
8	1.75×10^{16}	4.13×10^{16}	0.42
40	1.75×10^{16}	2.83×10^{17}	0.06
38	9.32×10^{16}	2.07×10^{17}	0.45
38	1.81×10^{16}	2.07×10^{17}	0.09

Table 5.2: First two rows: the capillary conditions of long-term ionisation experiments performed in ref. [121]. Last two rows: capillary conditions in the attempt to recreate these experiments for OES.

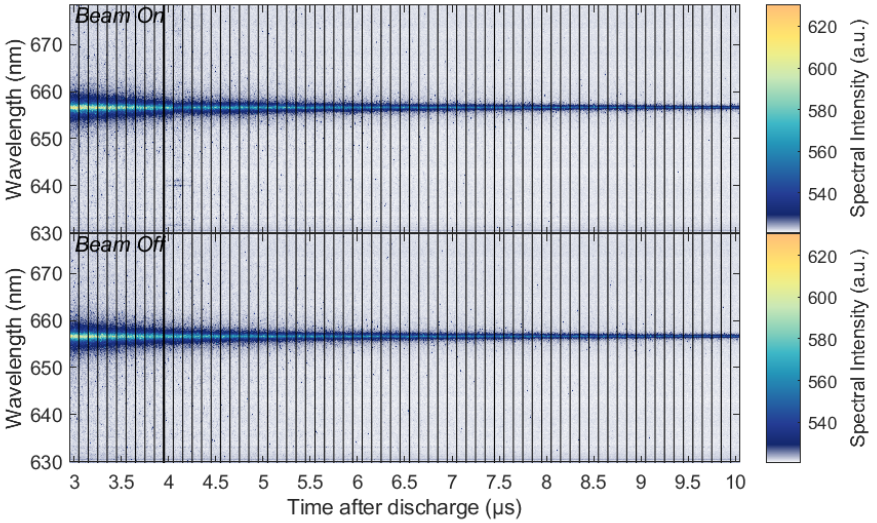

Figure 5.4: The spectrum evolution around the H-Alpha wavelength in argon at $2.07 \times 10^{17}\,cm^{-3}$ atomic gas density in the capillary as recorded with the OES. Beam arrival is recorded at 4 µs, denoted here as a black bar at the beginning of the 4 µs shot interval.

method originates from the hydrogen, comprising 3% of the volume in the gas supply of doped argon, its signal is often too low for small buffer pressure values. As such, the pressure in this investigation was kept at the same high value of 38 mbar, while the ionisation degree was selected to match closely to the original experiments.

5.3.1 High ionisation degree in argon

The measurement with OES in argon with an atomic gas density of $2.07 \times 10^{17}\,cm^{-3}$ is presented in fig. 5.4, where the beam interacted with plasma at 4 µs from the high-voltage discharge initiation (ionisation degree of $\alpha = 0.45$ at beam arrival time). Some beam and plasma interaction features can be seen at 4.1 µs: H-Alpha line becomes dimmer, likely due to plasma heating (see section 2.2.3), and additional

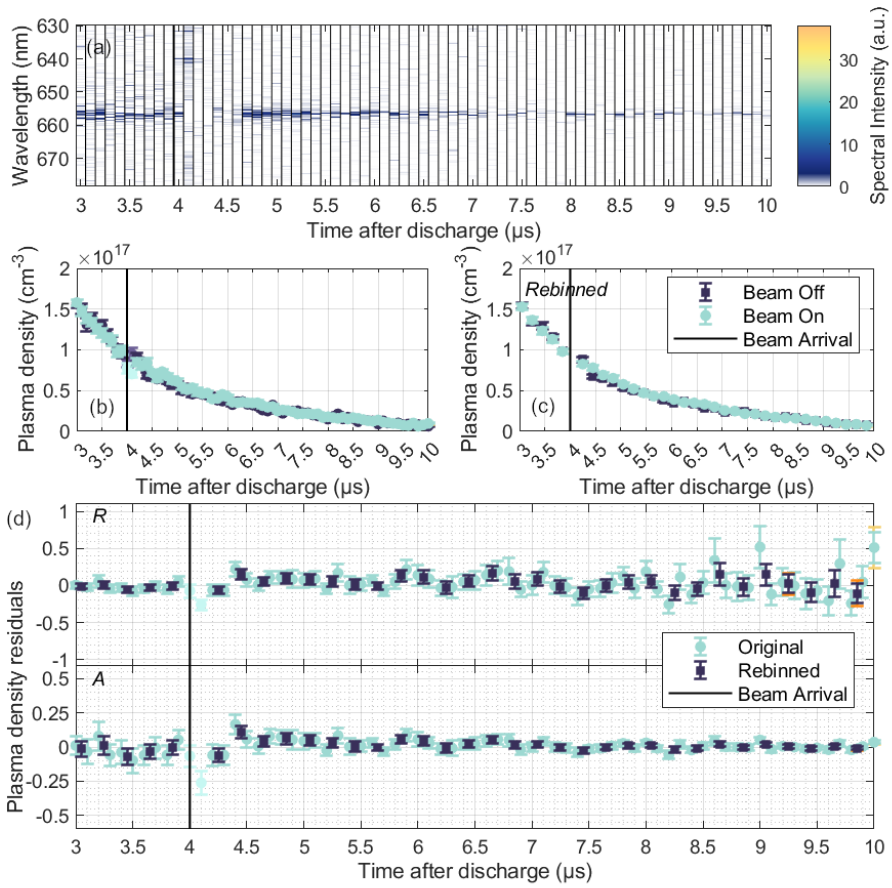

Figure 5.5: (a) The evolution of the surplus signal of the "Beam On" spectrum $Spectrum_{surplus} = Spectrum_{BeamOn} - SpectrumBeamOff$, where negative values of $Spectrum_{surplus}$ are set to zero. The beam and plasma interaction features can be seen at 4.1 µs. (b) Plasma density evolution in argon at $2.07 \times 10^{17}\,\mathrm{cm}^{-3}$ atomic gas density in the capillary, as measured with OES at the temporal resolution of 100 ns, and rebinning (c) reduces it to 200 ns. (d) relative plasma density change parameter R and absolute plasma density change parameter A.

argon lines appear at 640 nm. This suggests that there is a 100 ns offset for the estimated beam arrival time, which may occur due to the discharge trigger jitter during the determination of this timing. Alternatively, these beam-interaction effects may be simply delayed by $\mathcal{O}(100)$ ns; therefore, the exact beam arrival timing should be assumed to be known within the single timestep certainty. In this case, $\tau_{Beam} = 4 \pm 0.1$ µs; however, since the direction of the offset is the same for all data, it is not treated as uncertainty in comparisons of different timings.

The surplus of the spectrum signal in the "Beam On" case is shown in fig. 5.5 (a). While there is some surplus signal around the H-Alpha line, it is present both before and after the beam arrival, implying that there may not be any additional ionisation after beam arrival. However, the density values have to be extracted from the H-Alpha line to claim a lack of LTI with certainty. Both plasma density calculations are demonstrated in fig. 5.5 (b) as well as in fig. 5.5 (c), wherein the latter, the data is binned to reduce the overall jitter of the measurement by reducing

the temporal resolution (200 ns instead of 100 ns). Despite the beam arrival at 4 µs, both density measurements seem to evolve identically, suggesting that no observable additional ionisation has occurred.

The relative (R) and absolute (A) changes in plasma density are investigated for more precision. The fig. 5.5 (d) displays the relative plasma density change parameter R and the absolute plasma density change parameter A for unbinned and binned data. The binning helps reduce the jitter and see the evolution of both values more clearly. In addition, the yellow (orange) error bar is included, which represents the same error propagation as the light blue (navy) error bar, except that the uncertainty of the plasma density measurement is assumed to be equal to single-pixel resolution. This is done when the normally estimated plasma density measurement uncertainty is smaller than the single-pixel resolution. As explained earlier, this highlights the measurements where such small measurement uncertainty was acquired and may not be trustworthy given the highest OES resolution possible, i.e., one pixel. In this measurement, there are only a few (usually one) timesteps where the low error is calculated; thus, measurements are reliable. The plot indicates that both R and A are consistent with zero throughout the measurement window, thus concluding that there is no observed LTI with OES at the ionisation degree of $\alpha = 0.45$ in argon. This is consistent with the long-term-ion-motion-driven plasma channel evolution and recovery observed in refs. [121] and [122], and presented in chapter 4.

5.3.2 Low ionisation degree in argon

The same argon conditions, except for the lower ionisation degree, $\alpha = 0.09$, were measured, see fig. 5.6 and fig. 5.7. The beam interaction features at 8 µs and 8.1 µs are prominent, again signifying a beam arrival timing uncertainty of 100 ns. Unlike the case of high ionisation degree $\alpha = 0.45$, the signal surplus when the beam has interacted with plasma is very obvious for this low ionisation degree, see fig. 5.7 (a). In addition to the features occurring at beam arrival (8 µs), the surplus signal around the H-Alpha line appears at around 400 ns after interaction with the beam. This can be seen more accurately by comparing the density measurements from two datasets with and without beam interaction, see fig. 5.7 (b) and 5.7 (c). While the first measurements after beam arrival may be ignored because there are highly uncertain temperature conditions in the plasma at that point, the density with beam interaction is higher at 8.4 µs, i.e., 400 ns after beam arrival.

The calculated R and A values for this dataset are noisy, therefore the binned data in fig. 5.7 (d) for R and A are discussed. Both R and A show a significant LTI signal at 400 ns from the estimated beam arrival time, approximately $(20 \pm 10)\%$ for both. The R value reaches $(41 \pm 21)\%$ in 1400-1500 ns (or $(94 \pm 37)\%$ in 1400

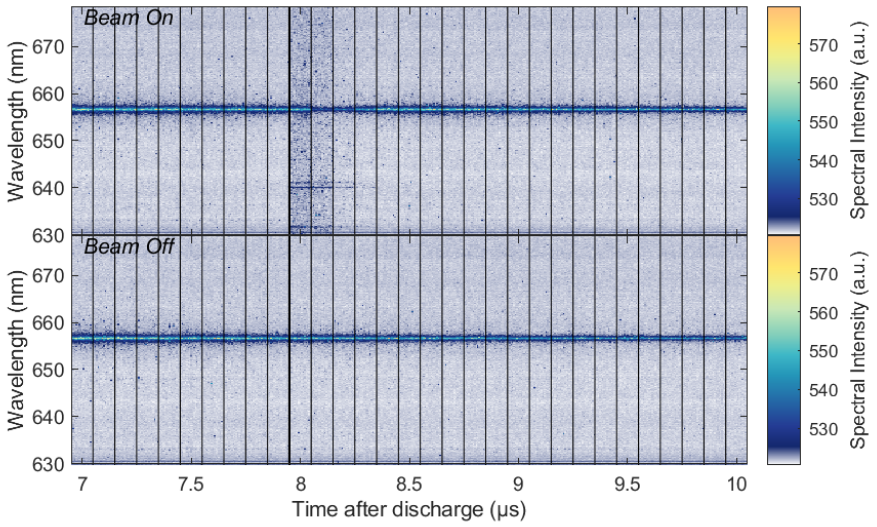

Figure 5.6: The spectrum evolution around the H-Alpha wavelength in argon at $2.07 \times 10^{17}\,\mathrm{cm}^{-3}$ atomic gas density in the capillary as recorded with the OES. Beam arrival is recorded at 8 µs, denoted here as a black bar at the beginning of the 8 µs shot interval.

ns, unbinned) from estimated beam arrival before undergoing another fluctuation in unbinned values and reaching the next peak of $(42 \pm 22)\%$ in 1600-1700 ns (or $(78 \pm 38)\%$ in 1700 ns, unbinned) from estimated beam arrival. At this peak, A is equal to $20\% \pm 9\%$, indicating that the absolute difference of densities of the two working points does not change over 1.6 µs.

Lowering the ionisation degree from $\alpha = 0.45$ to $\alpha = 0.09$ results in an LTI signal as observed on OES, with an onset at around 400 ns from beam interaction with the plasma, lasting for at least 1.3 µs. In contrast to the LTI effect observed with the probe bunch, the onset of long-term ionisation detectable with OES, which integrates signal radially and whose density resolution is $\sim 5 \times 10^{15}\,\mathrm{cm}^{-3}$ and temporal resolution 100-200 ns, is at a few hundred nanoseconds. This indicates that the more globally OES-observed long-term ionisation effect would evolve over this timescale, whereas the small on-axis plasma density changes detected with the probe bunch diagnostic of high temporal resolution indicate it can start as early as nanosecond timescale.

The LTI manifests in a constant density surplus over 1.3 µs, which for decaying plasma results in a binned relative density increase of around 40% at 1.4–1.7 µs from beam interaction timing, thus doubling from the measured 20% at onset 1 µs earlier. Given that the plasma decay rate is higher for higher densities, expected from eq. (2.2.30) and experimentally observed in section 3.2.3, the lack of density surplus reduction over at least 1 µs suggests that enough additional ionisation is occurring during this timescale to offset the losses through plasma decay. Indeed, as the R value displays, the plasma density is 94% (unbinned) of its value 1.4 µs after beam

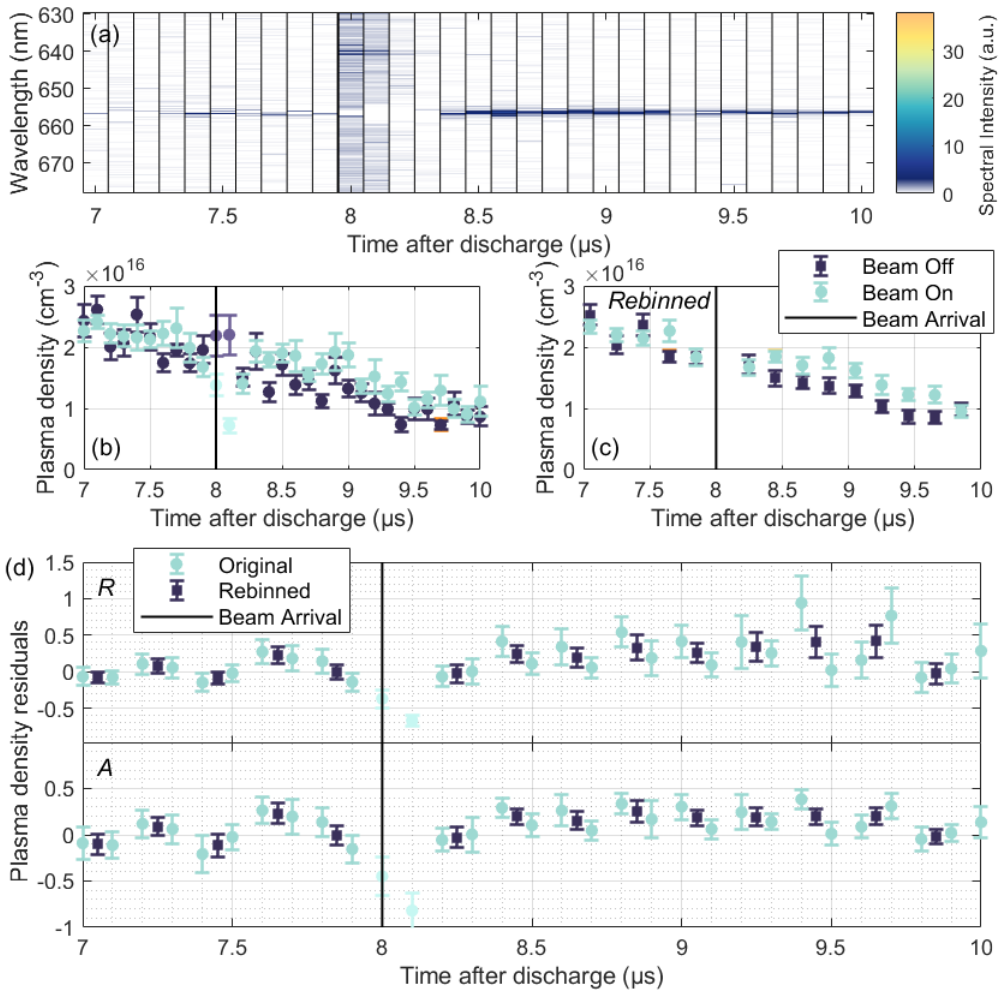

Figure 5.7: (a) The evolution of the surplus signal of the "Beam On" spectrum $Spectrum_{surplus} = Spectrum_{BeamOn} - SpectrumBeamOff$, where negative values of $Spectrum_{surplus}$ are set to zero. The beam and plasma interaction features can be seen at 8 µs. (b) Plasma density evolution in argon at 2.07×10^{17} cm^{-3} atomic gas density in the capillary, as measured with OES at the temporal resolution of 100 ns, and rebinning (c) reduces it to 200 ns. The black bar at 8 µs marks the beam arrival time, corresponding to ionisation degree $\alpha = 0.09$. (d) relative plasma density change parameter R and absolute plasma density change parameter A.

interaction when compared to the normal plasma density evolution without any beam. As a result, this additional ionisation can be concluded to be a long-lasting (microsecond-timescale) effect, suppressible with setting a high ionisation degree in the capillary during the passage of the beam, thus reducing the number of ionisable neutrals present.

5.3.3 Conditions for long-term ionisation occurrence

The investigations of long-term ionisation in argon with OES confirm what was observed with the probe bunch in ref. [121], where a signature consistent with higher on-axis plasma density was observed unless the beam traversed a capillary

with a low neutral gas density and high plasma density such as the 8 mbar working point in table 5.2. However, it was suggested that the higher plasma density may result in additional ionisation off-axis, which is outside the scope of the probe bunch. The higher plasma density at the perturber interaction time would result in a more intense plasma channel evolution and thus more depleted on-axis density. Because of this, most of the additional ionisation may occur at the edges of the plasma channel. This was not observed with the OES: the radially integrated signal did not show density growth for the ionisation degree of $\alpha = 0.45$ working point contrary to the expectation given its high plasma density.

Once again, the observations suggest there is more dependence on the second factor in eq. (2.2.27). It can be theorised that the LTI effect is more complex than a simple dependency on ionisation degree α and the neutral gas density, i.e., the first three factors in eq. (2.2.29).

5.4 Long-term ionisation at different argon plasma conditions

Changes of the observed LTI effect in argon can be observed by slightly changing the ionisation degrees. The data was collected over two different campaigns, where beam parameters, mostly the bunch profile and its density both transversely and longitudinally might have been slightly different. This could have resulted in different energy deposition by the beam to the plasma, so while not directly comparable, similarities between the two campaigns could imply the lack of sensitivity to the coupled energy to the plasma. To be more precise, the plasma heating could be occurring in such temperature ranges where the ionisation rate does not change significantly, see fig. 2.7. As for the capillary settings, two different neutral gas densities and three different ionisation degrees at the beam arrival time were investigated over the two campaigns, see table 5.4. The neutral gas density is selected to be high to promote a higher signal of the H-Alpha line from the hydrogen-doped argon and thus improve the resolution of the diagnostic. As for the plasma density, settings which resulted in stable beam-plasma interaction were chosen, which also then cover a wide range of ionisation degrees.

The results of the second campaign, where two different neutral gas densities were explored, may illuminate the relationship between LTI and the neutral gas density in the capillary, which is expected to be straightforward, see eq. (2.2.29) and fig. 2.8. On the other hand, in the first campaign, where the neutral gas densities were kept the same, the different proportions of ionised and neutral particles of the two working points might reveal LTI depending strongly on either plasma density or the available neutral particle density. Such a comparison cannot be made with

Ionisation degree α	Atomic gas density n_0 cm^{-3}	Cmp.	LTI onset	Peak R	Time of peak R	Plateau of A	Length of plateau
0.09	2.07×10^{17}	1	400 ns	(42 ± 22)%	1600-1700 ns	(20 ± 9)%	1200 ns
0.09	2.07×10^{17}	2	480 ns	(68 ± 18)%	1380-1480 ns	$(23 \pm 6(8))$%	1200 ns
0.07	1.51×10^{17}	2	1189 ns	$(73 \pm 29(36))$%	1589-1689 ns	$(30 \pm 10(12))$%	600 ns
0.04	2.07×10^{17}	1	400 ns	$(210 \pm 43(106))$%	1000-1100 ns	$(57 \pm 15(16))$%	1000 ns

Table 5.4: LTI signatures in argon expressed in key features of R and A evolution. All timings are given as a time from the interaction of the beam. The percentages in the brackets are the uncertainties represented by the yellow/orange error bars, defined by the resolution of the measurement. "Cmp." stands for "Campaign".

the results of the second campaign. The reason for this is the lack of knowledge of the exact gas density evolution in the discharge capillary. While it is known how the plasma density evolves, it is not known how much of the initial gas density, the value of which is used throughout this work, is expelled during the discharge, as explained in section 3.2.3. It may well depend on the initial gas density, as a lower one could result in more gas heating during the high-voltage discharge, thus leading to more expulsion to the vacuum due to a higher pressure gradient. As such, the gas density in the capillary at the beam arrival time might be smaller by a different factor for different initial gas densities. As such, while the estimated value of the ionisation degree at beam arrival is uncertain due to an unknown amount of the neutral gas in the capillary, the comparison of ionisation degrees is meaningful for working points with the same initial gas density.

The extracted features are detailed in table 5.4. The LTI onset is determined as the first R or A value that is significantly (over 1-sigma) above zero and is followed by points which satisfy this condition. If the data seems to have high jitter, where following points differ by around 1-sigma and fluctuate, such as in fig. 5.7 and fig. 5.9, the rebinned value is considered over the original and the onset timing is taken as the earlier bin value. The values that are not rebinned are considered for the onset for higher temporal resolution. For peak R the maximum achieved rebinned R value is selected, hence the time of the peak representing the interval of the bin. The plateau of A is identified as the approximately identical set of rebinned A values from the onset of the LTI signal until either the end of the scan or end of the LTI signal. The mean is taken to represent the value of this plateau, its uncertainty is the

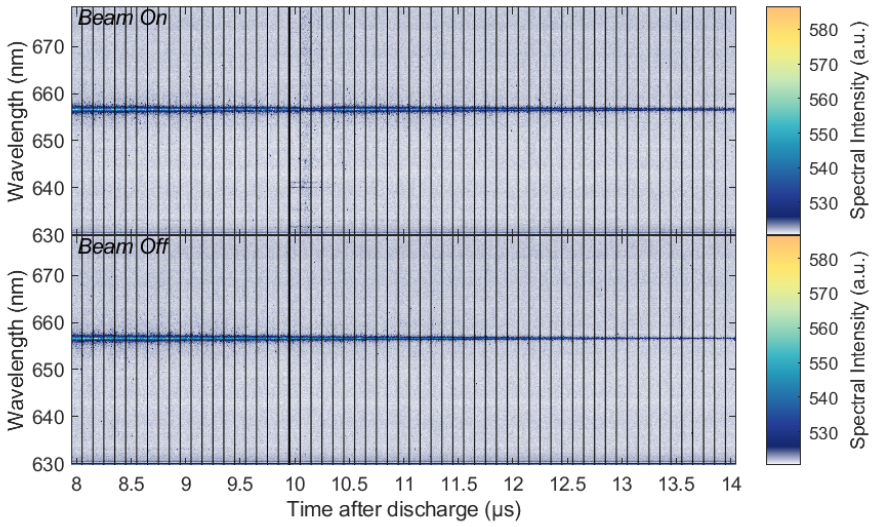

Figure 5.8: The spectrum evolution around the H-Alpha wavelength in argon at $2.07 \times 10^{17}\,\mathrm{cm}^{-3}$ atomic gas density in the capillary as recorded with the OES from 8 µs to 14 µs. Beam arrival is recorded at 10 µs, denoted here as a black bar at the beginning of the 10 µs shot interval. The H-Alpha line evolution in the top "Beam On" plot is perturbed by the beam arrival, which is manifested firstly in the dimming of the line, increasing background signal, and appearance of new lines at 640 nm and 630 nm around the arrival time of the beam. Then, there is more signal in the H-Alpha line at later timings than in data where no beam interacts with plasma, i.e., the bottom "Beam Off" plot.

mean of the errors of this set of points. The uncertainty in the brackets corresponds to the yellow error bar, i.e., where it represents the resolution limit.

The data for ionisation degree $\alpha = 0.09$ are presented in fig. 5.6 and fig. 5.7 from one measurement campaign, and the same ionisation degree but a different campaign in fig. 5.10 and fig. 5.11. Other ionisation degrees: $\alpha = 0.07$ fig. 5.12 and fig. 5.13, $\alpha = 0.04$ fig. 5.8 and fig. 5.9. In addition to the yellow error bars, the plots here include dimmed error bars, representing data points where a density below the broadening value of $4.97 \times 10^{15}\,\mathrm{cm}^{-3}$ was measured and, therefore, are not trustworthy. Indeed, due to the low H-Alpha signal in the unperturbed plasma dataset, the data in fig. 5.9 may be largely unreliable. Nevertheless, the unperturbed plasma density measurements do not exhibit severe noise, and while the plateau from 11 µs onwards might be an effect of this measurement resolution limit, the extracted R and A values before this will be used, whereas later values will be treated with caution.

5.4.1 Observed timescales and effect on the R and A values

This range of ionisation degrees does not seem to influence the timing of LTI onset greatly, i.e., $\alpha = 0.09$ and $\alpha = 0.04$ of the first campaign are identical within the measurement resolution. A slightly different value for $\alpha = 0.09$ of the second

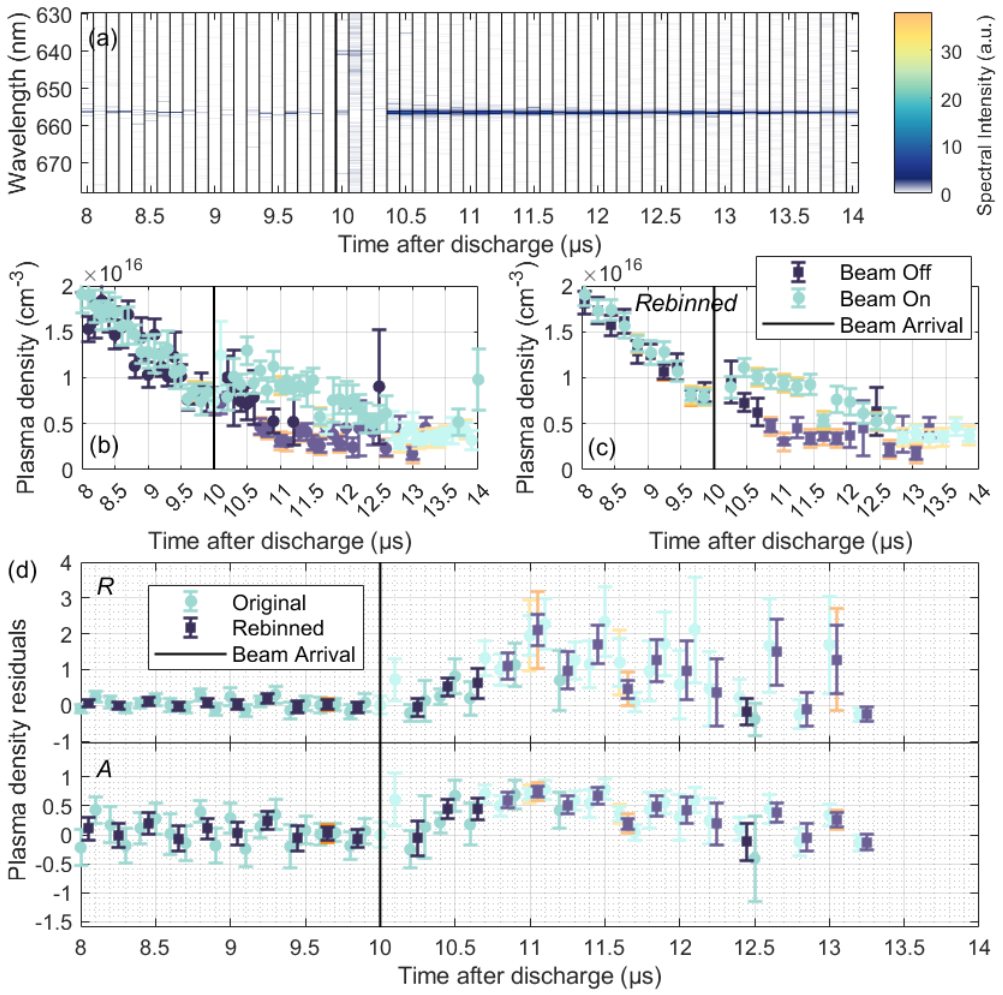

Figure 5.9: (a) The evolution of the surplus signal of the "Beam On" spectrum $Spectrum_{surplus} = Spectrum_{BeamOn} - SpectrumBeamOff$, where negative values of $Spectrum_{surplus}$ are set to zero. The beam and plasma interaction features can be seen at 10.0–10.3 µs. The surplus signal at later timescales indicates a long-term perturbation by the beam-plasma interaction. (b) Plasma density evolution in argon at $2.07 \times 10^{17}\,\mathrm{cm}^{-3}$ atomic gas density in the capillary as measured with OES from 8 µs to 14 µs at the temporal resolution of 100 ns, and rebinning (c) reduces it to 200 ns, thus reducing the noise in the data. The black bar at 10 µs marks the beam arrival time, corresponding to ionisation degree $\alpha = 0.04$. The measurements taken in the first 100 ns after beam arrival in the perturbed plasma may not satisfy the temperature conditions for the OES analysis, so the deduced plasma density value is ignored (dimmed colour). At later timings, the perturbed plasma density is higher than the unperturbed working point. (d) Plasma density residuals: relative plasma density change parameter R and absolute plasma density change parameter A. Both are consistent with zero before the beam arrival and positive after 10.7 µs until around 12.2 µs.

campaign could stem from the different electron beam setup. The peak of R occurs around 200 ns earlier in the case of the second campaign and it is also higher, although this discrepancy is within the temporal resolution of the measurement and the peak R values of both working points still agree within the uncertainties. This could suggest that a greater energy transfer occurred in the second campaign from

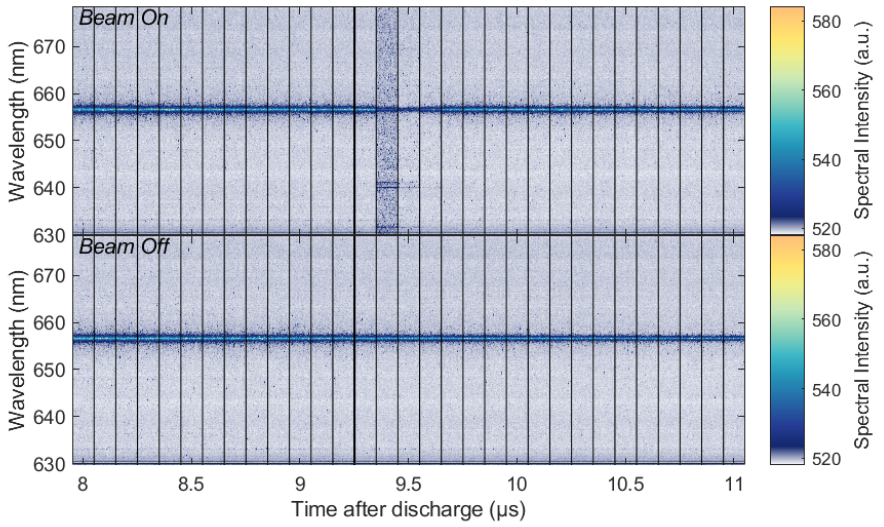

Figure 5.10: The spectrum evolution around the H-Alpha wavelength in argon at $2.07 \times 10^{17}\,\mathrm{cm}^{-3}$ atomic gas density in the capillary as recorded with the OES from 8 µs to 11 µs. Beam arrival is recorded at 9.32 µs, denoted here as a black bar at the beginning of the 9.3 µs shot interval. The H-Alpha line evolution in the top "Beam On" plot is perturbed by the beam arrival, which is manifested firstly in the dimming of the line, increasing background signal, and appearance of new lines at 640 nm and 630 nm around the arrival time of the beam. Then, there is more signal in the H-Alpha line at later timings than in data where no beam interacts with plasma, i.e., the bottom "Beam Off" plot.

the perturbed to plasma, resulting in faster ions and electrons, higher temperature of plasma, and thus increased ionisation rate and overall amount of reionised particles. The duration and the magnitude of the A plateau are the same for both working points $\alpha = 0.09$ from the two different campaigns, which suggests that the overall evolution of the additional ionisation is similar.

The almost 700 ns later onset for $\alpha = 0.07$ of the second campaign, could also suggest some LTI dependence on the atomic density of the gas and the plasma density, as in this case, both were smaller than for the $\alpha = 0.09$ working point. This is expected, as the overall density in the plasma is a factor in the collisional timescales eq. (2.2.11) and eq. (2.2.12), i.e., the timescale is inversely proportional to the overall density. For $\alpha = 0.07$, the peak R increased slightly and occurred 200 ns later than for $\alpha = 0.09$, so while the LTI effect is overall delayed, it is not diminished at this working point.

For the first campaign results, reducing the ionisation degree from $\alpha = 0.09$ to $\alpha = 0.04$ quintupled the achieved peak R value, which also peaked 600 ns earlier in the lower ionisation degree. The plateau observed in the A value almost tripled, but the duration differed by only 200 ns, i.e., a single timestep for the rebinned data. However, it is important to add that the duration of this plateau for the ionisation degree $\alpha = 0.04$ working point is extracted using the data measured below the

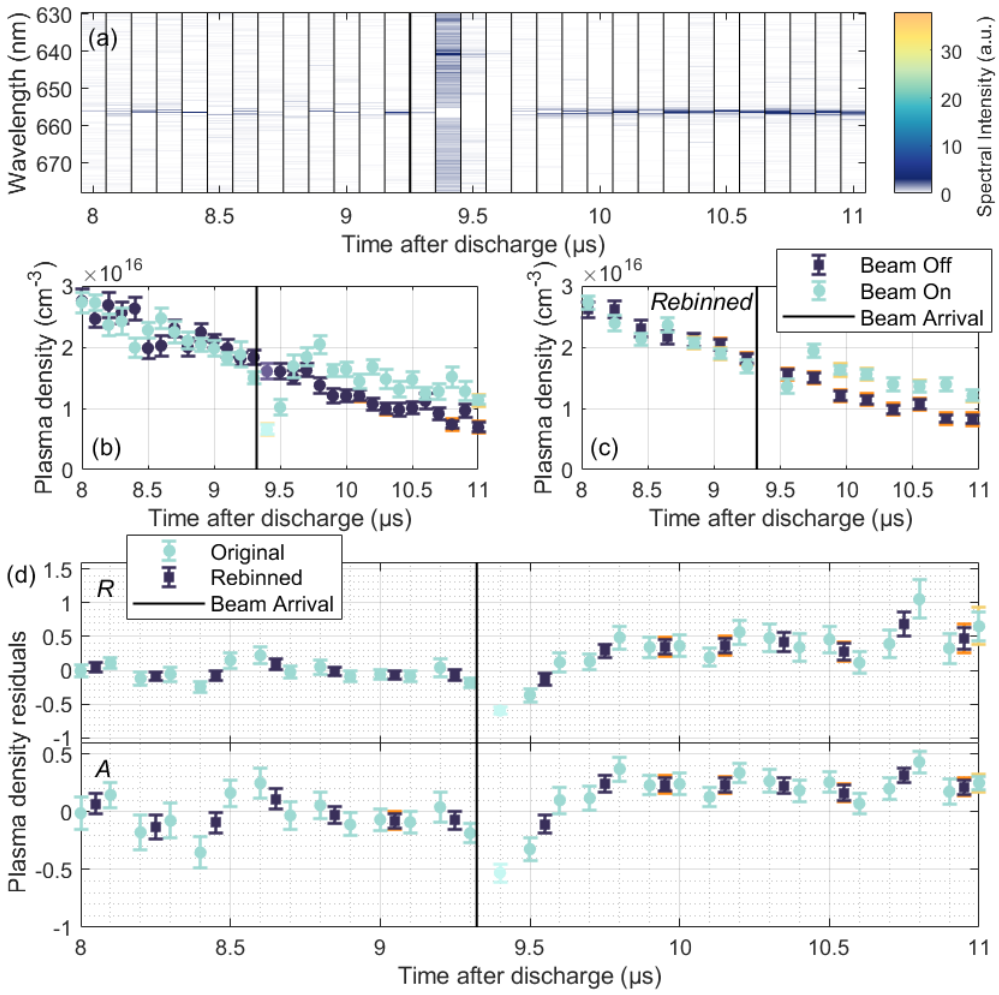

Figure 5.11: (a) The evolution of the surplus signal of the "Beam On" spectrum $Spectrum_{surplus} = Spectrum_{BeamOn} - SpectrumBeamOff$, where negative values of $Spectrum_{surplus}$ are set to zero. The beam and plasma interaction features can be seen at 9.4 µs. The surplus signal at later timescales indicates a long-term perturbation by the beam-plasma interaction. (b) Plasma density evolution in argon at 2.07×10^{17} cm^{-3} atomic gas density in the capillary, as measured with OES from 8 µs to 11 µs at the temporal resolution of 100 ns, and rebinning (c) decreases it to 200 ns, thus reducing the noise in the data. The black bar at 9.32 µs marks the beam arrival time, corresponding to ionisation degree $\alpha = 0.09$. The measurements taken in the first 100 ns after beam arrival in the perturbed plasma may not satisfy the temperature conditions for the OES analysis, so the deduced plasma density value is ignored (dimmed colour). At later timings, the perturbed plasma density is higher than the unperturbed working point. (d) Plasma density residuals: relative plasma density change parameter R and absolute plasma density change parameter A. Both are consistent with zero before the beam arrival and positive from 9.6 µs for the entirety of the scan.

resolution of the apparatus. As such, the LTI duration for $\alpha = 0.04$ may be longer. Data taken in the second campaign had A plateaus of similar magnitude, but the duration of the $\alpha = 0.07$ working point was half of the $\alpha = 0.09$ working point. Given that the LTI lifetime does not change for the same amount of neutrals but different ionisation degrees, the reduction of this lifetime for the $\alpha = 0.07$ working

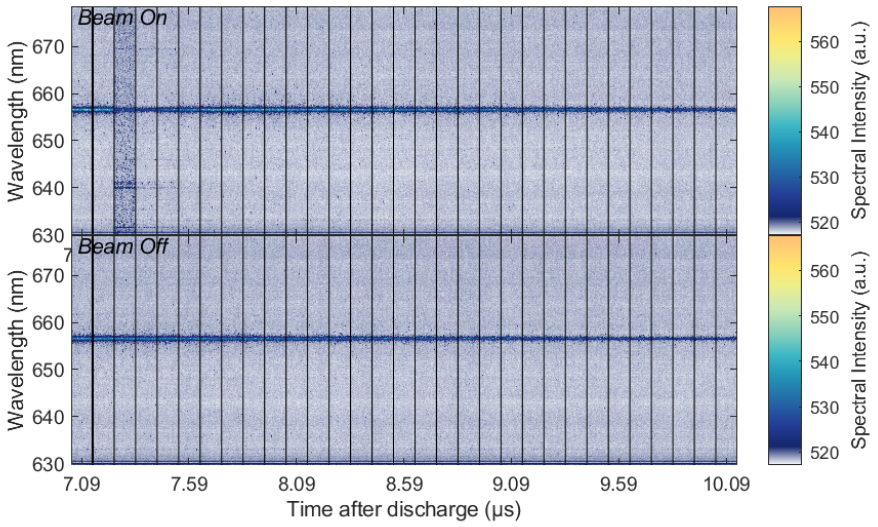

Figure 5.12: The spectrum evolution around the H-Alpha wavelength in argon at $1.51 \times 10^{17}\,\mathrm{cm}^{-3}$ atomic gas density in the capillary as recorded with the OES from 7.09 µs to 10.09 µs. Beam arrival is recorded at 7.2 µs, denoted here as a black bar at the beginning of the 7.19 µs shot interval. The H-Alpha line evolution in the top "Beam On" plot is perturbed by the beam arrival, which is manifested firstly in the dimming of the line, increasing background signal, and appearance of new lines at 640 nm and 630 nm around the arrival time of the beam. Then, there is more signal in the H-Alpha line at later timings than in data where no beam interacts with plasma, i.e., the bottom "Beam Off" plot.

point must stem from the different atomic gas density on-axis of the capillary. This may be a consequence of the timescale having an inverse dependency on the overall density.

5.4.2 Long-term ionisation dependency on neutral gas density and ionisation degree

This preliminary study reveals an obvious dependence of LTI on the neutral gas available to reionise, expressed via the ionisation degree for a given initial atomic gas density. For a lower ionisation degree and thus a higher amount of neutral particles, despite decreased charged particle density in the plasma, more long-term ionisation is observed, which stays approximately constant for the duration of LTI despite the overall plasma decay. As a consequence, when compared to decaying plasma, a generation of two-fold higher plasma density than without beam interaction can be observed for working points such as $\alpha = 0.04$, and also early in the LTI lifetime. On the other hand, the ionisation degree would not affect the onset timing and the lifetime of the LTI. These signatures seem to depend on the initial gas density, the reduction of which leads to delayed onset and decreased lifetime of LTI.

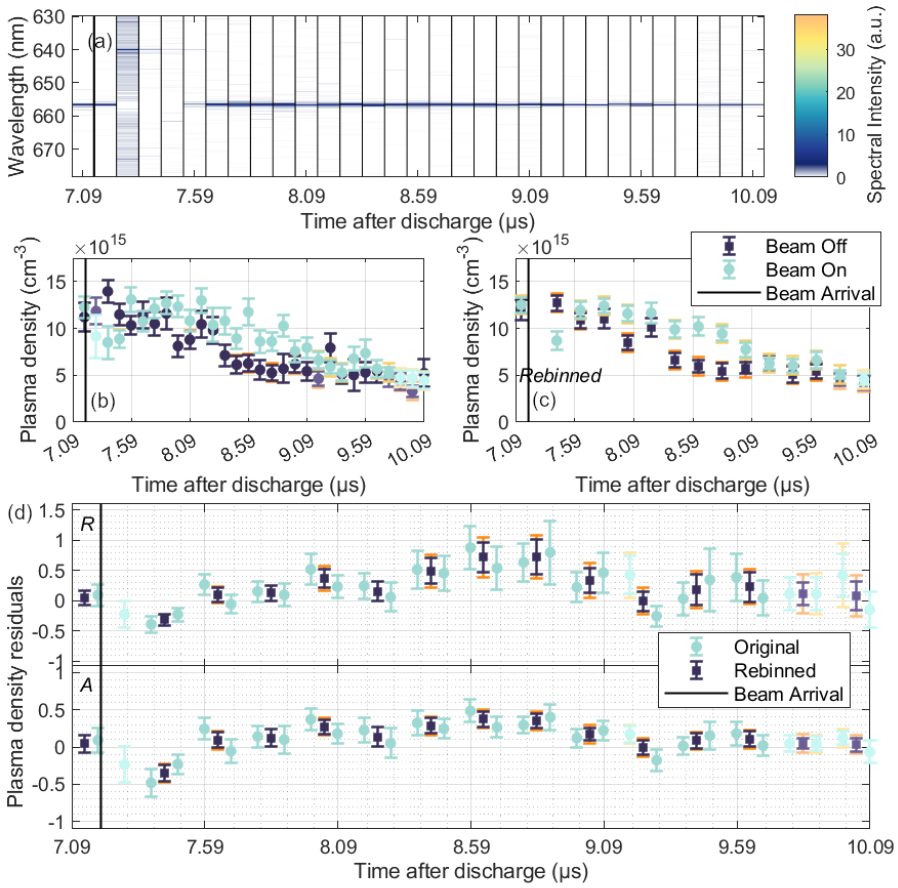

Figure 5.13: (a) The evolution of the surplus signal of the "Beam On" spectrum $Spectrum_{surplus} = Spectrum_{BeamOn} - SpectrumBeamOff$, where negative values of $Spectrum_{surplus}$ are set to zero. The beam and plasma interaction features can be seen at 7.29 µs. The surplus signal at later timescales indicates a long-term perturbation by the beam-plasma interaction; however, some signal can be seen at the one timestep recorded before beam arrival. (b) Plasma density evolution in argon at $1.51 \times 10^{17}\,\mathrm{cm}^{-3}$ atomic gas density in the capillary as measured with OES from 7.09 µs to 10.09 µs at the temporal resolution of 100 ns, and rebinning (c) reduces it to 200 ns, thus reducing the noise in the data. The black bar at 7.2 µs marks the beam arrival time, corresponding to ionisation degree $\alpha = 0.07$. The measurements taken in the first 100 ns after beam arrival in the perturbed plasma may not satisfy the temperature conditions for the OES analysis, so the deduced plasma density value is ignored (dimmed colour). At later timings, the perturbed plasma density is higher than the unperturbed working point. (d) Plasma density residuals: relative plasma density change parameter R and absolute plasma density change parameter A. Both are consistent with zero before the beam arrival and positive after 8.39 µs until around 9.19 µs.

5.5 Optical emission spectroscopy with hydrogen

The strong H-Alpha signal recorded in pure hydrogen and the lack of additional ionisation levels make hydrogen an attractive alternative species to investigate with OES. As in argon, the plasma density redistribution due to long-term ion motion and its recovery in hydrogen can be meaningfully investigated if the long-term ion-

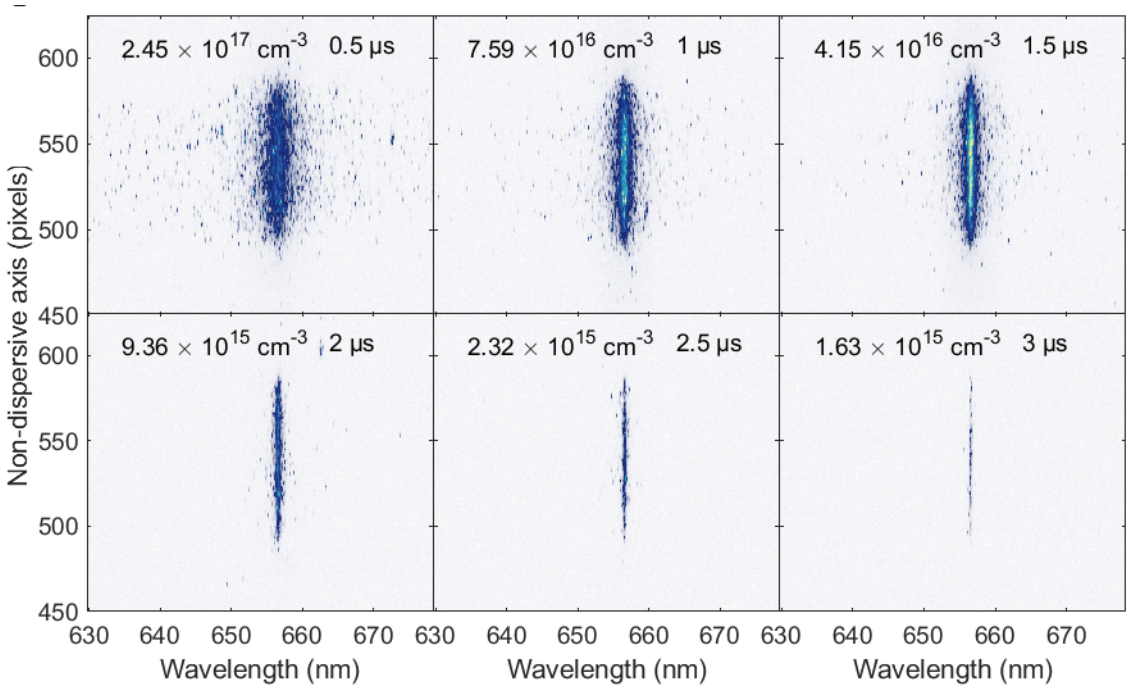

Figure 5.14: Optical Emission Spectroscopy (OES) images of hydrogen. The alpha linewidth decreases with the density and temperature of the plasma. Applying the Gigosos-Cardeñoso model for a given temperature, a density can be inferred from these images.

isation effect is suppressed. In addition, given the ionisation energy similarities of the hydrogen molecule, the hydrogen atom, and the argon atom, fundamentally, LTI should be similar for both gas species, see ionisation rates for a range of temperatures in fig. 2.7. Consequently, the key difference between argon and hydrogen is the ion mass, and the difference in their perturbed plasma evolution would be in the timescale, whether it is the evolution timescale and recovery duration of the plasma channel or the onset time and lifetime of the additional ionisation. To make the first observations of such temporal scaling, hydrogen was measured with OES, first in a working point with a high LTI signal, and then in a working point with suppressed LTI. The latter is then further investigated with the probe bunch diagnostic, presented in section 5.7.

OES measurements with hydrogen follow the same procedure as for argon, except for the fact that with 100% hydrogen in the capillary, not only is the H-Alpha signal much stronger but also there are no additional spectral lines in the field of view of the spectrometer system, see fig. 5.14. This eases analysis and allows for shorter temporal resolution of the measurement by not necessitating long gating times of the camera. This is necessary due to the much shorter timescales of hydrogen plasma evolution, as seen in fig. 3.20 (b) and (d).

On the other hand, such rapid hydrogen plasma evolution presents some challenges. The OES apparatus used at FLASHForward, as outlined in chapter 5.2.1,

cannot measure plasma density below $0.99 \times 10^{15}\,\mathrm{cm}^{-3}$, and the signal of around $5 \times 10^{15}\,\mathrm{cm}^{-3}$ is considered low. As such, OES is best as a diagnostic for plasma densities of $1 \times 10^{16}\,\mathrm{cm}^{-3}$ or higher. However, due to rapid hydrogen plasma decay rates, the OES-measurable hydrogen plasma exists only as long as the high-voltage discharge current is running regardless of the initial gas density in the capillary. The fast decay results in the density profile reflecting the current profile in terms of shape, necessitating the timesteps of the scan to be short to resolve this profile well, as described in section 3.2.3. This is especially accentuated at small capillary pressures, where plasma decays to low enough values before the arrival of the second current pulse of the high-voltage discharge, which reionises the plasma. Moreover, since the plasma decays very rapidly, different initial capillary gas density working points result in similar densities quite soon, around the time after the second current pulse, i.e., $\sim 1.5\,\mu\mathrm{s}$ after the discharge. This limits the choice of low ionisation degrees $\alpha \sim \mathcal{O}(10^{-1})$ in hydrogen plasma, as no increase in the gas pressure in the capillary can help achieve a plasma density for a given low ionisation degree which would produce a high H-Alpha signal on the OES. As a consequence, only relatively high ionisation degrees $\alpha \sim \mathcal{O}(1)$ of hydrogen plasma can be explored.

Finally, the arrival of the second current pulse at around $1.5\,\mu\mathrm{s}$ heats the plasma. The conditions of the plasma at that point may lead to different levels of heating, which interferes with the LTI signatures. In summary, the window in which hydrogen plasma has a low enough ionisation degree for LTI investigation, but high enough plasma density for OES measurements, is narrow from around $1\,\mu\mathrm{s}$ to $1.5\,\mu\mathrm{s}$, and the second current pulse at around $1.5\,\mu\mathrm{s}$ would also have to be avoided.

Despite these complications due to short timescales in hydrogen, the high H-Alpha signal allows for high-certainty measurements. Because of the high H-Alpha signal, the fitting error to the H-Alpha linewidth is small, around 1%. In addition, the measured OES density jitter of 12% is also lower than for argon. Since the bunch energy jitter in hydrogen at FLASHForward is of a few percent, the stability may not stem from the actual density being more stable in hydrogen. Other conditions, undetectable with the electron beam, such as temperature, are not expected to be any more stable in hydrogen than in argon. As a result, the OES measurement of 100% hydrogen plasma seems to be more stable by virtue of more H-Alpha line light counts collected by the spectrometer camera.

While the OES-measured density jitter and, thus, the estimated uncertainties are small, this does not result in small errors for R. Since the time window of where LTI can be investigated in hydrogen is small, the R value tends to have only a few reliable measurements with reasonable error sizes. Because of this, the yellow error bars and dimmed points, both of which signify low-density measurements and thus low estimated uncertainties (jitter tends to be low for low-density values), are

especially important for hydrogen analysis to help filter reliable measurements. On the other hand, because of the high H-Alpha signal, there is less jitter in the hydrogen density data, and therefore, binning is needed less.

5.6 Long-term ionisation in hydrogen measured with OES

Conditions for LTI are expected to not differ greatly for argon and hydrogen given the similarity of their ionisation rates (fig. 2.7). Consequently, similar working points could be explored in hydrogen as ones in argon to both observe LTI and witness its suppression. In argon, significant additional ionisation was observed for high neutral gas density of $\mathcal{O}(10^{17})\,\mathrm{cm}^{-3}$ and ionisation degrees $\alpha \sim \mathcal{O}(10^{-1})$ (or plasma densities of $\mathcal{O}(10^{16})\,\mathrm{cm}^{-3}$), and suppressed for $\alpha \sim \mathcal{O}(1)$ (or plasma densities of $\mathcal{O}(10^{17})\,\mathrm{cm}^{-3}$). When using argon, it is helpful to work with higher densities for argon since the 3% doped hydrogen H-Alpha results in a low signal-to-noise ratio when compared to pure hydrogen. For this reason, it is practical to explore LTI with OES using neutral gas densities of $\mathcal{O}(10^{17})\,\mathrm{cm}^{-3}$ in argon, as this allows to go to low enough ionisation degrees.

As discussed in section 5.5, hydrogen plasma ionisation degrees as low as $\alpha \sim \mathcal{O}(10^{-1})$ are not possible to record with the current OES setup. Because of this, the working points in hydrogen were chosen within a small range of relatively high ionisation degrees, i.e., $0.26 < \alpha < 0.28$, but a wide range of initial gas densities, i.e., $8 \times 10^{16} < n_a < 2 \times 10^{17} cm^{-3}$. The results are presented in table 5.6, and the data for ionisation degree $\alpha = 0.25 \pm 0.006$ and high neutral gas density is shown in fig. 5.15 and fig. 5.16, $\alpha = 0.26 \pm 0.009$ and lower neutral gas density in fig. 5.19 and fig. 5.20, and $\alpha = 0.28 \pm 0.006$ and lowest neutral gas density of the three in fig. 5.17 and fig. 5.18.

5.6.1 Difference in beam energy deposition in two campaigns

The first working point, ionisation degree $\alpha = 0.26$ was measured with an approximately two-fold higher atomic gas density than the other two working points. In addition, it was taken in a different campaign. While attempts were made to make the perturbing bunch parameters similar for both campaigns, the bunch-plasma interaction may have resulted in a stronger wakefield this time.

From preliminary investigations of the perturber bunch energy spectrum before and after plasma interaction, the bunch in the second campaign deposited approximately 7–12 mJ in 50 mm plasma capillary at a plasma density of $4.2 \times 10^{16}\,\mathrm{cm}^{-3}$, whereas the bunch from the first campaign deposited 4–9 mJ in 50 mm at a plasma

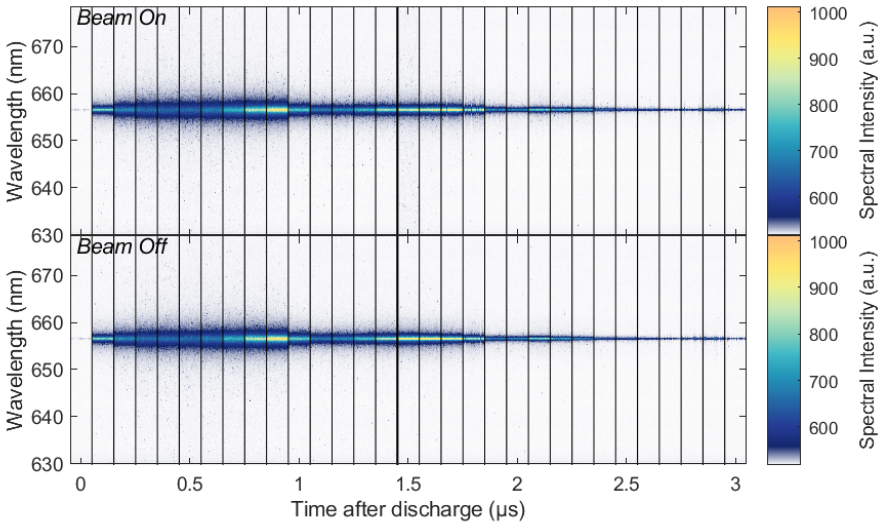

Figure 5.15: The spectrum evolution around the H-Alpha wavelength in hydrogen at $1.78 \times 10^{17}\,\mathrm{cm}^{-3}$ atomic gas density in the capillary, as recorded with the OES from 0 µs to 3 µs. Beam arrival is recorded at 1.46 µs, denoted here as a black bar at the beginning of the 1.5 µs shot interval. The H-Alpha line evolution in the top "Beam On" plot is perturbed by the beam arrival, which is manifested firstly in the very slight dimming of the line and increase of the background signal. These signatures are very faint for the pure hydrogen H-Alpha line due to its high signal-to-noise ratio. No new additional lines are observed in pure hydrogen at beam interaction timing. Later, there is more signal in the H-Alpha line at later timings than in data where no beam interacts with plasma, i.e., the bottom "Beam Off" plot. Both plots also reflect the hydrogen plasma evolution in a high-voltage discharge capillary, where the initial current pulse in the first microsecond discharges the gas to a high plasma density, and two other reflected current pulses sustain the hydrogen plasma for another 1.5 µs.

density of $2.5 \times 10^{16}\,\mathrm{cm}^{-3}$.

The large range in the estimation comes from the fact that the driving bunch in the plasma often loses charge, around 40% in the first campaign, and around 60% in the second. The charge is lost either at the initial energy of the bunch when the front of the bunch diverges before plasma wakefield forms and thus does not contain the charge with the focusing force, or after deceleration during the transport to the electron spectrometer. As a consequence, the uncertainty of energy deposited in plasma in the form of the wakefield is large. Nevertheless, this illustrates that the first campaign operated a bunch with a higher beam-plasma coupling, both due to high plasma density and potentially due to higher beam charge density and better beam size matching to the plasma fields, resulting in larger energy deposition. Together with higher initial gas density in the capillary, this working point should display more long-term ionisation than the other campaign.

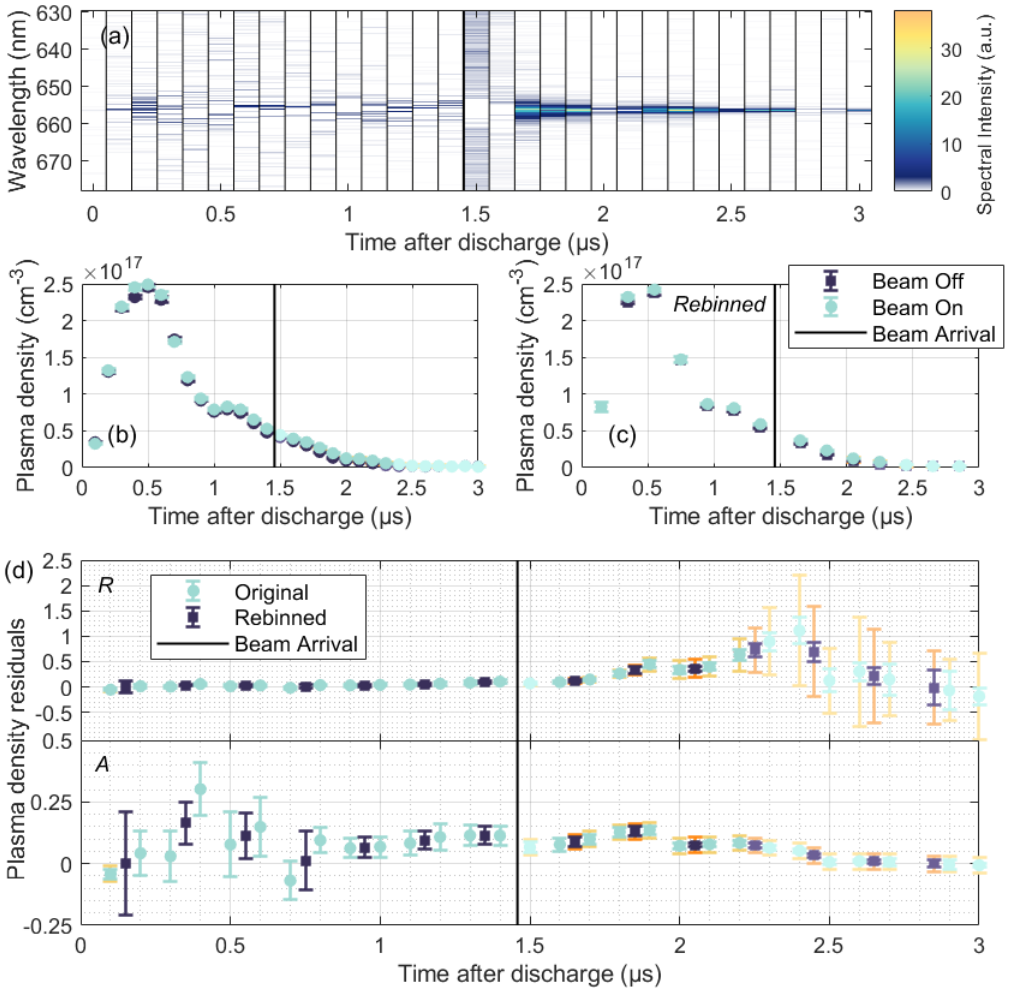

Figure 5.16: (a) The evolution of the surplus signal of the "Beam On" spectrum in hydrogen at $1.78 \times 10^{17}\,\mathrm{cm}^{-3}$ atomic gas density in the capillary, $Spectrum_{surplus} = Spectrum_{BeamOn} - SpectrumBeamOff$, where negative values of $Spectrum_{surplus}$ are set to zero. The beam and plasma interaction features can be seen at 1.5 µs. The surplus signal at later timescales indicates a long-term perturbation by the beam-plasma interaction. (b) Plasma density evolution in hydrogen at $1.78 \times 10^{17}\,\mathrm{cm}^{-3}$ atomic gas density in the capillary, as measured with OES from 0 µs to 3 µs at the temporal resolution of 100 ns, and rebinning (c) reduces it to 200 ns, thus reducing the noise in the data. The black bar at 1.46 µs marks the beam arrival time, corresponding to ionisation degree $\alpha = 0.25$. The measurements taken in the first 100 ns after beam arrival in the perturbed plasma may not satisfy the temperature conditions for the OES analysis, so the deduced plasma density value is ignored (dimmed colour). At later timings, the perturbed plasma density is higher than the unperturbed working point. (d) Plasma density residuals: relative plasma density change parameter R and absolute plasma density change parameter A. Both are consistent with zero before the beam arrival and positive after 1.6 µs until around 2.5 µs.

5.6.2 High initial gas density in hydrogen

Indeed, the result of this is a very obvious LTI signal in hydrogen, as observed on the OES. The surplus signal is clearly visible in fig. 5.16 (a), as well as the density,

Ionisation degree α	Atomic gas density n_0 cm^{-3}	Cmp.	LTI onset	Peak R	Time of peak R	Plateau of A	Length of plateau
0.25	1.78×10^{17}	2	342 ns	$(61 \pm 10(32))\%$, also $(104 \pm 26(108))\%$	742 ns, also 942 ns	$(13 \pm 2(3))\%$, or $(7 \pm 1(3))\%$	100 ns, or 200 ns
0.26	9.94×10^{16}	1	-	$(12 \pm 6(10))\%$, also $(27 \pm 15(41))\%$	117 ns, also 317 ns	$(7 \pm 3(6))\%$	0 ns
0.28	7.73×10^{16}	1	-	$(9 \pm 6(20))\%$	265 ns	$(3 \pm 2(6))\%$	0 ns

Table 5.6: LTI signatures in hydrogen expressed in key features of R and A evolution. All timings are given as a time from the interaction of the beam. The percentages in the brackets are the uncertainties represented by the yellow/orange error bars, defined by the resolution of the measurement. "Cmp." stands for "Campaign".

which is higher in the beam interaction case in 5.16 (b). The R value reaches a peak of $(61 \pm 10(32))\%$ in 742 ns from beam interaction, see fig. 5.16 (d), while there is also a higher signal, though unreliable due to low extracted density value and uncertainty, $(104 \pm 26(108))\%$ at 942 ns. The onset here is recorded at 342 ns, slightly earlier than for argon, signifying a faster LTI rate for hydrogen on the order of ~ 100 ns. Two plateaus of A can be identified in fig. 5.16 (d), a 100 ns long one at $(13 \pm 2(3))\%$, and a 200 ns long one after it, at $(7 \pm 1(3))\%$.

Comparing these hydrogen LTI results to argon, measured during the same data-taking campaign (the second argon campaign is the same as the first hydrogen campaign), it is interesting to note how, at similar atomic gas densities in the capillary (1.78×10^{17} cm^{-3} hydrogen, 2.07×10^{17} cm^{-3} argon), yet much higher ionisation degree in hydrogen ($\alpha_{H_2} = 0.24, \alpha_{Ar} = 0.09$), the LTI signals are similar within error bounds. To be more precise, a peak of $(61 \pm 10(32))\%$ was reached in hydrogen, and similarly, $(68 \pm 18)\%$ is the peak R value for argon. On the other hand, the difference appears in the timing of these peaks: 1380-1480 ns for argon and at almost half the delay from beam arrival time, i.e., at 742 ns, for hydrogen. While even higher and later peaks may be measured for hydrogen if the OES density measurement resolution allows for it, this suggests that the LTI timescale depends on the gas species, specifically via the ion mass.

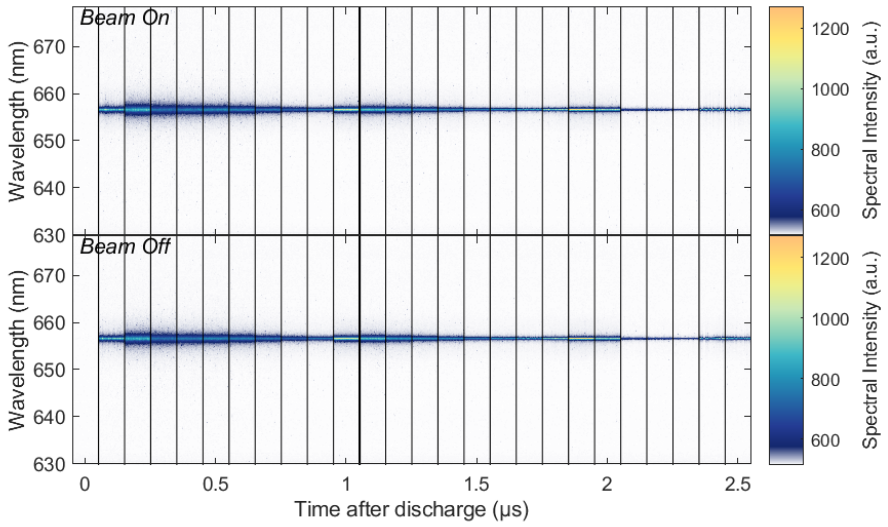

Figure 5.17: The spectrum evolution around the H-Alpha wavelength in hydrogen at $7.73 \times 10^{16}\,\mathrm{cm}^{-3}$ atomic gas density in the capillary as recorded with the OES from 0 µs to 2.5 µs. Beam arrival is recorded at 1.14 µs, denoted here as a black bar at the beginning of the 1.1 µs shot interval. The H-Alpha line evolution in the top "Beam On" plot is perturbed by the beam arrival, which is manifested firstly in the very slight increase of the background signal. The signature is very faint for the pure hydrogen H-Alpha line due to its high signal-to-noise ratio. No new additional lines are observed in pure hydrogen at beam interaction timing. Both plots also reflect the hydrogen plasma evolution in a high-voltage discharge capillary, where the initial current pulse in the first $900ns$ discharges the gas to a high plasma density, and two other reflected current pulses sustain the hydrogen plasma for another microsecond.

5.6.3 Low initial gas density in hydrogen

In order to suppress long-term ionisation in hydrogen, high ionisation degree working points were measured in the second hydrogen campaign, $\alpha = 0.28$ and $\alpha = 0.26$. Because of ion motion dependence on the plasma density, for comparison purposes, both working points were taken at a similar plasma density; therefore, to change the ionisation degree, the atomic gas density in the cell was adjusted, as shown in table 5.6. For the higher ionisation degree $\alpha = 0.28$, R predominantly stays consistent with zero, see fig. 5.18 (d). A value of $(9 \pm 6(20))\%$ is reached at 265 ns; however, the yellow error bars indicate that this uncertainty is likely too small, and thus, there is no significant signal. No obvious onset of LTI signal is observed, nor any A value plateau, unlike for argon LTI at low ionisation degrees, see fig. 5.18 (d). The lack of signal can be seen by directly comparing the two H-Alpha lines with and without beam interaction in fig. 5.17, and the surplus signal in fig. 5.18 (a). Furthermore, the density evolution appears to be the same, see fig. 5.18 (b).

The slightly lower ionisation degree $\alpha = 0.26$ results in a 2-sigma-significant R value of $(12 \pm 6(10))\%$ at 117 ns from beam interaction; however, here, the error is also unreliable, and the yellow bar does not suggest the same significance, see fig. 5.20 (d). Further differences in "Beam On" and "Off" measurements can be observed

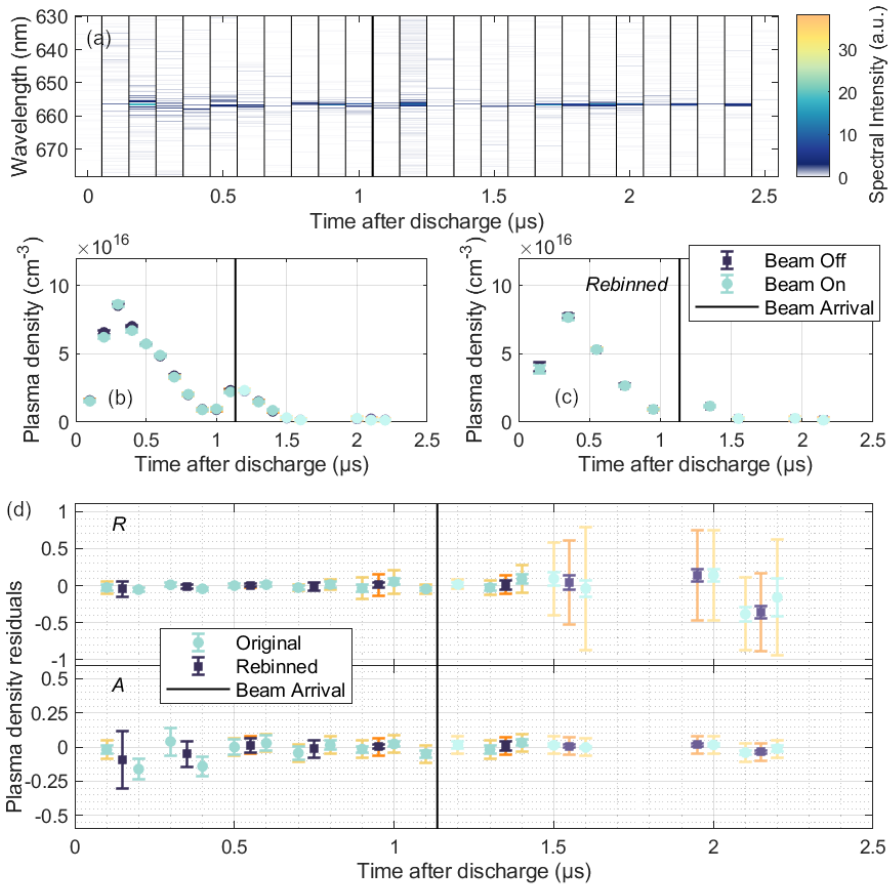

Figure 5.18: (a) The evolution of the surplus signal of the "Beam On" spectrum in hydrogen at $7.73 \times 10^{16}\,\mathrm{cm}^{-3}$ atomic gas density in the capillary, $Spectrum_{surplus} = Spectrum_{BeamOn} - SpectrumBeamOff$, where negative values of $Spectrum_{surplus}$ are set to zero. The beam and plasma interaction features can be seen at 1.2 µs. The lack of surplus signal at later timescales indicates that no long-term perturbation by the beam-plasma interaction is observed with the OES. (b) Plasma density evolution in hydrogen at $7.73 \times 10^{16}\,\mathrm{cm}^{-3}$ atomic gas density in the capillary, as measured with OES from 0 µs to 2.5 µs at the temporal resolution of 100 ns, and rebinning (c) reduces it to 200 ns, thus reducing the noise in the data. The black bar at 1.14 µs marks the beam arrival time, corresponding to ionisation degree $\alpha = 0.28$. The measurements taken in the first 100 ns after beam arrival in the perturbed plasma may not satisfy the temperature conditions for the OES analysis, so the deduced plasma density value is ignored (dimmed colour). At later timings, the perturbed plasma density is the same as the unperturbed working point. (d) Plasma density residuals: relative plasma density change parameter R and absolute plasma density change parameter A. Both are consistent with zero for the entirety of the scan.

with the R value, such as $(27 \pm 15(41))\%$ at 317 ns, but here the signal is also too low to deem the result reliable. Some surplus signals right after beam arrival can be seen in fig. 5.20 (a), but it does not translate to a significant density increase in fig. 5.20 (b). Although the ionisation degree was slightly decreased and the atomic gas density slightly increased, this is not sufficient to result in a significant LTI signal as measured with OES.

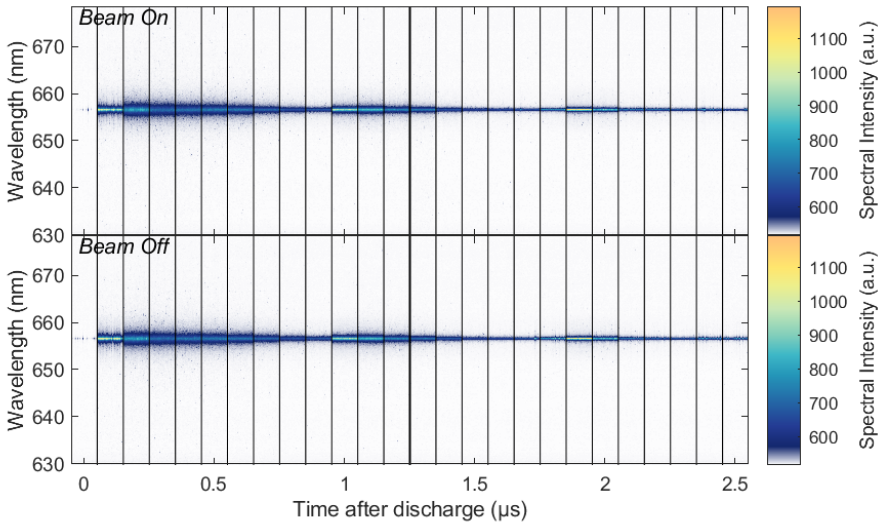

Figure 5.19: The spectrum evolution around the H-Alpha wavelength in hydrogen at $9.94 \times 10^{16}\,\mathrm{cm}^{-3}$ atomic gas density in the capillary as recorded with the OES from 0 µs to 2.5 µs. Beam arrival is recorded at 1.28 µs, denoted here as a black bar at the beginning of the 1.3 µs shot interval. The H-Alpha line evolution in the top "Beam On" plot is perturbed by the beam arrival, which is manifested firstly in the very slight increase of the background signal. The signature is very faint for the pure hydrogen H-Alpha line due to its high signal-to-noise ratio. No new additional lines are observed in pure hydrogen at beam interaction timing. Both plots also reflect the hydrogen plasma evolution in a high-voltage discharge capillary, where the initial current pulse in the first $900ns$ discharges the gas to a high plasma density, and two other reflected current pulses sustain the hydrogen plasma for another microsecond.

While the current data for OES hydrogen LTI proves to be limited, it serves as a helpful first insight into the long-term ion motion dynamics occurring in hydrogen, especially when compared to argon. Similarly to argon, no LTI signature can be observed with OES for high ionisation degrees; however, increasing the atomic gas density in the capillary resulted in the additional ionisation, albeit different beam parameters and higher plasma density may have had an effect as well through higher beam energy deposition. The timescales of LTI in hydrogen seem to be shorter: shorter onset timing is observed than for argon, the similar R peak value is reached faster, and the plateau of A is shorter by a few factors for similar initial neutral gas densities. On the other hand, the measurement window would have to be extended to confirm this, mainly by operating at higher pressures and higher plasma densities to suit the resolution limits of OES.

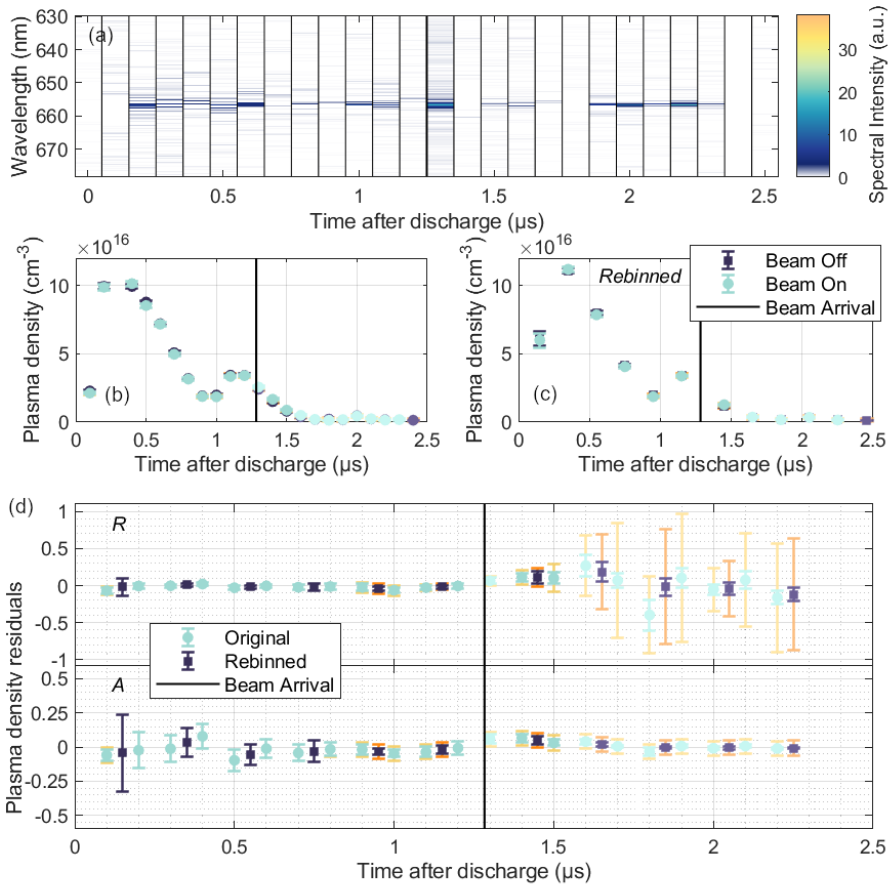

Figure 5.20: (a) The evolution of the surplus signal of the "Beam On" spectrum in hydrogen at $9.94 \times 10^{16}\,\mathrm{cm}^{-3}$ atomic gas density in the capillary, $Spectrum_{surplus} = Spectrum_{BeamOn} - SpectrumBeamOff$, where negative values of $Spectrum_{surplus}$ are set to zero. The beam and plasma interaction features can be seen at 1.3 µs. The lack of surplus signal at later timescales indicates that no long-term perturbation by the beam-plasma interaction is observed with the OES. (b) Plasma density evolution in hydrogen at $9.94 \times 10^{16}\,\mathrm{cm}^{-3}$ atomic gas density in the capillary, as measured with OES from 0 µs to 2.5 µs at the temporal resolution of 100 ns, and rebinning (c) reduces it to 200 ns, thus reducing the noise in the data. The black bar at 1.28 µs marks the beam arrival time, corresponding to ionisation degree $\alpha = 0.26$. The measurements taken in the first 100 ns after beam arrival in the perturbed plasma may not satisfy the temperature conditions for the OES analysis, so the deduced plasma density value is ignored (dimmed colour). At later timings, the perturbed plasma density is the same as the unperturbed working point. (d) Plasma density residuals: relative plasma density change parameter R and absolute plasma density change parameter A. Both are consistent with zero before the beam arrival and positive within 1-sigma at 1.4 µs if considering the resolution-defined yellow error bar. The rest of the data is either consistent with zero, or the signal is too low.

5.7 Probe bunch measurements of long-term ionisation in hydrogen

Hydrogen plasma recovery is expected to be similar to argon: there will be long-term ionisation under certain conditions, and removing those will allow the observation

of the plasma channel evolution and recovery without the additional ionisation. The discrepancy between the two species should emerge in the timescale of the recovery process as a consequence of different ion mass, but for that to be concluded, all other experimental parameters, which affect the ion motion timescale and signatures, such as plasma density (section 4.6) and atomic gas density (due to LTI), should be the same. Because of this, hydrogen was investigated with the probe bunch diagnostic, while the plasma density and ionisation degree were set to closely match the settings in ref. [122].

As shown already, $n_p = 2.79 \times 10^{16}\,\mathrm{cm}^{-3}$ and ionisation degree $\alpha = 0.28$ did not result in an LTI signal on OES, and neither did $\alpha = 0.26$ at low capillary pressure. Since the probe bunch diagnostic is much more sensitive to density changes (very low ones can be measured with the electron bunch, like in ref. [121]), and the temporal resolution of the diagnostic can be as low as 0.77 ns, a very small LTI signal may be measured which may be not observable with OES. Moreover, the probe bunch samples plasma at the axis, where the perturbing bunch interacted with the plasma previously, so larger effects may be perceived as opposed to the OES, which collects plasma light signal integrated radially. However, it may be harder to trust in the context of additional ionisation occurring, i.e., LTI may mask density redistribution effects, or vice versa, which are observed in the energy gain changes of the probe trailing bunch. While the LTI signatures may also be separated by comparing the probe bunch and OES measurements, the OES proved to have high constraints in terms of density and temporal resolution, as well as a lack of sensitivity to density changes on-axis given the radial integration of light by the apparatus. Nevertheless, the probe bunch cannot be used to measure the exact plasma density directly unless an extensive campaign of simulations is carried out like in ref. [121], therefore OES is still a crucial technique to understand LTI.

5.7.1 Processing data of the probe bunch in hydrogen

Probe bunch data taken with hydrogen plasma, spectra of which are shown in fig. 5.30 for $\alpha = 0.28$ and fig. 5.31 for $\alpha = 0.26$, is processed the same way as for argon, as described in section 4.2.2. However, a few unique aspects of this data required some divergence from the normal analysis procedure. Firstly, during the ion motion scans in hydrogen, there were shots with a low-charge probe trailing bunch. In general, the charge in the lower pressure dataset ranged from 0.2 to ~ 63.2 pC, with an average of 40.7 pC $\pm$ 12.7 pC (STD) (similar values for higher pressure dataset); some of this variance can be attributed to the general jitter of outcoming charge, other part - to the ion motion evolution in the plasma. For the former, the source is the unstable incoming charge, usually a consequence of changing probe bunch profile due to energy and orbit jitter at the scraper in the dispersive beamline; for

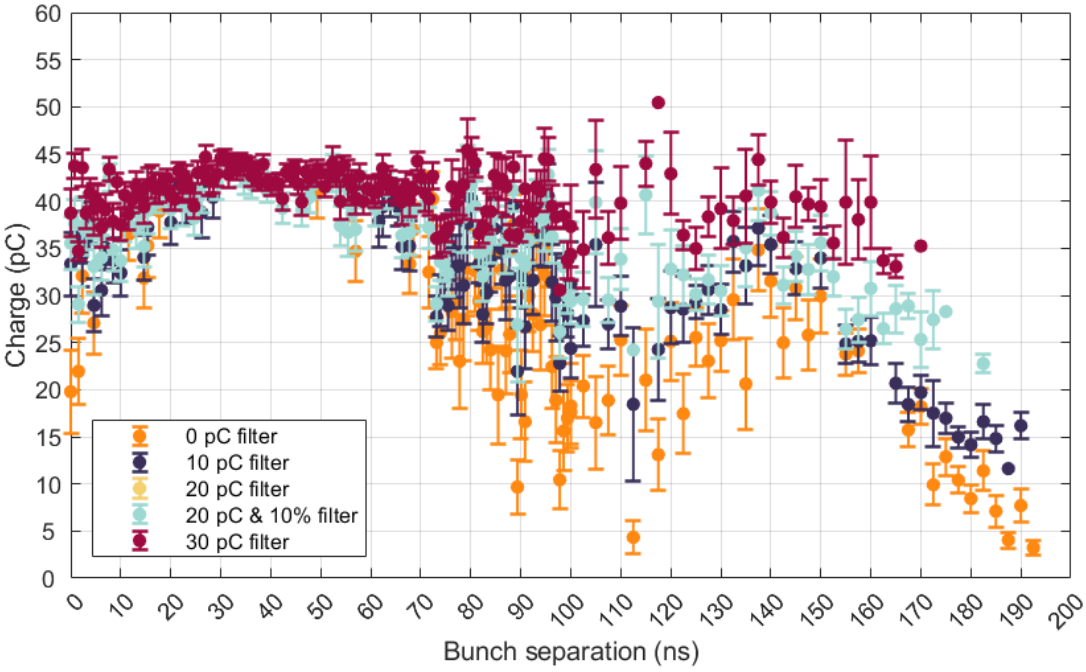

Figure 5.21: Unperturbed probe trailing bunch charge with different charge filtering and outlier removal.

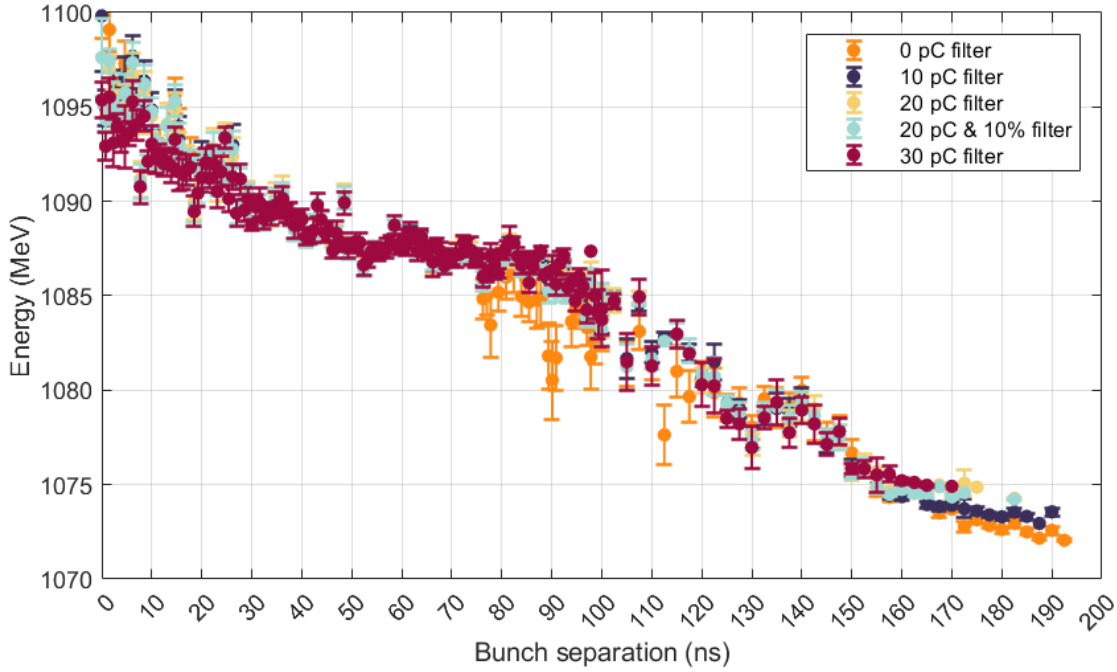

Figure 5.22: Unperturbed probe trailing bunch energy with different charge filtering and outlier removal.

this data, the toroid before the scraper measures a charge jitter of 0.7%, while after the scraper another downstream toroid indicated 2.7% charge jitter for the whole bunch.

A more important factor is also the plasma density jitter, where the changing trailing bunch matching conditions and transverse wakefield forces, in general, can result in more or less severe betatron oscillations and outcoming divergence of the

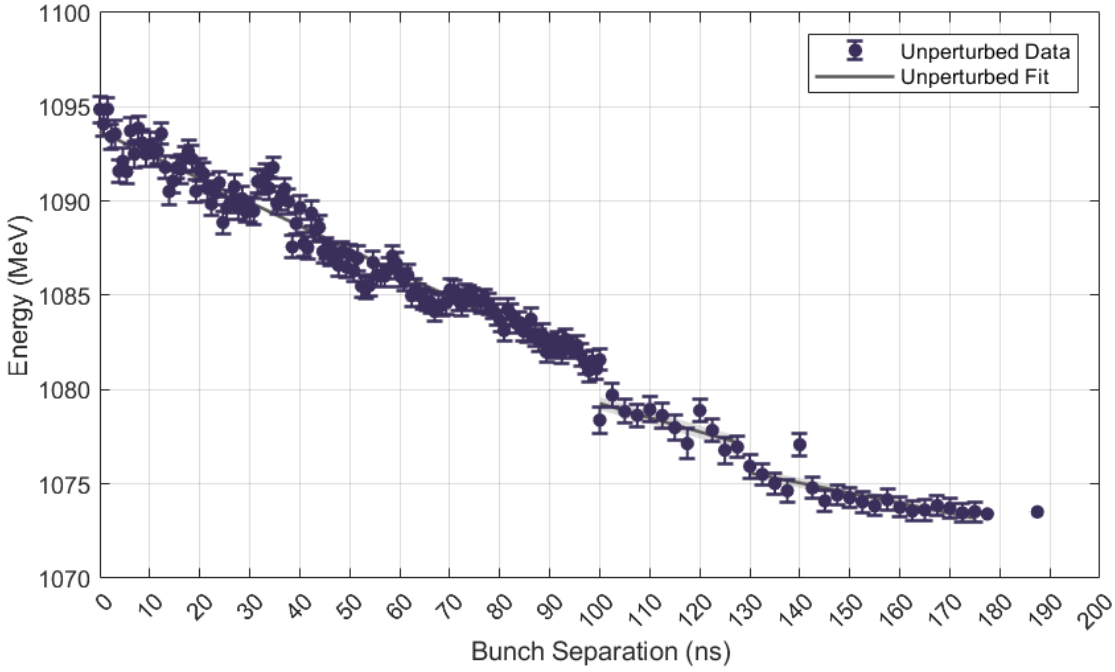

Figure 5.23: Unperturbed probe trailing bunch mean energy evolution up to 180 ns in hydrogen at ionisation degree $\alpha = 0.28$. The data was fit in three intervals: 0 to 100 ns, 100 to 130 ns, 130 to 180 ns.

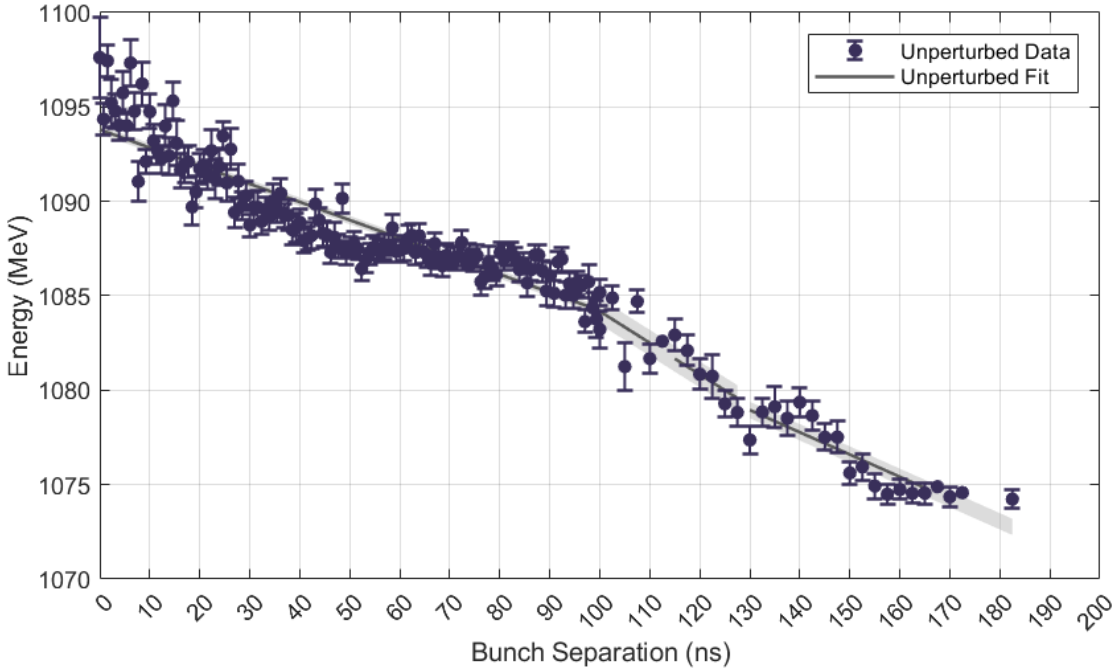

Figure 5.24: Unperturbed probe trailing bunch mean energy evolution up to 180 ns in hydrogen at ionisation degree $\alpha = 0.26$. The data was fit in three intervals: 0 to 100 ns, 100 to 130 ns, 130 to 180 ns.

bunch. This would lead to trailing bunch charge loss in the plasma or in the downstream beamline (respectively). Here, the surviving bunch part reaching the screen jittered 1.4% in size and 4.8% in charge on average for the lower pressure dataset and twice these values for the higher pressure dataset. Similarly, changing plasma density due to ion motion or plasma decay in a long scan could result in a loss of

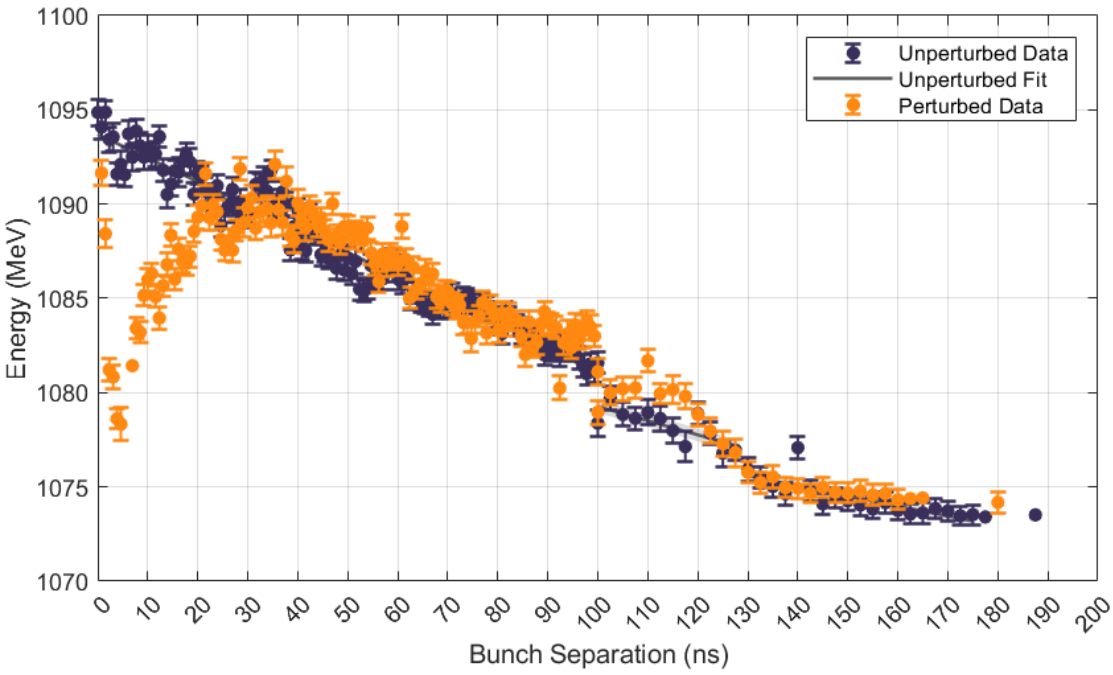

Figure 5.25: Mean energy evolution of the unperturbed and perturbed probe trailing bunches in hydrogen at ionisation degree $\alpha = 0.28$.

charge. However, this would manifest in the correlation with other perturbation features or as a trend towards later timescales in the scan rather than as a single-timestep jitter. After 100 ns, when the on-axis plasma density is decreasing (evident in the probe trailing bunch energy reduction), energy and charge correlate with a coefficient of 70%. Nevertheless, a reasonable high-charge filter may help remove the shots contributing to this data jitter. In this case, applying a 20 pC charge filter for the high-pressure dataset halves the charge jitter and reduces energy jitter from 2.7% to 2.1% for unperturbed data and from 2.1% to 1.9% for perturbed. Applying 30 pC does not result in such an improvement further and even increases the energy jitter. In addition, energy jitter can be improved by removing energy outliers in the 10th and 90th percentiles, reducing energy jitter from 2.1% and 1.9% for unperturbed and perturbed data, respectively, to 1.8% and 1.6%.

The effects of the charge filter and outlier removal are detailed in fig. 5.21 and fig. 5.22. As can be expected, the charge averages rise as the lower charge is cut, and the charge dipping at around 90 ns is ignored with stricter filters. For mean energies, this removes the high-jitter data at those timings; otherwise, these filters' effects do not appear significant. As expressed earlier, it helps reduce the jitter in energy and charge for each dataset step.

Another difference from the argon analysis is that the measurement campaign focused only on the probe trailing bunch energy as the best diagnostic for on-axis density changes. As such, only data where the trailing bunch energy was imaged with the diagnostic quadrupoles was taken. The trailing bunch shots were filtered

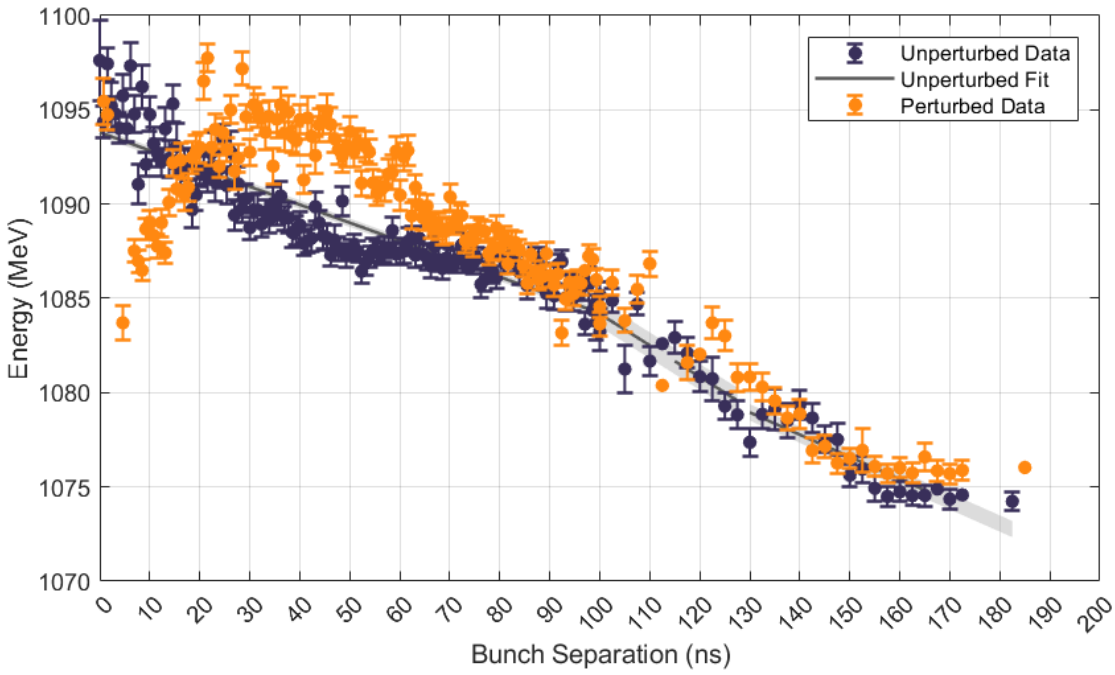

Figure 5.26: Mean energy evolution of the unperturbed and perturbed probe trailing bunches in hydrogen at ionisation degree $\alpha = 0.26$.

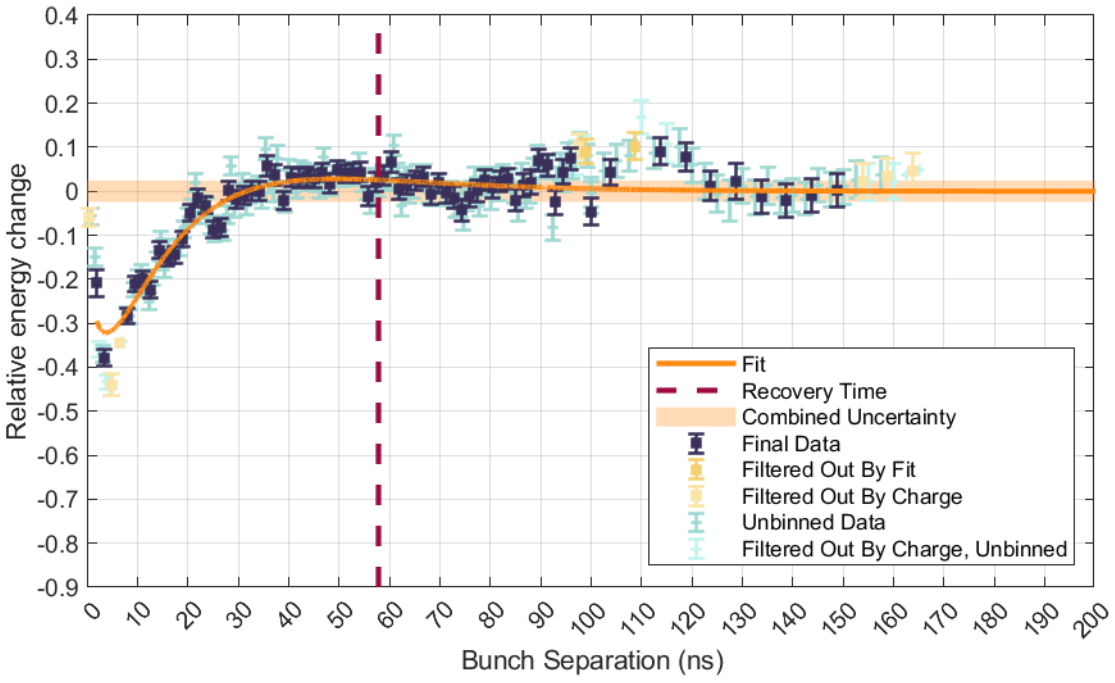

Figure 5.27: Probe trailing bunch relative energy change in hydrogen at ionisation degree $\alpha = 0.28$. Blue and light blue points correspond to the raw data, which is re-binned to get the navy points, fitted (orange line). Both sets of data are filtered by charge, i.e., light yellow points and light blue points correspond to the steps where over half of the shots were removed due to the charge filter. Yellow points are the outliers selected using the first fit attempt. The goodness-of-fit was $\chi^2 = 130$ for 69 degrees of freedom. The orange band around zero corresponds to the combined mean uncertainty of the measurement and the uncertainty of the fit. This band is then used to estimate the earliest recovery time, indicated by the dashed line.

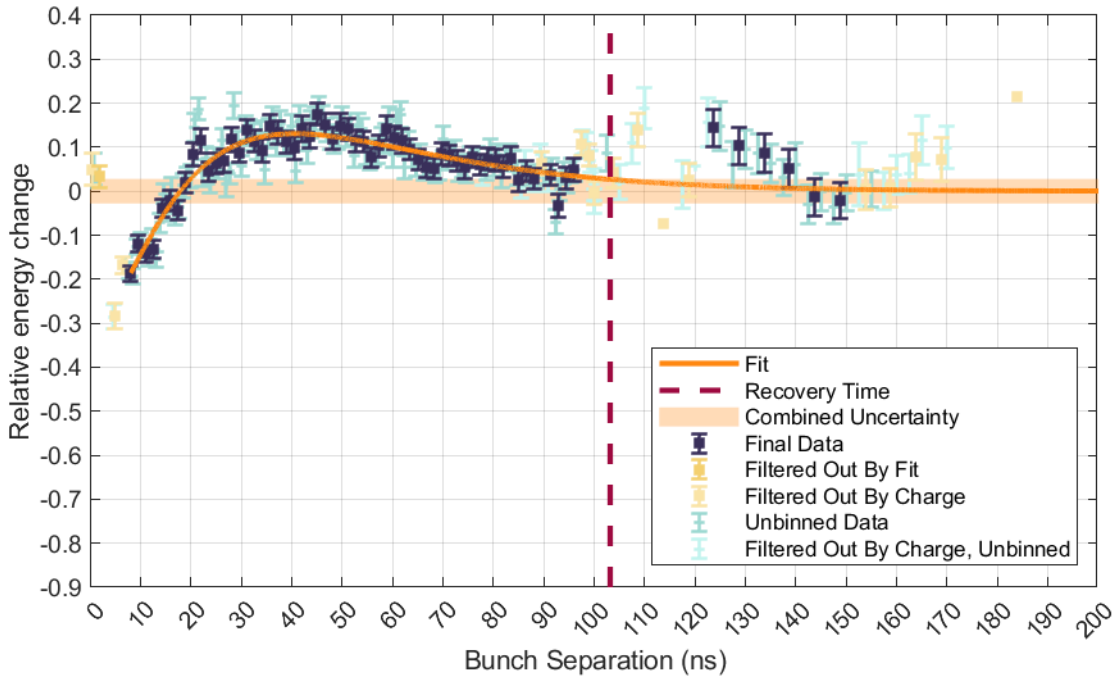

Figure 5.28: Probe trailing bunch relative energy change in hydrogen at ionisation degree $\alpha = 0.26$. Blue and light blue points correspond to the raw data, which is re-binned to get the navy points, fitted (orange line). Both sets of data are filtered by charge, i.e., light yellow points and light blue points correspond to the steps where over half of the shots were removed due to the charge filter. Yellow points are the outliers selected using the first fit attempt. The goodness-of-fit was $\chi^2 = 79$ for 61 degrees of freedom. The orange band around zero corresponds to the combined mean uncertainty of the measurement and the uncertainty of the fit. This band is then used to estimate the earliest recovery time, indicated by the dashed line.

by charge and energy as already described, and the mean was calculated for each timestep. The uncertainties were estimated by combining the standard error of the mean and the resolution of the ESPEC screen. The resolution of the screen is known to be 50 µm, which at different positions of the screen scales to a different energy resolution in MeV, denoted as σ_R. By using the energy calibration to calculate this energy resolution, $\sigma_{\bar{E}} = \sqrt{(\frac{std(E))}{\sqrt{N-1}})^2 + \sigma_R^2}$ is used as the uncertainty of the measured mean energy for each timestep. Despite the filtering and such uncertainty estimation, the unperturbed probe trailing bunch, which should normally decrease linearly with time due to the microsecond-timescale plasma decay, appears to fluctuate and show signs of drift, see fig. 5.23 and fig. 5.24. This is expected as the FLASH active-feedback system, which prevents such drifts, was turned off, as explained in section 3.1.1. In order to remove the fluctuations, a straight line is fit to the data, and for the lines to reflect the data well, three different intervals of consistent machine settings are chosen by examining how well the line fits those intervals with the χ^2 statistic. A low value of χ^2 should suggest an interval which has not suffered a drift in the machine setting in its duration, and therefore, this interval is chosen, see fig. 5.23 and fig. 5.24.

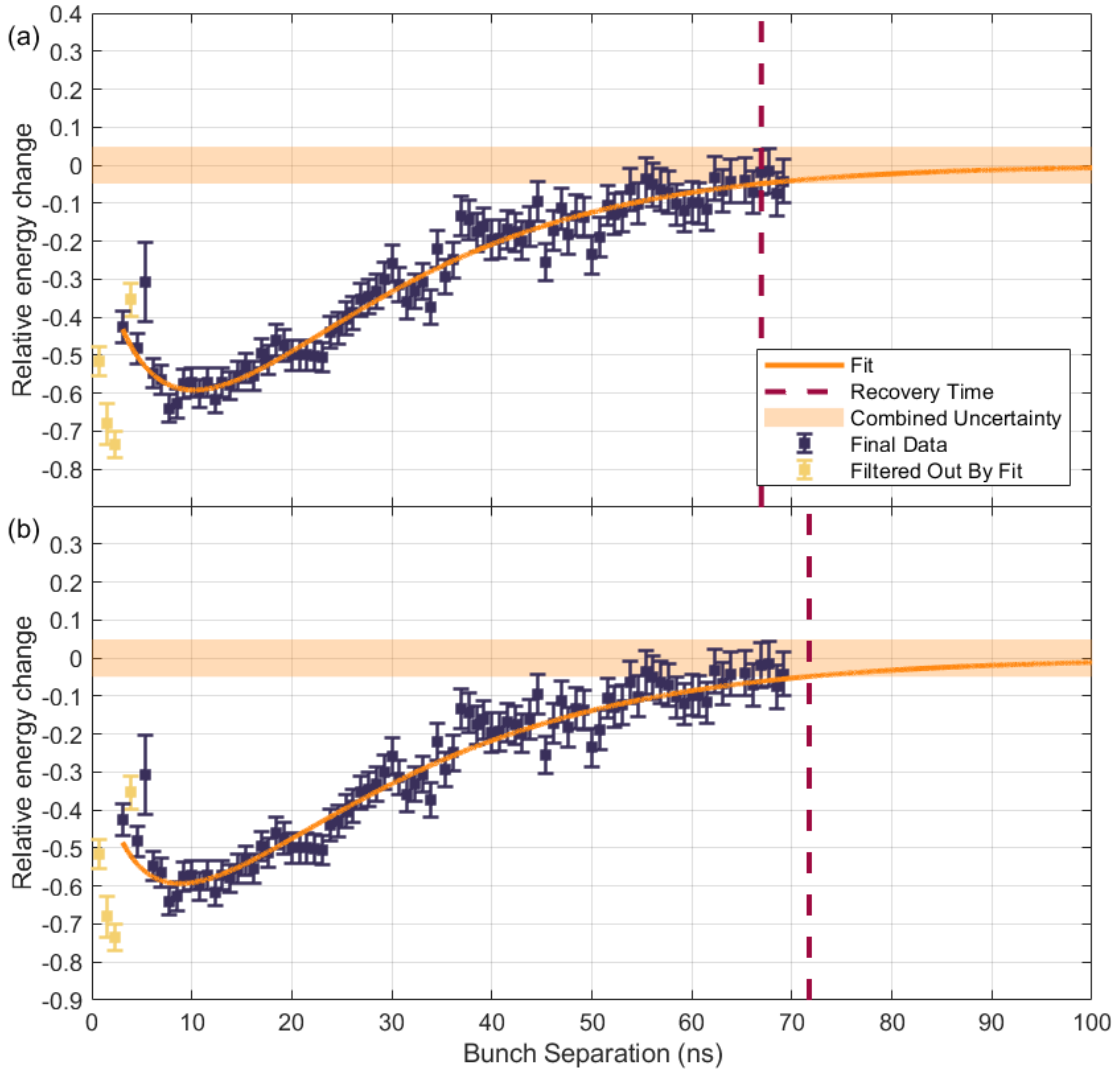

Figure 5.29: Probe trailing bunch relative energy change in argon at ionisation degree $\alpha = 0.42$. The data is fitted (orange line) with function (a) which is adapted $R(t) = -A\sqrt{t}e^{-Bt} + Cte^{-Bt}$ and (b) $R(t) = -A\sqrt{t}e^{-Bt}$ like in ref. [121]. Yellow points are the outliers selected using the first fit attempt. The goodness-of-fit was (a) $\chi^2 = 61$ and (b) $\chi^2 = 69$ for 86 and 87 degrees of freedom, respectively. The orange band around zero corresponds to the combined mean uncertainty of the measurement and the uncertainty of the fit. This band is then used to estimate the earliest recovery time, indicated by the dashed line.

5.7.2 Energy residuals fit function for long-term ionisation

In order to describe this positive probe trailing bunch energy residuals signature, associated with a higher on-axis plasma density, additional summand is added to the fitting function, $R(t) = -A\sqrt{t}e^{-Bt} + Cte^{-Bt}$. The function $g(t) = te^{-Bt}$ evolves similarly to $f(t) = \sqrt{t}e^{-Bt}$, i.e., it is zero at $t = 0\,\text{ns}$, and it has a peak, after which it decays exponentially. The difference between the two functions is the location of the peak; for $g(t) = te^{-Bt}$, the peak occurs for slightly higher t values than for

$f(t) = \sqrt{t}e^{-Bt}$. This can be seen by comparing the derivatives:

$$\frac{df}{dt} = \sqrt{t}e^{-Bt}(\frac{1}{2t} - B), t_{max} = \frac{1}{2B} \tag{5.7.1}$$

$$\frac{dg}{dt} = te^{-Bt}(\frac{1}{t} - B), t_{max} = \frac{1}{B}. \tag{5.7.2}$$

Adding the function $g(t)$, however, shifts the locations of these extrema. Nevertheless, the form of the function allows one to describe an opposite-sign, later-occurring peak in these energy residuals, which would be interpreted as higher on-axis plasma density. The timescale of the decay B would then be the same for both processes, i.e., for the ion motion channel evolution described by $f(t)$ and the long-term ionisation described by $g(t)$. While this is not strictly known, it can be assumed to be close to reality since both formations (plasma channel or additional plasma density) would decay under similar conditions, establishing the timescale.

The comparison of the two working points, i.e., with and without the perturbing bunch before, is carried out in the same manner as for argon, using the residuals formula eq. (4.3.6). Two filters are applied to the energy residuals: charge and fit. The former excludes the steps where half or more shots were removed due to low charge, i.e., being lower than 20 pC. The fit filter follows the same procedure as in ref. [121] and in section 4.5. First, the energy residuals are fitted with a function; then, the data that is further from the fitted function than three times the combined error of the fit and the data is removed. As a result, the data that does not pass the charge filter is marked light yellow, and the points not satisfying the fit filter condition are yellow. Then, the filtered data is fitted again with the same function, and new, more accurate parameters are acquired with improved χ^2 statistic. The results are presented in fig. 5.27 for $\alpha = 0.28$ and fig. 5.28 for $\alpha = 0.26$ and extracted parameters are summarised in table 5.8. In addition, ion motion recovery data in argon with the original and adjusted fitting function is included in fig. 5.29 and table 5.8.

5.7.3 Extracted features of the perturbed hydrogen plasma evolution

Unlike the argon data, which was fit with $R(t) = -A\sqrt{t}e^{-Bt}$, hydrogen energy residuals seem to cross the zero axis and signify a higher on-axis density in the perturbed case with positive residuals. This is obvious for the ionisation degree $\alpha = 0.26$ data in the interval between 20 ns and 100 ns, and again at 125 ns. However, for ionisation degree $\alpha = 0.28$, the positive energy residuals, which occur at around 50 ns and 115 ns, are much smaller. In fig. 5.25, 5.26, it can be seen how this is truly a consequence of the perturbed trailing bunch energy being higher

Working Point	A	C	B (ns^{-1})	1/B (ns)	$\tau_{rec.,5/B}$ (ns)	$\tau_{rec.,R\approx0}$ (ns)
Argon $\alpha = 0.42$, $R(t) = -A\sqrt{t}e^{-Bt}$	0.329 ± 0.007	-	0.057 ± 0.001	17.7 ± 0.3	88.5 ± 1.5	72
Argon $\alpha = 0.42$, new function	0.217 ± 0.036	-0.050 ± 0.015	0.070 ± 0.003	14.3 ± 0.6	71.5 ± 3.0	67
Hydrogen $\alpha = 0.28$	0.318 ± 0.021	0.057 ± 0.005	0.061 ± 0.004	16.4 ± 1.1	82.0 ± 5.5	58
Hydrogen $\alpha = 0.26$	0.296 ± 0.023	0.070 ± 0.006	0.049 ± 0.002	20.4 ± 0.8	102.0 ± 4.0	103

Table 5.8: Parameters of the function fitted to the probe trailing bunch residuals and estimated long-term ion motion recovery (rec.) time for each probe-bunch-examined gas species and ionisation degree. The recovery time is estimated in two ways: $\tau_{rec.,5/B}$ is the inverse of the fitted B parameter times a factor of five, and $\tau_{rec.,R\approx0}$ is the time at which the fitted function R is zero within the experimental resolution.

than the normally-evolving unperturbed. The dip in perturbed energy at around 75 ns and 87 ns, also coincides with a dip in the charge in fig. 5.21, which seems to break the trend of the slightly positive residuals lasting from around 50 ns to 120 ns. As these points do not correspond to particularly low charges, it is unclear whether they can be simply ignored. The fluctuations of the perturbed trailing bunch energy around the straight line fit to the unperturbed trailing bunch energy data from 75 ns onwards in fig. 5.25 result in the fluctuations of trailing bunch energy residuals around the zero axis from 75 ns onwards in fig. 5.27. They may be a consequence of either a drift in the machine settings when taking the perturbed data or a real plasma density evolution effect.

Furthermore, a recovery time can be estimated using this function, whether it is $R(t) = -A\sqrt{t}e^{-Bt}$ or $R(t) = -A\sqrt{t}e^{-Bt} + Cte^{-Bt}$. Given the exponential decay, the function does not ever reach zero for long timings, therefore experimental resolution has to be introduced to establish a condition for the function being consistent with zero. For this, the error of the fit and the mean of the measurement uncertainties are used: if the function is closer to the zero axis than the combination of the two errors, the timing at which this occurs can be defined as a recovery time, denoted by $\tau_{rec.,R\approx0}$ in table 5.8 and as a dashed vertical bar in all fitted energy residuals figures. Alternatively, the recovery time can be defined as the inverse of the fitted B parameter times a factor of five, denoted by $\tau_{rec.,5/B}$ in table 5.8. The two estimations

are presented for each working point in table 5.8.

By using the new function to fit argon probe trailing bunch energy residuals, a slightly shorter timescale of ion motion evolution (17.7 ns vs 14.3 ns) is estimated. The LTI-indicating parameter C for argon turns out to be -0.050 ± 0.015, and given that no LTI was observed in this time interval for argon, this is assumed to be consistent with an LTI-suppressed working point, i.e., the C parameter is either negative or close to zero. All analysis methods for hydrogen $\alpha = 0.28$ indicate that the C parameter is around 0.060–0.070, suggesting that LTI is occurring. For hydrogen $\alpha = 0.26$, the C is slightly higher, 0.070 ± 0.006. The effect of the ionisation degree is obvious, as the LTI signal in the probe trailing bunch energy residuals tends to increase for a lower ionisation degree.

As for the timescale of the evolution, parameter $1/B$, the lower ionisation degree seems to also increase it. For hydrogen $\alpha = 0.26$, the evolution timescale was estimated to be around 20 ns, 20.4 ± 0.8 ns. The higher ionisation degree working point resulted in a faster evolution, 16.4 ± 1.1 ns, tending towards the fastest, LTI-suppressed argon working point with a 14 ns (14.3 ± 0.6 ns) timescale. Despite this timescale, considering the $\tau_{rec.,R\approx0}$ estimation, the recovery of argon is reached at around 70 ns, longer than for hydrogen $\alpha = 0.28$, which is at 58 ns. This is a consequence of argon data having much stricter recovery conditions due to the data's low jitter. Hydrogen data suffered high jitter and thus high measurement uncertainty, so the estimated recovery times are biased towards earlier times. Normally, one could claim hydrogen long-term ion motion recovery much later than these timings, where conditions for equivalent plasma in perturbed and unperturbed cases are more reliable. This is more apparent by considering the $\tau_{rec.,5/B}$ recovery time estimation, where for hydrogen $\alpha = 0.28$ it is similar to the argon result. Nevertheless, comparing the two recovery times $\tau_{rec.,R\approx0}$ for hydrogen, the one for $\alpha = 0.26$ is twice as long as $\alpha = 0.28$, i.e., around 100 ns vs 60 ns. In addition, $\tau_{rec.,5/B}$ for $\alpha = 0.26$ is 20 ns longer than for $\alpha = 0.28$, thus indicating that LTI would delay the recovery of the plasma.

In summary, the probe bunch diagnostic allows the observation of on-axis plasma density changes at a very high temporal resolution. In hydrogen, equivalently to argon, an on-axis density reduction was observed for the first few nanoseconds. However, within twenty nanoseconds, a signature consistent with LTI appeared, which is not apparent in the high ionisation and low neutral gas density measurements in argon. This LTI effect was more significant for a lower ionisation degree in hydrogen and delayed the recovery of the plasma by tens of nanoseconds. This suggests that even if the LTI effect is not observable with OES, some ionisation may still be occurring in the vicinity of the axis. Additionally, this presents LTI as another long-term effect which must dissipate before acceleration can be performed under

the same plasma conditions, although it can be shortened by operating at higher ionisation degrees and lower initial neutral gas densities. Nevertheless, unlike the plasma density redistribution driven by the long-term ion motion, the long-term ionisation may not have any beam quality spoiling effects such as non-linear focusing fields. If it were only an increased on-axis density, this may even be harnessed in high-repetition-rate PWFA as a method for plasma density replenishment. This is further discussed in chapter 6.

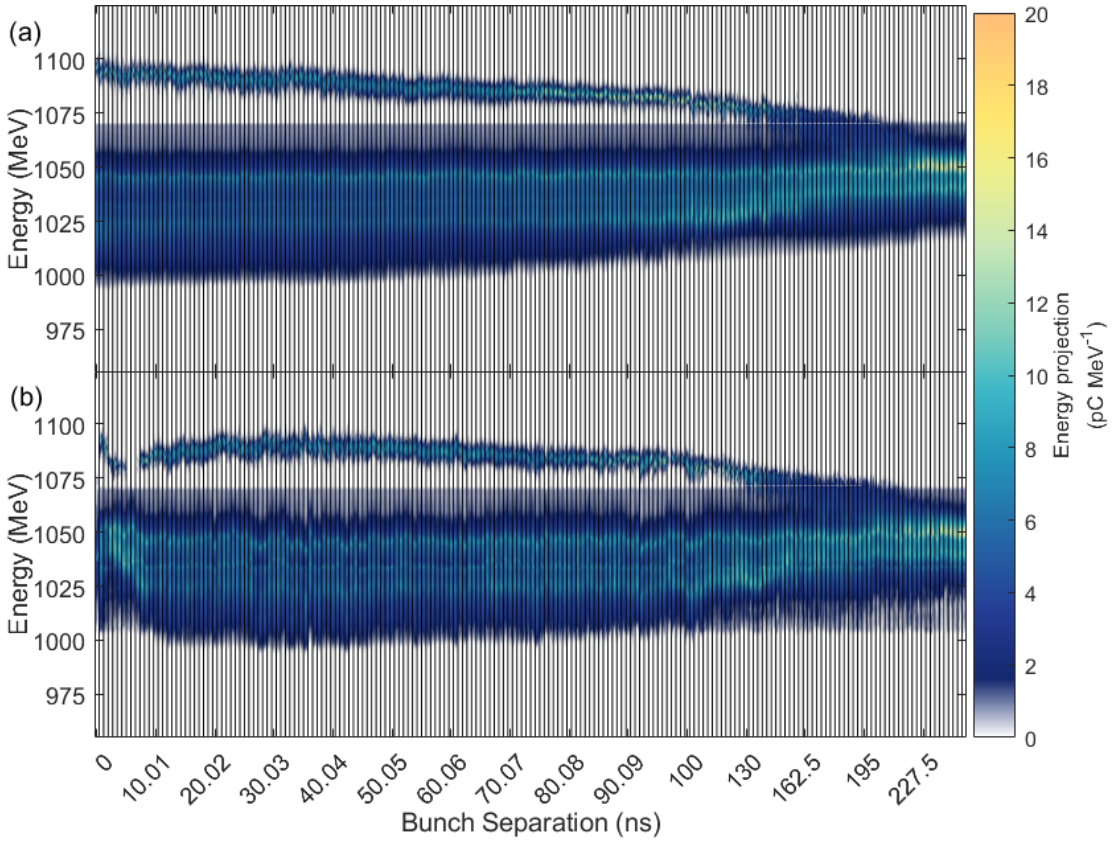

Figure 5.30: (a) Unperturbed and (b) perturbed probe bunch energy projections in hydrogen at ionisation degree $\alpha = 0.28$.

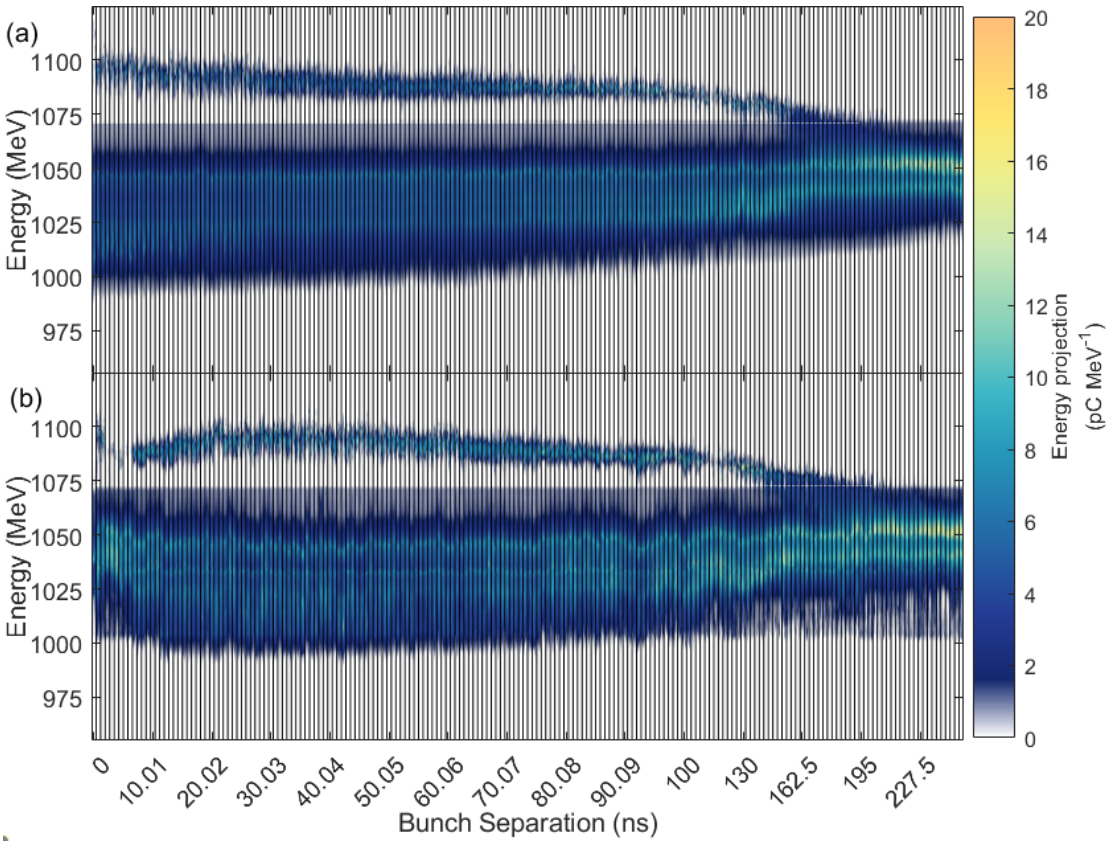

Figure 5.31: (a) Unperturbed and (b) perturbed probe bunch energy projections in hydrogen at ionisation degree $\alpha = 0.26$.

Chapter 6

Conclusion

6.1 Summary

Plasma-wakefield acceleration is a promising technology for future accelerator applications. However, PWFA at a high repetition rate, namely continuous kHz or burst-mode MHz operation, must be demonstrated to make its application a reality. As the driver deposits energy in the plasma, and the trailing bunch extracts it and is accelerated, there is a portion of the deposited energy which remains in the plasma. This energy feeds a range of processes that occur in plasma and preclude high-quality acceleration, thus the energy must dissipate, necessitating idle time before the next acceleration event.

Crucial investigations were carried out in the field which informed the processes and their timescale, which occur in the plasma as a result of a driven wakefield. The first observation of long-term ion motion was done by authors in ref. [102] and recently again at the AWAKE experiment in ref. [105], which resembled the theorised ion redistribution due to the ponderomotive force of the wakefield [103, 104, 170, 171]. The timescale of this long-term ion motion onset was observed to be in the range of a few to hundred picoseconds for these different experimental settings.

Additionally, another plasma density perturbation effect was observed by authors in ref. [100]. There, the deposited driver energy resulted in the surrounding neutral lithium ionisation by the moving ions and accompanying electrons, a process which is referred to as long-term ionisation in this work. An experimentally confirmed model of this evolution showed this to be the dominant process in the plasma over a nanosecond timescale.

It is clear that when considering the repetition rates needed in future facilities, the interest lies in the timescales of nanoseconds to a few microseconds. These re-

sults reveal that this is when the long-term ion motion and long-term ionisation will dominate the processes occurring in plasma, and also when they may dissipate. The investigation of how they affect the PWFA process and measurement of their lifetime, or in other words, the recovery time of plasma, are crucial tasks in the development of high-repetition-rate PWFA. The work done at FLASHForward before included further investigation of the plasma density redistribution driven by the long-term ion motion and on-axis plasma density increase due to long-term ionisation, presented in ref. [121]. To begin with, the probe electron driver and trailing bunch pair were utilised to investigate the changes in the on-axis plasma density and the plasma density channel curvature after the preceding bunch perturbation at nanosecond resolution. The argon plasma density channel would evolve from an on-axis density peak to an on-axis density depression, with the lowest density and peak channel curvature reached at around 10 nanoseconds. This nanoseconds channel evolution resembles the plasma waveguide formation, such as HOFI waveguides [43], where the redistribution is driven by a shock wave which forms from a high-pressure build-up on-axis. After perturbation, the channel dissipated through diffusive and conductive processes.

The exact lifetime of this channel and thus the plasma recovery time was measured at FLASHForward using this probe bunch diagnostic [122]. The same plasma-wakefield acceleration conditions, i.e., no perturbations on the probe driving and trailing bunch mean energies and the trailing bunch size were observed 63 nanoseconds after the previous bunch interaction with the plasma. This recovery time was measured at specific experimental settings: argon gas, $n_p \sim 10^{16}\,\mathrm{cm}^{-3}$ plasma density, and ionisation degree of $\alpha \sim 0.5$, which, if changed, would also affect the exact timing of the recovery.

While the timescale of this channel evolution has always been observed in the tens of nanoseconds range, it could be adjusted by changing experimental settings, namely plasma density and the ion mass. A lower plasma density would result in longer evolution as well as lower intensity of the plasma perturbation. The intensity could also be influenced by the driven wakefield strength; however, within the ranges explored, it did not affect the channel lifetime. As for the ion mass, it was expected that it may have a dependency on the square root of the ion mass. This would suggest that the plasma density channel could form and dissipate approximately 6 times faster in hydrogen than in argon. As a result, this informed the choice of hydrogen as an alternative to argon to explore in this work.

Besides long-term ion motion, additional ionisation effects may be taking place, and this was also presented in ref. [121]. A probe bunch diagnostic was used to observe the increase of on-axis plasma density over tens of nanoseconds up to microseconds in perturbed plasma for certain experimental settings. When the

initial plasma density is high and the density of neutral gas is low, in other words, when the degree of ionisation is high, no additional ionisation is observed. This ionisation-suppressing setting in argon was used in the investigations of the plasma density channel evolution, dependencies, and lifetime. However, if the degree of ionisation is reduced, and especially if the amount of neutral gas in the capillary is increased, the long-term ionisation would be observed, in some cases even masking the plasma density on-axis depression formation. This effect may present another obstacle to accelerating in plasma on the MHz timescale. While the method for suppressing the long-term ionisation was evident from these studies, the probe bunch diagnostic could only inform the plasma density change on the axis, and so an additional diagnostic would have to be used to confirm that the additional ionisation is not occurring off-axis for high degrees of ionisation.

The investigation of long-term ionisation in argon with optical emission spectroscopy was performed in this work. To begin with, by measuring the plasma density with OES, averaged transversely in the capillary, no additional ionisation was observed in argon for the ionisation degree equivalent to that set for the measurement of the recovery time in ref. [122]. This is consistent with the fact that no ionisation was observed with the probe bunch in these settings and also reveals that no significant ionisation may be happening off-axis.

Secondly, a range of ionisation degrees was explored in argon with OES, which indicated how the intensity and the timescale of long-term ionisation depends on the settings of the plasma. The onset of the long-term ionisation measured by the probe bunch in ref. [121] would occur over tens of nanoseconds, or for very low ionisation degrees even below the temporal resolution of the diagnostic, i.e., over less than a nanosecond. On the other hand, the onset of the more global long-term ionisation detectable with OES would be at a few hundred nanoseconds. Furthermore, its lifetime was measured to be at least a microsecond until the density would decay beyond the OES-detectable values. The onset and the lifetime would not change for a range of ionisation degrees at the same initial gas density; however, a lower initial gas density would result in a later onset and thus a shorter measurable duration.

Finally, as for the amount of ionisation, this scaled inversely with the ionisation degree. For the ionisation degree of $\alpha = 0.04$ the density could double with respect to the unperturbed plasma density. Interestingly, while the onset, if it can be interpreted to scale with the collisional timescale in the plasma, had an inverse dependence on the density of colliding particles as expected, the fact that the amount of long-term ionisation does not reduce for lower plasma densities cannot be explained by simple ionisation rate scalings. This dependency may stem from more nuanced relations between plasma density, wakefield strength, beam energy deposition, and plasma heating. This could be investigated experimentally by perturbing

plasma with bunches of different charge densities and thus driving wakefields of different strengths as well as adjusting both the perturber charge density and plasma density to change the amount of deposited energy in the plasma.

To investigate the plasma recovery time scaling with a different ion mass, the same probe bunch and OES measurements were performed in hydrogen. However, before this scaling can truly be measured, equivalent plasma conditions have to be set in hydrogen and argon. As a result, the long-term ionisation and the dependencies on plasma conditions in hydrogen were explored in this work. For similar initial atomic gas densities in the capillary, but a much higher ionisation degree $\alpha = 0.25$ in hydrogen, the observed LTI effect was of similar magnitude as in argon at ionisation degree $\alpha = 0.04$. Once again, this reveals the divergence of the LTI from simple ionisation rate scalings, as this gas species difference cannot be explained by the comparison of ionisation energy, and difference in wakefield strength. An intuitive difference discovered between argon and hydrogen LTI has been the onset and development timescale, which is expected from the ion mass term in the collisional timescales. In hydrogen, within the OES-detectable density window, the peak LTI would occur almost two times earlier than in argon.

Similar, yet slightly higher ionisation degrees, and much lower initial atomic gas density hydrogen working points were measured both with OES and the probe bunch. The OES measurements showed no additional ionisation above its resolution limits. However, the probe bunch indicated some on-axis plasma density increase, for both working points. The higher initial gas density working point in this set displayed a much higher LTI effect in the probe bunch diagnostic as expected from the investigations of LTI in argon. The rough recovery time estimation for both of these working points signified that despite the faster long-term ion motion evolution in hydrogen when compared to argon, the long-term ionisation would delay the recovery by tens of nanoseconds. For the higher initial atomic gas density working point, the recovery time was $\sim 100\,\mathrm{ns}$, and the lower initial atomic gas density working point resulted in a faster recovery.

From the measurements with the two diagnostics in argon and hydrogen and a range of plasma settings, this additional ionisation can be concluded to be a long-lasting microsecond-timescale effect if not suppressed. It is suppressible by setting a high ionisation degree in the capillary during the passage of the beam. In this case, while not fully suppressed, but minimised, it may delay the recovery of plasma from long-term ion motion by tens of nanoseconds.

The plasma channel driven by the long-term ion motion has been shown to have bunch-quality spoiling effects, mainly by loss of charge. As a result, for high-quality PWFA, it is necessary for this channel to dissipate and plasma to recover, the

timing of which was measured to be $\mathcal{O}(100)$ ns, which is not fundamentally limiting a MHz-burst repetition rate. The same could be assumed about long-term ionisation; however, whether it results in the spoilage of bunch quality as the non-uniform plasma channel does, is unknown.

6.2 Outlook

Contrary to long-term ion motion, long-term ionisation may only have the effect of increasing the trailing bunch energy gain because of the increased on-axis plasma density. In this case, long-term ionisation could be used as a technique to operate a PWFA module at a high repetition rate with some improvement to the accelerator efficiency. Firstly, this process would not define the shortest possible interbunch separation; that limit would still be the ion motion recovery at $\mathcal{O}(100)$ ns or hypothetically even lower at lower ion masses, allowing for MHz-bunch trains. Secondly, the ionisation, as a consequence of remaining energy in the plasma, could replace the technology necessary to maintain plasma at a uniform density during the bunch train i.e., successive high-voltage discharge pulses (in contrast to initial high-voltage discharge, which is necessary to create the plasma). This could not only reduce the resources needed to power such high-voltage pulser but also reduce the resources for cooling. This is because the same energy deposited in plasma that would be removed by the cooling system is now productive (maintains the plasma density), and the successive high-voltage pulser operation would not additionally heat the plasma source. However, the understanding of this effect is in its infancy. It would have to be explored, both in experiments and simulations, whether this ionisation lifetime is sufficient for desired interbunch separations of $\mathcal{O}(1)$ µs at 1 MHZ-bursts, and whether the beam quality and acceleration stability is preserved in these plasma conditions.

On the other hand, if further measurements and simulations reveal that a long-term ionisation occurs together with plasma density redistribution which results in non-uniform fields, the PWFA could not be operated during LTI. As a result, it would necessitate a specific usable parameter space of the plasma. In addition, if this parameter space is too restrictive and LTI cannot be easily suppressed, it may extend the plasma recovery lifetime, thus necessitating the field to focus on the development of CW kHz operation mode.

Both long-term ionisation and long-term ion motion are events triggered by the driven wakefield in the plasma once. However, for repeatable PWFA, the understanding of cumulative effects is also crucial. While both of the effects observed in this work may dissipate over a nanosecond-microsecond timescale, the resulting recovered plasma may have a high temperature. As it is being reionised by the

discharge for each following acceleration event, heat accumulates, and part of it conducts to the walls of the capillary. Thus, there may be a point, where the heat load on the structure of the plasma source will be too high, and it will require idle time before the next burst of bunches as well as a system of cooling. In addition, accumulating heating and higher temperature may affect the wakefield process, although some heating is tolerable [90, 95].

The long-term ion motion and long-term ionisation were investigated in this work with two different diagnostics and a range of experimental parameters, contributing to the understanding of the timescales and the dependencies of these effects. These findings imply that under certain plasma settings, the MHz-repetition rate could be theoretically feasible in plasma-wakefield accelerators. In order to confirm this, or find the alternative temporal bunch patterns for future accelerators, further studies may be conducted on the effect of long-term ionisation on the bunch quality as well as parameter ranges for its suppression.

Bibliography

[1] *The European X-Ray Free-Electron Laser Technical Design Report*, (2007), https://bib-pubdb1.desy.de/record/77248/files/european-xfel-tdr.pdf.

[2] B. Foster, R. D'Arcy, and C. A. Lindstrøm, "A hybrid, asymmetric, linear Higgs factory based on plasma-wakefield and radio-frequency acceleration", New Journal of Physics **25**, 093037 (2023) 10.1088/1367-2630/acf395, https://dx.doi.org/10.1088/1367-2630/acf395.

[3] G. E. Smith, "J. J. Thomson and The Electron: 1897-1899 An Introduction", The Chemical Educator **2**, 1–42 (1997) 10.1007/s00897970149a, https://doi.org/10.1007/s00897970149a.

[4] E. Rutherford, "LXXIX. The scattering of and particles by matter and the structure of the atom", The London, Edinburgh, and Dublin Philosophical Magazine and Journal of Science **21**, 669–688 (1911) 10.1080/14786440508637080, https://doi.org/10.1080/14786440508637080.

[5] J. C. Maxwell, "10 - Illustrations of the Dynamical Theory of Gases (Originally published in Phil. Mag., Vol. 19, pp. 19-32; Vol. 20, pp. 21-37 (1860); reprinted in The Scientific Papers of James Clerk Maxwell (ed. W. D. NIVEN), Cambridge University Press, 1890 Vol. I, pp. 377-409.)", *Kinetic Theory*, edited by S. BRUSH (Pergamon, 1965), pp. 148–171, https://doi.org/10.1016/B978-1-4831-9889-7.50017-3, https://www.sciencedirect.com/science/article/pii/B9781483198897500173.

[6] L. Boltzmann, "2. Weitere Studien über das Wärmegleichgewicht unter Gasmolekülen", *Kinetische Theorie II: Irreversible Prozesse* (De Gruyter, 1970), pp. 115–225, doi:10.1515/9783112596760-011, https://doi.org/10.1515/9783112596760-011.

[7] L. Boltzmann, "4. Über die Beziehung eines allgemeinen mechanischen Satzes zum zweiten Hauptsatze der Wärmetheorie", *Kinetische Theorie II: Irreversible Prozesse* (De Gruyter, 1970), pp. 240–247, doi:10.1515/9783112596760-013, https://doi.org/10.1515/9783112596760-013.

[8] C. Balarew, "The periodic table of chemical elements – history, nature, meaning", Pure and Applied Chemistry **91**, 2037–2042 (2019) doi:10.1515/pac-2019-0902, https://doi.org/10.1515/pac-2019-0902.

[9] A. Sessler, E. Wilson, and W. Scientific, *Engines of Discovery: A Century of Particle Accelerators*, EBL-Schweitzer (World Scientific, 2014), https://books.google.com/books?id=1oS6CgAAQBAJ.

[10] M. Ferrario and B. J. Holzer, "Introduction to Particle Accelerators and their Limitations", CAS - CERN Accelerator School: High Gradient Wakefield Accelerators (2020), https://arxiv.org/abs/2007.04075.

[11] J. M. J. Madey, "Stimulated Emission of Bremsstrahlung in a Periodic Magnetic Field", Journal of Applied Physics **42**, 1906–1913 (1971) 10.1063/1.1660466, https://doi.org/10.1063/1.1660466.

[12] B. Faatz et al., "Simultaneous operation of two soft x-ray free-electron lasers driven by one linear accelerator", New Journal of Physics **18**, 062002 (2016) 10.1088/1367-2630/18/6/062002, https://dx.doi.org/10.1088/1367-2630/18/6/062002.

[13] P. Emma et al., "First lasing and operation of an ångstrom-wavelength free-electron laser", Nature Photonics **4**, 641–647 (2010) 10.1038/nphoton.2010.176, https://doi.org/10.1038/nphoton.2010.176.

[14] W. Herr and B. Muratori, "Concept of luminosity", CAS - CERN Accelerator School: Intermediate Accelerator Physics, 10.5170/CERN-2006-002.361 (2006) 10.5170/CERN-2006-002.361, https://cds.cern.ch/record/941318.

[15] H. Wiedemann, *Particle Accelerator Physics*, Graduate Texts in Physics (Springer Open, 2015).

[16] *CLIC Conceptual Design Report*, (2012), https://clicdp.web.cern.ch/content/conceptual-design-report.

[17] G. Barr et al., *Particle physics in the LHC era*, First edition. (Oxford University Press, 2016).

[18] C. Accettura et al., "Towards a muon collider", The European Physical Journal C **83**, 864 (2023) 10.1140/epjc/s10052-023-11889-x, https://doi.org/10.1140/epjc/s10052-023-11889-x.

[19] L. Rossi, "The LHC main dipoles and quadrupoles toward series production", IEEE Transactions on Applied Superconductivity **13**, 1221–1228 (2003) 10.1109/TASC.2003.812639.

[20] *ILC Technical Design Report*, (2013), https://linearcollider.org/technical-design-report/.

[21] S. Dasu et al., *Strategy for Understanding the Higgs Physics: The Cool Copper Collider*, 2022, https://arxiv.org/abs/2203.07646.

[22] A. Abada et al., "FCC-ee: The Lepton Collider", The European Physical Journal Special Topics **228**, 261–623 (2019) 10.1140/epjst/e2019-900045-4, https://doi.org/10.1140/epjst/e2019-900045-4.

[23] W. Abdallah et al., *CEPC Technical Design Report (Accelerator)*, (Institute of High Energy Physics (IHEP), 2023), http://cepc.ihep.ac.cn/.

[24] A. Abada et al., "FCC-hh: The Hadron Collider", The European Physical Journal Special Topics **228**, 755–1107 (2019) 10.1140/epjst/e2019-900087-0, https://doi.org/10.1140/epjst/e2019-900087-0.

[25] W. Gai et al., "Experimental Demonstration of Wake-Field Effects in Dielectric Structures", Phys. Rev. Lett. **61**, 2756–2758 (1988) 10.1103/PhysRevLett.61.2756, https://link.aps.org/doi/10.1103/PhysRevLett.61.2756.

[26] B. D. O'Shea et al., "Observation of acceleration and deceleration in gigaelectron-volt-per-metre gradient dielectric wakefield accelerators", Nature Communications **7**, 12763 (2016) 10.1038/ncomms12763, https://doi.org/10.1038/ncomms12763.

[27] R. J. England et al., "Dielectric laser accelerators", Rev. Mod. Phys. **86**, 1337–1389 (2014) 10.1103/RevModPhys.86.1337, https://link.aps.org/doi/10.1103/RevModPhys.86.1337.

[28] V. I. Veksler, "The principle of coherent acceleration of charged particles", The Soviet Journal of Atomic Energy **2**, 525–528 (1957) 10.1007/BF01491001, https://doi.org/10.1007/BF01491001.

[29] T. Tajima and J. M. Dawson, "Laser Electron Accelerator", Phys. Rev. Lett. **43**, 267–270 (1979) 10.1103/PhysRevLett.43.267, https://link.aps.org/doi/10.1103/PhysRevLett.43.267.

[30] P. Chen et al., "Acceleration of electrons by the interaction of a bunched electron beam with a plasma", Physical review letters **54**, 693–696 (1985) 10.1103/PhysRevLett.54.693, https://link.aps.org/doi/10.1103/PhysRevLett.54.693.

[31] R. D. Ruth et al., "A Plasma Wake Field Accelerator", Particle Accelerators **17**, 171–189 (1985), https://cds.cern.ch/record/157249.

[32] D. Strickland and G. Mourou, "Compression of amplified chirped optical pulses", Optics Communications **56**, 219–221 (1985) https://doi.org/10.1016/0030-4018(85)90120-8, https://www.sciencedirect.com/science/article/pii/0030401885901208.

[33] A. Modena et al., "Electron acceleration from the breaking of relativistic plasma waves", Nature **377**, 606–608 (1995) 10.1038/377606a0, https://doi.org/10.1038/377606a0.

[34] J. Faure et al., "A laser-plasma accelerator producing monoenergetic electron beams", Nature **431**, 541–544 (2004) 10.1038/nature02963, https://doi.org/10.1038/nature02963.

[35] C. G. R. Geddes et al., "High-quality electron beams from a laser wakefield accelerator using plasma-channel guiding", Nature **431**, 538–541 (2004) 10.1038/nature02900, https://doi.org/10.1038/nature02900.

[36] S. P. D. Mangles et al., "Monoenergetic beams of relativistic electrons from intense laser-plasma interactions", Nature **431**, 535–538 (2004) 10.1038/nature02939, https://doi.org/10.1038/nature02939.

[37] A. J. Gonsalves et al., "Petawatt Laser Guiding and Electron Beam Acceleration to 8 GeV in a Laser-Heated Capillary Discharge Waveguide", Phys. Rev. Lett. **122**, 084801 (2019) 10.1103/PhysRevLett.122.084801, https://link.aps.org/doi/10.1103/PhysRevLett.122.084801.

[38] E. Esarey, C. B. Schroeder, and W. P. Leemans, "Physics of laser-driven plasma-based electron accelerators", Rev. Mod. Phys. **81**, 1229–1285 (2009) 10.1103/RevModPhys.81.1229, https://link.aps.org/doi/10.1103/RevModPhys.81.1229.

[39] D. J. Spence and S. M. Hooker, "Investigation of a hydrogen plasma waveguide", Phys. Rev. E **63**, 015401 (2000) 10.1103/PhysRevE.63.015401, https://link.aps.org/doi/10.1103/PhysRevE.63.015401.

[40] A. Butler, D. J. Spence, and S. M. Hooker, "Guiding of High-Intensity Laser Pulses with a Hydrogen-Filled Capillary Discharge Waveguide", Phys. Rev. Lett. **89**, 185003 (2002) 10.1103/PhysRevLett.89.185003, https://link.aps.org/doi/10.1103/PhysRevLett.89.185003.

[41] D. J. Spence, A. Butler, and S. M. Hooker, "Gas-filled capillary discharge waveguides", J. Opt. Soc. Am. B **20**, 138–151 (2003) 10.1364/JOSAB.20.000138, https://opg.optica.org/josab/abstract.cfm?URI=josab-20-1-138.

[42] C. G. Durfee and H. M. Milchberg, "Light pipe for high intensity laser pulses", Physical review letters **71**, 2409–2412 (1993) 10.1103/PhysRevLett.71.2409, https://link.aps.org/doi/10.1103/PhysRevLett.71.2409.

[43] R. Shalloo et al., "Hydrodynamic optical-field-ionized plasma channels", Physical Review E **97**, 053203 (2018) 10.1103/PhysRevE.97.053203, https://link.aps.org/doi/10.1103/PhysRevE.97.053203.

[44] W. P. Leemans et al., "GeV electron beams from a centimetre-scale accelerator", Nature Physics **2**, 696–699 (2006) 10.1038/nphys418, https://doi.org/10.1038/nphys418.

[45] J. D. Sadler et al., "Overcoming the dephasing limit in multiple-pulse laser wakefield acceleration", Phys. Rev. Accel. Beams **23**, 021303 (2020) 10.1103/PhysRevAccelBeams.23.021303, https://link.aps.org/doi/10.1103/PhysRevAccelBeams.23.021303.

[46] W. Horton and T. Tajima, "Pump depletion in the plasma-beat-wave accelerator", Phys. Rev. A **34**, 4110–4119 (1986) 10.1103/PhysRevA.34.4110, https://link.aps.org/doi/10.1103/PhysRevA.34.4110.

[47] E. Esarey et al., "Nonlinear Pump Depletion and Electron Dephasing in Laser Wakefield Accelerators", Advanced Accelerator Concepts: Eleventh Advanced Accelerator Concepts Workshop, Vol. 737, edited by V. Yakimenko, American Institute of Physics Conference Series (2004), pp. 578–584, 10.1063/1.1842594.

[48] B. Hidding et al., *Plasma Wakefield Accelerator Research 2019 - 2040: A community-driven UK roadmap compiled by the Plasma Wakefield Accelerator Steering Committee (PWASC)*, 2019, https://arxiv.org/abs/1904.09205.

[49] F. Salehi et al., "MeV electron acceleration at 1kHz with <10mJ laser pulses", Opt. Lett. **42**, 215–218 (2017) 10.1364/OL.42.000215, https://opg.optica.org/ol/abstract.cfm?URI=ol-42-2-215.

[50] L. Rovige et al., "Demonstration of stable long-term operation of a kilohertz laser-plasma accelerator", Phys. Rev. Accel. Beams **23**, 093401 (2020) 10.1103/PhysRevAccelBeams.23.093401, https://link.aps.org/doi/10.1103/PhysRevAccelBeams.23.093401.

[51] S. M. Hooker et al., "Multi-pulse laser wakefield acceleration: a new route to efficient, high-repetition-rate plasma accelerators and high flux radiation sources", Journal of physics. B, Atomic, molecular, and optical physics **47**, 234003–8 (2014) 10.1088/0953-4075/47/23/234003.

[52] J. Cowley et al., "Excitation and Control of Plasma Wakefields by Multiple Laser Pulses", Physical review letters **119**, 044802 (2017) 10.1103/PhysRevLett.119.044802, https://link.aps.org/doi/10.1103/PhysRevLett.119.044802.

[53] O. Jakobsson, S. M. Hooker, and R. Walczak, "Gev-Scale Accelerators Driven by Plasma-Modulated Pulses from Kilohertz Lasers", Phys. Rev. Lett. **127**, 184801 (2021) 10.1103/PhysRevLett.127.184801, https://link.aps.org/doi/10.1103/PhysRevLett.127.184801.

[54] J. J. van de Wetering, S. M. Hooker, and R. Walczak, "Multi-GeV wakefield acceleration in a plasma-modulated plasma accelerator", Phys. Rev. E **109**, 025206 (2024) 10.1103/PhysRevE.109.025206, https://link.aps.org/doi/10.1103/PhysRevE.109.025206.

[55] N. Delbos et al., "Lux – A laser–plasma driven undulator beamline", Nuclear Instruments and Methods in Physics Research Section A: Accelerators, Spectrometers, Detectors and Associated Equipment **909**, 3rd European Advanced Accelerator Concepts workshop (EAAC2017), 318–322 (2018) https://doi.org/10.1016/j.nima.2018.01.082, https://www.sciencedirect.com/science/article/pii/S0168900218301153.

[56] F. Albert et al., "2020 roadmap on plasma accelerators", New Journal of Physics **23**, 031101 (2021) 10.1088/1367-2630/abcc62, https://dx.doi.org/10.1088/1367-2630/abcc62.

[57] A. R. Maier et al., "Water-Window X-Ray Pulses from a Laser-Plasma Driven Undulator", Scientific Reports **10**, 5634 (2020) 10.1038/s41598-020-62401-4, https://doi.org/10.1038/s41598-020-62401-4.

[58] K. Baev et al., "X-ray Science at DESY: Upgrade Programs for the User Facilities FLASH and PETRA III", Synchrotron radiation news **37**, 4–11 (2024) 10.1080/08940886.2024.2312048, https://doi.org/10.1080/08940886.2024.2312048.

[59] J. Rosenzweig, "Nonlinear plasma dynamics in the plasma wake-field accelerator", Physical review letters **58**, 555–558 (1987) 10.1103/PhysRevLett.58.555, https://link.aps.org/doi/10.1103/PhysRevLett.58.555.

[60] J. B. Rosenzweig et al., "Acceleration and focusing of electrons in two-dimensional nonlinear plasma wake fields", Phys. Rev. A **44**, R6189–R6192 (1991) 10.1103/PhysRevA.44.R6189, https://link.aps.org/doi/10.1103/PhysRevA.44.R6189.

[61] T. Katsouleas, "Physical mechanisms in the plasma wake-field accelerator", Physical review. A, Atomic, molecular, and optical physics **33**, 2056–2064 (1986) 10.1103/PhysRevA.33.2056, https://link.aps.org/doi/10.1103/PhysRevA.33.2056.

[62] R. Keinigs and M. E. Jones, "Two-dimensional dynamics of the plasma wakefield accelerator", The Physics of Fluids **30**, 252–263 (1987) 10.1063/1.866183, https://doi.org/10.1063/1.866183.

[63] W. Lu et al., "A nonlinear theory for multidimensional relativistic plasma wave wakefields", Physics of plasmas **13**, 10.1063/1.2203364 (2006) 10.1063/1.2203364.

[64] W. Lu et al., "Nonlinear theory for relativistic plasma wakefields in the blowout regime", Physical review letters **96**, 165002 (2006) 10.1103/PhysRevLett.96.165002, https://link.aps.org/doi/10.1103/PhysRevLett.96.165002.

[65] C. E. Clayton et al., "Self-mapping the longitudinal field structure of a nonlinear plasma accelerator cavity", Nature Communications **7**, 12483 (2016) 10.1038/ncomms12483, https://doi.org/10.1038/ncomms12483.

[66] S. Schröder et al., "High-resolution sampling of beam-driven plasma wakefields", Nature Communications **11**, 5984 (2020) 10.1038/s41467-020-19811-9, https://doi.org/10.1038/s41467-020-19811-9.

[67] A. Knetsch et al., "Stable witness-beam formation in a beam-driven plasma cathode", Physical Review Accelerators and Beams **24**, 10.1103/physrevaccelbeams.24.101302 (2021) 10.1103/physrevaccelbeams.24.101302, http://dx.doi.org/10.1103/PhysRevAccelBeams.24.101302.

[68] J. C. Wood et al., "Brightness-Boosted Electron Bunches from a Plasma Accelerator", to be submitted (2024).

[69] S. Schröder et al., "Tunable and precise two-bunch generation at FLASHForward", Journal of Physics: Conference Series **1596**, 012002 (2020) 10.1088/1742-6596/1596/1/012002, https://dx.doi.org/10.1088/1742-6596/1596/1/012002.

[70] G. Loisch et al., "Observation of High Transformer Ratio Plasma Wakefield Acceleration", Phys. Rev. Lett. **121**, 064801 (2018) 10.1103/PhysRevLett.121.064801, https://link.aps.org/doi/10.1103/PhysRevLett.121.064801.

[71] K. V. Lotov, "Efficient operating mode of the plasma wakefield accelerator", Physics of Plasmas **12**, 053105 (2005) 10.1063/1.1889444, https://doi.org/10.1063/1.1889444.

[72] M. Tzoufras et al., "Beam Loading in the Nonlinear Regime of Plasma-Based Acceleration", Phys. Rev. Lett. **101**, 145002 (2008) 10.1103/PhysRevLett.101.145002, https://link.aps.org/doi/10.1103/PhysRevLett.101.145002.

[73] M. Litos et al., "High-efficiency acceleration of an electron beam in a plasma wakefield accelerator", Nature (London) **515**, 92–95 (2014) 10.1038/nature13882.

[74] C. A. Lindstrøm et al., "Energy-Spread Preservation and High Efficiency in a Plasma-Wakefield Accelerator", Phys. Rev. Lett. **126**, 014801 (2021) 10.1103/PhysRevLett.126.014801, https://link.aps.org/doi/10.1103/PhysRevLett.126.014801.

[75] F. Peña et al., *Energy Depletion and Re-Acceleration of Driver Electrons in a Plasma-Wakefield Accelerator*, 2024, https://arxiv.org/abs/2305.09581.

[76] C. Zhang et al., "Generation of meter-scale hydrogen plasmas and efficient, pump-depletion-limited wakefield excitation using 10 GeV electron bunches", Plasma physics and controlled fusion **66**, 25013 (2024) 10.1088/1361-6587/ad1ae4.

[77] C. A. Lindstrøm et al., "Emittance preservation in a plasma-wakefield accelerator", Nature Communications **15**, 6097 (2024) 10.1038/s41467-024-50320-1, https://doi.org/10.1038/s41467-024-50320-1.

[78] D. H. Whittum et al., "Electron-hose instability in the ion-focused regime", Phys. Rev. Lett. **67**, 991–994 (1991) 10.1103/PhysRevLett.67.991, https://link.aps.org/doi/10.1103/PhysRevLett.67.991.

[79] C. Huang et al., "Hosing Instability in the Blow-Out Regime for Plasma-Wakefield Acceleration", Phys. Rev. Lett. **99**, 255001 (2007) 10.1103/PhysRevLett.99.255001, https://link.aps.org/doi/10.1103/PhysRevLett.99.255001.

[80] T. J. Mehrling et al., "Accurate modeling of the hose instability in plasma wakefield accelerators", Physics of Plasmas **25**, 056703 (2018) 10.1063/1.5017960, https://doi.org/10.1063/1.5017960.

[81] A. Martinez de la Ossa, T. J. Mehrling, and J. Osterhoff, "Intrinsic Stabilization of the Drive Beam in Plasma-Wakefield Accelerators", Phys. Rev. Lett. **121**, 064803 (2018) 10.1103/PhysRevLett.121.064803, https://link.aps.org/doi/10.1103/PhysRevLett.121.064803.

[82] T. J. Mehrling et al., "Mechanisms for the mitigation of the hose instability in plasma-wakefield accelerators", Phys. Rev. Accel. Beams **22**, 031302 (2019) 10.1103/PhysRevAccelBeams.22.031302, https://link.aps.org/doi/10.1103/PhysRevAccelBeams.22.031302.

[83] T. J. Mehrling et al., "Mitigation of the Hose Instability in Plasma-Wakefield Accelerators", Phys. Rev. Lett. **118**, 174801 (2017) 10.1103/PhysRevLett.118.174801, https://link.aps.org/doi/10.1103/PhysRevLett.118.174801.

[84] J. B. Rosenzweig et al., "Effects of Ion Motion in Intense Beam-Driven Plasma Wakefield Accelerators", Phys. Rev. Lett. **95**, 195002 (2005) 10.1103/PhysRevLett.95.195002, https://link.aps.org/doi/10.1103/PhysRevLett.95.195002.

[85] E. Esarey et al., "Overview of plasma-based accelerator concepts", IEEE Transactions on Plasma Science **24**, 252–288 (1996) 10.1109/27.509991.

[86] A. Caldwell and K. V. Lotov, "Plasma wakefield acceleration with a modulated proton bunch", Physics of Plasmas **18**, 103101 (2011) 10.1063/1.3641973, https://doi.org/10.1063/1.3641973.

[87] W. D. Kimura et al., "Hollow plasma channel for positron plasma wakefield acceleration", Phys. Rev. ST Accel. Beams **14**, 041301 (2011) 10.1103/PhysRevSTAB.14.041301, https://link.aps.org/doi/10.1103/PhysRevSTAB.14.041301.

[88] S. Diederichs et al., "Positron transport and acceleration in beam-driven plasma wakefield accelerators using plasma columns", Phys. Rev. Accel. Beams **22**, 081301 (2019) 10.1103/PhysRevAccelBeams.22.081301, https://link.aps.org/doi/10.1103/PhysRevAccelBeams.22.081301.

[89] A. Doche et al., "Acceleration of a trailing positron bunch in a plasma wakefield accelerator", Scientific Reports **7**, 14180 (2017) 10.1038/s41598-017-14524-4, https://doi.org/10.1038/s41598-017-14524-4.

[90] S. Diederichs et al., "Temperature effects in plasma-based positron acceleration schemes using electron filaments", Physics of Plasmas **30**, 073104 (2023) 10.1063/5.0155489, https://doi.org/10.1063/5.0155489.

[91] S. Corde et al., "Multi-gigaelectronvolt acceleration of positrons in a self-loaded plasma wakefield", Nature **524**, 442–445 (2015) 10.1038/nature14890, https://doi.org/10.1038/nature14890.

[92] C. A. Lindstrøm, R. D'Arcy, and B. Foster, *Status of and upgrade concepts for HALHF: the hybrid, asymmetric, linear Higgs factory*, 2023, https://arxiv.org/abs/2312.04975.

[93] C. A. Lindstrøm, "Staging of plasma-wakefield accelerators", Phys. Rev. Accel. Beams **24**, 014801 (2021) 10.1103/PhysRevAccelBeams.24.014801, https://link.aps.org/doi/10.1103/PhysRevAccelBeams.24.014801.

[94] V. Lebedev, A. Burov, and S. Nagaitsev, "Efficiency versus instability in plasma accelerators", Phys. Rev. Accel. Beams **20**, 121301 (2017) 10.1103/PhysRevAccelBeams.20.121301, https://link.aps.org/doi/10.1103/PhysRevAccelBeams.20.121301.

[95] K. V. Lotov, "Fine wakefield structure in the blowout regime of plasma wakefield accelerators", Physical review special topics. PRST-AB. Accelerators and beams **6**, 9–14 (2003) 10.1103/PhysRevSTAB.6.061301, https://link.aps.org/doi/10.1103/PhysRevSTAB.6.061301.

[96] J. B. Rosenzweig et al., "Experimental Observation of Plasma Wake-Field Acceleration", Phys. Rev. Lett. **61**, 98–101 (1988) 10.1103/PhysRevLett.61.98, https://link.aps.org/doi/10.1103/PhysRevLett.61.98.

[97] V. Yakimenko et al., "FACET-II facility for advanced accelerator experimental tests", Phys. Rev. Accel. Beams **22**, 101301 (2019) 10.1103/PhysRevAccelBeams.22.101301, https://link.aps.org/doi/10.1103/PhysRevAccelBeams.22.101301.

[98] M. J. Hogan et al., "Plasma wakefield acceleration experiments at FACET", New Journal of Physics **12**, 055030 (2010) 10.1088/1367-2630/12/5/055030, https://dx.doi.org/10.1088/1367-2630/12/5/055030.

[99] I. Blumenfeld et al., "Energy doubling of 42GeV electrons in a metre-scale plasma wakefield accelerator", Nature **445**, 741–744 (2007) 10.1038/nature05538, https://doi.org/10.1038/nature05538.

[100] R. Zgadzaj et al., "Dissipation of electron-beam-driven plasma wakes", Nature communications **11**, 1–11 (2020) 10.1038/s41467-020-18490-w.

[101] C. Joshi et al., "Plasma wakefield acceleration experiments at FACET II", Plasma Physics and Controlled Fusion **60**, 034001 (2018) 10.1088/1361-6587/aaa2e3, https://dx.doi.org/10.1088/1361-6587/aaa2e3.

[102] M. F. Gilljohann et al., "Direct Observation of Plasma Waves and Dynamics Induced by Laser-Accelerated Electron Beams", Physical review. X **9**, 011046 (2019) 10.1103/PhysRevX.9.011046, https://link.aps.org/doi/10.1103/PhysRevX.9.011046.

[103] J. Vieira et al., "Ion motion in self-modulated plasma wakefield accelerators", Physical review letters **109**, 145005 (2012) 10.1103/PhysRevLett.109.145005, https://link.aps.org/doi/10.1103/PhysRevLett.109.145005.

[104] J. Vieira et al., "Ion motion in the wake driven by long particle bunches in plasmas", Physics of plasmas **21**, 10.1063/1.4876620 (2014) 10.1063/1.4876620.

[105] M. Turner et al., *Experimental Observation of Motion of Ions in a Resonantly Driven Plasma Wakefield Accelerator*, 2024, https://arxiv.org/abs/2406.16361.

[106] P. Muggli et al., "AWAKE readiness for the study of the seeded self-modulation of a 400 GeV proton bunch", Plasma Physics and Controlled Fusion **60**, 014046 (2017) 10.1088/1361-6587/aa941c, https://dx.doi.org/10.1088/1361-6587/aa941c.

[107] R. D'Arcy et al., "FLASHForward: plasma wakefield accelerator science for high-average-power applications", Philosophical Transactions of the Royal Society A: Mathematical, Physical and Engineering Sciences **377**, 20180392 (2019) 10.1098/rsta.2018.0392, https://royalsocietypublishing.org/doi/abs/10.1098/rsta.2018.0392.

[108] W. Ackermann et al., "Operation of a free-electron laser from the extreme ultraviolet to the water window", Nature Photonics **1**, 336–342 (2007) 10.1038/nphoton.2007.76, https://doi.org/10.1038/nphoton.2007.76.

[109] S. Schreiber and B. Faatz, "The free-electron laser FLASH", High Power Laser Science and Engineering **3**, e20 (2015) 10.1017/hpl.2015.16.

[110] C. A. Lindstrøm et al., "Progress of the FLASHForward X-2 high-beam-quality, high-efficiency plasma-accelerator experiment", Proceedings of The European Physical Society Conference on High Energy Physics — PoS(EPS-HEP2021), EPS-HEP2021 (2022), 10.22323/1.398.0880, http://dx.doi.org/10.22323/1.398.0880.

[111] J. Garland et al., "A Discharge Plasma Source Development Platform for Accelerators: The ADVANCE Lab at DESY", Proc. IPAC'22, International Particle Accelerator Conference 13 (2022), pp. 1886–1888, 10.18429/JACoW-IPAC2022-WEPOPT021, https://jacow.org/ipac2022/papers/wepopt021.pdf.

[112] L. Boulton et al., *Longitudinally resolved measurement of energy-transfer efficiency in a plasma-wakefield accelerator*, 2022, https://arxiv.org/abs/2209.06690.

[113] C. Lindstrøm and M. Thévenet, "Emittance preservation in advanced accelerators", Journal of Instrumentation **17**, P05016 (2022) 10.1088/1748-0221/17/05/P05016, https://dx.doi.org/10.1088/1748-0221/17/05/P05016.

[114] M. J. Hogan, "Electron and Positron Beam-Driven Plasma Acceleration", Rev. Accl. Sci. Tech. **09**, 63–83 (2016) 10.1142/S1793626816300036, https://doi.org/10.1142/S1793626816300036.

[115] T. Mehrling et al., "Transverse emittance growth in staged laser-wakefield acceleration", Phys. Rev. ST Accel. Beams **15**, 111303 (2012) 10.1103/PhysRevSTAB.15.111303, https://link.aps.org/doi/10.1103/PhysRevSTAB.15.111303.

[116] P. Muggli et al., "Meter-Scale Plasma-Wakefield Accelerator Driven by a Matched Electron Beam", Phys. Rev. Lett. **93**, 014802 (2004) 10.1103/PhysRevLett.93.014802, https://link.aps.org/doi/10.1103/PhysRevLett.93.014802.

[117] M. Thévenet et al., "Emittance growth due to misalignment in multistage laser-plasma accelerators", Phys. Rev. Accel. Beams **22**, 051302 (2019) 10.1103/PhysRevAccelBeams.22.051302, https://link.aps.org/doi/10.1103/PhysRevAccelBeams.22.051302.

[118] B. W. Montague, "Emittance growth from multiple scattering in the plasma beat-wave accelerator", 10.5170/CERN-1985-007.208 (1985) 10.5170/CERN-1985-007.208, https://cds.cern.ch/record/625633.

[119] Y. Zhao et al., "Modeling of emittance growth due to Coulomb collisions in plasma-based accelerators", Physics of plasmas **27**, 10.1063/5.0023776 (2020) 10.1063/5.0023776.

[120] B. Hidding et al., "Ultracold Electron Bunch Generation via Plasma Photocathode Emission and Acceleration in a Beam-Driven Plasma Blowout", Phys. Rev. Lett. **108**, 035001 (2012) 10.1103/PhysRevLett.108.035001, https://link.aps.org/doi/10.1103/PhysRevLett.108.035001.

[121] J. Chappell, "Experimental Study of Long Timescale Plasma Wakefield Evolution", PhD thesis (University College London, 2021).

[122] R. D'Arcy et al., "Recovery time of a plasma-wakefield accelerator", Nature **603**, 58–62 (2022) 10.1038/s41586-021-04348-8, https://doi.org/10.1038/s41586-021-04348-8.

[123] S. Corde, "Beam-driven plasma acceleration", Bad Honnef Physics School: Plasma Acceleration (2023).

[124] N. Barov and J. B. Rosenzweig, "Propagation of short electron pulses in underdense plasmas", Physical review. E, Statistical physics, plasmas, fluids, and related interdisciplinary topics **49**, 4407–4416 (1994) 10.1103/PhysRevE.49.4407, https://link.aps.org/doi/10.1103/PhysRevE.49.4407.

[125] L. Spitzer, *Physics of fully ionized gases / Lyman Spitzer, Jr.* 2nd rev. ed., Tracts on physics and astronomy ; no. 3 (Interscience, 1962).

[126] F. Chen, *Introduction to Plasma Physics and Controlled Fusion*, Third edition. (Springer Nature, 2015).

[127] J. M. Garland et al., "Combining laser interferometry and plasma spectroscopy for spatially resolved high-sensitivity plasma density measurements in discharge capillaries.", The Review of scientific instruments **92**, 013505 (2021) 10.1063/5.0021117.

[128] V. Lee et al., "Temporal evolution of the light emitted by a thin, laser-ionized plasma source", Phys. Plasmas **31**, 013104 (2024) 10.1063/5.0180416.

[129] C. Arran, "Techniques for high repetition rate laser wakefield acceleration", PhD thesis (University of Oxford, 2018).

[130] N. Bobrova et al., "Simulations of a hydrogen-filled capillary discharge waveguide", Physical review. E, Statistical, nonlinear, and soft matter physics **65**, 016407 (2002) 10.1103/PhysRevE.65.016407, https://link.aps.org/doi/10.1103/PhysRevE.65.016407.

[131] A. Esaulov et al., "MHD simulation of a fast hollow cathode capillary discharge", Plasma Physics and Controlled Fusion **43**, 571 (2001) 10.1088/0741-3335/43/4/313, https://dx.doi.org/10.1088/0741-3335/43/4/313.

[132] C. G. Durfee, J. Lynch, and H. M. Milchberg, "Development of a plasma waveguide for high-intensity laser pulses", Physical review. E, Statistical physics, plasmas, fluids, and related interdisciplinary topics **51**, 2368–2389 (1995) 10.1103/PhysRevE.51.2368, https://link.aps.org/doi/10.1103/PhysRevE.51.2368.

[133] P. Muggli et al., "Photo-ionized lithium source for plasma accelerator applications", IEEE transactions on plasma science **27**, 791–799 (1999) 10.1109/27.774685.

[134] M. J. Garland et al., "Plasma Sources and Diagnostics", 2019 CERN Accelerator School course on High Gradient Wakefield Accelerators, Sesimbra, Portugal (2019), https://doi.org/10.48550/arXiv.2007.08184.

[135] E. Gschwendtner et al., "AWAKE, The Advanced Proton Driven Plasma Wakefield Acceleration Experiment at CERN", Nuclear instruments methods in physics research. Section A, Accelerators, spectrometers, detectors and associated equipment **829**, 76–82 (2016) 10.1016/j.nima.2016.02.026.

[136] D. L. Bruhwiler et al., "Particle-in-cell simulations of tunneling ionization effects in plasma-based accelerators", Physics of Plasmas **10**, 2022–2030 (2003) 10.1063/1.1566027.

[137] S. Z. Li et al., "Head erosion with emittance growth in PWFA", AIP Conference Proceedings, Vol. 1507, 1 (2012), pp. 582–587, 10.1063/1.4773762.

[138] N. Vafaei-Najafabadi et al., "Limitation on the accelerating gradient of a wakefield excited by an ultrarelativistic electron beam in rubidium plasma", Phys. Rev. Accel. Beams **19**, 101303 (2016) 10.1103/PhysRevAccelBeams.19.101303, https://link.aps.org/doi/10.1103/PhysRevAccelBeams.19.101303.

[139] D. J. Spence and S. M. Hooker, "Investigation of a hydrogen plasma waveguide", Physical review. E, Statistical, nonlinear, and soft matter physics **63**, 1–4 (2001) 10.1103/PhysRevE.63.015401, https://link.aps.org/doi/10.1103/PhysRevE.63.015401.

[140] B. H. Broks, K. Garloff, and J. J. Van Der Mullen, "Nonlocal-thermal-equilibrium model of a pulsed capillary discharge waveguide", Physical review. E, Statistical, nonlinear, and soft matter physics **71**, 016401 (2005) 10.1103/PhysRevE.71.016401, https://link.aps.org/doi/10.1103/PhysRevE.71.016401.

[141] D. J. Spence, P. D. S. Burnett, and S. M. Hooker, "Measurement of the electron-density profile in a discharge-ablated capillary waveguide", Opt. Lett. **24**, 993–995 (Spence1999) 10.1364/OL.24.000993, https://opg.optica.org/ol/abstract.cfm?URI=ol-24-14-993.

[142] J. Townsend, *Electrons in Gases* (Hutchinson's Scientific and Technical Publications, 1948), https://books.google.com/books?id=NOafAAAAMAAJ.

[143] D. E. Davies and J. G. C. Milne, "First ionization coefficients in hydrogen, neon, and argon", British Journal of Applied Physics **10**, 301 (1959) 10.1088/0508-3443/10/7/301, https://dx.doi.org/10.1088/0508-3443/10/7/301.

[144] C. G. Durfee, T. R. Clark, and H. M. Milchberg, "Mode control in a two-pulse-excited plasma waveguide", Journal of the Optical Society of America. B, Optical physics **13**, 59–67 (1996) 10.1364/JOSAB.13.000059.

[145] T. R. Clark and H. M. Milchberg, "Time- and Space-Resolved Density Evolution of the Plasma Waveguide", Phys. Rev. Lett. **78**, 2373–2376 (1997) 10.1103/PhysRevLett.78.2373, https://link.aps.org/doi/10.1103/PhysRevLett.78.2373.

[146] N. Lemos et al., "Effects of laser polarization in the expansion of plasma waveguides", Physics of plasmas **20**, 10.1063/1.4825228 (2013) 10.1063/1.4825228.

[147] W. Lotz, "Electron-impact ionization cross-sections and ionization rate coefficients for atoms and ions from hydrogen to calcium", Zeitschrift für Physik **216**, 241–247 (1968) 10.1007/BF01392963, https://doi.org/10.1007/BF01392963.

[148] G. Voronov, "A Practical Fit Formula for Ionization Rate Coefficients of Atoms and Ions by Electron Impact: Z = 1–28", Atomic data and nuclear data tables **65**, 1–35 (1997) 10.1006/adnd.1997.0732.

[149] K. L. Bell et al., "Recommended Data on the Electron Impact Ionization of Light Atoms and Ions", Journal of Physical and Chemical Reference Data **12**, 891–916 (1983) 10.1063/1.555700.

[150] M. A. Lennon et al., "Recommended Data on the Electron Impact Ionization of Atoms and Ions: Fluorine to Nickel", Journal of Physical and Chemical Reference Data **17**, 1285–1363 (1988) 10.1063/1.555809, https://doi.org/10.1063/1.555809.

[151] A. V. Phelps, "Diffusion of charged particles in collisional plasmas. Free and ambipolar diffusion at low and moderate pressures", Journal of research of the National Institute of Standards and Technology **95**, 407–431 (1990) 10.6028/jres.095.035.

[152] H. R. Griem, *Principles of plasma spectroscopy / Hans R. Griem*, Cambridge monographs on plasma physics ; 2 (Cambridge University Press, 1997).

[153] X.-M. Zhu and Y.-K. Pu, "Optical emission spectroscopy in low-temperature plasmas containing argon and nitrogen: determination of the electron temperature and density by the line-ratio method", Journal of Physics D: Applied Physics **43**, 403001 (2010) 10.1088/0022-3727/43/40/403001, https://dx.doi.org/10.1088/0022-3727/43/40/403001.

[154] H. R. Griem, *Spectral line broadening by plasmas / Hans R. Griem*, Pure and applied physics ; v. 39 (Academic Press, 1974).

[155] M. A. Gigosos and V. Cardeñoso, "New plasma diagnosis tables of hydrogen Stark broadening including ion dynamics", Journal of Physics B: Atomic, Molecular and Optical Physics **29**, 4795 (1996) 10.1088/0953-4075/29/20/029, https://dx.doi.org/10.1088/0953-4075/29/20/029.

[156] M. Gigosos, M. González, and V. Cardeñoso-Payo, "Computer simulated Balmer-alpha, -beta and -gamma Stark line profiles for non-equilibrium plasmas diagnostics", Spectrochimica Acta Part B: Atomic Spectroscopy **58**, 1489 (2003) 10.1016/S0584-8547(03)00097-1.

[157] J. Rosenzweig, "Multiple-fluid models for plasma wake-field phenomena", Physical review. A, Atomic, molecular, and optical physics **40**, 5249–5255 (1989) 10.1103/PhysRevA.40.5249, https://link.aps.org/doi/10.1103/PhysRevA.40.5249.

[158] S. Lee et al., "Energy doubler for a linear collider", Phys. Rev. ST Accel. Beams **5**, 011001 (2002) 10.1103/PhysRevSTAB.5.011001, https://link.aps.org/doi/10.1103/PhysRevSTAB.5.011001.

[159] T. O. Raubenheimer, "An Afterburner at the ILC: The Collider Viewpoint", AIP conference proceedings **737**, 86–94 (2004) 10.1063/1.1842536.

[160] J. J. Su et al., "Plasma lenses for focusing particle beams", Phys. Rev. A **41**, 3321–3331 (1990) 10.1103/PhysRevA.41.3321, https://link.aps.org/doi/10.1103/PhysRevA.41.3321.

[161] M. J. Hogan et al., "Multi-GeV Energy Gain in a Plasma-Wakefield Accelerator", Phys. Rev. Lett. **95**, 054802 (2005) 10.1103/PhysRevLett.95.054802, https://link.aps.org/doi/10.1103/PhysRevLett.95.054802.

[162] S. Gessner et al., "Demonstration of a positron beam-driven hollow channel plasma wakefield accelerator", Nature communications **7**, 11785 (2016) 10.1038/ncomms11785.

[163] T. Chiou and T. Katsouleas, "High beam quality and efficiency in plasma-based accelerators", Physical review letters **81**, 3411–3414 (1998) 10.1103/PhysRevLett.81.3411, https://link.aps.org/doi/10.1103/PhysRevLett.81.3411.

[164] R. Gholizadeh et al., "Preservation of beam emittance in the presence of ion motion in future high-energy plasma-wakefield-based colliders", Physical review letters **104**, 155001 (2010) 10.1103/PhysRevLett.104.155001, https://link.aps.org/doi/10.1103/PhysRevLett.104.155001.

[165] C. Benedetti et al., "Emittance preservation in plasma-based accelerators with ion motion", Physical review. Accelerators and beams **20**, 111301 (2017) 10.1103/PhysRevAccelBeams.20.111301, https://link.aps.org/doi/10.1103/PhysRevAccelBeams.20.111301.

[166] T. J. Mehrling et al., "Suppression of Beam Hosing in Plasma Accelerators with Ion Motion", Physical review letters **121**, 264802 (2018) 10.1103/PhysRevLett.121.264802, https://link.aps.org/doi/10.1103/PhysRevLett.121.264802.

[167] V. A. Minakov, A. P. Sosedkin, and K. V. Lotov, "Accelerating field enhancement due to ion motion in plasma wakefield accelerators", Plasma physics and controlled fusion **61**, 114003 (2019) 10.1088/1361-6587/ab41a7.

[168] L. M. Gorbunov et al., "Ion momentum driven by a short intense laser pulse in an underdense plasma", Physics of Plasmas **7**, 375–381 (2000) 10.1063/1.873806, https://doi.org/10.1063/1.873806.

[169] L. M. Gorbunov, P. Mora, and R. R. Ramazashvili, "Steady ion momentum in nonlinear plasma waves", Phys. Rev. E **65**, 036401 (2002) 10.1103/PhysRevE.65.036401, https://link.aps.org/doi/10.1103/PhysRevE.65.036401.

[170] L. Gorbunov, P. Mora, and A. Solodov, "Plasma ions dynamics in the wake of a short laser pulse", Physical review letters **86**, 3332–3335 (2001) 10.1103/PhysRevLett.86.3332, https://link.aps.org/doi/10.1103/PhysRevLett.86.3332.

[171] L. M. Gorbunov, P. Mora, and A. A. Solodov, "Dynamics of a plasma channel created by the wakefield of a short laser pulse", Physics of plasmas **10**, 1124–1134 (2003) 10.1063/1.1559011.

[172] J. M. Dawson, "Nonlinear electron oscillations in a cold plasma", Physical review **113**, 383–387 (1959) 10.1103/PhysRev.113.383, https://link.aps.org/doi/10.1103/PhysRev.113.383.

[173] S. Sen Gupta and P. K. Kaw, "Phase Mixing of Nonlinear Plasma Oscillations in an Arbitrary Mass Ratio Cold Plasma", Phys. Rev. Lett. **82**, 1867–1870 (1999) 10.1103/PhysRevLett.82.1867, https://link.aps.org/doi/10.1103/PhysRevLett.82.1867.

[174] E. Adli et al., "Acceleration of electrons in the plasma wakefield of a proton bunch", Nature (London) **561**, 363–367 (2018) 10.1038/s41586-018-0485-4.

[175] V. K. Khudiakov, K. V. Lotov, and M. C. Downer, "Ion dynamics driven by a strongly nonlinear plasma wake", Plasma Physics and Controlled Fusion **64**, 045003 (2022) 10.1088/1361-6587/ac4523, https://dx.doi.org/10.1088/1361-6587/ac4523.

[176] M. Gilljohann, "Towards hybrid wakefield acceleration" (Ludwig-Maximilians-Universität München, 2022), http://nbn-resolving.de/urn:nbn:de:bvb:19-299858.

[177] K. V. Lotov, A. P. Sosedkin, and A. V. Petrenko, "Long-Term Evolution of Broken Wakefields in Finite-Radius Plasmas", Phys. Rev. Lett. **112**, 194801 (2014) 10.1103/PhysRevLett.112.194801, https://link.aps.org/doi/10.1103/PhysRevLett.112.194801.

[178] S. P. Mangles et al., "Electron acceleration in cavitated channels formed by a petawatt laser in low-density plasma", Physical review letters **94**, 245001 (2005) 10.1103/PhysRevLett.94.245001, https://link.aps.org/doi/10.1103/PhysRevLett.94.245001.

[179] R. Tarkeshian et al., "Transverse Space-Charge Field-Induced Plasma Dynamics for Ultraintense Electron-Beam Characterization", Physical review. X **8**, 021039 (2018) 10.1103/PhysRevX.8.021039, https://link.aps.org/doi/10.1103/PhysRevX.8.021039.

[180] A. Picksley et al., "Meter-scale conditioned hydrodynamic optical-field-ionized plasma channels", Physical review. E **102**, 053201 (2020) 10.1103/PhysRevE.102.053201, https://link.aps.org/doi/10.1103/PhysRevE.102.053201.

[181] L. O. Silva et al., "Ponderomotive force of quasiparticles in a plasma", Physical review. E, Statistical physics, plasmas, fluids, and related interdisciplinary topics **59**, 2273–2280 (1999) 10.1103/PhysRevE.59.2273, https://link.aps.org/doi/10.1103/PhysRevE.59.2273.

[182] G. I. Taylor, "The formation of a blast wave by a very intense explosion I. Theoretical discussion", Proc. Roy. Soc. (London) **201**, 159–174 (1950), http://www.jstor.org/stable/98395 (visited on 08/08/2024).

[183] G. I. Taylor, "The Formation of a Blast Wave by a Very Intense Explosion. II. The Atomic Explosion of 1945", Proc. Roy. Soc. (London) **201**, 175–186 (1950) 10.1098/rspa.1950.0050.

[184] R. Shalloo, "Hydrodynamic optical-field-ionized plasma waveguides for laser plasma accelerators", PhD thesis (University of Oxford, 2018).

[185] G. J. Hutchens, "Approximate near-field blast theory: A generalized approach", Journal of applied physics **88**, 3654–3658 (2000) 10.1063/1.1288785.

[186] K. Tiedtke et al., "The soft x-ray free-electron laser FLASH at DESY: beamlines, diagnostics and end-stations", New Journal of Physics **11**, 023029 (2009) 10.1088/1367-2630/11/2/023029, https://dx.doi.org/10.1088/1367-2630/11/2/023029.

[187] S. V. Milton et al., "Exponential Gain and Saturation of a Self-Amplified Spontaneous Emission Free-Electron Laser", Science **292**, 2037–2041 (2001) 10.1126/science.1059955, https://www.science.org/doi/abs/10.1126/science.1059955.

[188] M. Röhrs et al., "Time-resolved electron beam phase space tomography at a soft x-ray free-electron laser", Physical Review Special Topics-Accelerators and Beams **12**, 050704 (2009) 10.1103/PhysRevSTAB.12.050704, https://link.aps.org/doi/10.1103/PhysRevSTAB.12.050704.

[189] P. González Caminal, "Time-Resolved Phase-Space Characterisation of Plasma-Wakefield-Accelerated Electrons at FLASHForward", Dissertation (Universität Hamburg, 2022), 10.3204/PUBDB-2022-03578, https://bib-pubdb1.desy.de/record/480259.

[190] S. Wesch, *private communication*, 2024.

[191] E. Schneidmiller et al., "Two-colour operation of a soft x-ray FEL with alternation of undulator tunes", Applied Sciences **13**, 67 (2023) 10.3390/app13010067.

[192] J. Fraser, R. Sheffield, and E. Gray, "A new high-brightness electron injector for free electron lasers driven by RF linacs", Nuclear Instruments and Methods in Physics Research Section A: Accelerators, Spectrometers, Detectors and Associated Equipment **250**, 71–76 (1986) https://doi.org/10.1016/0168-9002(86)90862-4, https://www.sciencedirect.com/science/article/pii/0168900286908624.

[193] P. Piot et al., "Generation and Characterization of Electron Bunches with Ramped Current Profiles in a Dual-Frequency Superconducting Linear Accelerator", Phys. Rev. Lett. **108**, 034801 (2012) 10.1103/PhysRevLett.108.034801, https://link.aps.org/doi/10.1103/PhysRevLett.108.034801.

[194] K. Flöttmann et al., "Generation of Ultrashort Electron Bunches by Cancellation of Nonlinear Distortions in the Londitudinal Phase Space", (2001).

[195] S. Ackermann et al., "FLASH2020+ Conceptual Design Report", (2020), https://bib-pubdb1.desy.de/record/434950/files/FLASH2020pCDR.pdf.

[196] M. Scholz et al., "Extraction Arc for FLASH II", FEL'12, Nara, Japan, TUPD33 (2012), pp. 305–307, https://accelconf.web.cern.ch/FEL2012/papers/tupd33.pdf.

[197] P. Muggli et al., "Simple method for generating adjustable trains of picosecond electron bunches", Phys. Rev. ST Accel. Beams **13**, 052803 (2010) 10.1103/PhysRevSTAB.13.052803, https://link.aps.org/doi/10.1103/PhysRevSTAB.13.052803.

[198] E. Saldin, E. Schneidmiller, and M. Yurkov, "On the coherent radiation of an electron bunch moving in an arc of a circle", Nuclear Instruments and Methods in Physics Research Section A: Accelerators, Spectrometers, Detectors and Associated Equipment **398**, 373–394 (1997) https://doi.org/10.1016/S0168-9002(97)00822-X, https://www.sciencedirect.com/science/article/pii/S016890029700822X.

[199] C. E. Clayton et al., "Transverse Envelope Dynamics of a 28.5-GeV Electron Beam in a Long Plasma", Phys. Rev. Lett. **88**, 154801 (2002) 10.1103/PhysRevLett.88.154801, https://link.aps.org/doi/10.1103/PhysRevLett.88.154801.

[200] A. Aschikhin et al., "The FLASHForward facility at DESY", Nuclear Instruments and Methods in Physics Research Section A: Accelerators, Spectrometers, Detectors and Associated Equipment **806**, 175–183 (2016) https://doi.org/10.1016/j.nima.2015.10.005, https://www.sciencedirect.com/science/article/pii/S0168900215012103.

[201] M. W. Guetg et al., "Optimization of free electron laser performance by dispersion-based beam-tilt correction", Phys. Rev. ST Accel. Beams **18**, 030701 (2015) 10.1103/PhysRevSTAB.18.030701, https://link.aps.org/doi/10.1103/PhysRevSTAB.18.030701.

[202] D. Lipka et al., "Development of Cavity BPM for the European XFEL", proceedings of LINAC (2010).

[203] C. A. Lindstrøm et al., "Matching small β functions using centroid jitter and two beam position monitors", Phys. Rev. Accel. Beams **23**, 052802 (2020) 10.1103/PhysRevAccelBeams.23.052802, https://link.aps.org/doi/10.1103/PhysRevAccelBeams.23.052802.

[204] I. Okunev, I. Morozov, and N. Nefedov, "X-FEL Quadrupole with Gradient of 100 T/m", Physics Procedia **84**, 101–107 (2016) 10.1016/j.phpro.2016.11.018.

[205] F. Peña, PhD thesis (Universität Hamburg, 2024).

[206] R. D'Arcy et al., "Longitudinal Phase Space Reconstruction at FLASHForward Using a Novel Transverse Deflection Cavity, PolariX-TDS", 10.18429/JACoW-IPAC2018-TUPML017 (2018) 10.18429/JACoW-IPAC2018-TUPML017.

[207] B. Marchetti et al., "X-band TDS project", Proc. IPAC'17, MOPAB044 (2017) 10.18429/JACoW-IPAC2017-MOPAB044, https://cds.cern.ch/record/2289148.

[208] A. Grudiev, "Design of Compact High power RF Components at X-band", (2016), https://cds.cern.ch/record/2158484.

[209] S. Jaster-Merz et al., "5D tomographic phase-space reconstruction of particle bunches", arXiv preprint arXiv:2305.03538 (2023), https://arxiv.org/abs/2305.03538.

[210] W. An et al., "Strategies for mitigating the ionization-induced beam head erosion problem in an electron-beam-driven plasma wakefield accelerator", Phys. Rev. ST Accel. Beams **16**, 101301 (2013) 10.1103/PhysRevSTAB.16.101301, https://link.aps.org/doi/10.1103/PhysRevSTAB.16.101301.

[211] A. Gonsalves et al., "Transverse interferometry of a hydrogen-filled capillary discharge waveguide", Physical review letters **98**, 025002 (2007) 10.1103/PhysRevLett.98.025002, https://link.aps.org/doi/10.1103/PhysRevLett.98.025002.

[212] L. Schaper et al., "Longitudinal gas-density profilometry for plasma-wakefield acceleration targets", Nuclear Instruments and Methods in Physics Research Section A: Accelerators, Spectrometers, Detectors and Associated Equipment **740**, Proceedings of the first European Advanced Accelerator Concepts Workshop 2013, 208–211 (2014) https://doi.org/10.1016/j.nima.2013.10.052, https://www.sciencedirect.com/science/article/pii/S0168900213014332.

[213] X. L. Xu et al., "Physics of Phase Space Matching for Staging Plasma and Traditional Accelerator Components Using Longitudinally Tailored Plasma Profiles", Phys. Rev. Lett. **116**, 124801 (2016) 10.1103/PhysRevLett.116.124801, https://link.aps.org/doi/10.1103/PhysRevLett.116.124801.

[214] C. E. Doss et al., "Laser-ionized, beam-driven, underdense, passive thin plasma lens", Phys. Rev. Accel. Beams **22**, 111001 (2019) 10.1103/PhysRevAccelBeams.22.111001, https://link.aps.org/doi/10.1103/PhysRevAccelBeams.22.111001.

[215] J. van Tilborg et al., "High-sensitivity plasma density retrieval in a common-path second-harmonic interferometer through simultaneous group and phase velocity measurement", Physics of Plasmas **26**, 023106 (2019) 10.1063/1.5080269, https://doi.org/10.1063/1.5080269.

[216] J. van Tilborg et al., "Density characterization of discharged gas-filled capillaries through common-path two-color spectral-domain interferometry", Opt. Lett. **43**, 2776–2779 (2018) 10.1364/OL.43.002776, https://opg.optica.org/ol/abstract.cfm?URI=ol-43-12-2776.

[217] P. Comon and C. Jutten, *Handbook of Blind Source Separation : Independent Component Analysis and Applications.* (Elsevier Science, 2010).